

Anblagan, Devasuda (2012) MRI of foetal development.
PhD thesis, University of Nottingham.

Access from the University of Nottingham repository:
<http://eprints.nottingham.ac.uk/30592/1/575373.pdf>

Copyright and reuse:

The Nottingham ePrints service makes this work by researchers of the University of Nottingham available open access under the following conditions.

This article is made available under the University of Nottingham End User licence and may be reused according to the conditions of the licence. For more details see:
http://eprints.nottingham.ac.uk/end_user_agreement.pdf

For more information, please contact eprints@nottingham.ac.uk

MRI of Foetal Development

Devasuda Anblagan, B.Sc.

Thesis Submitted to the University of Nottingham
for the Degree of Doctor of Philosophy

June 2012

Abstract

Foetal MRI represents a non-invasive imaging technique that allows detailed visualisation of foetus in utero and the maternal structure. This thesis outlines the quantitative imaging techniques used to investigate the effect of maternal diabetes and maternal smoking on foetal development at 1.5 Tesla.

The effect of maternal diabetes on placental blood flow and foetal growth was studied. The placental images were acquired using Echo Planar Imaging and blood flow was measured using Intra Voxel Incoherent Motion. The results indicate that peak blood flow in the basal plate and chorionic plate increases across gestation in both normal and diabetic pregnancies. Conversely, diffusion in the whole placenta decreases across gestation, with a more pronounced decrease in diabetic placentae.

Following this, a method was developed to use a T_1 weighted fat suppressed MRI scan to quantify foetal fat images in-utero. In addition, Half Fourier Single-shot Turbo spin Echo (HASTE) and balanced Fast Field Echo (bFFE) were used to acquire images encompassing the whole foetus in three orthogonal planes. These scans were used to measure foetal volume, foetal length and shoulder width. The data shows that foetal fat volume and intra-abdominal fat were increased in foetuses of diabetic mothers at third trimester.

The HASTE and bFFE sequences were also used to study the effect of maternal smoking on foetal development. Here, foetal organ volumes, foetal and placental volume, shoulder width and foetal length were measured using a semi automatic approach based on the concept of edge detection and a stereological method, the Cavalieri technique. The data shows that maternal smoking has significant negative effect on foetal organ growth and foetal growth, predominantly foetal kidney and foetal volume.

The work described here certainly has a great potential in non-invasive assessment of abnormal placental function and can be used to study foetal development.

**This thesis is dedicated to my
parents who have given me the
opportunity of education and
unconditional love throughout
my life.**

Anblagan Veerapandian

and

Letchumy Mari

Acknowledgements

It would not have been possible to write this doctoral thesis without the invaluable help and support of the kind people around me whose contribution came in assorted ways to the research and making of the thesis. It is of great pleasure to convey my gratitude to those who deserve special mention in my humble acknowledgements here.

First and foremost, I would like to extend my deepest respect and eternal gratitude to my supervisor, Professor Penny Gowland, for her supervision, guidance and advice throughout my time as her student. Above all, she has always been accessible and provided me with unflinching encouragement and support in the most needed times. Her truly scientific intuition and dedication to research has been an inspiration to many, including me. It has enriched my growth as a student, researcher and scientist in the making. I am in great debt to her, more than she knows.

I owe my deepest gratitude to Dr Nia Wyn Jones, Dr Ruta Deshpande and Dr George Bugg for recruiting all the participants for my studies and their valuable science discussion on matters relating to foetal development. A very special thank you goes to Dr Nia Wyn Jones for her guidance in different statistical models and being such a great friend. I am also very grateful to Carolyn Costigan and Dr Caroline Hoad for assisting with the MR scans conducted for this thesis. This thesis would never have taken shape without their expert involvement. I would also like to thank Professor Tomas Paus, Professor Peter Mansell and Professor Neil Roberts for their collaborative work and constructive comments on the work reported in this thesis.

I would also like to take the opportunity to recognise the support and assistance provided by the staff at the Sir Peter Mansfield Magnetic Resonance Centre. Special mention needs to be directed towards Dr Andrew Peters for unstinting support on computing issues. I would also like to extend my gratitude to Dr Samuel Wharton for stimulating computer-programming discussion. My heartfelt thanks go to Peter Roberts for his kindness, friendship and support throughout the process of writing up my thesis. Further thank you goes to all my colleagues

in the office who created the perfect atmosphere to work in: Dr Andreas Bungert, Dr Amany Alsuraihi, Dr Jenni Dixon, Dr Waldek Senczenko, Andre Autunes, Dr Olivier Mougin, Dr Emma Hall, Glyn Spencer, Anna Blazejewska, Gemma Chaddock, Stephen Bawden, Paula Croal, Mahamoud Hussein, Darren Price, Theodore Hughes Riley, Dr Rosa Sanchez, Dr Josef Granwehr, Dr Elisa Placidi, Dr Ali Al-Radaideh, Dr Ian Driver, Thomas Allan, Joanne Hale, Dr David Lilburn, Gerda Grimnisdottir, Jack Harmer and Maria Liljeroth. A warm thank you to Lesley Martin and Elizabeth Croal for providing various administration support.

Words fail to express my deepest appreciation to my parents and sister for their inseparable support and prayers. They have endlessly loved, motivated and cheered me in the most stressful times of my life. My dad has been the pillar for many of my achievements. He has tirelessly accompanied me during the most crucial periods of my life, exams. When I was a school student, he would stay up at night accompanying me while I revised for exams. When I left home to further my studies abroad, he made sure he woke up early every morning to check on me before I went to bed every night. As for my mom, besides her supportive words and care, her everlasting love came in a different shape and taste, healthy delicious dishes. My sister has always been a good friend to share my thoughts and joy. Her encouragement has led me to complete various challenging tasks, such as this thesis. I would also like to thank my friends Bona Burlison and Joshua Gaskin for keeping me sane by accompanying me to countless dance nights, movies and social events.

Finally, thank you God for introducing me to a life full of joy and challenge that made me a stronger individual. I would like to thank everybody who was important to the successful achievement of this thesis, as well as express my apology that I could not mention one by one personally.

Contents

- CHAPTER 1: INTRODUCTION 1
 - 1.1 THE SCOPE OF THIS THESIS 2
- CHAPTER 2: MAGNETIC RESONANCE IMAGING 4
 - 2.1 OVERVIEW 4
 - 2.2 BASIS PRINCIPLES OF MAGNETIC RESONANCE IMAGING 4
 - 2.2.1 NUCLEAR MAGNETIC RESONANCE THEORY 4
 - 2.2.1.1 CLASSICAL MODEL..... 7
 - 2.2.1.2 QUANTUM MODEL.....10
 - 2.2.2 INTERACTION WITH OSCILLATING ELECTROMAGNETIC FIELD (B_1)..... 13
 - 2.2.2.1 LABORATORY FRAME OF REFERENCE..... 14
 - 2.2.2.2 ROTATING FRAME OF REFERENCE..... 16
 - 2.2.3 FREE INDUCTION DECAY (FID) 18
 - 2.2.4 BLOCH EQUATIONS..... 19
 - 2.2.5 RELAXATION AND MEASUREMENT OF NMR PARAMETERS 19
 - 2.2.5.1 LONGITUDINAL RECOVERY (T_1 RELAXATION)..... 20
 - 2.2.5.2 TRANSVERSE DECAY (T_2 RELAXATION)..... 24
 - 2.2.5.3 REVERSIBLE LOSS OF TRANSVERSE COHERENCE (T_2^* RELAXATION)..... 26
 - 2.2.5.4 PROTON DENSITY (PD)..... 27
 - 2.2.6 FACTORS AFFECTING THE RELAXATION TIMES 27
 - 2.2.6.1 MEASUREMENT FREQUENCY (FIELD STRENGTH)..... 27
 - 2.2.6.2 VISCOSITY AND TEMPERATURE..... 28
 - 2.2.6.3 WATER CONTENT..... 29
 - 2.2.6.4 PARAMAGNETIC CONTENT..... 29
 - 2.3 PRINCIPLE OF MR IMAGING.....32
 - 2.3.1 MAGNETIC FIELD GRADIENTS 33
 - 2.3.1.1 SLICE SELECTION 34
 - 2.3.1.2 SPATIAL ENCODING..... 36
 - 2.3.1.2.1 FREQUENCY ENCODING..... 37
 - 2.3.1.2.2 PHASE ENCODING..... 38
 - 2.3.2 FOURIER TRANSFORM AND K-SPACE 40

2.3.2.1 THEORY..... 40

2.3.2.2 SIGNAL SAMPLING..... 43

2.3.3 MR IMAGING TECHNIQUES 44

2.3.3.1 FAST LOW ANGLE SHOT..... 45

2.3.3.2 HALF FOURIER SINGLE-SHOT TURBO SPIN ECHO..... 47

2.3.3.3 BALANCED FAST FIELD ECHO..... 48

2.3.3.4 ECHO PLANAR IMAGING..... 50

2.3.3.5 PULSED GRADIENT SPIN ECHO..... 55

2.3.4 MR ARTEFACTS..... 58

2.3.4.1 PATIENT RELATED MR ARTEFACTS..... 59

2.3.4.2 SIGNAL PROCESSING DEPENDENT ARTEFACTS..... 63

2.3.4.3 HARDWARE RELATED ARTEFACTS..... 66

2.4 COMPONENTS OF A MAGNETIC RESONANCE IMAGING SYSTEM 68

2.4.1 MAGNET..... 69

2.4.2 GRADIENT SYSTEM 71

2.4.3 RADIO FREQUENCY SYSTEM 72

2.4.4 COMPUTER SYSTEM..... 73

2.5 REFERENCES 74

CHAPTER 3: FOETAL MAGNETIC RESONANCE IMAGING..... 80

3.1 OVERVIEW 80

3.2 INTRODUCTION TO FOETAL IMAGING 80

3.2.1 AVAILABILITY AND ACCESSIBILITY..... 82

3.2.2 MATERNAL IMAGING FACTORS 82

3.2.3 GESTATIONAL AGE..... 83

3.2.4 IMAGE RESOLUTION 84

3.2.5 THREE DIMENSIONAL RENDERING OF SURFACE ANATOMY..... 85

3.2.6 OPERATOR DEPENDENCE..... 85

3.2.7 DURATION OF THE EXAMINATION 85

3.2.8 OTHER ISSUES..... 86

3.2.9 CONCLUSION 86

3.3 SAFETY OF FOETAL MAGNETIC RESONANCE IMAGING..... 86

3.3.1 STATIC FIELD..... 87

3.3.2 TIME-VARYING MAGNETIC GRADIENT FIELDS 91

3.3.3 RADIO FREQUENCY FIELDS 93

3.3.4 GENERAL SAFETY 94

3.3.5 CONCLUSION	95
3.4 REFERENCES	97
CHAPTER 4: ANATOMY AND DEVELOPMENT OF FOETUS	103
4.1 OVERVIEW	103
4.2 INTRODUCTION TO FOETAL IMAGING	103
4.2.1 PLACENTA	106
4.2.2 FOETAL BRAIN.....	110
4.2.3 FOETAL RESPIRATORY SYSTEM	111
4.2.4 FOETAL LIVER	115
4.2.5 FOETAL URINARY SYSTEM	116
4.3 CONCLUSION	119
4.4 REFERENCES	120
CHAPTER 5: THE EFFECT OF MATERNAL DIABETES ON PLACENTAL BLOOD FLOW.....	123
5.1 OVERVIEW	123
5.2 INTRODUCTION.....	124
5.2.1 INTRA VOXEL INCOHERENT MOTION (IVIM)	127
5.2.2 RELIABILITY AND REPRODUCIBILITY	129
5.3 METHOD	131
5.3.1 RECRUITMENT CRITERIA.....	132
5.3.2 SCANNING PROTOCOL	132
5.3.3 DATA ANALYSIS.....	133
5.3.3.1 MOTION CORRECTION	134
5.3.3.2 RELIABILITY AND REPRODUCIBILITY ASSESSMENT OF THE MEASUREMENT ANALYSED ON THE IVIM PROGRAM	140
5.3.3.2.1 INTRA-OBSERVER AND INTER-OBSERVER RELIABILITY TEST	141
5.3.3.2.2 COMPARISON BETWEEN SINGLE AND MULTIPLE MASKING.....	141
5.3.3.2.3 SLICE-BY-SLICE COMPARISON	142
5.3.3.3 THE APPLICATION OF THE IVIM PROGRAM TO STUDY THE EFFECT OF MATERNAL DIABETES ON PLACENTAL BLOOD FLOW	142
5.4 RESULTS.....	143
5.4.1 RELIABILITY AND REPRODUCIBILITY ASSESSMENT OF THE MEASUREMENT ANALYSED ON THE IVIM PROGRAM	143
5.4.1.1 INTRA-OBSERVER AND INTER-OBSERVER RELIABILITY TEST	143

5.4.1.2 COMPARISON BETWEEN SINGLE AND MULTIPLE MASKING.....	151
5.4.1.3 SLICE-BY-SLICE COMPARISON.....	153
5.4.2 THE APPLICATION OF THE IVIM PROGRAM TO STUDY THE EFFECT OF MATERNAL DIABETES ON PLACENTAL BLOOD FLOW	155
5.4.2.1 STUDY POPULATION.....	155
5.4.2.2 CLINICAL OUTCOMES.....	156
5.4.2.3 THE APPLICATION OF THE IVIM.....	156
5.4.2.4 COMPARISON OF MEAN <i>F</i> AND MEAN <i>D</i> MEASUREMENTS.....	164
5.5 DISCUSSION AND CONCLUSION	165
5.5.1 RELIABILITY AND REPRODUCIBILITY OF THE IVIM PROGRAM.....	167
5.5.2 THE APPLICATION OF THE IVIM PROGRAM TO STUDY THE EFFECT OF MATERNAL DIABETES ON PLACENTAL BLOOD FLOW	169
5.6 REFERENCES	174
 CHAPTER 6: THE EFFECT OF MATERNAL DIABETES ON FOETAL ADIPOSITY	 182
6.1 OVERVIEW	182
6.2 INTRODUCTION.....	183
6.3 METHOD	185
6.3.1 RECRUITMENT CRITERIA.....	186
6.3.2 SCANNING PROTOCOL	186
6.3.3 DATA ANALYSIS.....	188
6.3.3.1 FOETAL ADIPOSITY QUANTIFICATION PROGRAM.....	188
6.3.3.2 THE APPLICATION OF FOETAL ADIPOSITY QUANTIFICATION PROGRAM TO STUDY THE EFFECT OF MATERNAL DIABETES ON FOETAL ADIPOSITY.....	193
6.3.3.3 INTRA-ABDOMINAL FAT.....	193
6.3.3.4 FOETAL VOLUME.....	194
6.3.3.5 FOETAL LENGTH AND SHOULDER WIDTH.....	194
6.3.3.6 FOETAL VOLUME INDEX.....	194
6.3.3.7 STATISTICAL ANALYSIS TO STUDY THE EFFECT OF MATERNAL DIABETES ON FOETAL GROWTH.....	195
6.4 RESULTS.....	196
6.4.1 FOETAL ADIPOSITY QUANTIFICATION PROGRAM.....	196
6.4.1.1 VALIDITY OF THE FOETAL ADIPOSITY QUANTIFICATION PROGRAM.....	196
6.4.1.2 RELIABILITY AND REPRODUCIBILITY OF THE FOETAL FAT MEASUREMENT ANALYSED USING THE FOETAL ADIPOSITY QUANTIFICATION PROGRAM.....	196
6.4.2 THE EFFECT OF MATERNAL DIABETES ON FOETAL GROWTH	198

6.4.2.1 STUDY POPULATION.....	198
6.4.2.2 ULTRASOUND MEASUREMENTS AND CLINICAL OUTCOMES.....	199
6.4.2.3 FOETAL MR MEASUREMENTS.....	200
6.4.2.4 CORRELATION BETWEEN CLINICAL MEASUREMENTS AND FOETAL MR MEASUREMENTS.....	205
6.4.2.5 INTRA-ABDOMINAL FAT.....	206
6.5 DISCUSSION AND CONCLUSION	206
6.6 REFERENCES	212
 CHAPTER 7: THE EFFECT OF MATERNAL SMOKING ON FOETAL ORGAN GROWTH	
7.1 OVERVIEW	216
7.2 INTRODUCTION.....	217
7.3 METHOD	219
7.3.1 RECRUITMENT CRITERIA.....	219
7.3.2 SCANNING PROTOCOL	220
7.3.3 DATA ANALYSIS.....	222
7.3.3.1 FOETAL ORGAN, PLACENTA AND FOETAL VOLUME.....	222
7.3.3.2 FOETAL LENGTH AND SHOULDER WIDTH.....	224
7.3.3.3 STATISTICAL ANALYSIS TO STUDY THE EFFECT OF MATERNAL SMOKING ON FOETAL GROWTH.....	224
7.4 RESULTS.....	225
7.4.1 THE EFFECT OF MATERNAL SMOKING ON FOETAL GROWTH	225
7.4.1.1 STUDY POPULATION.....	225
7.4.1.2 ULTRASOUND MEASUREMENTS AND CLINICAL OUTCOMES.....	226
7.4.1.3 FOETAL MR MEASUREMENTS.....	227
7.5 DISCUSSION AND CONCLUSION	234
7.6 REFERENCES	239
 CHAPTER 8: CONCLUSION	
8.1 FUTURE WORK.....	251
8.2 FINAL OVERVIEW	252
 APPENDIX.....	 253

Chapter 1

Introduction

Magnetic Resonance Imaging (MRI) was introduced to the medical diagnostic world as a potential non-invasive imaging technique in the early 1970s. It is based on the concept of Nuclear Magnetic Resonance (NMR). Since then, MRI has undergone various scientific and technological advancements, emerging as a powerful diagnostic technique and an invaluable imaging modality to visualise the internal structure of the human body. Its ability to produce images with excellent and a wide range of image contrast has made it a modality of choice in the clinical and research environments to investigate function of the human body. Here, MRI was used to study foetal development.

Foetal MRI was first performed in 1983 to primarily study fetuses' central nervous system. At that time, every case was a challenge due to the limitation of sequences with duration of several minutes. So, maternal sedation and foetal immobilisation were necessary to improve foetal image quality. However, with the advent of fast MR sequence such as Half Fourier Single-Shot Turbo Spin Echo (figure 1.1) that allows images to be acquired in a second, foetal MRI has been revolutionised. Since then, MRI has been progressively developed to study the foetal thorax, gastrointestinal tract, kidneys and cervical masses. In addition, development and application of Echo Planar Imaging, which was able to freeze physiological motion, broadened the horizon of foetal imaging area, enabling scientists and clinicians to study diffusion and perfusion of the foetal brain and placenta. With all this advancement, foetal MRI is gradually establishing itself as a complementary imaging tool with respect to ultrasound in detecting foetal disease and abnormalities in-utero.

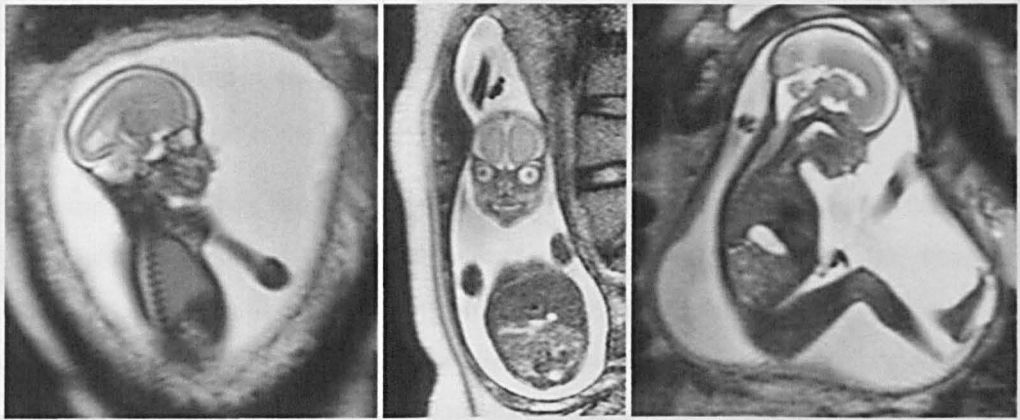


Figure 1.1: MR images acquired using Half Fourier Single-Shot Turbo Spin Echo (HASTE) sequence.

1.1 The Scope of this Thesis

This thesis documents the work conducted by the author between the year 2008 and 2011 at the Sir Peter Mansfield Magnetic Resonance Centre (SPMMRC) of the University of Nottingham. The main aim of the present study was to exploit the improved functionality of MRI to investigate the effect of maternal diabetes and maternal smoking on foetal development using quantitative imaging techniques at 1.5 Tesla using a Philips Achieva MRI system.

Chapter 2 provides the background theory that underpins this thesis. It begins with the origins and fundamental principles of NMR with respect to the relaxation phenomena. Following this, basic principles of MRI are discussed based on magnetic field gradients (slice selection, phase encoding and frequency encoding gradients), k-space, the Fourier transform and development of imaging techniques. Finally, a review of the main MR hardware and its function is presented.

Chapter 3 reviews the relative value of both MRI and Ultrasound in prenatal and perinatal diagnosis. This is discussed by addressing the advantages and disadvantages of each imaging modality in foetal imaging. The chapter also provides an overview of the risks of MRI exposure to fetuses and mothers.

Chapter 4 explores the process of foetal growth and development of the placenta, foetal brain, respiratory system, liver and urinary system. This chapter serves as an introduction to the foetal studies conducted by the author.

Chapter 5 describes the methods used to measure placental blood perfusion in the placenta, basal plate and chorionic plate. The first part of the chapter investigates the reliability and reproducibility of the program developed to measure placental perfusion. The second part of the chapter explains the methods used to acquire, process and statistically analyse the effect of maternal diabetes on placental blood flow, with respect to normal pregnancies. The chapter also reports the effect of maternal diabetes on placental growth.

Chapter 6 discusses the methods used to acquire, process and estimate foetal adiposity using T_1 weighted fat suppressed MRI scan and a MATLAB program developed specifically for this purpose. The first part of the chapter investigates the reliability and reproducibility of the measurements of foetal adiposity acquired using the MATLAB program. The second part applies this technique to study the effect of maternal diabetes on foetal adiposity. In addition, the chapter also reports the effect of maternal diabetes on foetal growth: shoulder width, foetal length and volume.

Chapter 7 reports the effect of maternal smoking on foetal volume and foetal organ growth. The chapter describes the techniques applied to acquire, process and estimate foetal organ volumes, foetal and placental volume, shoulder width and foetal length.

Chapter 8 summarises the findings obtained in chapter 5 to 7 and concludes the work described in this thesis, highlighting some areas for further development.

Chapter 2

Magnetic Resonance Imaging

2.1 Overview

This chapter aims to introduce readers to the basic principles of Magnetic Resonance Imaging as described in the literature [1; 2; 3; 4; 5; 6; 7; 8; 9; 10; 11; 12]. The author starts with a brief description of nuclear magnetic phenomenon and its origin. Following this, the chapter will progress to discuss the relaxation mechanism and biophysical principles that affects the measurement of nuclear magnetic resonance. A section detailing the formation of MR images covering the theory of k-space and Fourier transform follows this. Then, the author details some relevant imaging sequence used in the experimental work of this thesis. Limitations of the magnetic field in MR imaging will also be visited. Finally, the author takes the initiative to detail the general aspects of MR hardware and its accessories to assist the understanding of the whole process of image formation in conjunction with the principles of MRI and NMR.

2.2 Basis Principles of Magnetic Resonance Imaging

2.2.1 Nuclear Magnetic Resonance Theory

Magnetic Resonance Imaging is based on the principle of Nuclear Magnetic Resonance (NMR), which was independently discovered by Felix Bloch [13] from the University of Stanford and Edward Purcell [14] from the University of Harvard in 1946, for which they were jointly awarded the Nobel Prize in Physics

in 1952 [12]. NMR refers to the study of the resonant behaviour of nuclei under the influence of a magnetic field.

The atom is a basic unit of matter. It consists of a central nucleus surrounded by clouds of negatively charged electrons. The nuclear mass consists of a mixture of positively charged protons and electrically neutral neutrons. Those atomic nuclei with an odd number of protons or neutrons or both have an intrinsic spin angular momentum, I called nuclear spin, while atomic nuclei with an even number of protons and neutrons have no net spin. This nuclear spin can be quantitatively described using the spin quantum number, I , that can take integer or half values depending on the number of protons and neutrons within the nucleus. If the total number of protons and neutrons is odd, the nucleus would have a half-integer spin. Conversely, if the total number of protons and neutrons is even, the nucleus would have an integer spin. The magnitude of total intrinsic angular momentum of a nucleus, pointing along the spin axis of each state is given by,

$$|I| = \hbar \sqrt{I(I+1)} \quad (\text{Eq 2.1})$$

where \hbar is the reduced Planck's constant ($\frac{h}{2\pi}$), equivalent to 1.054×10^{-34} Js or 6.582×10^{-16} eVs. The intrinsic angular momentum value determines the magnitude, but not the axis of the intrinsic spin angular momentum. Since nuclei are electrically charged, they possess magnetic dipole moments, μ , which are described by,

$$\mu = \gamma I \quad (\text{Eq 2.2})$$

where γ is the gyromagnetic ratio, which is a constant, unique for each nuclear isotope possessing a spin. Gyromagnetic ratio is the ratio of the nucleus' magnetic moment to its angular momentum, which can be described using the equation below:

$$\gamma = \frac{q}{2m_p} g \quad (\text{Eq 2.3})$$

where q is the charge of ^1H nucleus, m_p is the mass of the ^1H nucleus and g is the g -factor of the nucleus, which is 5.5855 for a free proton. The gyromagnetic ratio can be positive or negative: if γ is positive, the μ and \mathbf{I} are aligned parallel to each other, otherwise they are aligned anti-parallelly.

In order to be NMR sensitive, a nucleus must have spin. Hydrogen is the most commonly used active nucleus in clinical MRI. This is understandable since ^1H is the most abundant isotope in the human body, which is composed of approximately 75% – 80% of fat and water. Furthermore, the hydrogen nucleus consists of one proton that has a relatively large magnetic dipole moment and high gyromagnetic ratio, which is capable of generating relatively large NMR signals. While the ^1H isotope is favoured in MR imaging, NMR is primarily focussed on the elements with high gyromagnetic ratio. The most common MRI active nuclei are listed in Table 2.1, detailing their intrinsic spin properties, gyromagnetic ratio and natural abundance.

Nucleus	Intrinsic Spins, \mathbf{I}	Gyromagnetic Ratio, γ (MHz T ⁻¹)	Natural Abundance (%)
^1H	$\frac{1}{2}$	42.58	99.98
^2H	1	6.54	0.015
^3H	$\frac{1}{2}$	45.41	0
^{13}C	$\frac{1}{2}$	10.71	1.11
^{14}N	1	3.08	99.6
^{15}N	$\frac{1}{2}$	-4.32	0.37
^{17}O	$\frac{5}{2}$	5.77	0.04
^{19}F	$\frac{1}{2}$	100	40.05
^{23}Na	$\frac{3}{2}$	100	11.26
^{31}P	$\frac{1}{2}$	100	17.24

Table 2.1: The properties of a selection of nuclei used in MR [5].

The interaction of magnetic moments with the external magnetic field can be depicted using two models: Classical Model or Quantum Model. Here, Classical and Quantum Model will be considered based on ^1H isotope, since it is the only isotope used in the experiments of this thesis.

2.2.1.1 Classical Model

A nuclear magnetic moment in the presence of a magnetic field will experience a torque, which attempts to realign the magnetic moment with the field, causing the angular momentum to change at a rate $\frac{d\mathbf{I}}{dt}$. The resulting torque, $\boldsymbol{\tau}$ can be expressed as,

$$\boldsymbol{\tau} = \boldsymbol{\mu} \times \mathbf{B} = \frac{d\mathbf{I}}{dt} \quad (\text{Eq 2.4})$$

where \mathbf{B} is the magnetic field. Equation 2.4 can be simplified using equation 2.2 to arrive at:

$$\frac{d\boldsymbol{\mu}}{dt} = \gamma \boldsymbol{\mu} \times \mathbf{B} \quad (\text{Eq 2.5})$$

This means that $\frac{d\mathbf{I}}{dt}$ is perpendicular to the magnetic dipole moment, $\boldsymbol{\mu}$ and applied magnetic field, \mathbf{B}_0 and therefore \mathbf{I} , since $\boldsymbol{\mu}$ is parallel to \mathbf{I} . This phenomenon is known as the gyroscope effect; the same phenomenon that causes a spinning top to precess. The magnetic field exerts torque causing the magnetic dipole to precess around the applied magnetic field axis, \mathbf{B}_0 , at a resonant angular frequency or Larmor frequency, ω_L :

$$\omega_L = \gamma B_0 \quad (\text{Eq 2.6})$$

This Larmor equation is true for a single spinning charged particle in an external field without any other influence. However, it must be modified in the presence of other local factors such as chemical shift, which will be discussed later.

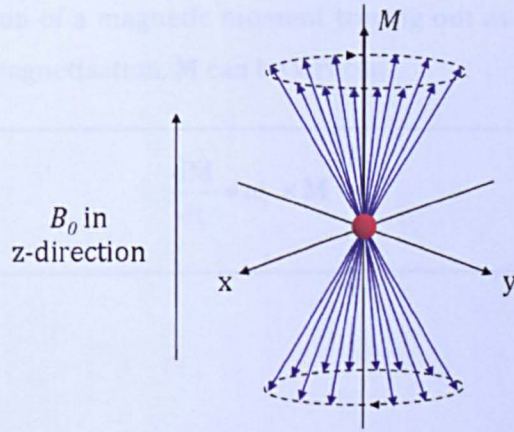


Figure 2.1: Precession of a magnetic dipole moment, μ about an applied magnetic field, B_0 .

In equilibrium, where the magnetic field is directed along the z-axis and independent of time,

$$\mathbf{B} = B_0 \mathbf{k} \quad (\text{Eq 2.7})$$

Equation 2.5 can be written in terms of its vector components as,

$$\frac{d\mu_x}{dt} = \gamma \mu_y B_0 \quad (\text{Eq 2.8a})$$

$$\frac{d\mu_y}{dt} = -\gamma \mu_x B_0 \quad (\text{Eq 2.8b})$$

$$\frac{d\mu_z}{dt} = 0 \quad (\text{Eq 2.8c})$$

which has solutions,

$$\mu_x(t) = \mu_x(0) \cos(\gamma B_0 t) + \mu_y(0) \sin(\gamma B_0 t) \quad (\text{Eq 2.9a})$$

$$\mu_y(t) = -\mu_x(0) \sin(\gamma B_0 t) + \mu_y(0) \cos(\gamma B_0 t) \quad (\text{Eq 2.9b})$$

$$\mu_z(t) = \mu_z(0) \quad (\text{Eq 2.9c})$$

Therefore, the motion of a magnetic moment tracing out as a precessional cone resulting from net magnetisation, \mathbf{M} can be written

$$\frac{d\mathbf{M}}{dt} = \omega_L \times \mathbf{M} \quad (\text{Eq 2.10})$$

Chemical Shift

Negatively charged electron clouds surround the nucleus. These electrons generally affect the shielding effect experienced by the nuclei in a static magnetic field, causing a shift in the Larmor frequency. This phenomenon known as chemical shift relies on the precise electron distribution within the molecule. Two independent research groups first observed this phenomenon in 1950 [15; 16; 17].

The effective magnetic field, B_{eff} , experienced by the spins can be described as

$$B_{eff} = (1 - \sigma) B_0 \quad (\text{Eq 2.11})$$

where σ is the chemical shift shielding constant. It increases linearly with the induced field generated by the electrons of the molecules and the applied magnetic field.

The chemical shift parameter, δ , measured in parts per million (ppm) can be computed using the equation below:

$$\delta = \left(\frac{\omega - \omega_{ref}}{\omega_{ref}} \right) \times 10^6 \text{ ppm} \quad (\text{Eq 2.12})$$

where ω_{ref} is the fixed reference frequency, which is normally the resonant frequency of a ^1H isotope in tetramethylsilane. This measureable chemical shift parameter is very useful in NMR spectroscopy. It provides information about the chemical compound of the nuclei in a sample. In clinical MRI, ^1H isotopes in water and fat molecules contribute to the formation of MR images. The chemical shift

between these two components is 3.5 ppm (approximately 220 Hz at 1.5 T) [10; 12]. This is illustrated in figure 2.2.

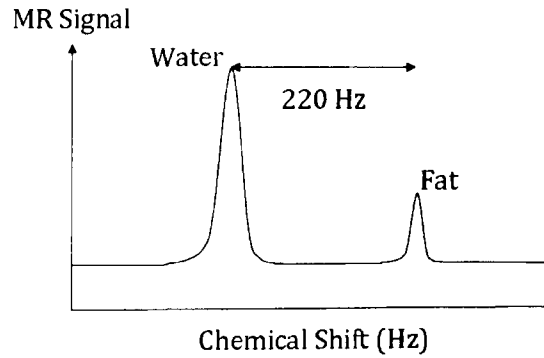


Figure 2.2: Chemical shift between protons in water and fat molecules.

2.2.1.2 Quantum Model

In an ordinary circumstance, the nuclear spins are randomly oriented. However, in the presence of an applied external magnetic field (B_0), the nuclear spins associated with magnetic dipole moments behave like tiny compass needles, experiencing an aligning force with the external field. Normally, the magnetic dipole moment in a quantum model can only have $(2I + 1)$ orientations, corresponding to $(2I + 1)$ energy levels, where I is the quantum number of the nucleus. Therefore, the ^1H isotope can adopt one of the two discrete orientations relative to B_0 , since it has a quantum number $I = \frac{1}{2}$. The two alignments occupy different energy levels. The spins can be parallel (spin up $|\alpha\rangle$) or anti-parallel (spin down $|\beta\rangle$). The measurable z-component of the magnetic dipole moment can be described as,

$$\mu_z = \gamma I_z \quad (\text{Eq 2.13})$$

or

$$\mu_z = \gamma \hbar m \quad (\text{Eq 2.14})$$

where m represents the quantum number ($m = -I, -I + 1, \dots, I$). μ_z can be aligned with or against the applied magnetic field, with magnetic dipole moment

precessing about B_0 at an angular frequency ω_L . This precession is like a motion of spinning top.

The differences in the energy, ΔE , between the two spin states is proportional to the applied magnetic field. For a ^1H isotope, the difference in the energy can be defined as,

$$\begin{aligned}
 \Delta E &= -\boldsymbol{\mu} \cdot \mathbf{B} \\
 &= -\left[\mu_{-1/2} - \mu_{1/2} \right] B_0 \\
 &= -\left[\left(-\frac{1}{2} \gamma \hbar \right) - \left(+\frac{1}{2} \gamma \hbar \right) \right] B_0 \\
 &= \gamma \hbar B_0
 \end{aligned} \tag{Eq 2.15}$$

Applying electromagnetic energy at the Larmor frequency, ω_L , can induce transitions between the two energy states, as shown in figure 2.3. This is the basis for an NMR experiment.

$$\omega_L = \frac{\Delta E}{\hbar} = \gamma B_0 \tag{Eq 2.16}$$

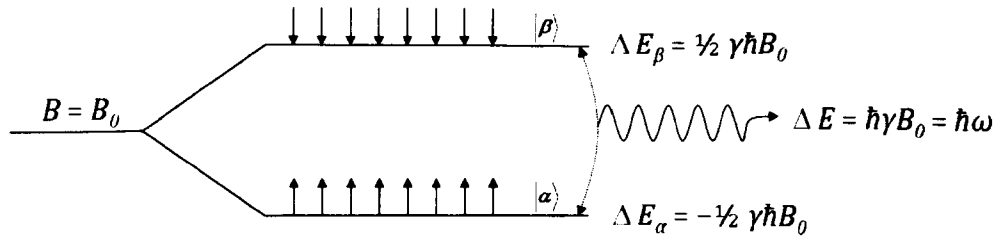


Figure 2.3: Energy level diagram for $I = \frac{1}{2}$ system.

Boltzmann Distribution

The distribution of spins between energy states can be described using Boltzmann statistics. In an equilibrium state, the distribution of the spins occupying the two energy states is dependent on the temperature, T , and the field strength, B_0 . Normally, the spins would prefer to occupy the lower energy state.

This is usually the spin up state, $|\alpha\rangle$ for a ^1H isotope. The Boltzmann distribution at equilibrium can be described as,

$$\begin{aligned}\frac{N_\beta}{N_\alpha} &= \exp\left(\frac{-\Delta E}{k_B T}\right) \\ &= \exp\left(\frac{-\hbar\omega_L}{k_B T}\right)\end{aligned}\quad (\text{Eq 2.17})$$

where N_β is the number of spins in the higher energy state, N_α is the number of spins in the lower energy state, k_B is the Boltzmann constant ($1.38 \times 10^{-23} \text{ J K}^{-1}$) and T is the absolute temperature.

At room temperature, $k_B T \gg \Delta E$,

$$\begin{aligned}\frac{N_\beta}{N_\alpha} &\approx 1 + \left(\frac{-\hbar\omega_L}{k_B T}\right) \\ N_\beta &\approx N_\alpha \left[1 + \left(\frac{-\hbar\omega_L}{k_B T}\right)\right]\end{aligned}\quad (\text{Eq 2.18})$$

Then, the population differences between spin up and spin down states (n) can be defined as:

$$\begin{aligned}n &= N_\alpha - N_\beta \\ &= \frac{N_\alpha \hbar\omega_L}{k_B T} \\ &= \frac{N_\alpha \hbar\gamma B_z}{k_B T}\end{aligned}\quad (\text{Eq 2.19})$$

Since the total number of spins in both energy states is given by $N_{tot} = N_\alpha + N_\beta$ and $N_\alpha \approx N_\beta$ at this limit, $N_{tot} \approx 2N_\alpha$. So, n can be described as:

$$n = \frac{N_{tot} \hbar\gamma B_z}{2k_B T}\quad (\text{Eq 2.20})$$

At 310 K and field strength 1 T, the fractional excess for ^1H isotope is approximately 3.3×10^{-6} spins. The vector sum of the magnetic dipole moments

in the resulting spin population difference would give rise to a net magnetisation, $|\mathbf{M}|$ that can be detected for NMR. This net magnetisation is low and is the reason for intrinsically low signal to noise ratio in NMR experiments. At equilibrium, many individual spins are distributed around the precessional cone. Hence, there is no net magnetisation along the x- and y-axis, and the net magnetisation is aligned with the z-axis. The net magnetisation per unit volume of sample in an equilibrium state can be described as,

$$\begin{aligned} |\mathbf{M}| &= N_{\alpha} \mu_{z\alpha} + N_{\beta} \mu_{z\beta} \quad \text{where } \mu_{z\beta} = -\mu_{z\alpha} \\ &= N_{\alpha} \mu_{z\alpha} - N_{\beta} \mu_{z\alpha} \\ &= (N_{\alpha} - N_{\beta}) \mu_{z\alpha} \end{aligned} \quad (\text{Eq 2.21})$$

Since $\mu_{z\alpha} = \frac{\hbar\gamma}{2}$ and using equation 2.20, $|\mathbf{M}|$ can be described as:

$$\begin{aligned} |\mathbf{M}| &= n \mu_{z\alpha} \\ &= \frac{N_{\text{tot}} (\hbar\gamma)^2 B_z}{4 k_B T} \end{aligned} \quad (\text{Eq 2.22})$$

Equation 2.22 encapsulates Curie's Law.

2.2.2 Interaction with Oscillating Electromagnetic Field (\mathbf{B}_1)

The applied static magnetic field, \mathbf{B}_0 is conventionally defined to lie along the z-axis of the Cartesian coordinate system. Hence, the net magnetisation, \mathbf{M}_0 , at equilibrium is a result of the combined longitudinal magnetisation, which lies along the z-axis. It does not possess a transverse magnetisation component. In order to detect the NMR signal, the longitudinal magnetisation should be perturbed from its equilibrium state by applying an oscillating radio-frequency magnetic field, \mathbf{B}_1 . This field is perpendicular to the static magnetic field (\mathbf{B}_0), and oscillates in phase with the precessing magnetic moments at the Larmor

frequency, ω_L . The oscillating magnetic field, \mathbf{B}_1 , is much smaller than the static magnetic field, \mathbf{B}_0 (of the order of μT).

2.2.2.1 Laboratory Frame of Reference

Application of an oscillating magnetic field, \mathbf{B}_1 , to nuclear spin systems would induce transitions between two energy levels. $\mathbf{B}_1(t)$ may be resolved into two rotating components:

$$\mathbf{B}_a(t) = B_1 [\mathbf{i} \cos(\omega t) + \mathbf{j} \sin(\omega t)] \quad (\text{Eq 2.23a})$$

$$\mathbf{B}_c(t) = B_1 [\mathbf{i} \cos(\omega t) - \mathbf{j} \sin(\omega t)] \quad (\text{Eq 2.23b})$$

\mathbf{B}_a rotates in an anticlockwise direction and \mathbf{B}_c rotates in a clockwise direction. This is demonstrated in figure 2.4.

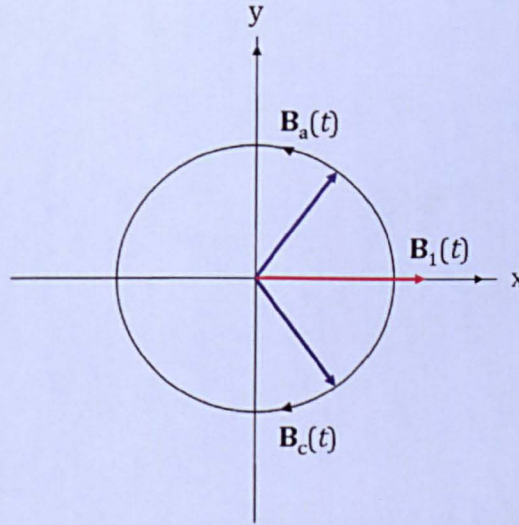


Figure 2.4: An applied linearly polarised field, $\mathbf{B}_1(t)$ decomposed into two counter rotating fields, $\mathbf{B}_a(t)$ and $\mathbf{B}_b(t)$.

Since equations 2.5 and 2.8 are also applicable for oscillating magnetic fields, the motion of the magnetic moment resulting from net magnetisation can be defined as,

$$\frac{d\mathbf{M}}{dt} = \gamma \mathbf{M} \times [\mathbf{B}_0 \mathbf{k} + \mathbf{B}_1(t)] \quad (\text{Eq 2.24})$$

With the understanding that B_0 is much larger than B_1 and rotation of B_1 is of similar frequency to the precession on frequency of \mathbf{M} , the counter-rotating component can be neglected (\mathbf{B}_a) and only \mathbf{B}_c needs to be considered. Hence, the resulting torque from \mathbf{B}_c and \mathbf{M} (provided they are of similar frequency) can be described as,

$$\boldsymbol{\tau} = \mathbf{M} \times \mathbf{B}_c \quad (\text{Eq 2.25})$$

This is shown in figure 2.5.

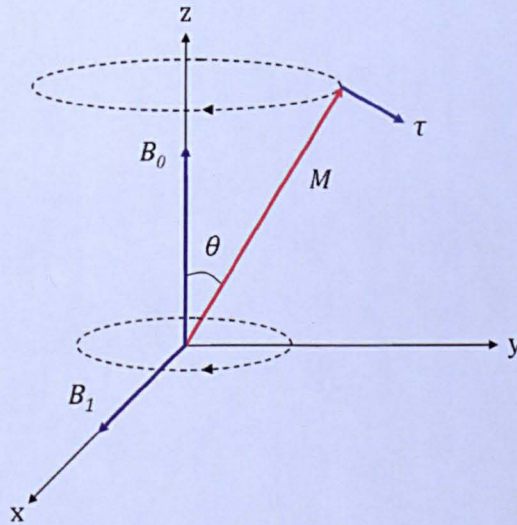


Figure 2.5: The torque experienced by the precessing magnetic dipole moment, μ due to the effect of the B_1 field.

In the classical model, a continuum of orientations is available. Conversely, in the quantum model with spins- $\frac{1}{2}$, only two orientations corresponding to μ_α and μ_β are available. Hence, the torque due to \mathbf{B}_c induces transitions between α and β spin states, with the energy coming from the radio-frequency field. This

phenomenon is one of resonance because the effect of \mathbf{B}_e is strongest when ω is equivalent to ω_L .

2.2.2.2 Rotating Frame of Reference

In contrast to the laboratory frame, which has a coordinate of x , y and z , the rotating frame rotates clockwise around the z -axis in the xy plane at a frequency ω . In the rotating frame of reference, the \mathbf{B}_1 and magnetic moment are considered to be stationary. To transform to the rotating frame, a fictitious field of amplitude $-\frac{\omega}{\gamma}$ must be applied, which on resonance will cancel \mathbf{B}_0 . Hence, \mathbf{B}_0 is removed from the equations of motion. The coordinates of the rotating frame of reference are denoted as x' , y' and z . In this frame, \mathbf{B}_1 is stationary along the x' axis. The motion of \mathbf{M} in the rotating frame can be described as,

$$\frac{d\mathbf{M}}{dt} = \gamma \mathbf{M} \times \left[\mathbf{k} \left(B_0 - \frac{\omega}{\gamma} \right) + \mathbf{i}' B_1 \right] \quad (\text{Eq 2.26})$$

which can be written in terms of an effective magnetic field, B_{eff} :

$$\frac{d\mathbf{M}}{dt} = \gamma \mathbf{M} \times B_{eff} \quad (\text{Eq 2.27})$$

where $|B_{eff}| = |B_1|$ on resonance. This precession of magnetisation around the axis of the B_{eff} field, is shown in figure 2.6.

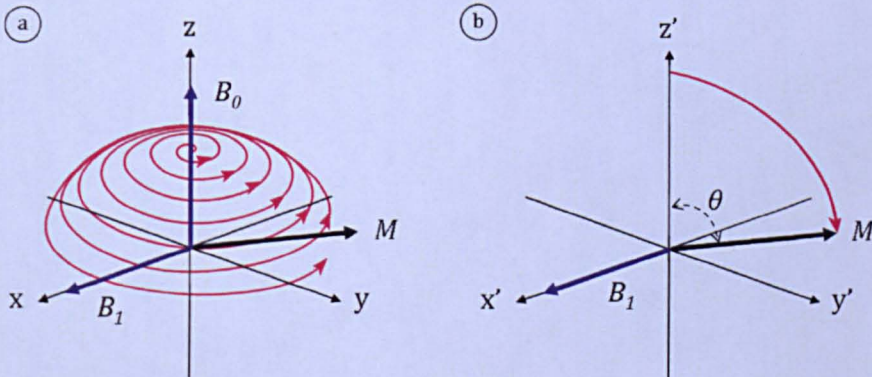


Figure 2.6: (a) Laboratory and (b) rotating frames of reference.

On resonance, when $\omega = \omega_L$, the x-component of the field vanishes, causing the vector to precess around \mathbf{B}_1 in the zy' plane at an angular frequency, $\omega = \gamma B_1$. This resulting magnetisation rotates at an angle, θ :

$$\theta = \gamma |\mathbf{B}_1| t_w \quad (\text{Eq 2.28})$$

where t_w is the duration of the rotation.

In order to rotate the magnetisation at different angles, the B_1 field is applied for different times. The most commonly employed pulses are either 90° or 180° . Application of a 90° radio frequency pulse would tip the \mathbf{M} previously aligned with the B_0 field into the $x'y'$ plane yielding a transverse magnetisation, M_{xy} . Similarly, application of a 180° radio frequency pulse (twice the amplitude or duration of a 90° pulse) would invert the longitudinal magnetisation to lie along the $-z$ -axis. Therefore, 180° radio frequency pulses are also known as inversion pulse.

2.2.3 Free Induction Decay (FID)

Application of a 90° pulse or transverse magnetisation causes the spins making up the magnetisation, \mathbf{M} to be in phase with each other. These spins precess in the transverse plane at ω_L . This results in the production of an electrical voltage in a coil tuned to the Larmor frequency. This voltage is the base to the observable MRI signal. The signal amplitude depends on the degree to which any longitudinal magnetisation can be tilted to the transverse plane directly after switching off the radio frequency pulse. Hence, this signal will persist until the spins have dephased and lost their transverse consistency. The representation of the signal decay is illustrated in figure 2.7.

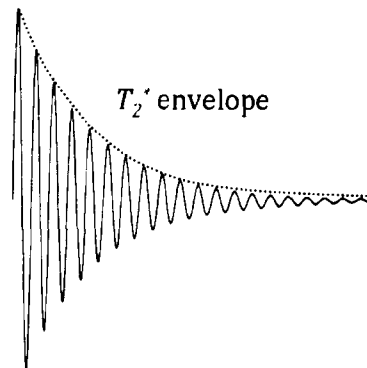


Figure 2.7: Free induction decay (FID).

The signal decay takes the form of a sine wave, which decays exponentially by $\exp\left(-\frac{t}{T_2^*}\right)$ at a base frequency,

$$\Delta\omega = \omega_0 - \gamma B_L$$

(Eq 2.29)

where ω_0 is the frequency of the transmitter and γB_L is the Larmor frequency of the samples. $\Delta\omega = 0$ for an on resonance sample.

2.2.4 Bloch Equations

The Bloch equations are a set of equations introduced by Felix Bloch in 1946. They are used in NMR to describe the behaviour of nuclear magnetisation (M_x , M_y , M_z) during excitation and relaxation that are defined as a function of relaxation times, T_1 and T_2 . These equations are also known as the equations of motion of nuclear magnetisation, which can be described as,

$$\frac{dM_x}{dt} = \gamma (M_y B_z - M_z B_y) - \frac{M_x}{T_2} \quad (\text{Eq 2.30a})$$

$$\frac{dM_y}{dt} = \gamma (M_z B_x - M_x B_z) - \frac{M_y}{T_2} \quad (\text{Eq 2.30b})$$

$$\frac{dM_z}{dt} = \gamma (M_x B_y - M_y B_x) - \frac{M_z - M_0}{T_1} \quad (\text{Eq 2.30c})$$

where $B_x = B_1 \cos(\omega t)$, $B_y = B_1 \sin(\omega t)$ and $B_z = B_0$ [10; 13]. The magnetic field along the x-axis (B_x) and the y-axis (B_y) describes the rotation of the applied magnetic field, B_1 , in the transverse plane. Here, equation 2.30a and 2.30b describe the transverse magnetisation behaviour during the excitation and relaxation periods by quoting T_2 , while equation 2.30c describes the longitudinal magnetisation resulting from excitation and relaxation by referring to T_1 .

2.2.5 Relaxation and Measurement of NMR Parameters

Microscopically, the application of a radio frequency pulse increases the energy in the system, exciting low energy spins. However, when the radio frequency pulse is switched off, the spin system is only under the influence of the applied static magnetic field, B_0 . This means the spins will return to the equilibrium state by losing the energy absorbed from the radio frequency pulse and realigning themselves with the B_0 field, in accordance with the Boltzmann distribution. This process is known as relaxation. This relaxation process can occur through energy released between spins (spin-spin) and between spins and their surroundings (spin-lattice). These simultaneous and independent interactions result in two

relaxation components: transverse decay and longitudinal recovery. This will be discussed in detail in section 2.2.5.1 and 2.2.5.2.

The most common physical mechanism that contributes to relaxation is the dipole–dipole interaction. It occurs between the magnetic moment of a nucleus and the magnetic moments of other nuclei or entities (electrons, atoms and molecules) surrounding it. It depends on the distance between nuclei and the orientation relative to the external magnetic field. The tumbling of the molecules within the sample causes the dipole–dipole coupling to constantly change as the vector relationships change, causing the production of fluctuating magnetic fields at each nucleus. When these fluctuations occur at the Larmor frequency, it will give rise to a radio frequency magnetic field that can produce nuclear relaxation through spin flipping. These dipole–dipole interactions occur commonly in protons since it has the highest magnetic dipole.

The spin–spin, spin–lattice and dipole–dipole interactions are the mechanisms that generate the MR contrast. These images will provide signal intensities that will reflect the NMR characteristics of tissues. Here, the four most commonly used parameters; T_1 , T_2 , T_2^* and PD , will be discussed with respect to the manner these values vary in different types of tissue.

2.2.5.1 Longitudinal Recovery (T_1 Relaxation)

The longitudinal or spin lattice relaxation is a process where the spin system returns to its Boltzmann equilibrium distribution after perturbation by a radio frequency pulse, which occurs through energy exchange between the spins and the thermal lattice. This process involves realignment of the magnetic moments with \mathbf{B}_0 , causing the net magnetisation to align along the z-axis. The rate of the net magnetisation's growth towards its equilibrium value, M_0 , is exponential and equivalent to the longitudinal recovery time, T_1 .

Following a 90° radio frequency pulse, the longitudinal recovery of M_z can be described as,

$$M_z(t) = M_0 \left(1 - e^{-\frac{t}{T_1}} \right) \quad (\text{Eq 2.31})$$

where T_1 is the longitudinal relaxation time. It is the time required for approximately 63% of the longitudinal magnetisation, M_0 , to be restored in the tissues [12]. The longitudinal recovery of the magnetisation M_z is shown in figure 2.8.

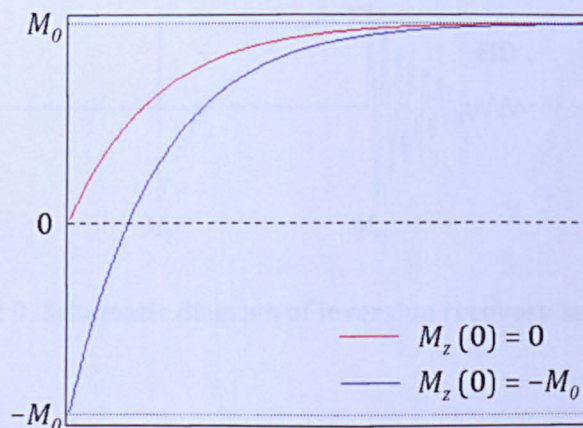


Figure 2.8: Relaxation of the longitudinal magnetisation $M_z(t)$ for saturation recovery (red line) and inversion recovery (blue line).

Measurement of Longitudinal T_1 Relaxation Time

Longitudinal relaxation time, T_1 , is an important intrinsic biophysical property of the tissues. This parameter is useful in various applications to study tissue characteristics and contrast agent uptake. Moreover, it is used to measure perfusion and blood volume. It is also important in sequence development.

T_1 can be measured by using the inversion recovery sequence. This sequence involves application of a 180° or inversion radio frequency pulse, that causes the longitudinal magnetisation, \mathbf{M}_0 , to be inverted to the $-z$ -axis. Hence, \mathbf{M}_z recovers from $-\mathbf{M}_0$. This inversion pulse reverses the equilibrium magnetisation without inducing phase coherence (transverse magnetisation). In an inversion recovery sequence, a delay time called inversion time, TI , is allowed for the inverted longitudinal magnetisation to partially recover. Following this, a 90° radio frequency pulse is applied to flip the partially recovered longitudinal magnetisation into the transverse xy plane, as shown in figure 2.9.

This will give rise to an FID with an amplitude proportional to the longitudinal magnetisation existing at time TI . The initial amplitude of the FID in an inversion recovery experiment depends on the size of M_z prior to the 90° pulse.

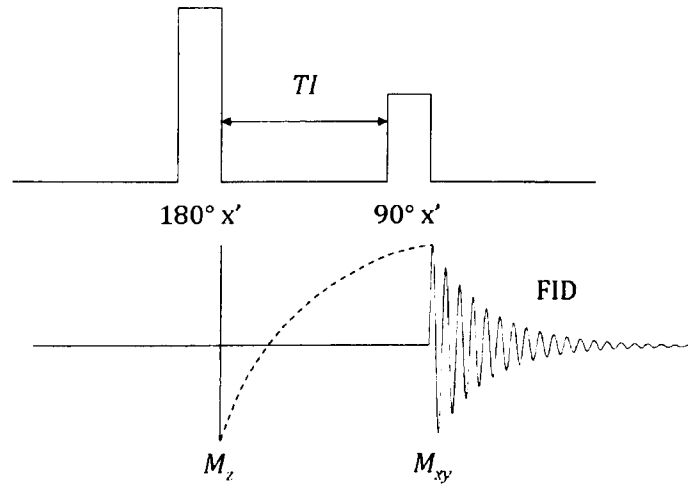


Figure 2.9: Schematic diagram of inversion recovery sequence.

While the inverting pulse tends to invert the net magnetisation of all the tissue types within the selected slab, different tissues recover at different rates depending on their longitudinal relaxation times, T_1 . This is demonstrated in figure 2.10. By the time of 90° pulse application, these tissues will have different amounts of recovered magnetisation, resulting in different signal intensities in the final MR image. The relationship between T_1 and TI in inversion recovery can be described using the equation below:

$$M_z(t) = M_0 \left(1 - 2e^{-\frac{TI}{T_1}} \right) \quad (\text{Eq 2.32})$$

To measure T_1 , it would be necessary to vary TI . However, a long repetition time ($> 5 T_1$) should be allowed before applying the next inversion pulse. This is to allow the magnetisation to fully recover to its equilibrium state. On completing data collection, a mathematical fit can be performed to equation 2.32 for T_1 and M_0 variables.

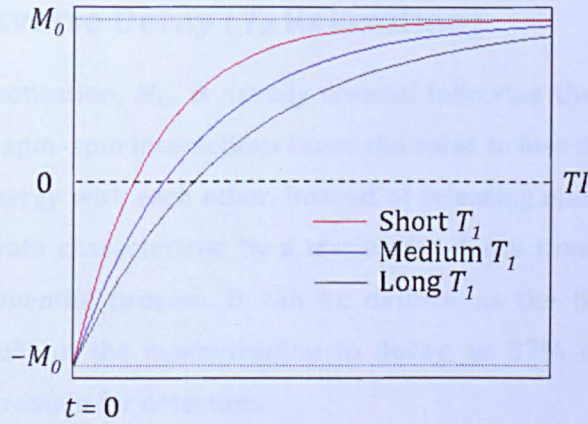


Figure 2.10: Longitudinal recovery of three different tissues.

Inversion recovery can also be applied to suppress signals (null) from certain tissues: fluid (Fluid attenuated inversion recovery, FLAIR) and fat (short inversion time inversion recovery, STIR). In these cases, a predetermined TI is applied resulting in signal from a specific tissue intercepting at the zero point along the z -axis. With $M_z = 0$, equation 2.32 can be used to derive the null TI as,

$$TI_{null} = T_1 \ln(2) \quad (\text{Eq 2.33})$$

It is important to note that all these are done with the assumption that flip angles are perfectly applied. Hence, inaccuracy in flip angle application could be a source of error. In addition, saturation recovery with at least 5 different repetition times, TR s ($90^\circ - TR - 90^\circ - TR$) can also be employed to measure T_1 . The magnetisation after a single TR can be described as [10],

$$M_z(t) = M_0 \left(1 - e^{-\frac{TR}{T_1}} \right) \quad (\text{Eq 2.34})$$

However, the signal model needs to be modified to take account of shot to shot saturation in steady state.

2.2.5.2 Transverse Decay (T_2 Relaxation)

Transverse magnetisation, M_{xy} , is usually created following the application of a 90° pulse, where spin-spin interactions cause the spins to lose their coherence as they exchange energy with each other, instead of releasing energy to the lattice. M_{xy} decays at a rate characterised by a transverse decay time, T_2 , which is an irreversible exponential process. It can be defined as the time required for approximately 63% of the magnetisation to decay, or 37% of the transverse magnetisation to remain for detection.

The transverse magnetisation decay can be described as,

$$M_{xy} = M_0 e^{-\frac{TE}{T_2}} \quad (\text{Eq 2.35})$$

where TE represents the echo time. It is the time between the first excitation of radio frequency pulse and echo detection. Echo detection will be explained later.

Measurement of Transverse T_2 Relaxation Time

In practice, T_2 cannot be estimated by simply measuring the decay constant of the FID since the NMR signals decay faster than predicted effect of T_2 alone. This is because an extra dephasing originating from magnetic field inhomogeneity accelerates the FID. This can be explained as,

$$\frac{1}{T_2^*} = \frac{1}{T_2} + \frac{1}{T_2''} \quad (\text{Eq 2.36})$$

where T_2^* is the relaxation time characterising the accelerated decay rate and T_2'' is the decay rate arising due to the dephasing effect of the inhomogeneous static field, B_0 . Since the extra dephasing, T_2'' , is reversible, this factor can be removed with the application of a spin echo pulse sequence, which was introduced by Hahn in 1950 [18]. Figure 2.11 shows a basic sequence comprising a 90° pulse followed by a 180° pulse after a $\frac{TE}{2}$ time. The 180° pulse is often referred to as a refocusing pulse since it reverses the dephasing effects of the field

inhomogeneity. The only resulting in signal degradation is due to irreversible spin-spin interaction effects.

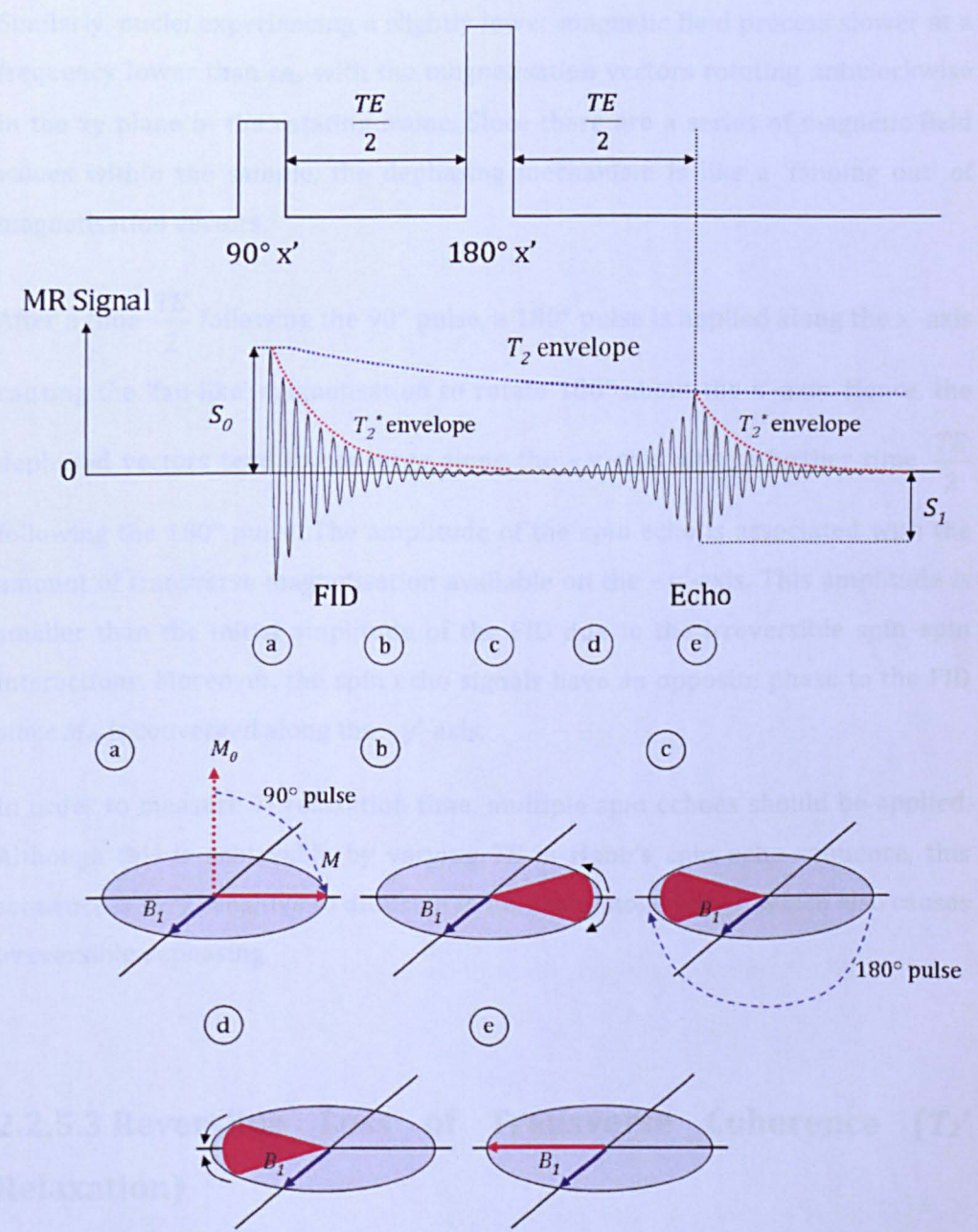


Figure 2.11: A basic sequence comprising a 90° pulse followed by a 180° pulse.

On application of a spin echo pulse sequence, a 90° pulse is applied along the x' -axis. This causes the magnetisation, M , to be tipped from the z -axis to the y' -axis as shown in figure 2.11. Following this, the magnetisation, M , starts to dephase with time constant T_2^* due to B_0 inhomogeneity and spin-spin interactions during a time $\frac{TE}{2}$. In the laboratory frame, some nuclei at slightly higher

magnetic field precess very fast at a frequency higher than ω_L , with the magnetisation vectors rotating clockwise in the xy plane in the rotating frame. Similarly, nuclei experiencing a slightly lower magnetic field precess slower at a frequency lower than ω_L , with the magnetisation vectors rotating anticlockwise in the xy plane in the rotating frame. Since there are a series of magnetic field values within the sample, the dephasing mechanism is like a 'fanning out' of magnetisation vectors.

After a time $\frac{TE}{2}$ following the 90° pulse, a 180° pulse is applied along the x'-axis causing the 'fan-like' magnetisation to rotate 180° about the x'-axis. Hence, the dephased vectors tend to converge along the -y'-axis after a further time $\frac{TE}{2}$ following the 180° pulse. The amplitude of the spin echo is associated with the amount of transverse magnetisation available on the -y'-axis. This amplitude is smaller than the initial amplitude of the FID due to the irreversible spin-spin interactions. Moreover, the spin echo signals have an opposite phase to the FID since M_{xy} is converged along the -y'-axis.

In order to measure T_2 relaxation time, multiple spin echoes should be applied. Although this is achievable by varying TE in Hahn's spin echo sequence, this sequence is very sensitive to diffusion in field inhomogeneities, which also causes irreversible dephasing.

2.2.5.3 Reversible Loss of Transverse Coherence (T_2^* Relaxation)

The applied magnetic field, B_0 , is never completely homogeneous. This gives rise to extra dephasing that leads to faster transverse decay. However, the signal decay due to magnetic field inhomogeneity is reversible. This can be described using another decay time constant, T_2^* , that is depicted using the equation below:

$$\frac{1}{T_2^*} = \gamma \Delta B_0 \quad (\text{Eq 2.37})$$

where ΔB_0 represents the field inhomogeneity. The variation in B_0 is due to two factors: the engineering limitations of the magnet and the variation in the susceptibility properties of tissues used in the experiment. Nonetheless, the application of a spin echo sequence, short echo times, static field shimming and accurate slice positioning to avoid tissue-air interfaces can reduce the effect of B_0 variation.

2.2.5.4 Proton Density (PD)

Proton density or spin density refers to the number of protons per unit volume in a sample. It is proportional to the amount of magnetisation, M_0 , before a 90° pulse excitation, the initial amplitude of the FID following a 90° pulse and the density of water in tissue.

2.2.6 Factors Affecting the Relaxation Times

The T_1 and T_2 relaxation times can be affected by many intrinsic (tissue properties) and extrinsic (operator dependent) factors. Here, the main factors affecting the relaxation times will be discussed with respect to the field strength, water content, viscosity, temperature and paramagnetic component of tissues.

2.2.6.1 Measurement Frequency (Field Strength)

In 1968, Koenig et al. [19] published a paper demonstrating an increase in T_1 of Nuclear Magnetic Relaxation Dispersion for a protein with increasing field strength (figure 2.12). In addition, the T_1 relaxation process becomes more efficient when $\tau_c \omega_0 = 1$, where τ_c is the rotational correlation time. This result also agrees with an in vivo study conducted using five different magnetic field strengths in the range of 0.2 T to 7 T, that demonstrated an increase in T_1 with increasing B_0 [20]. In contrast to T_1 , which depends on the number of spins binding to the protein surface and magnetic field strength, T_2 is less dependent on magnetic field strength but is greatly influenced by the number of protons binding to the protein surface [10; 19].

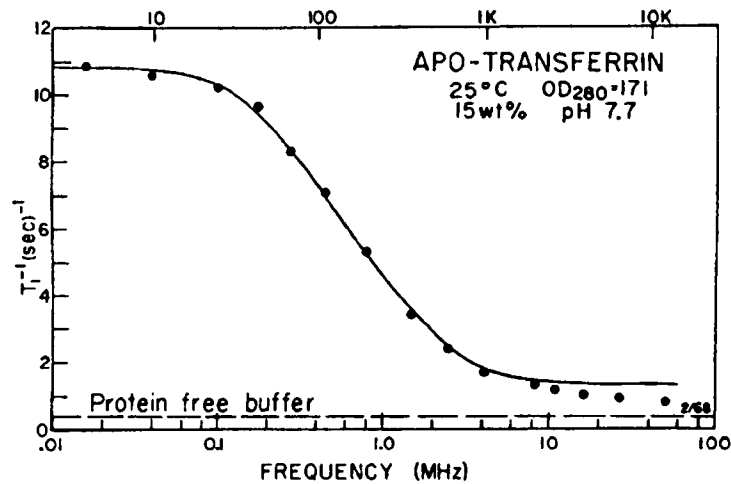


Figure 2.12: Nuclear magnetic resonance dispersion data for a protein solution [19].

2.2.6.2 Viscosity and Temperature

Koenig et al. [19] also studied the effect of temperature and viscosity of a diamagnetic protein on T_1 relaxation time. Their work demonstrated an increase in the T_1 with increasing temperature. Conversely, T_1 is seen decreasing with increasing viscosity. This is due to the mobility effect of the molecules within the sample. Figure 2.13 shows the effect of temperature and viscosity on T_1 .

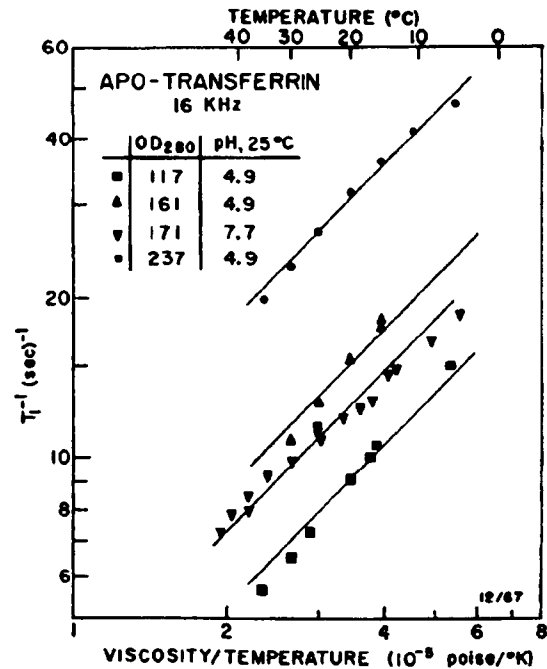


Figure 2.13: Temperature dependence of longitudinal relaxation rate in protein solution [19].

2.2.6.3 Water Content

T_1 and T_2 relaxation times vary between tissues due to variation in the amount of water binding in the tissue. In reality, the water molecules are usually in fast exchange between three states (structured, bound, free tissues) and the fraction of time spent in each state is proportional to water content in each state. Hence, the observed T_1 is a weighted mean of the relaxation time at each state and can be described as,

$$\frac{1}{T_1^{obs}} = \frac{F^{bound}}{T_1^{bound}} + \frac{F^{structure}}{T_1^{structure}} + \frac{F^{free}}{T_1^{free}} \quad (\text{Eq 2.38})$$

where F represents the fraction at each state.

Generally, since T_1^{bound} is short, only a small fraction of water content in tissue is required to be in the bound compartment to decrease the observed T_1 . While a similar equation can be derived for T_2 , the bound compartment of T_2 is not directly observable in vivo. Moreover, fast exchange is not always achievable for T_2 . Nonetheless, T_2 can be investigated using magnetisation transfer technique that will allow indirect measurement of short T_2 [10].

2.2.6.4 Paramagnetic Content

Endogenous or exogenous paramagnetic material can affect T_1 and T_2 relaxation times by influencing the relaxation of protons. Some of the most common endogenous substances used in MR imaging are Fe^{3+} and Mn^{2+} that are present at different concentrations in the human body. Conversely, exogenous paramagnetic components refer to contrast agents injected into the body to improve image contrast of normal and abnormal tissues. They are also used to differentiate the image contrast of normal tissues with each other. Paramagnetic gadolinium (which will be discussed later) and super-paramagnetic iron oxide are the two most commonly used contrast agents. Unlike most diamagnetic body tissues that are only weakly magnetised in the presence of a magnetic field, these two elements become strongly magnetised in the presence of a magnetic field

[10]. They can either have a positive or negative effect on the signal, by decreasing T_1 , T_2 and T_2^* times [21].

Paramagnetic contrast agents usually have unpaired electrons in the outer shell. These unpaired electrons have parallel spins that add together to produce net electron spin. This gives rise to a net electronic magnetic moment, μ , that generates a strong, fluctuating, alternating magnetic field in the presence of protons, which stimulates their relaxation. Moreover, since the ratio of electron's charge to its mass is much larger than that of a proton (equation 2.3), the electron's gyromagnetic ratio is 653 times that of a proton. This affects the relaxation times greatly [1].

If the paramagnetic contrast agent is administered at low concentrations, the signal intensity of water-based tissues will increase in a T_1 -weighted sequence due to a decrease in T_1 relaxation time. Conversely, when this contrast agent is administered at a higher concentration, the T_2 will be shortened causing the tissue signals to decrease. However, different metals affect the relaxation time differently. This is greatly dependent on the relaxivity of the contrast agent, which is defined as a change in relaxation time. This is produced by a change in concentration.

Super-paramagnetic contrast agents are also recognised by the abbreviation SPIOs (small particle iron oxide) or USPIOs (ultrasmall particle iron oxide). They are usually available in a range of particle sizes and hydrodynamic diameters. This contrast agent is useful in liver imaging [22; 23; 24]. During imaging, the super-paramagnetic contrast agent is usually injected into the body in the form of suspended colloids of iron oxide nanoparticles to reduce the T_2 signals of absorbing tissues. These super-paramagnetic contrast agents are composed of paramagnetic atoms in a crystal lattice that can increase the magnetic moments by a factor of 10 – 1000 in the vicinity of an external magnetic field. Following the removal of an applied magnetic field, the parallel spin alignments in the super-paramagnetic contrast agents are disrupted by Brownian molecular motion. This results in zero net magnetisation [12].

Application of large diameter super-paramagnetic iron oxide particles (≥ 50 nm) will shorten the T_2 , causing substantial loss in signal intensity due to low relaxivity. Therefore, they are also known as negative contrast agents with most pronounced effect on T_2 -weighted sequences. Conversely, application of small

diameter super-paramagnetic iron oxide particle (≤ 20 nm) can be used as positive or negative contrast agents [12]. They are currently being developed as blood pool contrast agents for MR angiography [25].

Gadolinium

The gadolinium (Gd^{+3}) based contrast agent has seven unpaired electrons in its outer shell and hence possess a large magnetic moment [26]. It also has 9 coordination sites where the water can interact with the unpaired electrons. Gadolinium in its elemental state is toxic. However, it can be chelated to a ligand such as DTPA (diethylene triamine pentaacetic acid) that eliminates gadolinium's toxicity but preserves its paramagnetic properties. This results in a new arrangement with 8 occupied and 1 unoccupied coordination sites. Hence, there is only 1 possible site for water interaction, resulting in a decrease in gadolinium's relaxivity. Nonetheless, the water relaxation time is still greatly influenced by the large magnetic moment [10; 27].

The Gd-DTPA has high T_1 relaxivity, stability, distributes rapidly in the extracellular fluid space and is quickly excreted via the kidneys [27]. Gadolinium behaves like any other element in inhomogeneous magnetic field; its dipole - dipole interactions result in a decrease in T_1 and T_2 relaxation times of proton. Application of low concentration gadolinium will shorten the T_1 and tissues accumulating this agent will create enhanced signal intensity on T_1 -weighted images. However, at concentrations higher than 1 mmol kg^{-1} gadolinium (ten times the standard dose), the effect on T_2 starts to dominate causing a loss in the signal [10]. Gadolinium also shortens T_2^* , but at a lesser extent compared to T_1 . Moreover, since T_2^* occurs very rapidly, its effect is only seen briefly when gadolinium first passes through the capillary bed [11]. However, it is important to note that the effect on T_2^* is predominantly dependent on the inhomogeneity of the distribution.

2.3 Principle of MR Imaging

Magnetic Resonance Imaging (MRI) has been recognised as one of the most important medical advancements of the last century. It has introduced mankind to a different level of study of human anatomy, revealing the structure and function of the human body. Since its development in the 1970s, MRI has evolved from an exclusively experimental imaging modality to a clinically important tool. It has undergone continuous development in pulse sequence and hardware design, in an effort to cater for different clinical applications.

In 1973, Paul Lauterbur realised that the application of a varying magnetic field across a sample induces a variation in the proton Larmor frequency [28]. Subsequently, he proposed using gradients in the magnetic field to localise NMR signals in order to produce two-dimensional images of a sample. This was done by applying a linear gradient at different angles to a sample and combining these projections using a back projection reconstruction method. At a similar time, Peter Mansfield realised the relationship between the MR signal in a gradient and optical diffraction. He applied this to study solids and proposed several methods to selectively excite a slice through a sample, including the slice selection technique used in exact form at present [29]. Following this, Richard R. Ernst's group presented the first Fourier imaging method using non-selective excitation and orthogonal linear gradient to produce two-dimensional Fourier encoded images [30]. This served as a foundation to propose and develop the fast imaging technique that lead to the development of MRI. In 1977, Peter Mansfield introduced a fast imaging technique known as Echo Planar Imaging (EPI) that is capable of acquiring MR images in seconds. This imaging sequence will be discussed in detail in section 2.3.3.4.

The contributions of Paul Lauterbur and Peter Mansfield to the development of MRI within the medical research community was recognised and awarded with a Nobel Prize in Medicine in 2003. Similarly, the effort of Richard R. Ernst in introducing Fourier Transform NMR spectroscopy was also awarded a Nobel Prize in Chemistry in 1991.

2.3.1 Magnetic Field Gradients

Before NMR signals can be used to create an image of a sample, the precise location of the source of signals should be defined. This can be done by superimposing a small (of the order of mT m^{-1}), spatially varying magnetic gradient field, \mathbf{G} , onto the main magnetic field, \mathbf{B}_0 . This process known as spatial encoding is conducted to ensure that the magnetic field strength varies in a controlled way along the designated axis.

In practice, each scanner has three orthogonal configured gradient coils, which produce field gradients when current flows through loops of wires situated around the magnet's bore. Each gradient field generates its own magnetic field (G_x, G_y, G_z) that interacts with the main magnetic field (by either adding or subtracting). This leads to linear variation of the field and Larmor frequency, ω_L , as a function of distance from the centre of the magnet bore. Ideally, the total resulting magnetic field is always along the z-axis, regardless of the direction of the applied gradient. This resulting magnetic field at a specific location (\mathbf{r}) during the application of field gradients can be described as,

$$B_z(\mathbf{r}) = B_0 + \mathbf{G} \cdot \mathbf{r} \quad (\text{Eq 2.39})$$

where \mathbf{G} can be described as,

$$\mathbf{G} = G_x \mathbf{i} + G_y \mathbf{j} + G_z \mathbf{k} \quad (\text{Eq 2.40})$$

where $G_x = \frac{dB_z}{dx}, G_y = \frac{dB_z}{dy}, G_z = \frac{dB_z}{dz}$
and $\mathbf{r} = x \mathbf{i} + y \mathbf{j} + z \mathbf{k}$

Hence, the Larmor frequency of the precessing spins in the sample will vary according to,

$$\omega_L = \gamma (B_0 + G_x x + G_y y + G_z z) \quad (\text{Eq 2.41})$$

The magnetic field gradient plays a number of important roles in MRI. It dephases and rephases the magnetic moments of nuclei, locates a slice within a selected plane of scan (slice selection), spatially encodes the NMR signals of anatomy along the long (frequency encoding) and short (phase encoding) axis, as well as motion and flow encoding. Moreover, it is important to note that the applications of these gradients are inter-changeable, so that imaging is possible at different angles including obliquely to the principle axes by linear combination of gradients.

2.3.1.1 Slice Selection

A spatial selective radio frequency pulse can be employed for various functions in MR imaging. This includes excitation, refocusing, inversion and spatial presaturation of magnetisation, which are achievable through the application of slice selective gradients [31; 32; 33]. Garraway, Grannel and Mansfield initially introduced the slice selection technique in 1974 [34]. It is a technique to excite the spins in an isolated plane within the sample or patient that is being imaged. Slice selection is achievable with the application of a radio frequency pulse that only affects a limited part of the sample in the presence of a linear field gradient along the direction of the desired slice (figure 2.14). This procedure excites those spins (dominated by their position) with Larmor frequency similar to the frequency of the applied radio frequency pulse.

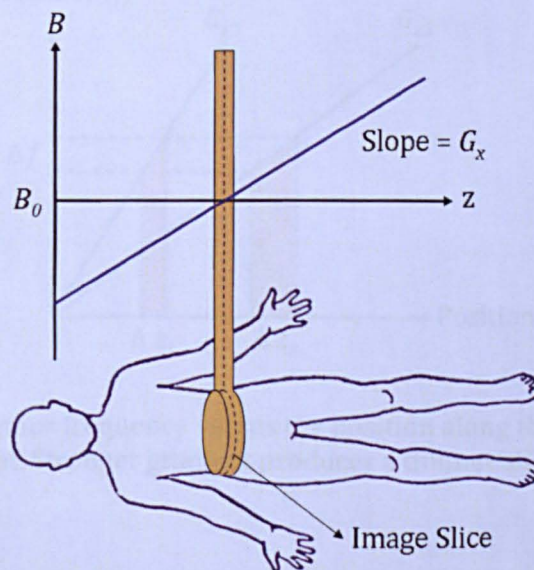


Figure 2.14: Linear variation of the total magnetic field as a function of z .

To excite a transverse slice, the gradient magnetic field is applied along the z-axis, G_z , in the presence of B_0 . This causes a linear position-dependent variation in the Larmor frequency of the spins in the z-direction, corresponding to a slice thickness:

$$\Delta z = \frac{\Delta \omega}{\gamma G_z} \quad (\text{Eq 2.42})$$

where $\Delta \omega$ is the bandwidth frequency centred at the carrier frequency, ω_0 . The carrier frequency establishes the position of the slice along the pre-determined direction and the transmit bandwidth determines the range of the spins within the slice that needs to be excited. Hence, the Larmor frequency in the slice along the z-direction is,

$$\omega_L = \gamma (B_0 + G_z z) \quad (\text{Eq 2.43})$$

In order to select a slice, it is necessary to apply a strong radio frequency pulse over a narrow bandwidth frequency, so that only spins in that range of frequencies are excited. This principle is used in multi-slice imaging. Figure 2.15 demonstrates the effect of increasing the amplitude of the slice-selection gradient on slice thickness for a fixed bandwidth frequency.

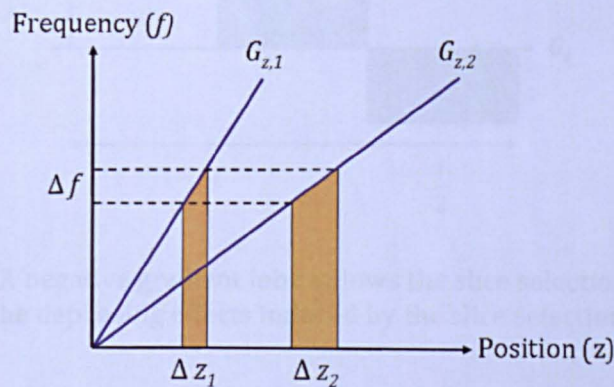


Figure 2.15: Larmor frequency versus the position along the slice selection gradient. Stronger gradient produces a thinner slice (Δz).

Following the application of a radio frequency pulse, the shape of the B_1 envelope determines the distribution of the magnetisation along the z-axis. In order to

select a slice with a rectangular profile, spins within the slice should undergo uniform precession with a flip angle, θ , of 90° and the spins outside the slice should not be perturbed (zero flip angle). A sinc $\left(\frac{\sin(a)}{a}\right)$ shaped pulse, where

$a = \gamma G_z \Delta z \frac{t}{2}$, is often used to achieve a near ideal slice profile. This modulation will produce a rectangular frequency slice profile for small flip angles, where the spin system responds linearly to the pulse. This system consists of several adjacent lobes of alternating polarity. However, the central lobe is the highest and widest lobe. To achieve a perfectly rectangular slice profile, a sinc pulse with infinite number of lobes should be applied. Unfortunately, application of a large number of lobes will increase the repetition time (TR) and echo time (TE). It will also increase the flow and off-resonance effects.

The sinc pulse selection gradient introduces a linear phase variation, which causes a continuous phase shift resulting in loss of phase coherence. This problem can be overcome by applying a reversed slice gradient for half the duration of the initial slice selection period. This is shown in figure 2.16.

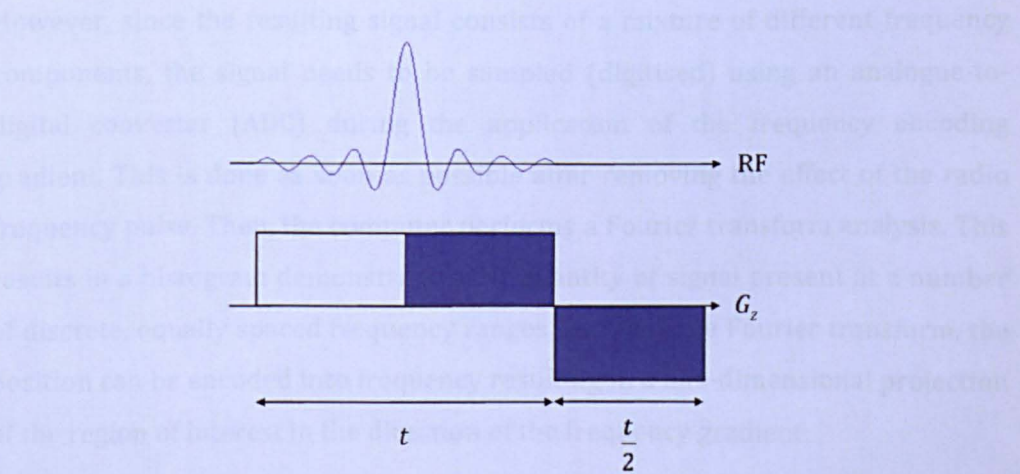


Figure 2.16: A negative gradient lobe follows the slice selection excitation to refocus the dephasing effects induced by the slice selection gradient.

2.3.1.2 Spatial Encoding

Following slice selection, the resulting signals do not have spatial information along the remaining two axes. Hence, the signals along these axes should be

encoded using the spatial encoding technique that comprises two steps: frequency encoding and phase encoding.

2.3.1.2.1 Frequency Encoding

Frequency encoding is commonly used to acquire spatial frequency information following a radio frequency excitation. It is used in many MRI pulse sequences: projection acquisition [28] and Fourier imaging [30; 35]. Frequency encoding is a process of encoding signals along the long axis (x) of the anatomy. This can be achieved by switching on the frequency encoding field gradient while measuring the NMR signals (image readout). For this reason, the frequency encoding gradient is also called the readout gradient.

The application of a constant linear frequency encoding gradient along the x -axis will change the precessional frequency of the spins making up the signal. This precessional frequency can be described using equation 2.43 as a function of position along the frequency encoding gradient axis (x).

However, since the resulting signal consists of a mixture of different frequency components, the signal needs to be sampled (digitised) using an analogue-to-digital converter (ADC) during the application of the frequency encoding gradient. This is done as soon as possible after removing the effect of the radio frequency pulse. Then, the computer performs a Fourier transform analysis. This results in a histogram demonstrating the quantity of signal present at a number of discrete, equally spaced frequency ranges. By using the Fourier transform, the position can be encoded into frequency resulting in a one-dimensional projection of the region of interest in the direction of the frequency gradient.

In practice, the FID is usually measured as either a spin echo or gradient echo, since acquiring the FID right after the pulse will lead to errors in determining the phase of the data. Figure 2.17 shows the frequency encoding gradient applied to measure the gradient echo rather than the FID. The dephasing lobe generates a symmetrical gradient echo. The gradient echo normally lies in the centre of the frequency encoding gradient, provided the area under the negative lobe is half of the area under the positive lobe. The time between the excitation and echo measurement is known as the echo time (TE). In order to avoid signal loss due to relaxation processes, it is vital that the dephasing process occurs rapidly.

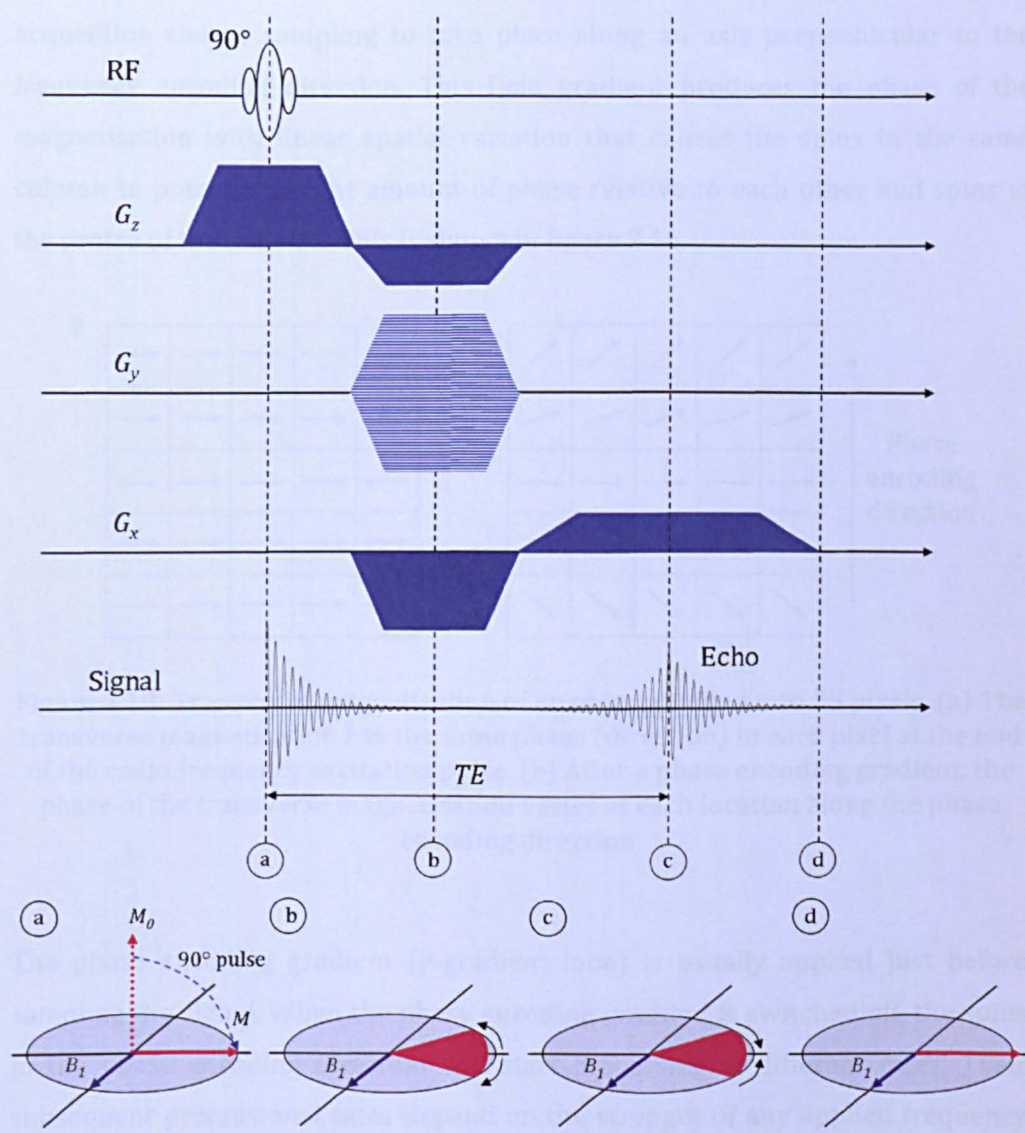


Figure 2.17: Schematic representation of gradient echo sequence.

2.3.1.2.2 Phase Encoding

Phase encoding plays an important role in localising the NMR signals orthogonal to the frequency encoding direction, with the intention of generating a two-dimensional image.

Following slice selection and frequency encoding, NMR signals have been located to a specific slice within a desired plane encoded along a pre-determined direction. The spins in the pixels of the same column are all in phase since all of these spins precess at the same frequency. However, application of a phase encoding gradient to the transverse magnetisation prior to frequency encoding

acquisition causes sampling to take place along an axis perpendicular to the frequency encoding direction. This field gradient produces the phase of the magnetisation with linear spatial variation that causes the spins in the same column to possess different amount of phase relative to each other and spins at the centre of the magnet. This is shown in figure 2.18.

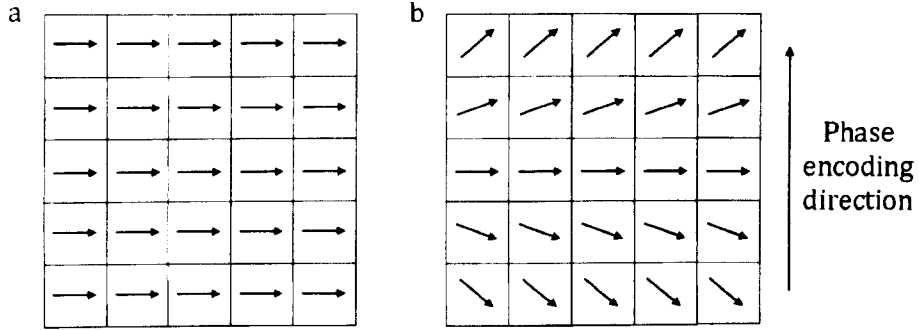


Figure 2.18: Transverse magnetisation of an object divided into 25 pixels. (a) The transverse magnetisation has the same phase (direction) in each pixel at the end of the radio frequency excitation pulse. (b) After a phase encoding gradient, the phase of the transverse magnetisation varies at each location along the phase encoding direction.

The phase encoding gradient (y-gradient lobe) is usually applied just before sampling the signal. When the phase encoding gradient is switched off, the spins in the phase encoding direction will start precessing at different rates. Their subsequent precessional rates depend on the strength of any applied frequency encoding gradient, while their relative phase depends on the strength and duration of application of the phase encoding gradient and the spin's position along the phase encoding direction.

At the end of the phase encoding pulse ($t = T$), the phase, ϕ (in radians) of the signal due to transverse magnetisation is given by,

$$\phi(t) = \gamma y \int_0^T G_y(t) dt = k_y y \quad (\text{Eq 2.44})$$

where k_y is the k-space location. In contrast to frequency encoding that samples all of the data following a single radio frequency excitation pulse, phase encoding needs to be repeated a number of times corresponding to the number of k-space lines that needs to be sampled.

The resulting signals can be reconstructed using Fourier transformation to restore the spatial information of the sample or patient. Phase encoding can also be applied in three-dimensional volume acquisition. In this case, the sample will need to be reconstructed by three-dimensional inverse Fourier transformation.

2.3.2 Fourier Transform and k-Space

Jean Baptiste Joseph Fourier initiated the Fourier transform [36]. Fourier realised that complex signals can be rewritten as an infinite sum of simple sinusoidal waves [37]. The Fourier series describes complicated wave information in terms of simple sines and cosines. The Fourier transform decomposes a complicated signal into amplitude and frequencies of its simple wave components [38]. In MRI, this concept is used to encode the frequency and phase encoding information of the signals within k-space to construct MR images.

2.3.2.1 Theory

Grannel and Mansfield initially introduced the concept of reciprocal space in NMR in 1973 [29]. Then, in 1983, Ljunggren and Twieg independently introduced the k-space theory which is widely used in MRI [39; 40]. In MRI, k-space refers to the two or three-dimensional Fourier transform domain of an ordinary space, in which the time varying NMR signals resulting from precessing spins or magnetisation are stored in the form of a raw data matrix. In this Fourier space, the conjugate of the distance (\mathbf{r}) in which the images are acquired before being Fourier transformed to Cartesian image space (x, y, z) is represented by a variable \mathbf{k} (k_x, k_y, k_z) and the domain representing the spatial frequency distribution of the MR image is called k-space. This concept brings simplicity to the understanding and application of many pulse sequences.

The k-space is used to visualise the trajectories of the spins' phase under the influence of field gradients. The k-space of a two-dimensional image has two axes perpendicular to each other: the horizontal axis (frequency encoding axis) and vertical axis (phase encoding axis). The representation of the k-space of an image is shown in figure 2.19. When signals are measured using a frequency encoding

gradient, the horizontal lines are filled within the k-space. However, as mentioned before, this sequence will need to be repeated a number of times (N), with different phase encoding each time, resulting in N k-space lines corresponding to N amplitudes. This is conducted with the intention to fill in different vertical lines in k-space.

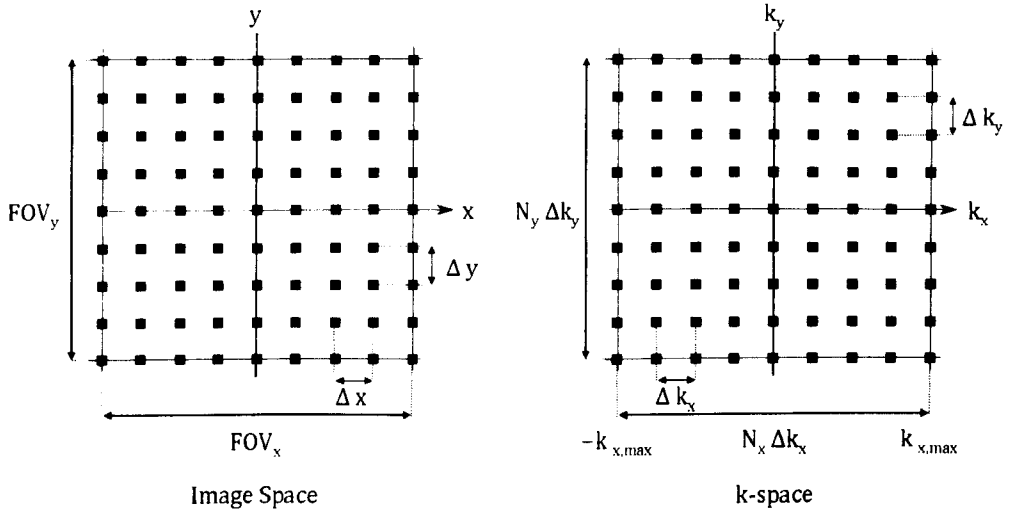


Figure 2.19: The relationship between image space and k-space.

The central lines of the k-space are filled with information from low amplitude phase encoding gradients (small or zero dephasing) that consists of data with low spatial frequencies and high signal amplitude. Conversely, the outer lines appearing at the edge of the k-space are filled with information from positive and negative phase encoding amplitudes that consists of data with high spatial frequencies detailing the fine details of the image.

When the magnetic field gradient is switched on for a time t along one dimension, the signal acquired at a location (r) is given by,

$$S(t) = \int \rho(r) e^{i\phi(t)} dr \quad (\text{Eq 2.45})$$

where the accumulated phase, ϕ , due to application of a magnetic field gradient is,

$$\begin{aligned}\phi(r, t) &= -\int \omega_g(r, t) dr \\ &= -\gamma r \int_0^t G(t) dt\end{aligned}\quad (\text{Eq 2.46})$$

Then, the one-dimensional signal can be written as,

$$S(t) = \int \rho(r) e^{ikr} dr$$

where $k = \gamma \int_0^t G(t) dt$

The total encoded signal, S , representing the spin density acquired in two dimensions at time t'' and pseudo-time T can be described as,

$$S(t'') = \iint \rho(x, y) e^{i(xk_x + yk_y, T)} dx dy \quad (\text{Eq 2.48})$$

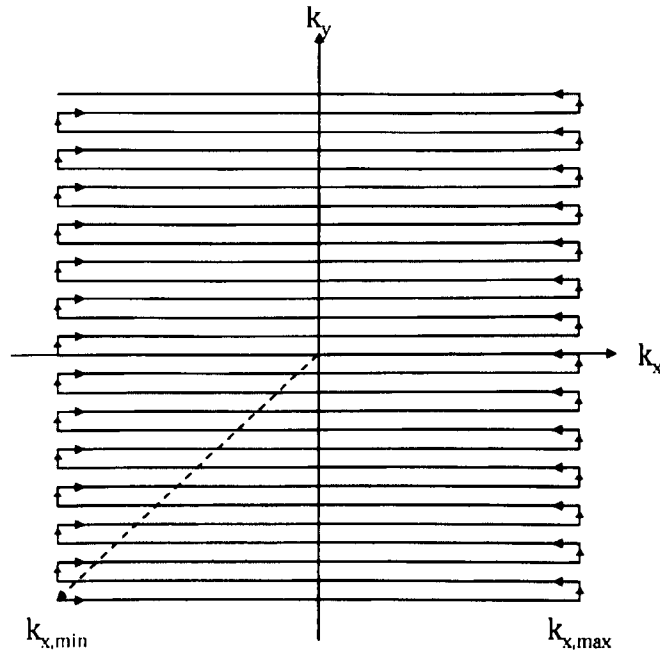


Figure 2.20: A k-space acquisition trajectory commonly used in the Echo Planar Imaging sequence.

While the k-space trajectories navigate in a continuous path (figure 2.20), the signals are only sampled at discrete intervals along the path. The field of view

(FOV) of the resulting image depends on the spacing of the measurements made in k-space. The field of view in the direction of frequency encoding (FOV_{FE}) is given by,

$$FOV_{FE} = \frac{\Delta\omega}{\gamma G_{FE}} \quad (\text{Eq 2.49})$$

where $\Delta\omega$ is the image bandwidth and G_{FE} is the strength of the frequency encoding gradient. The field of view in the direction of phase encoding (FOV_{PE}) is given by,

$$FOV_{PE} = \frac{2\pi}{\gamma \tau_L G_0} \quad (\text{Eq 2.50})$$

where G_0 is the phase encoding step size and τ_L is duration prior to signal sampling. Hence, the voxel size along the frequency encoding direction, Δx , and phase encoding direction, Δy , is given by,

$$\begin{aligned} \Delta x &= \frac{FOV_{FE}}{M} \\ &= \frac{\Delta\omega}{\gamma G_{FE} M} \end{aligned} \quad (\text{Eq 2.51})$$

$$\begin{aligned} \text{and } \Delta y &= \frac{FOV_{PE}}{N} \\ &= \frac{2\pi}{\gamma \tau_L G_0 N} \end{aligned} \quad (\text{Eq 2.52})$$

where M is the matrix size in the frequency encoding direction and N is the number of phase encoding steps.

2.3.2.2 Signal Sampling

MR images are acquired using an analogue-to-digital converter (ADC) and stored temporarily in the computer in the form of MR signals that are made up of pixels. The ADC acquires MR signals at a sampling rate corresponding to a sampling

frequency, f_s , with a range of frequencies known as receive bandwidth, rBW . This can be described as,

$$f_s = \frac{1}{T_s} = rBW \quad (\text{Eq 2.53})$$

where T_s is the time space between two adjacent sample points. If T_s is large, the sampling rate is low and there is a possibility that high frequencies will be under-sampled (aliasing). To avoid the aliasing phenomenon, overlapping of high and low frequency components, the sampling rate must satisfy the Nyquist Theorem. This theorem states that the maximum frequency signal that can be accurately digitised at a certain sampling frequency should be half of the sampling frequency. This is described as the Nyquist frequency, f_N , that is given by,

$$f_N = \frac{1}{2} f_s \quad (\text{Eq 2.54})$$

Furthermore, low receive bandwidth is prone to cause chemical shift artefacts. Both aliasing and chemical shift artefacts will be discussed in detail in section 2.3.4.2.

2.3.3 MR Imaging Techniques

Conventional MRI is a slow imaging technique. It is inadequate for imaging foetal and moving structures such as the heart, liver and stomach. The primary limits on these imaging times are caused by long relaxation times, SNR and spatial resolution. Hence, many new pulse sequences and imaging techniques have been developed in the mid 1980s to accelerate imaging procedure. Some of these techniques are being employed in current MR studies: Fast Low Angle Shot (FLASH) and Turbo Field Echo (TFE).

MRI is also capable of acquiring three-dimensional volumes. This is achievable by simultaneously exciting a volume rather than a slice every TR time, along with application of additional phase encoding gradients along the volume selection

direction to provide the additional spatial encoding (section 2.3.1). The sample's spatial information (two phase and one frequency encodings) is stored in a three-dimensional k-space and a three-dimensional Fourier transform can be used to reconstruct the MR images (section 2.3.2). With three-dimensional volume imaging, it is possible to image more slices and thin slices with improved profile. The latter is ideal for volume rendering and multiplanar reformatting. However, the disadvantage of three-dimensional images is that they are more susceptible to motion artefacts.

2.3.3.1 Fast Low Angle SHot

Fast Low Angle SHot (FLASH) is a spoiled gradient echo pulse sequence that was first presented by Axel Haase et al. in 1986 [41; 42]. This sequence is also known by a variety of names, including spoiled gradient echo (SPGR) in the GE system and T_1 Fast Field Echo (T_1 -FFE) in the Philips system. The abbreviation FLASH is commonly used in the Siemens system. This sequence is primarily used for fast anatomical imaging. Figure 2.21 shows a schematic representation of the FLASH sequence in three-dimensional Cartesian encoding.

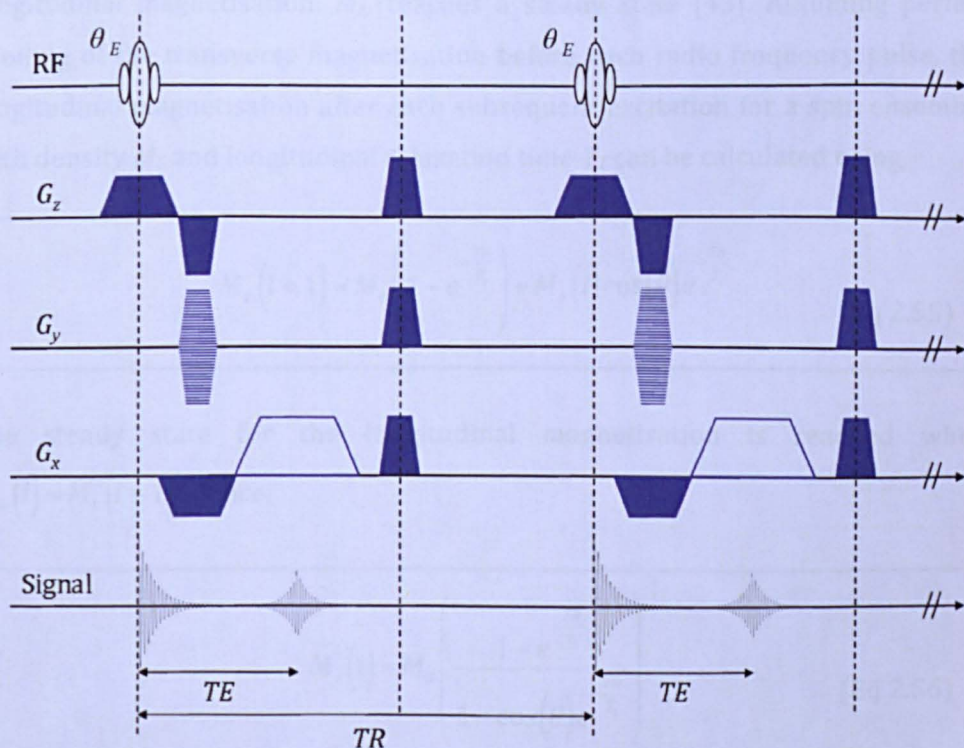


Figure 2.21: Schematic representation of the three dimensional FLASH pulse sequence.

The FLASH sequence consists of a series of radio frequency pulses of flip angle, θ , with pulses separated by a time TR . In practice, this sequence uses an excitation pulse of flip angle in the range of $20^\circ - 30^\circ$ ($< 90^\circ$). Hence, the recovery of longitudinal magnetisation can take place in a shorter period of time and, therefore, the sequence will require a short repetition time, TR . Each excitation pulse is applied along with a z-gradient slice selection, which creates transverse magnetisation in the selected slice that produces a FID. Then, the FID is dephased and subsequently rephased into a gradient echo using a frequency encoding gradient, G_x . The y-gradient and z-gradient traces demonstrate the two perpendicular phase encoding lobes applied before the acquisition, and the opposite polarity phase rewinder lobe applied after the acquisition, in order to dephase all M_{xy} .

The simplest method to produce a T_2^* -weighting contrast is to make TE relatively long and select TR that is at least four to five times T_1 , so that the longitudinal magnetisation recovers between excitation pulses. If TR is less than $5 T_2$, spoiling will have to be used. Application of a low flip angle will give rise to sufficient transverse magnetisation. However, the longitudinal magnetisation remains relatively unperturbed. Following a sufficient number of excitation pulses, the longitudinal magnetisation, M_z , reaches a steady state [43]. Assuming perfect spoiling of the transverse magnetisation before each radio frequency pulse, the longitudinal magnetisation after each subsequent excitation for a spin ensemble with density M_0 and longitudinal relaxation time T_1 can be calculated using,

$$M_z(i+1) = M_0 \left(1 - e^{-\frac{TR}{T_1}} \right) + M_z(i) \cos(\theta) e^{-\frac{TR}{T_1}} \quad (\text{Eq 2.55})$$

The steady state for the longitudinal magnetisation is reached when $M_z(i) = M_z(i+1)$. Hence,

$$M_z(i) = M_0 \left(\frac{1 - e^{-\frac{TR}{T_1}}}{1 - \cos(\theta) e^{-\frac{TR}{T_1}}} \right) \quad (\text{Eq 2.56})$$

It is important to predict the time required for a steady state to be achieved. This

information is useful in estimating the number of start up pulses required (those applied without data collection), so that k-space data is not collected when magnetisation is approaching a steady state.

The flip angle that maximises the signal is called the Ernst angle, θ_E . This angle can be described as,

$$\theta_E = \arccos\left(e^{-\frac{TR}{T_1}}\right) \quad (\text{Eq 2.57})$$

The Ernst angle lies in the range of $0^\circ - 90^\circ$ and monotonically increases with the ratio $\frac{TR}{T_1}$. When $\theta < \theta_E$, it is an indication that the signal can be increased by increasing the flip angle, since creating more transverse magnetisation compensates the further loss of longitudinal magnetisation.

2.3.3.2 Half Fourier Single-Shot Turbo Spin Echo

Half Fourier Single-shot Turbo spin Echo is a type of single-shot fast spin echo (FSE). It is also known by the abbreviation HASTE in the Siemens system, SS-FFE in the GE system, and UFSE in the Philips system. The HASTE sequence is primarily used in two-dimensional imaging to freeze bowel and respiratory motion for abdominal imaging and improve temporal resolution in dynamic studies. The true temporal resolution, R , measured in frames per second for two-dimensional phase encoded acquisition is given by,

$$R = \frac{1}{N_{shot} TR NEX} \quad (\text{Eq 2.58})$$

where N_{shot} is the number of radio frequency excitations per complete k-space traversal and NEX is the number of signal averages.

In HASTE, it is essential to maximise the echo train length (N_{etl}) to acquire images with better spatial resolution. For fixed echo train duration, the maximal N_{etl} can be increased with shortening of echo spacing (ESP). ESP can be minimised by

increasing the receiver bandwidth, increasing the slew rate and shortening the refocusing pulse width (often at the expense of reduced flip angle of degraded slice profile). Unfortunately, even with these changes, the N_{etl} is often insufficient to acquire the desired number of phase encoding steps for the full k-space area. Therefore, asymmetric k-space sampling is usually used and images are reconstructed using half k-space reconstruction.

HASTE uses a phase-alternated echo train combined with half Fourier acquisition to increase the frame rate to the range of 1 – 2 frames per second. The half Fourier acquisition enables us to acquire slightly more than half the data by missing half the phase encoding gradient steps (either positive or negative). So, the data is only collected and stored in the upper or lower half of the k-space. Then, the other half of the data can be estimated by using complex conjugate synthesis (property of Fourier transform of real functions). By doing this, approximately 50% of the scan time can be saved without a significant effect on spatial resolution. However, this will result in a 30% loss in SNR. HASTE can also be conducted in the form of three-dimensional acquisition by using a single shot along one spatial direction [10].

The series of refocusing pulses for HASTE carries significant radio frequency energy, especially at field strengths of 1.5 T or higher. In practice, the flip angles of these refocusing pulses are usually in the range of $120^\circ - 160^\circ$ ($< 180^\circ$). However, to further minimise patient heating in real-time, the flip angle of the refocusing pulse can be varied as a function of position in the echo train [44].

2.3.3.3 Balanced Fast Field Echo

Balanced Fast Field Echo is a rewind gradient echo pulse sequence. It is also commonly known by the abbreviation bFFE in the Philips system, True-FISP in the Siemens system, and FIESTA in the GE system. It is primarily used in cardiac imaging, where it provides excellent SNR and contrast between blood and the myocardium [45; 46]. It provides greater signal than a FLASH sequence, often at an expense of reduced contrast. In this sequence, reversing the sign of the gradient lobes, or sometimes only reversing the phase encoding gradient, refocuses the transverse magnetisation. Hence, the resulting signal contains FID

enhanced with an echo containing coherent transverse magnetisation components.

The gradient echo signal strength is given by [10],

$$\text{Signal} = \rho \left(\frac{\sin(\theta) \left[1 - e^{-\frac{TR}{T_1}} \right] \left[e^{-\frac{TE}{T_2}} \right]}{\left[1 - \cos(\theta) e^{-\frac{TR}{T_1}} \right] - e^{-\frac{TR}{T_2}} \left[e^{-\frac{TR}{T_1}} - \cos(\theta) \right]} \right) \quad (\text{Eq 2.59})$$

where ρ is the number of nuclei per unit volume. In rewind gradient echo sequences, if TR is much smaller than T_1 and T_2 , $e^{-\frac{TR}{T_2}} \approx 1 - \frac{TR}{T_2}$ and equation 2.59 can be simplified to [10],

$$\text{Signal} = \rho \left(\frac{\sin(\theta) \left[e^{-\frac{TE}{T_2}} \right]}{1 + \frac{T_1}{T_2} - \cos(\theta) \left(\frac{T_1}{T_2} - 1 \right)} \right) \quad (\text{Eq 2.60})$$

This means that the signal depends on the flip angle, θ , and the ratio of $\frac{T_2}{T_1}$, but is independent of TR . If $\theta = 90^\circ$ [10],

$$\begin{aligned} \text{Signal} &= \frac{\rho}{1 + \frac{T_1}{T_2}} \\ &\approx \frac{\rho T_2}{T_1} \quad \text{if } T_1 \gg T_2 \end{aligned} \quad (\text{Eq 2.61})$$

At longer TR (> 100 ms) and $TR > T_2$, there is not much difference between rewind and spoiled gradient sequences. In general, a rewind gradient echo produces images with good myelographic effect. It is also good for imaging high contrast between fluid and solid structures in rapid imaging, since the signals are relatively independent of TR . However, rewind gradient echo sequences are sensitive to motion and flow (destroys the steady state transverse coherence)

since they are formed from a combination of refocused and fresh transverse magnetisation. Fortunately, bFFE sequences employ balanced rewinding gradients in all three directions. Therefore, a three-dimensional Fourier transform can be applied by adding phase encoding and rewinding on the slice selection axis, which is in the rephasing lobes. A representation of a bFFE sequence is shown in figure 2.22.

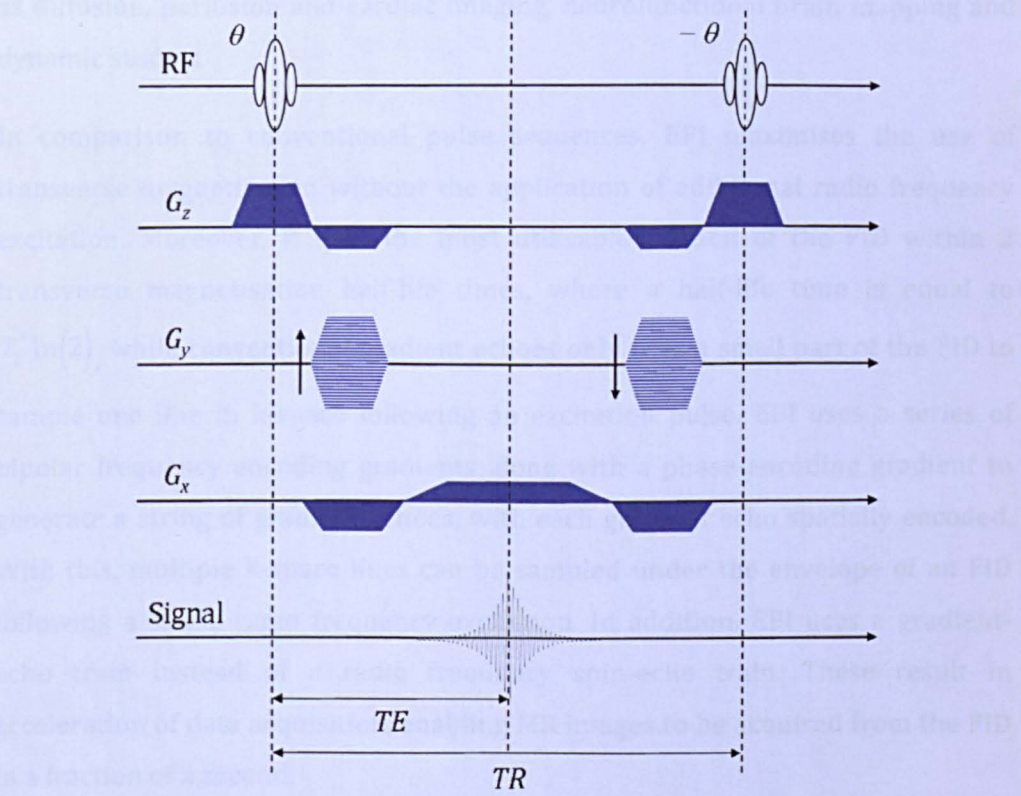


Figure 2.22: Schematic representation of a bFFE pulse sequence.

The limitation of bFFE is that it requires high performance gradient technology to obtain good shimming and a very short TE . If this is not accomplished, images can become degraded with banding artefacts (spacing inversely proportional to the field inhomogeneity).

2.3.3.4 Echo Planar Imaging

Echo planar imaging (EPI) is the fastest pulse sequence with highest SNR per unit time known in MRI. It was first proposed by Peter Mansfield in 1977, following primary development conducted in the University of Nottingham [47; 48; 49; 50].

EPI was first implemented with the aim of 'one shot imaging' using an echo Fourier transform imaging technique that has since been recalled. In 1983, Mansfield's group developed a high speed scanner operating at 4 MHz which incorporated an EPI sequence to image children's hearts at a resolution of 32×32 pixels, and later at a resolution of 64×64 pixels for an adult heart [51]. The EPI sequences have been the basis of many advanced MRI applications, such as diffusion, perfusion and cardiac imaging, neurofunctional brain mapping and dynamic studies.

In comparison to conventional pulse sequences, EPI maximises the use of transverse magnetisation without the application of additional radio frequency excitation. Moreover, it uses the most utilisable portion of the FID within 2 transverse magnetisation half-life times, where a half-life time is equal to $T_2^* \ln(2)$, while conventional gradient echoes only uses a small part of the FID to sample one line in k-space following an excitation pulse. EPI uses a series of bipolar frequency encoding gradients along with a phase encoding gradient to generate a string of gradient echoes, with each gradient echo spatially encoded. With this, multiple k-space lines can be sampled under the envelope of an FID following a single radio frequency excitation. In addition, EPI uses a gradient-echo train instead of a radio frequency spin-echo train. These result in acceleration of data acquisition, enabling MR images to be acquired from the FID in a fraction of a second.

EPI pulse sequences can be used for either two or three-dimensional acquisition. However, the majority of EPI applications are based on two-dimensional sequences, which apply orthogonal slice selection, frequency encoding and phase encoding gradient waveforms. While the slice selection gradient waveforms are similar to the conventional gradient echo and spin echo sequences, the frequency and phase encoding gradients produce different k-space trajectories compared to conventional gradient waveforms. The resulting data needs additional processing before image reconstruction using a Fourier transform. The five types of EPI that will be discussed here are gradient echo EPI, spin echo EPI, inversion-recovery EPI, single-shot EPI, and multishot EPI.

In general, EPI is more prone to artefacts (especially Nyquist ghosting) compared to conventional gradient echo and spin echo imaging. This will be discussed in detail in section 2.3.4.2.

Gradient Echo EPI

Gradient echo EPI is also known as GE-EPI or GRE-EPI. It is a time efficient, low-resolution T_2^* -weighted pulse sequence with high SNR. The GE-EPI pulse sequence starts with an application of a selective excitation pulse that produces an FID signal. The flip angle of the excitation pulse is usually set to 90° to maximise the SNR on GE-EPI. Then, a series of spatially encoded gradient echoes are generated under the envelope of the FID using different combinations of frequency and phase encoding gradient waveforms. This determines the starting point of the k-space trajectory along the phase encoding direction (the first k-space line to fill).

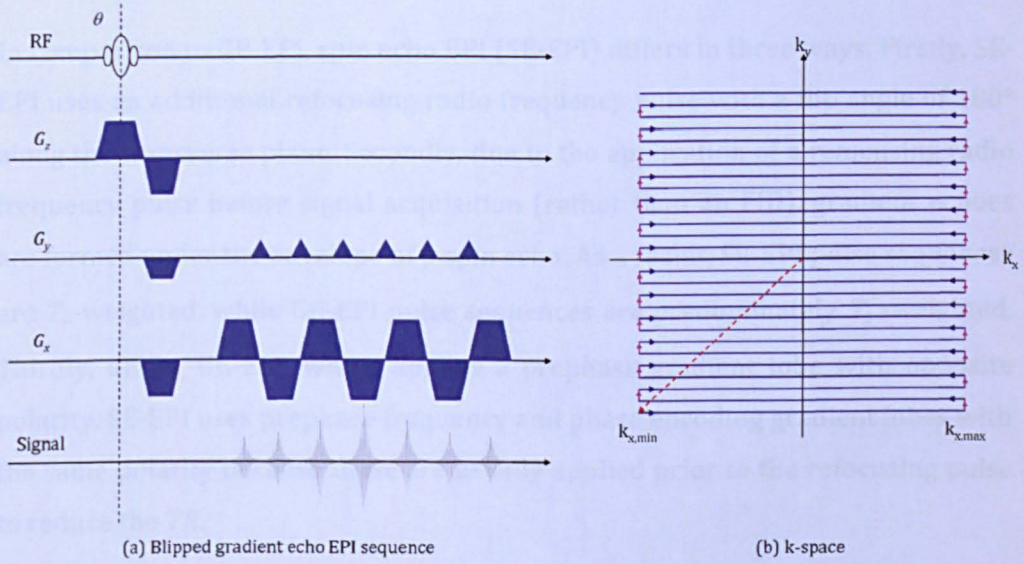


Figure 2.23: Schematic representation of (a) blipped gradient echo EPI sequence and (b) its k-space trajectory.

The frequency encoding gradient creates echoes, while the phase encoding gradient changes the acquisition of the k-space according to the trajectories. The blips of the phase encoding are shown in figure 2.23. In GE-EPI, each k-space line along the phase encoding direction is acquired using a different TE . Therefore, the amplitude of the corresponding gradient echo decays according to,

$$S(n_e) = S_0 e^{-\frac{TE(n_e)}{T_2^*}} \quad (\text{Eq 2.62})$$

where S_0 is the signal at $t = 0$ and n_e is the echo index in the echo train. Normally, at the end of the GE-EPI pulse sequence, a spoiler gradient is employed to dephase the remaining transverse magnetisation before applying the next excitation pulse.

Since GE-EPI is based on T_2^* contrast, it plays an important role in functional MRI such as Bold Oxygenation Level Dependent (BOLD) contrast that depends on susceptibility variations.

Spin Echo EPI

In comparison to GE-EPI, spin echo EPI (SE-EPI) differs in three ways. Firstly, SE-EPI uses an additional refocusing radio frequency pulse with a flip angle of 180° along the transverse plane. Secondly, due to the application of a refocusing radio frequency pulse before signal acquisition (rather than an FID), gradient echoes are formed under the envelope of a spin echo. As a result, SE-EPI pulse sequences are T_2 -weighted, while GE-EPI pulse sequences are predominately T_2^* -weighted. Thirdly, unlike GE-EPI, which applies a prephase gradient lobe with opposite polarity, SE-EPI uses prephase frequency and phase encoding gradient lobes with the same polarity because these are usually applied prior to the refocusing pulse to reduce the TE .

Similar to GE-EPI, SE-EPI requires crusher gradients that straddle the refocusing pulse to dephase the unwanted FIDs from the refocusing pulse. A schematic representation of spin echo EPI is shown in figure 2.24.

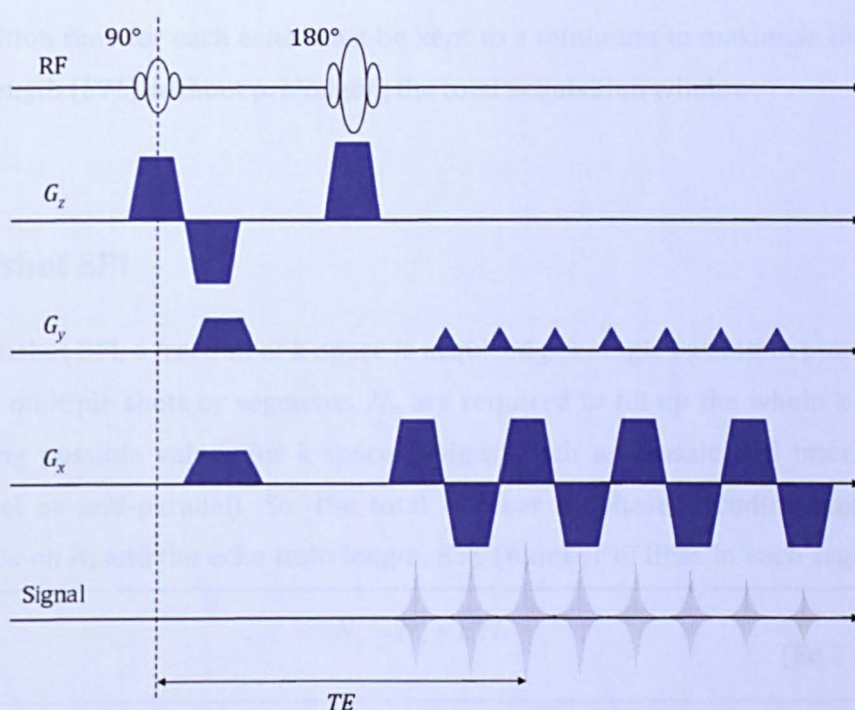


Figure 2.24: Schematic representation of spin echo EPI sequence.

Inversion-Recovery EPI

Inversion-Recovery EPI (IR-EPI) is another form of EPI pulse sequence used to attenuate cerebrospinal fluid (as in FLAIR), measure tissue perfusion with arterial spin labelling, prepare T_1 -weighted images and produce T_1 maps. As its name suggests, this sequence uses an inversion recovery module prior to a GE-EPI or SE-EPI pulse sequence [52].

Single-Shot EPI

Single-shot EPI was initially developed as a single-shot pulse sequence, where only a single radio frequency excitation pulse is applied to acquire an entire two-dimensional data set needed for image reconstruction. Single-shot EPI provides excellent temporal resolution. However, it is prone to producing images with compromised quality (low SNR, low spatial resolution and pronounced artefacts) and places stringent requirements on the gradient and radio frequency hardware (gradient amplitude, slew rate and receiver bandwidth). In single-shot EPI, the

acquisition time for each echo must be kept to a minimum to maximise the echo train length (*ETL*) without prolonging the total acquisition window.

Multishot EPI

In multishot EPI, a fraction of k-space is acquired per single excitation pulse [53]. Hence, multiple shots or segments, N_s , are required to fill up the whole k-space, adopting possible values for k-space designs; such as mosaic and interleaved (parallel or anti-parallel). So, the total number of phase encoding steps, N_y , depends on N_s and the echo train length, *ETL* (number of lines in each segment).

$$N_y = N_s \times ETL \quad (\text{Eq 2.63})$$

In contrast to single-shot EPI, the echo train length does not restrict multishot EPI. Multishot EPI also places less stringent requirements on the gradient and radio frequency hardware compared to single-shot EPI. Therefore, multishot EPI with shorter *ETL* than single-shot EPI is capable of producing images with reduced blurring, reduced ghost intensity, less distortion and better SNR. Multishot EPI with shorter *ETL* will increase the imaging time by a factor of N_{shots} . The scan time is given by,

$$\text{Scan Time} = TR \times N_{packages} \times N_{shot} \times NEX \quad (\text{Eq 2.64})$$

where *NEX* is the number of signal averages and $N_{packages}$ represents the number of acquisitions of passes. As a result, the combination of k-space from different shots makes multishot EPI much more sensitive to motion artefacts.

2.3.3.5 Pulsed Gradient Spin Echo

Pulsed gradient spin echo (PGSE) is the most commonly employed method for producing diffusion-weighted contrast. Stejskal and Tanner initially introduced this sequence in 1965 [54]. The PGSE sequence is made up of a pair of 90° and

180° radio frequency pulses to form a spin echo, with large and equal gradient lobes applied on either side of the 180° pulse (figure 2.25).

The basic idea of the PGSE sequence is that the spins are dephased following the first gradient. Then, the 180° pulse is applied to refocus any reversible losses in spin phase coherence. Here, the 180° pulse effectively changes the sign of the subsequent gradient pulse and therefore the two pulsed gradients are practically equal and opposite. However, the spins would not experience an equal and opposite gradient if they have moved during or between the applications of the two pulsed gradients.

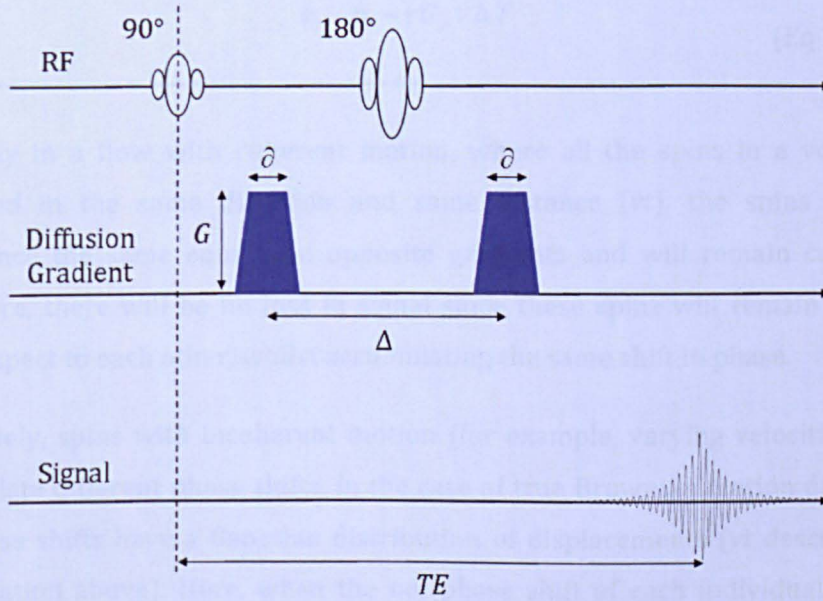


Figure 2.25: Schematic representation of PGSE sequence.

The PGSE sequence can be used to measure velocity. Consider a spin at an initial position, y_0 , moving along the y -axis with velocity v . After a time t , the spin has moved a distance vt . It experiences a shift in phase (ϕ) when it encounters the first pulsed gradient. This gradient, initiated at $t = 0$, reaches its maximum, G_y , and remains at G_y for a time T . Hence, the phase shift from the first gradient is given by,

$$\begin{aligned}\phi_1 &= \gamma G_y \int_0^T (y_0 + vt) dt \\ &= \gamma G_y \left(y_0 T + \frac{vT^2}{2} \right)\end{aligned}\quad (\text{Eq 2.65})$$

Then, after $t = \Delta$, the application of the second gradient pulse, equal and opposite to the first gradient, shifts the spin's phase by,

$$\begin{aligned}\phi_2 &= \gamma G_y \int_{\Delta}^{\Delta+T} (y_0 + vt) dt \\ &= \gamma G_y \left(y_0 T + \frac{vT^2}{2} + v\Delta T \right)\end{aligned}\quad (\text{Eq 2.66})$$

Hence, the resulting net phase shift is,

$$\phi_1 - \phi_2 = \gamma G_y v \Delta T \quad (\text{Eq 2.67})$$

Normally in a flow with coherent motion, where all the spins in a voxel are displaced in the same direction and same distance (vt), the spins will all experience the same equal and opposite gradients and will remain coherent. Therefore, there will be no loss in signal since these spins will remain aligned with respect to each other, whilst accumulating the same shift in phase.

Conversely, spins with incoherent motion (for example, varying velocities) will accumulate different phase shifts. In the case of true Brownian motion diffusion, the phase shifts have a Gaussian distribution of displacements (vt described in the equation above). Here, when the net phase shift of each individual spin is averaged over each voxel, the phase shifts arising from incoherent motion will partially cancel out each other. This results in attenuation of the spin echo.

The degree of diffusion weighting (b -factor) can be controlled by manipulating the strength of the gradient (G), the pulse width (Δ) and the timing element (∂).

The value of b in the PGSE sequence is given by,

$$b = \gamma^2 G^2 \partial^2 \left(\Delta - \frac{\partial}{3} \right) \quad (\text{Eq 2.68})$$

The diffusion-weighted contrast behaves slightly like reverse T_2 contrast. Tissues with high water concentration have very mobile molecules that give rise to lower signal intensity, while tissues with solid and static tissues give a stronger signal.

The signal strength of the PGSE sequence is given by,

$$S(b) = S(0)e^{-bD} \quad (\text{Eq 2.69})$$

where $S(b)$ is the signal for a particular b -value and D is the apparent diffusion coefficient or self diffusion coefficient of the tissue ($\text{mm}^2 \text{s}^{-1}$). In practice, although PGSE measurements are modelled as diffusion, this measurement contains contributions from other movement sources, such as microcirculation in pseudo-random capillary systems that also gives rise to intra voxel incoherent motion (IVIM). The diffusion and microcirculation that occurs simultaneously in each voxel affects the signal attenuation of the PGSE sequence. This signal attenuation can be described as,

$$S(b) = S(0) \left[(1-f)e^{-bD} + fe^{-bD^*} \right] \quad (\text{Eq 2.70})$$

where D^* is the pseudo-diffusion coefficient and f is the perfusion fraction or fractional volume occupied by incoherently moving spins in the voxel. To measure the apparent diffusion coefficient it is necessary to apply a range of b -values and perform a 'least squares' fit. Then, D , D^* and f can be estimated by fitting the signal intensities obtained for images acquired using different b -values to the equation in 2.70 [55].

2.3.4 MR Artefacts

As with any imaging modality, magnetic resonance imaging suffers from a number of artefacts that are either caused by the patients, signal processing inadequacy, or the limitations of the scanner itself. An artefact is an artificial features appearing in an image that is not actually present in the original object. It can affect diagnostic quality and sometimes can be confused with pathology.

2.3.4.1 Patient Related MR Artefacts

Motion Artefacts

One of the most common artefacts in MRI is the motion artefact that either causes ghost images or diffuses noise in the image in the phase-encoding direction. This artefact originates due to a significant difference between the acquisition time in the frequency encoding and phase encoding direction. Normally, sampling at all of the rows in the matrix in the frequency encoding direction takes place during a single echo (milliseconds), while sampling in the phase encoding direction takes several seconds or minutes. This complete set of k-space data is then converted to an MR image by the application of a Fourier Transform. Since major physiological movements occur in seconds, it is too slow to affect the frequency encoding, but has a substantial effect in the phase encoding direction [56].

Ghost images are caused by pulsating or periodic motion such as the movement of blood vessels, cardiac motion and cerebrospinal fluid (CSF), while non-periodic motion can result in diffuse image noise as shown in figure 2.26. The intensity of the ghost image increases with extent of movement and signal intensity from the moving tissue [56]. The fractional separation (SEP) between the ghost can be described as,

$$SEP = \frac{TR \times N_y \times NEX}{T(\text{motion})} \quad (\text{Eq 2.71})$$

or

$$SEP = \frac{\text{acquisition time}}{T(\text{motion})} \quad (\text{Eq 2.72})$$

where $T(\text{motion})$ represents the period of motion of the structure [57].

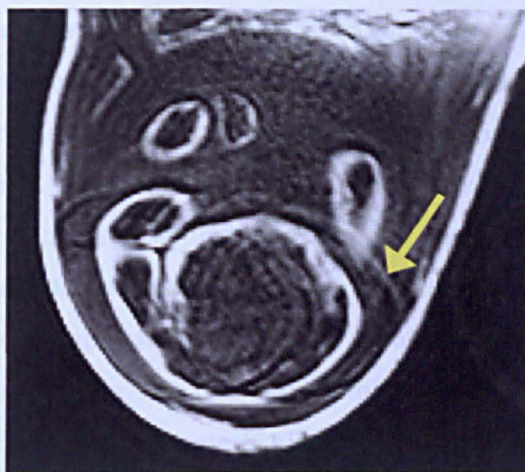


Figure 2.26: Motion artefact (indicated using arrow) due to foetal motion.

Several methods can be used to reduce motion artefacts. The simplest solution is to request the patients to remain as still as possible, or immobilise the patients using pads and immobilisation straps (if necessary, sedating patients in pain) and use glucagon in the abdomen to reduce artefacts due to bowel peristalsis [57]. Alternatively, motion correction using cardiac or respiratory gating (triggering) could be incorporated into scanning protocols. Additionally, motion artefacts can be overcome by suppressing the signals of the tissues causing the artefacts, using a shorter dimension of matrix in the phase-encoding direction, applying view-ordering or phase-reordering methods, and switching the frequency and phase encoding directions to move the artefacts out of the field of interest [56; 58].

Flow Effects

Flow effects in MRI may produce a range of artefacts: altered intravascular signal (flow enhancement or flow related signal loss) or motion artefacts (ghost images or spatial misregistration). Flow enhancement (inflow effect) results when fully magnetised protons enter the imaged slice yielding high signal in comparison to the rest of the surroundings, while the stationary protons have not fully regained their magnetisation. Conversely, flow related signal loss occurs when high velocity flow causes the protons entering the image to be removed before the application of a 180° pulse. Consequently, the magnetisation effect on these protons does not contribute to the echo [56].

The easiest way to avoid flow artefacts is to apply spatial saturation bands outside the field of view or in the slice direction. In such cases, before the application of the radio frequency imaging pulse, the spatial saturation bands apply a 90° pulse to all the tissues within the band. Therefore, the blood flowing from the saturation band into the imaging slice will not have time to recover its magnetisation in the z-direction and consequently will not produce any signal. It is important to note that spatial saturation bands raise pulse sequence time. This reduces the number of slices that can be possibly imaged in a given TR . It also increases the specific absorption rate (SAR), so care should be taken in dealing with such imaging sequence in foetal MRI and patients with impaired thermoregulation conditions or who are febrile [10].

Alternatively, dephasing effects can be corrected by employing a technique called gradient moment nulling (gradient moment rephasing or flow compensation). Here, extra gradient pulses with carefully calculated strengths and durations are incorporated into the pulse sequence in attempt to produce zero net phase effect from moving and static protons. This reduces the velocity induced phase angles, producing a single image of the vessel on the final image. While application of gradient moment nulling does not increase the SAR, the extra gradients will increase the minimum TE , and therefore will reduce the number of slices that can be possibly acquired [10].

Magic Angle Artefacts

Magic angle artefacts are most frequently seen in ligaments and tendons (rotator cuff and patellar tendon) that are oriented at a certain angle (55°) relative to the main magnetic field. The majority composition of tendons is collagen that possesses an anisotropic property. The T_2 of tendons depend on the orientations of this structure. However, the properties of this structure vary with the direction of measurement causing T_2 of the tendon to be slightly increased at the magic angle. While this effect is negligible at long TE , it increases the signal intensity when TE is short causing the tendons to appear brighter in T_1 and PD weighted images. This increased intensity artefacts can potentially be confused with pathology [57].

Susceptibility Artefacts

Susceptibility artefacts occur at interfaces between tissues with different magnetic susceptibilities that cause local magnetic fields to distort the external magnetic field, altering the precession frequency in the tissue leading to spatial mismapping of information. Metal artefacts are a special case of susceptibility artefacts. Most metals have much higher susceptibilities compared to body tissues, creating larger magnetic field inhomogeneities around the metal object. The extent of image distortion depends on the pulse sequence, imaging parameters, type of material (stainless steel inflicts a greater distortion effect compared to titanium alloy) [59] and type of interface (the greatest effects are at soft tissue-metal interfaces). Metal artefacts are caused by internal (surgical clips, spinal hardware and orthopaedic devices) or external ferromagnetic (cobalt containing make up) materials. Metal artefacts are variable; it can result in image distortion, total image loss and peripheral high signal [56]. Moreover, metals are generally good conductors. They absorb energy from the radio frequency excitation pulses and can pose safety hazard. This will be discussed in detail in section 3.3 of Chapter 3.

Susceptibility artefacts can be reduced by aligning the long axis of an implant or metal device parallel to the long axis of the external field. This is possible with an open magnet and mobile extremity imaging [60; 61]. Alternative methods include choosing the appropriate frequency encoding since susceptibility artefacts are most distinct in this direction, applying fast imaging sequences, using smaller voxel sizes, increasing readout bandwidth, avoiding application of gradient echo imaging in presence of metal, and using only spin echo sequence in cases where the images are severely degraded by metal artefacts [10; 59; 60; 61]. In addition, a metal artefact reduction sequence (MARS) can be employed, where additional gradients are applied along the slice selection direction at the time the frequency encoding is applied [56; 61].

2.3.4.2 Signal Processing Dependent Artefacts

Aliasing

Aliasing or wrap around results when the selected field of view is smaller than the body part that is being imaged in the phase encoding direction. The body part outside the field of view will be exposed to certain magnetic field gradients that may correspond to a higher frequency than the maximum frequency (f_{max}) that is being sampled. This Nyquist limit was discussed in section 2.3.2.2, and the sampling rate must be twice the maximum frequency that occurs in the body (Nyquist sampling rate). Since the computer cannot recognise frequency above f_{max} and below f_{min} , any frequency outside the bandwidth's frequency range will be aliased to a frequency existing within the bandwidth. Hence, the higher frequency will be identified as a lower frequency and lower frequency as higher frequency within the accepted bandwidth. The apparent frequency, f_A is given by,

$$f_A = f_T - f_N \quad (\text{Eq 2.73})$$

where f_T is the actual frequency and f_N is the Nyquist frequency [57]. As a result, the body part that lies beyond the edge of the field of view is projected to the opposite side of the image.

In practice, scanners usually apply a low pass filter with Nyquist frequency to avoid aliasing. This is done to remove the high frequency components ($> f_N$) of the signal in the frequency encoding direction. If this filter is applied on its own, the signal at the periphery of the FOV will weaken since the filter has a sloping edge close to the Nyquist frequency known as 'filter roll-off'. Therefore, oversampling technique is normally employed to overcome aliasing problem. Frequency oversampling involves increasing the sampling frequency of the ADC, which results in an increase in the Nyquist frequency (cut-off frequency). While this filtered signal at the new cut-off frequency still have a roll-off edge, the remaining signals at initial cut-off frequency is accurately represented and have no attenuation due to filtering. In contrast, the only way to avoid aliasing artefact in phase encoding direction is to avoid having signals from outside the FOV. While this is achievable by increasing the number of phase encoding steps, it can increase the image time and reduce signal to noise ratio (SNR).

Chemical Shift Artefact

Chemical shift artefacts commonly occur at the fat-water interfaces along the frequency or phase encoding direction. These artefacts are generally noticed in the spine at the vertebral body end plates, in the abdomen or the orbits where fat and other tissues form borders. Chemical shift artefacts appear due to different resonance environment between protons in fat and water; the protons in water resonate at higher frequency than those in fat. Since the polarity of frequency encoding is in the x-direction, higher frequencies are misregistered to right and lower frequencies are misregistered to the left. So, water protons are relatively shifted to the right towards higher frequencies and fat protons are shifted to the left towards lower frequencies. This shifting will result in variation in signal void and overlap, that leads to formation of dark and bright bands on the T_1 weighted or PD weighted conventional spin echo image. For example, in the spine, chemical shifts cause one end of the plate to appear thicker than the opposite end. In the abdomen and orbits, chemical shifts forms a black border at one fat-water interface and a bright border at the other end [57].

In EPI, chemical shifts artefacts usually occur along the phase encoding direction because of very low bandwidth. For spins with a chemical shift of frequency separation, Δf_{cs} (in Hertz), relative to reference frequency, the chemical shift produces a spatial shift (Δy_{cs}) along the phase encoding direction which can be described as,

$$\Delta y_{cs} = \frac{\Delta f_{cs}}{\Delta \nu_{phase}} L_y \quad (\text{Eq 2.74})$$

$$= \frac{t_{esp}}{N_{shots}} \Delta f_{cs} L_y \quad (\text{Eq 2.75})$$

$$\text{where } \Delta f_{cs} = \gamma \times B_0 \times \delta \quad (\text{Eq 2.76})$$

where t_{esp} is the echo spacing, Δy_{cs} is the bandwidth and L_y is the field of view along the phase encoding direction. Since equation 2.74 shows that chemical shifts are inversely related to number of shots (N_{shots}), multishot EPI is less sensitive to chemical shift artefacts [8].

Chemical shift artefacts depend on magnet's field strength and the shift is greater at higher field strengths. Therefore, the receiver bandwidth should be larger than the frequency offset of fat (Δf), so that the chemical shift artefacts are represented by fewer voxels. Alternatively, fat suppression techniques can be employed to overcome this artefact by eliminating the fat signals. This can be achieved by applying spectrally selective pulses prior to the imaging sequence. Provided that the pulse's bandwidth is wide enough to cover the fat frequencies, the spectrally selective pulse will only flip the longitudinal magnetisation of fat into the transverse plane. Then, the transverse magnetisation of fat is destroyed using one or more spoilers. This is achieved by quickly applying subsequent excitation pulse that will flip the longitudinal magnetisation vector of water protons only into the transverse plane and avoid the recovery of the longitudinal magnetisation of fat. To offset the fast recovery of fat magnetisation, the time between the saturation pulse and readout pulse is normally short [62].

Gibbs Phenomenon

Gibbs phenomenon or truncation artefacts are caused by the under-sampling of high frequencies at sharp boundaries in the image [63; 64]. The lack of appropriate high frequency components gives rise to an oscillation at a sharp transition known as a ringing artefact. This phenomenon normally occurs near the sharp boundaries, where high contrast interfaces or transition occur in the body (brain or skull, CSF or cord, fluid or meniscus in the knee) and causes regularly spaced parallel alternating bright and dark bands that slowly fade away with distance. However, these bright and dark signals can be mistaken for lesion (pseudo syrinx of the spinal cord or pseudo tear of the knee meniscus). The ringing artefacts are more pronounced in smaller digital matrix sizes [56; 57].

Gibbs artefacts can be corrected by increasing the matrix size for a given field of view, filtering the k-space data prior to Fourier transform, employing Gegenbauer reconstruction and Bayesian approaches [65; 66; 67].

Partial Volume

Partial volume artefacts arise when the dimension of voxel is larger than the size of the structure that is imaged. Hence, the object loses its identity in the MR image when the signal over the voxel is being averaged causing loss of detail and spatial resolution. Using smaller pixel size or slice thickness can reduce these artefacts, but it also results in poorer SNR in the image [56].

2.3.4.3 Hardware Related Artefacts

External Magnetic Field Inhomogeneity

MR imaging is conducted based on the assumption that external magnetic field (B_0) is homogeneous. When the B_0 is inhomogeneous, it leads to mismapping of tissues that results in intensity variation, spatial distortion, or both. This non-uniformity of the B_0 is usually due to improper shimming, environmental factors, or the far extremes of newer short-bore magnets. Spatial distortion occurs from long-range field gradients, which cause spins to resonate at Larmor frequencies that are different than the Larmor frequencies prescribed by the imaging sequence. Intensity distortion results when the field homogeneity in a location is less or greater than in the rest of the imaged object. The T_2^* in this region is different and thus, the signal will tend to differ [56; 57].

Gradient Field Artefacts

As previously mentioned, magnetic field gradients are used to spatially encode the location of signals that arise from excited protons within the imaged volume. While the slice selection gradient defines the desired slice, phase encoding and frequency encoding gradients provide the spatial information in the remaining two axes. Any deviation in the gradient would result in image distortion.

The gradients usually produce a linear magnetic field gradient over a limited distance. Therefore, very large field of view may comprise regions with nonlinear gradient and the field strength is loss at the periphery as the distance increase from the centre of applied gradient. This effect of nonlinearity at the periphery

leads to image distortion when anatomical compression takes place at the edge of the field of view, which is more prominent in coronal and sagittal imaging due to increased distance from isocentre. Although many systems apply a correction to the image to stretch out the pixels onto a rectangular field of view, a curved edge is formed on the image. Several approaches can be taken to correct gradient field artefacts. These include reducing the field of view by lowering gradient field strength or decreasing the frequency bandwidth of radio frequency signal [10; 56].

Radio Frequency Noise

Radio frequency noise artefact is caused when an unwanted stray external radio frequency signal (for example from TV channels, radio, computers, medical devices, mobile phones and fluorescent lights) is detected. This artefact is similar to the radio frequency feed through, but it occurs at a specific frequency or specific frequencies of the stray external radio frequency rather than at zero frequency. Normally, narrow band noise is projected perpendicular to the frequency encoding direction, while broader noise disrupts the image over a larger area. For this reason, it is important to plan the shielding of the scanner room by implementing proper installation and radio frequency shielding (Faraday cage) to eliminate unwanted stray radio frequency interference [56; 57; 68].

Some of the most common radio frequency noise artefacts are zero line, star artefacts and zippers. Zero line and star artefacts are due to system noise or any cause of radio frequency pollution within the scanner room (e.g.: originating from sparking). If these artefacts persist, it is advisable to check the sources of the system noise such as bad electronics, loose connections to surface coils or source of radio frequency pollution [56; 68]. Zippers appear as a band of alternating bright and dark dots (sometimes two or three pixels wide) extending across the image in the phase encoding direction. They are usually through the image centre and are caused by an imperfect Faraday cage with radio frequency pollution originating from outside the cage. This is generally due to the scanner room door being left open. It can also occur due to a break in the radio frequency screened room (the imperfect metal shield built into the walls, floor and ceiling of the scan room). In such a case, the artefacts will be present on all images and the

manufacturer’s engineers should be called to investigate the problem [10; 56; 68].

2.4 Components of a Magnetic Resonance Imaging System

To have a good understanding of the image formation process, it is important to understand the physical principles of MRI and NMR, with knowledge of basic features of the MRI scanner. The essential components of an MRI system include the magnet that generates the static field, gradient coils for spatial encoding, a radio frequency system that excites and detects the nuclear induction signals and computer for system control, data acquisition, image reconstruction and post-processing [12]. Figure 2.27 is a schematic representation of a typical MRI system.

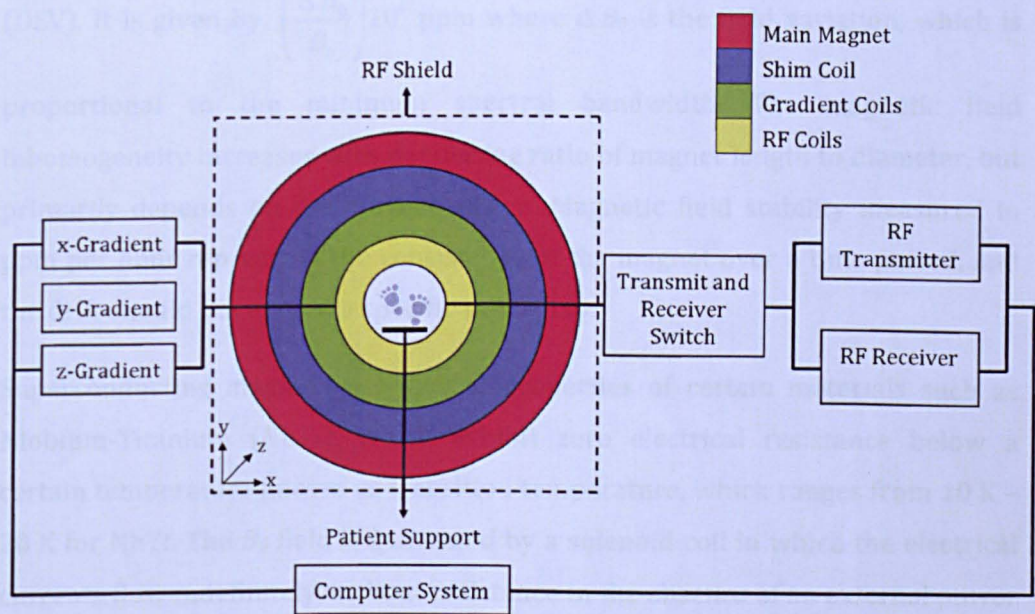


Figure 2.27: Components of an MRI system.

2.4.1 Magnet

The magnet is the main component of the MRI system. It generates the magnetic field. At present, magnets for clinical MRI are available at field strength between 0.2 T and 3.0 T, while magnet for research purposes can be of higher field strengths (currently up to 9.4 T). Normally, the SNR increases with increasing field strength since the nuclear magnetisation is increased. There are two types of magnet: permanent and electromagnetic magnet (electromagnet can be resistive or superconducting). For practical use, all of the magnets in use should achieve three main requirements: strength, uniformity (homogeneity) and stability.

Magnetic field strength is measured in Tesla, where 1 T = 10000 gauss. 1 T is approximately 20000 times the earth field, which is 0.5 gauss. The magnetic field strength does not fall abruptly outside the bore of the magnet; instead it fades away gradually with increasing distance. The magnetic field homogeneity of a magnet is quoted in parts per million over a given diameter of a spherical volume

(DSV). It is given by, $\left(\frac{\Delta B_0}{B_0}\right)10^6$ ppm where ΔB_0 is the field variation, which is

proportional to the minimum spectral bandwidth. The magnetic field inhomogeneity increases with decreasing ratio of magnet length to diameter, but primarily depends on the magnet design. Magnetic field stability measured in ppm per hour represents the consistency of the magnet over a time period, and the drift should not exceed a specific value [10].

Superconducting magnets use special properties of certain materials such as Niobium-Titanium (NbTi), which exhibit zero electrical resistance below a certain temperature known as transition temperature, which ranges from 10 K – 20 K for NbTi. The B_0 field is generated by a solenoid coil in which the electrical currents flow indefinitely without resistance in the absence of an external power source. These coils become superconducting when immersed in liquid helium (boiling point at 4.2 K) and permanently cooled to near absolute zero. The helium is enclosed in a high-vacuum cryostat that is thermally insulated and shielded against radiation. Modern magnets are equipped with a cryorefrigerator (cold head) that stabilises the shield temperature (~ 20 K). Superconducting magnets produce a strong, stable and highly homogeneous magnetic field.

During installation, the superconducting magnet is ramped up or energised to the required field strength using an external electrical field. Once the desired field strength is achieved, the external electrical power can be removed. However, the current will continue flowing with a long decay constant, A :

$$A = \frac{L}{R_e} \quad (\text{Eq 2.77})$$

where L is the inductance and R_e is the electrical resistance. The stored energy of the magnet, E (Joule) is given by,

$$E = \frac{1}{2} L I^2 \quad (\text{Eq 2.78})$$

where L is the wire's inductance (in henrys) and I is the electrical current (in amps).

The magnet cannot be rapidly switched off in emergency. Magnet quenching occurs when any part of the superconducting coils heats up causing superconductivity loss that leads the electrical resistance to rise and impede the current flow in the coil. The rapid drop in current flow and subsequent loss of field strength would cause the stored magnetic energy to convert to heat, which causes rapid boil-off of the liquid helium forming gaseous helium that expands very quickly. This evaporated helium should be vented outside of the magnet room to avoid suffocation and cold burns. Magnet quenching is a serious event that can occur due to a projectile accident, failure of the cooling system, mechanical vibrations or induced field. However, with the recent architecture of superconducting magnet incorporating the state-of-the-art magnet technology, quenching is becoming a rare event [9; 69].

Shielding is very important in MR systems since all magnets produce a fringe field (stray magnetic field) that extends beyond the magnet in all three directions (x, y, z). This stray field can affect the equipment in adjacent rooms and increases the risk of the projectile effect. The magnetic field can be shielded using two approaches. The first approach is a passive method that involves attaching very heavy iron layers around the magnet room and covering the magnet room with a

layer of stainless steel. This is mainly used at ultra-high field. The second method involves active shielding using secondary coils. These coils would produce a magnetic field opposing the fringe field's direction. This sort of shielding reduces the fringe fields by limiting the spatial distribution of the magnet outside the magnet room. However, it will also reduce the internal magnetic field [9; 10; 70].

Most magnets suffer from some inhomogeneity as a result of design limitations or compromises. Therefore, shimming is important to improve a magnet's homogeneity. This can be achieved using fixed passive and active shimming at installation. The former involves placing pieces of steel or iron at certain locations within the magnet bore and outside the scanner's surface. The amount and location of these materials are normally determined using a simulation process run on a computer. The latter involves adding additional superconducting coils inside the magnet bore where currents of accurately pre-determined magnitude can flow. These secondary superconducting coils can also be placed in the cryostat. The scanner's homogeneity can also be adjusted by conducting 'scan by scan' shimming, which is performed by the scanner at the beginning of scan on a per-patient basis using dynamic shimming. Here, the gradient coils are used to produce specific magnetic field homogeneity. Both techniques will optimise magnetic field homogeneity and therefore, reduce image geometric distortion [9; 10; 69; 70].

2.4.2 Gradient System

As discussed in section 2.3.1, spatial localisation of the MR signal is only achievable with the assistance of the gradient system. This system is made up of three orthogonal linear magnetic field gradients, each with its own amplifier that alters the magnetic field strength along the x, y and z directions. These gradients can either be switched separately or together to define and image a slice. Generally, the gradient along the axis of the superconducting magnet is called the slice selection gradient (z-axis), the left-right direction is called the frequency encoding gradient (x-axis) and the top-bottom direction is called the phase-encoding gradient (y-axis). While these gradients are oriented orthogonal to each other, each gradient produces a magnetic field parallel to the main magnetic field, B_0 . The gradient's magnetic field is produced from current flowing in the loops of

coils placed inside the magnet bore. Each gradient has its own magnetic field, which interacts with the main magnetic field by adding to or subtracting from B_0 , causing the magnetic field and Larmor frequency to vary linearly as a function of distance from the centre of the magnet bore. The geometric centre of the magnet is called the isocenter (null point) where the field strength is not affected by any of the three gradients.

Although the gradient coils generate magnetic fields that are relatively small compared to the main magnetic fields, these coils still need currents of several hundred amperes. The gradient field measured in mT m^{-1} depends on the amount of electric current flowing through the gradient coils and the gradient coil size and efficiency, while its direction depends on the sign of the electric current. The gradient performance is measured based on maximum gradient strength, rise time (time to maximum gradient amplitude, which depends on inductance) and slew rate (maximum gradient amplitude per rise time). The high currents are required since the gradient should be strong enough to overcome the main magnetic field inhomogeneity and short enough to prevent signal loss due to relaxation, predominantly T_2^* . Moreover, the gradient fields should be extremely stable to avoid image distortion [9; 69].

2.4.3 Radio Frequency System

The radio frequency system comprises a radio frequency transmitter and receiver along with radio frequency coils. This system generates the oscillating B_1 field that excites the sample and detects the resulting NMR system. This process starts with the formation of the radio frequency pulse in the transmission unit. Initially, a modulator mixes the pulse envelope from the waveform controller to the reference waveform produced by an adjustable frequency synthesizer that is resonating at a frequency near the Larmor frequency. Then, the radio frequency pulse passes through an amplifier that amplifies it by a certain gain. Following this, the radio frequency current from the power amplifier flows through the radio frequency coil, generating a magnetic field. This homogenous oscillating magnetic field excites the sample. Subsequently, the system switches to receiver mode and the receiving unit detects the weak rotating magnetic field generated when the magnetic moments release their energy while returning to their initial

energy state. This received energy is converted back to an electrical signal via Faraday induction.

The signal is amplified by a sensitive, low noise pre-amplifier, so that it is less sensitive to external interference. Then, the amplified signal and input from the system reference oscillator are sent to a quadrature demodulator where the frequency is demodulated by the Larmor frequency leaving the envelope available for further processing steps. The demodulator has two inputs: one representing the real part and the other representing the imaginary part of the signal. The imaginary part is at off-phase by 90° relative to the reference oscillator. The quadrature detection allows measurement of both frequency and phase of the NMR signal. Then, the demodulator signal is low pass filtered to avoid image wrap around or aliasing in the frequency encoding direction. Finally, the outputs of the anti-aliasing filters are digitised using an Analogue to Digital Converter before being sent to the host computer [10].

2.4.4 Computer System

The MRI scanner is controlled by a computer workstation. This computer is very important in controlling and coordinating scans. Its main roles include controlling the gradients and radio frequency coils via a waveform controller (a series of Digital to Analogue Controllers), acquiring data and reconstructing and storing the images of the scanned object. The scanner interface enables the radiographers to adapt the sequence during imaging (for example: motion correction or for a larger field of view). Three dimensional and functional studies would require a high capacity computer with large memory and high data transfer rates. In addition, there is also a physiological monitoring system to monitor the patient inside the scanner room.

2.5 References

- [1] P.G. Morris. (1986), Nuclear Magnetic Resonance Imaging in Medicine and Biology, Oxford Sciend Press, Oxford.
- [2] P. Mansfield, and P.G. Morris. (1982), NMR Imaging in Biomedicine, Academic Press, New York.
- [3] F. Bloch. (1946), Nuclear Induction. Physical Review Online Archive (Prola) **70** 460-474.
- [4] N. Bloembergen, E.M. Purcell, and R.V. Pound. (1948), Relaxation Effects in Nuclear Magnetic Resonance Absorption. Physical Review **73** 679-712.
- [5] M.H. Levitt. (2001), Spin Dynamics: Basic of Nuclear Magnetic Resonance, John Wiley and Sons, Ltd., Chishester, UK.
- [6] J.A. Koutcher, and C.T. Burt. (1984), Principles of Nuclear Magnetic Resonance. Journal of Nuclear Medicine **25** 101-111.
- [7] P.T. Callaghan. (1991), Principles of Nuclear Magnetic Resonance Microscopy, Oxford Science Press.
- [8] M.A. Bernstein, K.F. King, and X.J. Zhou. (2004), Handbook of MRI Pulse Sequences, Elsevier Academic Press, USA.
- [9] M. NessAiver. (1997), All you really need to know about MRI Physics, Baltimore.
- [10] D.W. McRobbie, E.A. Moore, M.J. Graves, and M.R. Prince. (2003), MRI From Picture to Proton, Cambridge University Press, Cambridge, United Kingdom.
- [11] C. Westbrook, C.K. Roth, and J. Talbot. (2005), MRI In Practice, Blackwell Publishing Ltd, Oxford.
- [12] E.J. Rummeny, P. Reimer, and W. Heindel. (2006), MR Imaging of the Body, Thieme, Stuttgart, Germany.
- [13] F. Bloch, W.W. Hansen, and M. Packard. (1946), Nuclear Induction. Physical Review **69** 127-127.
- [14] E.M. Purcell, H.C. Torrey, and R.V. Pound. (1946), Resonance Absorption by Nuclear Magnetic Moments in a Solid. Physical Review **69** 37-38.
- [15] S.-i. Nagaoka. (2007), A Short History of Three Chemical Shifts. Journal of Chemical Education **84** 801.
- [16] W.G. Proctor, and F.C. Yu. (1951), On the Nuclear Magnetic Moments of Several Stable Isotopes. Physical Review **81** 20-30.

- [17] W.C. Dickinson. (1950), Dependence of the ^{19}F Nuclear Resonance Position on Chemical Compound. *Physical Review* **77** 736-737.
- [18] E.L. Hahn. (1950), Spin Echoes. *Physical Review* **80** 580-594.
- [19] S.H. Koenig, and W.E. Schillinger. (1969), Nuclear Magnetic Relaxation Dispersion in Protein Solutions. *Journal of Biological Chemistry* **244** 3283-3289.
- [20] W.D. Rooney, G. Johnson, X. Li, E.R. Cohen, S.-G. Kim, K. Ugurbil, and C.S. Springer. (2007), Magnetic field and tissue dependencies of human brain longitudinal $^1\text{H}_2\text{O}$ relaxation in vivo. *Magnetic Resonance in Medicine* **57** 308-318.
- [21] C. Burtea, S. Laurent, L. Elst, R.N. Muller, W. Semmler, and M. Schwaiger. (2008), Contrast Agents: Magnetic Resonance Molecular Imaging I, Springer Berlin Heidelberg.
- [22] H. Nakamura, N. Ito, F. Kotake, Y. Mizokami, and T. Matsuoka. (2000), Tumor-detecting capacity and clinical usefulness of SPIO-MRI in patients with hepatocellular carcinoma. *Journal of Gastroenterology* **35** 849-855.
- [23] A. Tanimoto, G. Wakabayashi, H. Shinmoto, S. Nakatsuka, S. Okuda, and S. Kuribayashi. (2005), Superparamagnetic iron oxide-enhanced MR imaging for focal hepatic lesions: a comparison with CT during arteriportography plus CT during hepatic arteriography. *Journal of Gastroenterology* **40** 371-380.
- [24] T. Araki. (2000), SPIO-MRI in the detection of hepatocellular carcinoma. *Journal of Gastroenterology* **35** 874-876.
- [25] P. Loubeyre, S. Zhao, E. Canet, H. Abidi, S. Benderbous, and D. Revel. (1997), Ultrasmall superparamagnetic iron oxide particles (AMI 227) as a blood pool contrast agent for MR angiography: Experimental study in rabbits. *Journal of Magnetic Resonance Imaging* **7** 958-962.
- [26] J.A. Pople. (1959), High-resolution nuclear magnetic resonance McGraw Hill, New York.
- [27] H.J. Weinmann, R.C. Brasch, W.R. Press, and G.E. Wesbey. (1984), Characteristics of gadolinium-DTPA complex: a potential NMR contrast agent. *American Journal of Roentgenology* **142** 619-624.
- [28] P.C. Lauterbur. (1973), Image Formation by Induced Local Interactions: Examples Employing Nuclear Magnetic Resonance. *Nature* **242** 190-191.
- [29] P. Mansfield, and P.K. Grannell. (1973), NMR 'diffraction' in solids? *Journal of Physics C: Solid State Physics* **6** L422.

- [30] A. Kumar, D. Welte, and R.R. Ernst. (1975), NMR Fourier zeugmatography. *Journal of Magnetic Resonance* **18** 69-83.
- [31] P.C. Lauterbur, D.M. Kramer, W.V. House, and C.-N. Chen. (1975), Zeugmatographic high resolution nuclear magnetic resonance spectroscopy. Images of chemical inhomogeneity within macroscopic objects. *Journal of the American Chemical Society* **97** 6866-6868.
- [32] P. Mansfield, A.A. Maudsley, and T. Bains. (1976), Fast scan proton density imaging by NMR. *Journal of Physics E: Scientific Instruments* **9** 271.
- [33] D.I. Hoult. (1977), Zeugmatography - criticism of the concept of a selective pulse in presence of a field gradient. *Journal of Magnetic Resonance* **26** 165-167.
- [34] A.N. Garroway, P.K. Grannell, and P. Mansfield. (1974), Image formation in NMR by a selective irradiative process. *Journal of Physics C: Solid State Physics* **7** 457-462.
- [35] W.A. Edelstein, J.M. Hutchison, G. Johnson, and T. Redpath. (1980), Spin warp NMR imaging and applications to human whole-body imaging. *Physics in Medicine and Biology* **25** 751-6.
- [36] R.N. Bracewell. (1978), *Fourier transform and its applications*, McGraw-Hill, New York.
- [37] J.F. James. (2002), *A student's guide to Fourier transforms with applications in physics and engineering*, Cambridge University Press, Cambridge, UK.
- [38] T.A. Gallagher, A.J. Nemeth, and L. Hacin-Bey. (2008), An Introduction to the Fourier Transform: Relationship to MRI. *American Journal of Roentgenology* **190** 1396-1405.
- [39] S. Ljunggren. (1983), A simple graphical representation of Fourier-based imaging methods. *Journal of Magnetic Resonance* **54** 338-343.
- [40] D.B. Twieg. (1983), The k-trajectory formulation of the NMR imaging process with applications in analysis and synthesis of imaging methods. *Medical physics* **10** 610-21.
- [41] A. Haase, J. Frahm, D. Matthaei, W. Hanicke, and K.D. Merboldt. (1986), FLASH imaging. Rapid NMR imaging using low flip-angle pulses. *Journal of Magnetic Resonance* (1969) **67** 258-266.
- [42] J. Frahm, K.D. Merboldt, H. Bruhn, M.L. Gyngell, W. Hänicke, and D. Chien. (1990), 0.3-second flash mri of the human heart. *Magnetic Resonance in Medicine* **13** 150-157.

- [43] W. Hanicke, K.D. Merboldt, D. Chien, M.L. Gyngell, H. Bruhn, and J. Frahm. (1990), Signal strength in subsecond FLASH magnetic resonance imaging: the dynamic approach to steady state. *Medical physics* **17** 1004-10.
- [44] R.F. Busse, S.J. Riederer, J.G. Fletcher, A.E. Bharucha, and K.R. Brandt. (2000), Interactive fast spin-echo imaging. *Magnetic Resonance in Medicine* **44** 339-348.
- [45] J.r. Barkhausen, S.G. Ruehm, M. Goyen, T. Buck, G. Laub, and J.r.F. Debatin. (2001), MR Evaluation of Ventricular Function: True Fast Imaging with Steady-State Precession versus Fast Low-Angle Shot Cine MR Imaging: Feasibility Study1. *Radiology* **219** 264-269.
- [46] V.S. Deshpande, S.M. Shea, G. Laub, O.P. Simonetti, J.P. Finn, and D. Li. (2001), 3D magnetization-prepared true-FISP: A new technique for imaging coronary arteries. *Magnetic Resonance in Medicine* **46** 494-502.
- [47] M.J. Stehling, A.M. Howseman, R.J. Ordidge, B. Chapman, R. Turner, R. Coxon, P. Glover, P. Mansfield, and R.E. Coupland. (1989), Whole-body echo-planar MR imaging at 0.5 T. *Radiology* **170** 257-263.
- [48] P. Mansfield. (1977), Multi-planar imaging formation using NMR spin echoes. *Journal of Physics C: Solid State Physics* **10** 55-58.
- [49] P. Mansfield. (1984), Real-time echo-planar imaging by NMR. *British medical bulletin* **40** 187-90.
- [50] M.K. Stehling, R. Turner, and P. Mansfield. (1991), Echo-planar imaging: magnetic resonance imaging in a fraction of a second. *Science* **254** 43-50.
- [51] R. Rzedzian, P. Mansfield, M. Doyle, D. Guilfoyle, B. Chapman, R.E. Coupland, A. Chrispin, and P. Small. (1983), Real-time Nuclear Magnetic Resonance Clinical Imaging in Paediatrics. *The Lancet* **322** 1281-1282.
- [52] M.K. Stehling, R.J. Ordidge, R. Coxon, and P. Mansfield. (1990), Inversion-recovery echo-planar imaging (IR-EPI) at 0.5 T. *Magnetic Resonance in Medicine* **13** 514-517.
- [53] G.C. McKinnon. (1993), Ultrafast interleaved gradient-echo-planar imaging on a standard scanner. *Magnetic Resonance in Medicine* **30** 609-616.
- [54] E.O. Stejskal, and J.E. Tanner. (1965), Spin Diffusion Measurements: Spin Echoes in the Presence of a Time-Dependent Field Gradient. *Journal of Chemical Physics* **42** 288-292.
- [55] R. Turner, D. Le Bihan, J. Maier, R. Vavrek, L.K. Hedges, and J. Pekar. (1990), Echo-planar imaging of intravoxel incoherent motion. *Radiology* **177** 407-414.

- [56] L.J. Erasmus, D. Hurter, M. Naude, H.G. Kritzing, and S. Acho. (2004), A short overview of MRI artefacts. *South African Journal of Radiology* **8** 13-17.
- [57] R.H. Hashemi, W.G. Bradley, and C.J. Lisanti. (2004), *MRI: the basics*, Lippincott Williams & Wilkins, Philadelphia.
- [58] T.D. Nguyen, G. Ding, R. Watts, and Y. Wang. (2001), Optimization of view ordering for motion artifact suppression. *Magnetic Resonance Imaging* **19** 951-957.
- [59] J.S. Suh, E.K. Jeong, K.H. Shin, J.H. Cho, J.B. Na, D.H. Kim, and C.D. Han. (1998), Minimizing artifacts caused by metallic implants at MR imaging: experimental and clinical studies. *American Journal of Roentgenology* **171** 1207-13.
- [60] A.M. Viano, S.A. Gronemeyer, M. Haliloglu, and F.A. Hoffer. (2000), Improved MR imaging for patients with metallic implants. *Magnetic Resonance Imaging* **18** 287-295.
- [61] S.D. Chang, M.J. Lee, P.L. Munk, D.L. Janzen, A. MacKay, and Q.-S. Xiang. (2001), MRI of spinal hardware: comparison of conventional T1-weighted sequence with a new metal artifact reduction sequence. *Skeletal Radiology* **30** 213-218.
- [62] T.A. Bley, O. Wieben, C.J. François, J.H. Brittain, and S.B. Reeder. Fat and water magnetic resonance imaging. *Journal of Magnetic Resonance Imaging* **31** 4-18.
- [63] S.J. Lee. (1998), An improved method for reduction of truncation artifact in magnetic resonance imaging. *Proceedings of SPIE: Applications of Digital Image Processing* **4360** 587-598.
- [64] R.A. Elgavish, and D.B. Twieg. (2003), Improved depiction of small anatomic structures in MR images using Gaussian-weighted spirals and zero-filled interpolation. *Magnetic Resonance Imaging* **21** 103-112.
- [65] R. Archibald, and A. Gelb. (2002), A method to reduce the Gibbs ringing artifact in MRI scans while keeping tissue boundary integrity. *Medical Imaging, IEEE Transactions on* **21** 305-319.
- [66] T. Bakir, and S.J. Reeves. (2000), A filter design method for minimizing ringing in a region of interest in MR spectroscopic images. *Medical Imaging, IEEE Transactions on* **19** 585-600.

- [67] R.R. Schultz, and R.L. Stevenson. (1994), A Bayesian approach to image expansion for improved definition. *Image Processing, IEEE Transactions on* **3** 233-242.
- [68] E. Pusey, R.B. Lufkin, R.K. Brown, M.A. Solomon, D.D. Stark, R.W. Tarr, and W.N. Hanafée. (1986), Magnetic resonance imaging artifacts: mechanism and clinical significance. *Radiographics* **6** 891-911.
- [69] D. Weishaupt, V.D. Köchli, and B. Marincek. (2006), *How Does MRI Work? An Introduction to the Physics and Function of Magnetic Resonance Imaging*, Springer, Verlag Berlin Heidelberg, Germany.
- [70] A.D. Elster, and J.H. Burdette. (2001), *Questions & Answers in Magnetic Resonance Imaging*, Mosby, Missouri.

Chapter 3

Foetal Magnetic Resonance Imaging

3.1 Overview

This chapter gives a brief review of the increasing usage of MRI with respect to ultrasound in prenatal diagnosis. With obstetricians often faced with question on which imaging modality is better in diagnosing the various prenatal conditions, the author has taken the opportunity to discuss the advantages and disadvantages of each modality with respect to their importance in foetal imaging.

In addition, the author will provide an overview of the risks of MRI exposure during pregnancy to the mother and foetus. A detailed discussion on how the static field, time varying magnetic field and radio frequency fields interact with the human body, particularly the foetus will be presented in this chapter. Following this, reviews of recent studies on outcomes of MRI scans conducted in foetuses, adults and animals will be presented. Finally, the author will discuss some other factors that may compromise foetal well-being.

3.2 Introduction to Foetal Imaging

Driven by ongoing technical and scientific advancement, foetal MRI is emerging from being an exclusive prenatal research modality to a clinically important tool. MRI surfaced as a potentially powerful non-invasive diagnostic technique in prenatal and perinatal studies in 1983 [1; 2]. It has been widely employed to

study the development of the foetal central nervous system, gastrointestinal tract, genitourinary system, respiratory system and placental abnormalities [3; 4].

On the other hand, ultrasound arrived as the predominant imaging modality in Obstetrics and Gynaecology in the 1960s, after Professor Ian Donald published a breakthrough paper describing the use of ultrasound in diagnosing abdominal masses in *The Lancet* in 1958 [5]. Since then, ultrasound has been used extensively in monitoring and diagnosing foetal abnormalities in prenatal and perinatal medicine.

The construction of ultrasound images is very different from MR images. Unlike MRI, ultrasound is based on sound waves. The ultrasound transducer converts the electrical power into high frequency sound waves that are transmitted into the body. These sound waves are inaudible to human ears since they are in the range of 2 MHz to 15 MHz. They propagate through tissue and are partially reflected from the interface between tissues with different sound conducting characteristics, returning to the transducer as echoes. The scanner produces the ultrasound images by determining the direction of the echoes and calculating the time taken for the echoes to travel back to the transducer from the time the sound waves were transmitted. This information is used to calculate the depth of the tissues interfering with the echoes and to subsequently produce an image of the tissues. Lower frequency sound waves have longer wavelengths and are capable of travelling deeper into the body, but produce images with low resolution. Conversely, higher frequency sound waves have shorter wavelengths and a larger attenuation coefficient. Hence, they can image smaller structures with high resolution, but are limited by the depth of penetration of the sound wave into the body.

Normally, transabdominal ultrasound is the first choice for obstetric scans. It generally involves placing and moving a transducer, covered with warmed lubricant jelly, on the pregnant abdomen. The movement of the transducer will enable the sonographers to visualise the foetal organs and placenta, and measure the biparietal diameter, femur length, abdominal and head circumference and crown-rump length (CRL) [6; 7; 8]. However, in early pregnancy, transvaginal ultrasound (a higher frequency ultrasound) is preferred due to its ability to produce images with higher spatial resolution, even if it is limited by lower

penetration capability. This is essential when the foetal organs are small because transvaginal probes are able to get closer to the foetus, to overcome the lack of penetration. Conversely, in later stage of pregnancy, ultrasound with greater penetration capability is essential to see deeper into the foetus.

With improvement in technical and image quality in both MRI and ultrasound, questions have surfaced on which modality is better in prenatal assessment. In this review, the advantages and disadvantages of both imaging methods will be put into perspective with respect to the most important imaging factors.

3.2.1 Availability and Accessibility

At present, ultrasound is more established in clinical use due to its widespread availability and established safety. It is recognised as a non-invasive, cost-effective, bedside imaging tool that is capable of producing images with high anatomical resolution in real-time [1]. On the contrary, although MRI has been recognised as an imaging tool to complement ultrasound, MRI is very expensive and is not widely available. For these reasons, ultrasound is ideal as a screening tool.

3.2.2 Maternal Imaging Factors

Ultrasound scans are known to be difficult and technically limited when dealing with obese mothers, patients with multiple pregnancy and patients suffering from oligohydramnios (deficiency of amniotic fluid) or polyhydramnios (excess of amniotic fluid). In these cases, the image quality of ultrasound is compromised due to interference of the ultrasound beam and inconsistent penetration through maternal structures. Normally, the sonographers will need to use high frequency transabdominal ultrasound for high-resolution images of the foetus. However, high frequency ultrasound will not be able to penetrate deep inside the maternal pelvis where the foetus is buried. Although sonographers can employ transvaginal ultrasound scans, critics have raised concerns on the safety of the transducer being much closer to the foetus compared to transabdominal ultrasound. Nonetheless, this technique produces better images of the foetus in

the first and second trimester, but proves to be challenging in the third trimester [1; 9].

While MRI has been recognised as an imaging tool to assist ultrasound in cases involving obese mothers, there are similar issues and limitations in performing foetal MRI in these patients. The main concern is that the large mother may not fit inside the MRI unit, especially when placed in the decubitus position, since the upper limit of the abdominal circumference in the supine position is about 140 cm and the table weight is usually limited to 150 kg (this varies for different types of scanner). On the other hand, if the mother was successfully positioned in the scanner, the image quality of the intrauterine regions of interest may still be compromised. If scanning using phased array coils (for example: cardiac coils) fails, an integrated coil can be used. Although this will enable the investigator to examine a bigger area of interest, it will lead to a reduction in the image resolution [4; 9]. Moreover, the mother's tissues will be near the edge of the bore where the RF gradient and static magnetic fields are inhomogeneous.

3.2.3 Gestational Age

After decades of advancement in obstetric imaging, ultrasound still remains as the primary imaging choice in the first trimester. Ultrasound is particularly useful in producing images with clear representation of the foetal gestation and nuchal translucency in the first trimester. On the contrary, due to the restrictions of the slice thickness and partial volume averaging, MRI does not have adequate resolution to produce images with accurate foetal anatomy in the first trimester. In addition to this, there is insufficient evidence of safety during the vulnerable first trimester when the fetuses are generally sensitive to teratogens. For these reasons, most obstetric practices have opted to avoid MRI scans in the first trimester, unless the benefits outweigh the potential risks [4].

In contrast, ultrasound imaging of the abdomen and uterine appendages becomes more difficult with advancing gestation, especially in the third trimester. This is due to the displacement of the gas filled bowel by the enlarging uterus and decrease in the amniotic fluid. Consequently, sonographers often encounter problems while imaging the foetal brainstem from the midline sagittal view, which is important in evaluating the foetal brain. Although the foetal position is

an important criterion in the success of foetal brain imaging using ultrasound, foetal position cannot be altered unless it is medically necessary. Therefore, the anterior border of the brainstem may not be optimally observed due to beam attenuation [4]. Moreover, despite the little space available in the pregnancy sac at late gestation, foetal head movements are more pronounced, possibly disrupting ultrasound and MR images. However, with current advancement in ultrasound and fast imaging MR sequences, foetal images can be captured by freezing foetal motion.

For MRI, mothers at later gestation may experience difficulty in remaining still during the scan. Moreover, foetal MRI can also be challenging when the foetal head is engaged within the lesser pelvis at late gestation: poor signal may result from unfavourable coil geometry when the coil is positioned on the decubitus maternal abdomen [4; 9].

3.2.4 Image Resolution

Ultrasound employs high frequency probes that are capable of imaging small foetal structures, such as hair and eyelashes. They are also useful for imaging nuchal translucency in the first trimester [4]. This is particularly true for transvaginal ultrasound images, which are obtained by transducer placement into the vagina. They produce images with better resolution. Nevertheless, ultrasound images are still occasionally criticised for insufficient contrast to provide detailed information on foetal anomalies. Ultrasound is also limited in accurate prediction of lung development and maturation, in terms of determining whether the foetal lung has attained sufficient development to sustain neonatal survival. This is commonly related to congenital diaphragmatic hernia, oligohydramnios or lung parenchyma [10; 11].

As for foetal MRI, the smallest voxel size that can be obtained with the current technology is about $0.8 \text{ mm} \times 0.8 \text{ mm} \times 3.0 \text{ mm}$. In addition, foetal MRI is also restricted by the slice thickness, which limits the imaging of smaller and thinner foetal structures [4]. For example, identification of meningeal lining in meningoceles can be very difficult, due to partial-volume averaging of thinned meningeal leafs with the adjacent cerebrospinal fluid and amniotic fluid [12].

3.2.5 Three Dimensional Rendering of Surface Anatomy

At present, the ultrasound produces planar and volume rendered 3-dimensional images that are able to undergo multiplanar reconstruction to produce 3- and 4-dimensional foetal surface anatomy. Although MRI can produce 3-dimensional reconstructed images, the images obtained from foetal MRI lack anatomical details due to the application of dynamic sequences with a thick slab. For this reason, the foetal facial portrayal would be less detailed [4; 13; 14].

3.2.6 Operator Dependence

The quality and accuracy of ultrasound imaging is greatly operator dependent and requires expertise in sonography. Sonographers will have to acquire and interpret images in real time. In comparison to ultrasound, MRI is somewhat less operator dependent. Although expertise is required to position slices and acquire data during the course of the scan, interpretation of MR images can be done at a later time by a radiologist [4; 15]. Nonetheless, in cases involving artefacts that may represent true pathology, both ultrasound and MRI operators would require advice from experts (radiologists or physicists).

3.2.7 Duration of the Examination

Normally, the detailed ultrasound screening carried out in the second trimester in singleton pregnancies takes approximately an hour. However, this procedure can extend to 2 hours or more depending on foetal position, multiple pregnancy or anomalies detected. In some cases, foetal echocardiography may be required, or the patient may be requested to return for further diagnostic sessions if images obtained were not satisfactory. Conversely, foetal MRI in singleton pregnancies can be conducted in a shorter period. In our department, basic foetal anatomical imaging using HASTE and FISP is completed in 15 to 20 minutes, whilst the scan sessions take about 30 minutes. This includes repetitive

sequences because of foetal motion. The scan period is shorter in foetal MRI since it employs fast imaging sequences that compensate for foetal motion [4].

3.2.8 Other Issues

Unlike ultrasound, foetal MRI can be very challenging for patients suffering from back pain and claustrophobia. This condition can be enhanced in the third trimester of pregnancy, when pregnant patients may have difficulty lying supinely and are traumatised when placed in a magnet considered to be small for their size. Conversely, they may also display anxiety when confronted with the magnet for the first time. In our experience, claustrophobia is a minor problem when patients are given adequate briefing and comforted before examination [4; 12]. In some cases, patients are calmer when an MR assistant is present by their side in the scanner room throughout the scan. Additionally, foetal MRI cannot be performed in cases involving maternal pacemakers and ferromagnetic implants.

3.2.9 Conclusion

In conclusion, ultrasound is ideal for screening, while MRI is a complementary screening modality employed in suspected pathology or complex cases in addition to ultrasound in prenatal diagnosis. In addition, MR images are easier to interpret compared to ultrasound images, and have proved to be useful in patient counselling and management [16; 17; 18; 19; 20; 21].

3.3 Safety of Foetal Magnetic Resonance Imaging

Foetal MRI has certainly gained an important role in the management of complicated pregnancy development. Nonetheless, the endless advancement in foetal MRI technology has alerted medical practitioners to possible adverse

effects on the developing foetus, mother and MR workers. In 2007, the Health Protection Agency released safety guidelines for patients and volunteers undergoing MRI procedures. These guidelines highlighted restrictions that are required to be implemented when imaging infants, pregnant women, febrile patients and in other impaired circumstances [22].

The uterine environment contains electrically conductive and thermally insulating fluids. If foetal development is interrupted during the process of cell differentiation and migration, it may lead to fully developed organs with compromised functionality. This issue often gives rise to doubts on the safety of any intervention in early pregnancy, including MRI. Moreover, unlike adults participating in MR scans, foetuses are unable to provide informed consent for themselves. Hence, the investigators are expected to be more responsible and cautious in ensuring the safety of the MR exposure to the foetus.

The Health Protection Agency has paid attention to three main safety considerations in conducting foetal MRI. These areas of concern include static fields, pulsed radio frequency and time-varying electromagnetic gradient fields. As discussed in Chapter 2, the static field plays an important role in polarising the nuclear magnetisation, the radio frequency fields are used to excite the nuclear spins to obtain a signal, and the time varying magnetic field arises from the switching of magnetic field gradients that are essential for image encoding [9; 23].

3.3.1 Static Field

All human beings are continually exposed to the magnetic field of the earth, which is approximately 0.5 G or 5×10^{-5} T. This field is weak and people are generally unaware of its existence, unless if alerted by magnetic compasses [24]. The production of strong magnetic fields was made achievable with the discovery of electromagnets in the early 19th century. However, the available power supplies and the heating of the current carrying coils limited the fields available until superconductors were discovered in the mid 20th century. Subsequently, at that point of time, fields of the order of tesla became available [25].

Initially, only a handful of people were exposed to these strong magnetic fields. They were individuals involved in specific professions, such as experimental high-energy physics. However, with 1.5 T MRI entering the clinical world in the 1980s, people were introduced to a new degree of human exposure to magnetic fields [25]. Since then, the exploration and expansion of MRI applications has led to a growth in the number of scanners used throughout the world. This has subsequently contributed to the increase in the number of people receiving MR scans and an increase in the level of exposure to the participants and the MR workers.

The primary danger in MRI is associated with acceleration of ferromagnetic materials positioned in close proximity to the stray field of the magnet. The outcome of accelerating metal objects can be very severe. It may inflict life-threatening injuries to the patient lying in the MR scanner and potentially to the foetus. The probability of this risk is increased when scanning pregnant patients since there is an increased likelihood of other healthcare professionals with no MR background accompanying the subject into the scanner room. For these reasons, it is important to train the staff meticulously and implement all the appropriate local working rules. It is also vital to regularly monitor and maintain a non-magnetic scanner room layout [9].

Following the issue described above, there are also concerns pertaining to the torques or translational forces on metal objects implanted in the body. These magnetised implants will tend to rotate in the scanner, such that their magnetic moment will come into alignment with the scanner's magnetic field. This twisting may produce local tissue irritation that can lead to oedema formation [9; 25]. Moreover, similar translational effects may occur in these foreign bodies, potentially harming the subject's health. For instance, displacement or distortion of prostheses such as cochlear implants and intra-cranial vascular and surgical clips, can occur [26].

Nonetheless, the utmost concern is the threat to the functionality of medical metal or electronic implants. There is a strong possibility of erratic and inappropriate pacemaker functionality during and after scanning [26]. However, these risks can be mitigated with a careful pre-MRI screening procedure conducted by MR staff. They should take extra care in checking biomedical implants, devices and components associated with lead wires that have or have

not obtained FDA approval and claim to be MR safe or compatible. The MR scans involving these implants should be conducted based on manufacturers guidelines and recommendations. Besides this, staff should also request patients to remove all body piercings that may be harmful to their health [9; 25; 27].

There have also been concerns about the threat following the changes in the force on blood moving through the static field, called the magnetohydrodynamic effect. Normally, the force, \mathbf{F} , produced by current flowing in tissues is [25]

$$\mathbf{F} = \mathbf{J} \times \mathbf{B}$$

(Eq 3.1)

where \mathbf{J} represents the electric current density and \mathbf{B} is the magnetic field. The electric current density of tissues is determined using the tissue's electrical conductivity (σ) and the electric field, \mathbf{E} [25]:

$$\mathbf{J} = \sigma \mathbf{E}$$

(Eq 3.2)

However, in cases involving tissue movement with velocity, \mathbf{v} the motion induced electric field would be in terms of $\mathbf{v} \times \mathbf{B}$. Hence, the electric current density would be [25]:

$$\mathbf{J} = \sigma (\mathbf{E} + \mathbf{v} \times \mathbf{B})$$

(Eq 3.3)

At very high fields ($> 16 \text{ T}$), when an electrically conducting fluid, such as blood flows in an applied magnetic field, a transverse electromotive force (EMF) is developed. As a consequence, patients may experience compensatory changes in blood pressure and encounter small electric voltages on the body surface as a result of small-induced current density produced in the tissues. This induced EMF is proportional to the magnetic field strength and the velocity of blood flow [9; 25].

At present, there is no consistent clinical evidence demonstrating any significant magnetohydrodynamic effect at the field strengths currently used. In addition, the EMF's are largest at the surface and not at the centre of the magnet where the foetus is positioned. Nevertheless, this may be an issue if foetuses were scanned at higher field strengths since they are more sensitive to these effects compared

to adults. Foetuses have their own aortic blood flow system, which is similar to adults [28]. However, since the foetal blood pressure is somewhat lower than in adults, any force inflicted on the blood might be more significant. Moreover, unlike adults lying in scanner configurations, the foetus can lie in any orientation with respect to the direction of the static field. As the magnetohydrodynamic effect is largest when the field and velocity of blood are perpendicular, the effect will be increased if the foetus is aligned in such way that the direction of flow is perpendicular to the magnetic field [9; 29; 30]. In adults, this often occurs in the aortic arch but in a foetus it may occur in the body of the aorta if the foetus is lying transverse to the static field.

Furthermore, users of high field MRI scanners (> 2 T) are known to experience disorientation or subtle perception of movement while working close to or within the magnet's bore. This effect is called magnetic-field-induced vertigo, which is an outcome of either an induced EMF, by a weak magnetohydrodynamic force affecting the endolymphatic tissues of the inner ear, or diamagnetic anisotropy of the otoliths of the inner ear receptors [22; 31]. Other effects include the effect on sensory organs leading to a metallic taste in the mouth, and sometimes magnetophosphenes where subjects experience flashes of light. In some cases associated with longer exposure, nausea or motion sickness, which may last for a few hours, can accompany the sensation of vertigo. Although these effects are transient and do not cause health hazards, scanner manufacturers often advise staff to move the patient's bed slowly into the magnet to keep the peak rate of change of field to less than 1 T s^{-1} . This should not be an issue in foetal MRI, since pregnant patients are scanned using low field MR scanners and they are more likely to move slowly while climbing onto the MR bed [9; 23; 32].

In addition to the issues discussed so far, the major concern of foetal MRI is the effect of high-level exposure to the static field, which might result in detrimental effects on embryogenesis, chromosomal structuring and foetal development. Although several human foetal studies have been conducted in recent years to identify foetal growth retardation in pregnant mothers exposed to MRI in late gestation period, there is no clear evidence of disability or retardation in human foetuses [33]. Nonetheless, investigations conducted on pregnant mice demonstrated reduction in foetal weight and crown-rump length. There was also evidence of increased abortion rate and some deleterious effects on spermatogenesis and embryogenesis in mice [34]. A study conducted on frog

eggs in a static magnetic field provided data suggesting alteration in early segmentation of the frog embryo. This could be an outcome resulting from variations in magnetic susceptibility of the different components in a cell involved in segmentation. However, this effect did not persist to impede in later development [35].

Besides the foetus and pregnant subjects, scientists have also recognised the importance of studying the effects of static fields on pregnant MRI staff members. In 1993, a group in the USA conducted a survey consisting of four questionnaires that covered 1421 pregnancies. This study investigated the effect of static field exposure to the fertility, length of gestation, birth weight, pregnancy outcomes and offspring's gender of the female MRI staff in frequent contact with the scanner. The data collected from this study did not demonstrate any statistically significant effect on the offspring of these pregnant MR staff [36]. Nonetheless, pregnant workers are advised to avoid remaining within the MRI scanner room during the actual scanning process. They should also be given an option not to enter the scanner room [23; 37].

At present, there is no consistent evidence suggesting magnetic field exposure is harmful to foetuses. The few cases of injuries reported relating to humans are due to the inadvertent presence of ferromagnetic materials or cardiac pacemakers. Nevertheless, with advancement in MR technology and field strengths used in human studies, scientists should continue their efforts to regularly inspect for signs of unexpected field-related health issues.

3.3.2 Time-Varying Magnetic Gradient Fields

The gradient coils used in MRI add approximately linear variations to the static field. They are time-varying magnetic fields that are of low frequency range (0 – 1 kHz), and can induce electric currents within conducting objects, including the human body [23; 38; 39; 40]. At sufficiently high amplitudes, the gradient induced electric fields are known to stimulate nerves or muscles in adults. In addition, at extremely high levels, cardiac stimulation or even ventricular fibrillation can occur. These stimulation thresholds for scanners are usually determined by examining adults. Hence, there is a possibility that the differences in the geometry of pregnant women could lead to an increased risk of

stimulations in certain conditions. Although this is not a life threatening risk to pregnant mothers, it can be very uncomfortable. As for the foetus, the induced current will be lower since it is near the centre of the coil [9; 39; 40].

A major concern with time-varying gradient fields is that the acoustic noise generated can reach up to 120 dB_A. This occurs due to rapid switching of the currents within the gradient coils and the strong magnetic field, which combine to produce Lorentz forces that cause the coils to vibrate and produce loud knocking noises. This loud sound depends on electric field, magnetic field and time varying magnetic field ($\frac{dB}{dt}$). Since the foetus' ear is completely formed by the 20th gestation week, it will be able to detect and respond to sounds [41] received through airborne noise transmitted across the maternal body wall and mechanical vibrations experienced because the mother is lying in contact with the scanner bed. At present, research has shown that foetuses respond to low frequency sounds (100 Hz, 250 Hz, 1000 Hz and 3000 Hz), but there is no evidence suggesting abnormalities in foetus' hearing function [9; 33; 42]. The noise level reaching the foetal cochlea is suppressed because the foetus is insulated by the mother's abdominal wall. More importantly, the amniotic fluid filling the foetal ear will attenuate the noise in a frequency dependent manner, preventing the normal amplification of sound by the ear. Nevertheless, care should be taken to limit the noise level exposure to the foetus. It should be noted that if high noise levels are applied frequently throughout pregnancy, there is a possibility of poor pregnancy outcome [43; 44].

In addition to protecting the foetus from noise, pregnant women participating in MRI should also be given adequate hearing protection to reduce maternal noise exposure. Moreover, they should be mechanically isolated from the scanner's bed by using dense mattresses. This will reduce the mechanical vibration experienced by the pregnant women and foetus. Furthermore, during pulse sequence development, it is essential for MR staff to assess the loudness of the pulse sequences applied in foetal MRI. It is advisable to avoid loud pulse sequences if other alternatives exist [9].

3.3.3 Radio Frequency Fields

The major concern with radio frequency (RF) fields is the production of relatively large heat deposition that may lead to thermal heating of the tissues, causing local burns. The RF fields induce eddy currents in the tissues, and these increase molecular motion and generate heat, resulting in absorption of RF energy. The average RF exposure is simply described in terms of Specific Absorption Rate (SAR) [45]:

$$\text{SAR} = 0.5 \left(\frac{\sigma \pi^2 f^2 r^2 B_1^2 D}{\rho} \right) \quad (\text{Eq 3.4})$$

where f = Larmor frequency, r = conductor loop radius B_1 = RF field strength, D = duty cycle or total RF pulse times/TR and ρ = mass density.

In the last few decades, several studies have been conducted to identify the effect of RF heating on adults and fetuses. These include monitoring the temperature of poorly vascularised tissues such as the eye lens and heating sensitive structures such as the testes and organs with no pain sensors such as the brain [33]. These studies found evidence suggesting that the human body has the capability to lose heat through the skin by conduction and increased cutaneous blood flow. Nonetheless, RF burns can develop in adults when they are in close contact with the RF coils or extraneous electrical conductors such as ECG leads, RF coil leads and metal implants. RF burns can also take place in adults with tattoos. The colours on tattoo pigments are created with organic substances; some contain iron oxide, which seems to be related to heating during MRI scans. These effects occasionally happen when the pigment's material are arranged in a ring or loop pattern [46; 47; 48; 49]. This loop-like structure, formed through physical contact or a looped tattoo, promotes electric conduction that may result in RF burns [9; 47].

The mechanisms discussed above do not operate as a threat to fetuses in the well-insulated maternal body. The foetal and maternal circulations are independent of each other. For this reason, it is particularly difficult to predict the temperature change in fetuses. The foetus' body temperature exceeds the maternal temperature due to the heat produced by the foetus' metabolism. Unlike adults, fetuses lose heat by conducting heat into amniotic fluid and

across the uterine wall. They also lose heat via the large blood flow through the placenta and umbilical cord. However, heat loss in foetuses is relatively inefficient. Hence, pregnant patients should be scanned in a scanner with good air flow through the bore, reasonable room temperature, and not be covered with a blanket during scans [50; 51].

Moreover, until further information is available, foetal MRI should only be conducted using low SAR sequences ($< 2 \text{ W kg}^{-1}$), since this requires lower RF power and reduces the production of heat [52; 53]. SAR level can be reduced by reducing the number of slices, increasing TR , reducing RF tipping angle and reducing echo train length in rapid imaging sequences such as HASTE [54]. If application of high SAR sequences is necessary, the sequence should be applied for as short a time as possible and the high SAR sequences should be interleaved with low SAR sequences. In addition, foetal MRI should be conducted with care or avoided if possible in non-urgent cases involving pregnant patients with impaired thermoregulation conditions or who are febrile [50].

3.3.4 General Safety

While considering the safety of MRI, it is important to inspect the risks and benefits of other techniques employed in foetal MRI. Over the years, many MR scans have been performed using intravenous contrast agents, since it is particularly useful in improving the visibility of abnormal structures or lesions in the body. Studies have shown that approximately 30% – 40% of more than 7 – 10 million MR examinations performed every year included administration of gadolinium chelates such as Magnevist (Gd-DTPA), ProHance (Gd-HP-D03 A) or Omniscan (Gd-DTPA-BMA) [55].

In 2006, the usage of gadolinium based contrast agents was linked to Nephrogenic Systemic Fibrosis (NSF). It is a disease arising in patients with renal failure, especially patients with severe kidney impairment [56; 57; 58; 59]. Neonates and infants up to 1 year of age are exposed to the NSF risk since their kidneys are not completely developed [60]. In the case of the foetus, only minutes after administration of a gadolinium based contrast agent to the mother, this contrast agent is transported into the amniotic fluid almost exclusively by glomerular filtration and foetal kidney excretion. Subsequently, the amniotic fluid

is swallowed by the foetus causing the contrast agent to continuously alternate within the foetal gastrointestinal tract and foetal urinary system, causing it to be retained within the pregnancy sac [55; 61]. Although there is no data to uphold the hazard of this mechanism, the safety of this situation is questionable, particularly given the known issues of long-term exposure to gadolinium in an adult. For this reason, usage of gadolinium is not recommended in foetal MRI.

In the year 2000, a study on Magnevist conducted on rats (at 2.5 times the human dose, 0.1 mmol kg⁻¹) and rabbits (at 7.5 times the human dose) demonstrated delay in foetal development without evidence of congenital anomalies [62; 63]. Moreover, there is data suggesting increase in foetal loss when the ProHance dose is increased [63]. Considering all these risks, the use of contrast agents during pregnancy should be discouraged unless there are compelling clinical reasons [60].

While the safety issues related to magnetic fields and hardware have been addressed in detail, it is essential to practice some common safety procedures to reduce the anxiety experienced by the mothers participating in the MR scans. This will impact on the foetal well-being during scans. MR practitioners should pay importance to investigating the patient's previous health conditions and identifying the psychological risk of claustrophobia. If necessary, an MR assistant should be assigned to accompany and remain with the patient throughout the scan procedure. It is also vital to identify syncopal symptoms. Pregnant patients lying supinely are exposed to the risk of aortacaval compression. The gravid uterus may compress the inferior vena cava and aorta causing a decrease in blood returning to the heart. This leads to a decrease in cardiac output that may result in a feeling of faintness. However, tilting the patient onto her side or elevating the right hip by 15 – 20 cm usually overcomes this problem [9; 64].

3.3.5 Conclusion

In conclusion, determining the safety of MR imaging is challenging since it is not possible to prove its safety, only to disprove it. At present, there is no clear evidence suggesting foetal MRI leads to foetal mortality or morbidity. Nonetheless, it would be wise to take precautionary measures to avoid potential hazards while conducting foetal MRI. This includes limiting the total scanning

time for safety reasons and patient comfort, and applying sequences with reduced amplitude for low frequency switching gradients to reduce the sound levels, vibration effects and the risk of nerve stimulation. It is also advisable to avoid foetal MRI in the first trimester to avoid the risk of teratogenic effects. All the safety measures described in this chapter were practiced in these studies.

3.4 References

- [1] C. Garel, H. Brisse, G. Sebag, M. Elmaleh, J.-F. Oury, and M. Hassan. (1998), Magnetic resonance imaging of the fetus. *Pediatric Radiology* **28** 201-211.
- [2] F.W. Smith, A.H. Adam, and W.D. Phillips. (1983), NMR imaging in pregnancy. *Lancet* **1** 61-2.
- [3] M. Cannie, J. Jani, S. Dymarkowski, and J. Deprest. (2006), Fetal magnetic resonance imaging: luxury or necessity? *Ultrasound in Obstetrics and Gynecology* **27** 471-476.
- [4] D. Pugash, P.C. Brugger, D. Bettelheim, and D. Prayer. (2008), Prenatal ultrasound and fetal MRI: The comparative value of each modality in prenatal diagnosis. *European Journal of Radiology* **68** 214-226.
- [5] I. Donald, J. Macvicar, and T. Brown. (1958), Investigation of abdominal masses by pulsed ultrasound. *Lancet* **1** 1188-1195.
- [6] F.P. Hadlock, R.L. Deter, R.B. Harrist, and S.K. Park. (1984), Estimating fetal age: computer-assisted analysis of multiple fetal growth parameters. *Radiology* **152** 497-501.
- [7] D. Levine. (2001), Three-dimensional Fetal MR Imaging: Will It Fulfill Its Promise? *Radiology* **219** 313-315.
- [8] M.J. Shepard, V.A. Richards, R.L. Berkowitz, S.L. Warsof, and J.C. Hobbins. (1982), An evaluation of two equations for predicting fetal weight by ultrasound. *American Journal of Obstetrics and Gynecology* **142** 47-54.
- [9] D. Prayer. (2011), *Fetal MRI*, Springer.
- [10] F. Rypens, T. Metens, N. Rocourt, P. Sonigo, F. Brunelle, M.P. Quere, L. Guibaud, B. Maugey-Laulom, C. Durand, F.E. Avni, and D. Eurin. (2001), Fetal Lung Volume: Estimation at MR Imaging--Initial Results. *Radiology* **219** 236-241.
- [11] T. Keller, A. Rake, S.A. Michel, B. Seifert, J. Wisser, B. Marincek, and R. Kubik-Huch. (2004), MR assessment of fetal lung development using lung volumes and signal intensities. *European Radiology* **14** 984-989.
- [12] T. Huisman, E. Martin, R. Kubik-Huch, and B. Marincek. (2002), Fetal magnetic resonance imaging of the brain: technical considerations and normal brain development. *European Radiology* **12** 1941-1951.
- [13] R.A. Kubik-Huch, S. Wildermuth, L. Cettuzzi, A. Rake, B. Seifert, R. Chaoui, and B. Marincek. (2001), Fetus and Uteroplacental Unit: Fast MR Imaging with

- Three-dimensional Reconstruction and Volumetry-Feasibility Study1. *Radiology* **219** 567-573.
- [14] Cornelia F Hagmann, Nicola J. Robertson, Wee C. Leung, Kling W. Chong, and L.S. Chitty. (2008), Foetal brain imaging: ultrasound or MRI. A comparison between magnetic resonance imaging and a dedicated multidisciplinary neurosonographic opinion. *Acta P&Eiatrica* **97** 414-419.
- [15] H. Shinmoto, and S. Kuribayashi. (2003), MRI of fetal abdominal abnormalities. *Abdominal Imaging* **28** 877-886.
- [16] D. Levine. (2004), Fetal magnetic resonance imaging. *Journal of Maternal-Fetal Neonatal Medicine* **15** 85-94.
- [17] D. Levine. (2001), Ultrasound versus Magnetic Resonance Imaging in Fetal Evaluation. *Topics in Magnetic Resonance Imaging* **12** 25-38.
- [18] D. Levine, P.D. Barnes, J.R. Madsen, J. Abbott, T. Mehta, and R.R. Edelman. (1999), Central Nervous System Abnormalities Assessed With Prenatal Magnetic Resonance Imaging. *Obstetrics & Gynecology* **94** 1011-1019.
- [19] E. Whitby, M.N. Paley, N. Davies, A. Sprigg, and P.D. Griffiths. (2001), Ultrafast magnetic resonance imaging of central nervous system abnormalities in utero in the second and third trimester of pregnancy: comparison with ultrasound. *BJOG: An International Journal of Obstetrics & Gynaecology* **108** 519-526.
- [20] F.V. Coakley, H. Hricak, R.A. Filly, A.J. Barkovich, and M.R. Harrison. (1999), Complex Fetal Disorders: Effect of MR Imaging on Management-Preliminary Clinical Experience. *Radiology* **213** 691-696.
- [21] E.M. Simon, R.B. Goldstein, F.V. Coakley, R.A. Filly, K.C. Broderick, T.J. Musci, and A.J. Barkovich. (2000), Fast MR Imaging of Fetal CNS Anomalies in Utero. *American Journal of Neuroradiology* **21** 1688-1698.
- [22] H.P. Agency. (2007), Protection of Patients and Volunteers Undergoing MRI Procedures (R.P. Division, Ed., Chilton, Didcot, Oxfordshire).
- [23] J.P. De Wilde, A.W. Rivers, and D.L. Price. (2005), A review of the current use of magnetic resonance imaging in pregnancy and safety implications for the fetus. *Progress in Biophysics and Molecular Biology* **87** 335-353.
- [24] P.F. Mottelay. (1922), Bibliographical history of electricity and magnetism chronologically arranged., Charles Griffing & Co, London.
- [25] J.F. Schenck. (2000), Safety of Strong, Static Magnetic Fields. *Journal of Magnetic Resonance Imaging* **12** 2-19.

- [26] A.K.A. Silva, E.L. Silva, E.S.T. Egito, and A.S. Carrico. (2006), Safety concerns related to magnetic field exposure. *Radiation and Environmental Biophysics* **45** 245-252.
- [27] A.M. Sawyer-Glover, and F.G. Shellock. (2000), Pre-MRI Procedure Screening: Recommendations and Safety Considerations for Biomedical Implants and Devices. *Journal of Magnetic Resonance Imaging* **12** 92-106.
- [28] K. Marsall, A. Lindblad, G. Lingman, and S.H. Eik-Nes. (1984), Blood flow in the fetal descending aorta; intrinsic factors affecting fetal blood flow, i.e. fetal breathing movements and cardiac arrhythmia. *Ultrasound in Medicine & Biology* **10** 339-348.
- [29] K. Marsal, A. Lindblad, G. Lingman, and S.H. Eik-Nes. (1984), Blood flow in the fetal descending aorta; intrinsic factors affecting fetal blood flow, i.e. fetal breathing movements and cardiac arrhythmia. *Ultrasound in Medicine & Biology* **10** 339-348.
- [30] Y. Kinouchi, H. Yamaguchi, and T.S. Tenforde. (1996), Theoretical analysis of magnetic field interactions with aortic blood flow. *Bioelectromagnetics* **17** 21-32.
- [31] F. de Vocht, T. Stevens, P. Glover, A. Sunderland, P. Gowland, and H. Kromhout. (2007), Cognitive effects of head-movements in stray fields generated by a 7 Tesla whole-body MRI magnet. *Bioelectromagnetics* **28** 247-255.
- [32] P.M. Glover, I. Cavin, W. Qian, R. Bowtell, and P.A. Gowland. (2007), Magnetic-Field-Induced Vertigo: A Theoretical and Experimental Investigation. *Bioelectromagnetics* **28** 349-361.
- [33] R.D. Kok, M.M. de Vries, A. Heerschap, and P.P. van den Berg. (2004), Absence of harmful effects of magnetic resonance exposure at 1.5 T in utero during the third trimester of pregnancy: a follow-up study. *Magnetic Resonance Imaging* **22** 851-854.
- [34] M. Mevissen, S. Buntenkötter, and W. Löscher. (1994), Effects of static and time-varying (50-Hz) magnetic fields on reproduction and fetal development in rats. *Teratology* **50** 229-237.
- [35] J.M. Denegre, J.M. Valles, K. Lin, W.B. Jordan, and K.L. Mowry. (1998), Cleavage planes in frog eggs are altered by strong magnetic fields. *Proceedings of the National Academy of Sciences* **95** 14729-14732.

- [36] E. Kanal, J. Gillen, J.A. Evans, D.A. Savitz, and F.G. Shellock. (1993), Survey of Reproductive Health Among Female MR Workers. *Obstetrical & Gynecological Survey* **48** 724-725.
- [37] E. Kanal, J.P. Borgstede, A.J. Barkovich, C. Bell, W.G. Bradley, J.P. Felmlee, J.W. Froelich, E.M. Kaminski, E.K. Keeler, J.W. Lester, E.A. Scoumis, L.A. Zaremba, and M.D. Zinninger. (2002), American College of Radiology White Paper on MR Safety. *American Journal of Roentgenology* **178** 1335-1347.
- [38] J.S. Daniel, D.B. Joe, and A.N. John. (2000), Review of Patient Safety in Time-Varying Gradient Fields. *Journal of Magnetic Resonance Imaging* **12** 20-29.
- [39] J. Reilly. (1989), Peripheral nerve stimulation by induced electric currents: Exposure to time-varying magnetic fields. *Medical and Biological Engineering and Computing* **27** 101-110.
- [40] J.P. Reilly. (1992), Principles of Nerve and Heart Excitation by Time-varying Magnetic Fields. *Annals of the New York Academy of Sciences* **649** 96-117.
- [41] J.C. Birnholz, and B.R. Benacerraf. (1983), The development of human fetal hearing. *Science* **222** 516-518.
- [42] H.P. Agency. (2008), Protection of Patients and Volunteers Undergoing MRI Procedures (C.a.E.H. Radiation, Ed.)
- [43] D.S. Richards, B. Frentzen, K.J. Gerhardt, M.E. McCann, and R.M. Abrams. (1992), Sound Levels in the Human Uterus. *Obstetrics & Gynecology* **80** 186-190.
- [44] P. Glover, J. Hykin, P. Gowland, J. Wright, I. Johnson, and P. Mansfield. (1995), An assessment of the intrauterine sound intensity level during obstetric echo-planar magnetic resonance imaging. *British Journal of Radiology* **68** 1090-1094.
- [45] D.I. Hoult, and P.C. Lauterbur. (1979), The sensitivity of the zeugmatographic experiment involving human samples. *Journal of Magnetic Resonance* (1969) **34** 425-433.
- [46] M.L. Kreidstein, D. Giguere, and A. Freiberg. (1997), MRI Interaction with Tattoo Pigments: Case Report, Pathophysiology, and Management. *Plastic and Reconstructive Surgery* **99** 1717-1720.
- [47] M. Vahlensieck. (2000), Tattoo-related cutaneous inflammation (burn grade I) in a mid-field MR scanner. *European Radiology* **10** 197-197.

- [48] W.A. Wagle, and M. Smith. (2000), Tattoo-Induced Skin Burn During MR Imaging. *American Journal of Roentgenology* **174** 1795.
- [49] M.F. Dempsey, and B. Condon. (2001), Thermal Injuries Associated with MRI. *Clinical Radiology* **56** 457-465.
- [50] P.A. Gowland, and J.D. Wilde. (2008), Temperature increase in the fetus due to radio frequency exposure during magnetic resonance scanning. *Physics in Medicine and Biology* **53** L15-L18.
- [51] K. Satoru, and et al. Temperature elevation in the fetus from electromagnetic exposure during magnetic resonance imaging. *Physics in Medicine and Biology* **55** 2411.
- [52] J.W. Hand, and et al. Numerical study of RF exposure and the resulting temperature rise in the foetus during a magnetic resonance procedure. *Physics in Medicine and Biology* **55** 913.
- [53] J.W. Hand, Y. Li, E.L. Thomas, M.A. Rutherford, and J.V. Hajnal. (2006), Prediction of specific absorption rate in mother and fetus associated with MRI examinations during pregnancy. *Magnetic Resonance in Medicine* **55** 883-893.
- [54] D.W. McRobbie, E.A. Moore, M.J. Graves, and M.R. Prince. (2003), *MRI From Picture to Proton*, Cambridge University Press, Cambridge, United Kingdom.
- [55] G.S. Frank, and K. Emanuel. (1999), Safety of magnetic resonance imaging contrast agents. *Journal of Magnetic Resonance Imaging* **10** 477-484.
- [56] P. Marckmann, L. Skov, K. Rossen, A. Dupont, M.B. Damholt, J.G. Heaf, and H.S. Thomsen. (2006), Nephrogenic Systemic Fibrosis: Suspected Causative Role of Gadodiamide Used for Contrast-Enhanced Magnetic Resonance Imaging. *Journal of the American Society of Nephrology* **17** 2359-2362.
- [57] C. Rydahl, H.S. Thomsen, and P. Marckmann. (2008), High Prevalence of Nephrogenic Systemic Fibrosis in Chronic Renal Failure Patients Exposed to Gadodiamide, a Gadolinium-Containing Magnetic Resonance Contrast Agent. *Investigative Radiology* **43** 141-144.
- [58] D.R. Broome, M.S. Girguis, P.W. Baron, A.C. Cottrell, I. Kjellin, and G.A. Kirk. (2007), Gadodiamide-Associated Nephrogenic Systemic Fibrosis: Why Radiologists Should Be Concerned. *American Journal of Roentgenology* **188** 586-592.

- [59] B. Dale R. (2008), Nephrogenic systemic fibrosis associated with gadolinium based contrast agents: A summary of the medical literature reporting. *European Journal of Radiology* **66** 230-234.
- [60] P.A. Gowland, W. Kucharczyk, G. Bongartz, R.R. Price, and M.R. Prince. (2007), Special issue: MR safety. *Journal of Magnetic Resonance Imaging* **26** 1177-1178.
- [61] F. Garcia-Bournissen, A. Shrim, and G. Koren. (2006), Safety of gadolinium during pregnancy. *Canadian Family Physician* **52** 309-10.
- [62] V.M. Runge. (2000), Safety of approved MR contrast media for intravenous injection. *Journal of Magnetic Resonance Imaging* **12** 205-213.
- [63] S.M. Chung. (2002), Safety Issues in Magnetic Resonance Imaging. *Journal of Neuro-Ophthalmology* **22** 35-39.
- [64] D. Farine, and P.G. Seaward. (2007), When it Comes to Pregnant Women Sleeping, Is Left Right? *Journal of Obstetrics and Gynaecology Canada* **29** 841-842.

Chapter 4

Anatomy and Development of Foetus

4.1 Overview

Pregnancy is a pivotal part of human development. The mother's body must create, nurture, oxygenate and adequately nourish foetuses to prepare for the challenges of life outside the womb. The purpose of this chapter is to provide readers with concise information on the phases of foetal development in the uterus. The author will explore the process of foetal growth and development of placenta, foetal brain, respiratory system, liver and urinary system by reviewing the response and adaptation of the foetuses to potential stressful intrauterine environment. This chapter will serve as an introduction to the foetal studies conducted by the author for her PhD project.

4.2 Introduction to Foetal Imaging

The average duration of foetal development is 38 weeks or 266 days [1], that starts with fertilisation of two haploid living cells: an oocyte (female germ cell) and a spermatozoon (male germ cell). The oocyte is a large cell consisting of 23 chromosomes, surrounded by a thick membrane called the zona pellucida. It is approximately 120 μm in diameter. Conversely, the spermatozoon is a small-specialised male cell, which also has a total of 23 chromosomes. It has a head of 3 – 4 μm diameter and 5 μm long. The head of the spermatozoon contains the nucleus, which bears the DNA information, and it moves using the flagellum or tail that is on average 55 μm in length [1].

Fertilisation takes place in the ampullary region of the fallopian tube. The results of the fertilisation process are: determination of offspring's sex, restoration of the diploid number of chromosomes and initiation of cleavage. Fertilisation is initiated when a single spermatozoon penetrates through the zona pellucida, in an attempt to integrate with the oocyte. This integration results in the establishment of pronuclei containing either the maternal or paternal chromosomes. After approximately 30 – 36 hours of encounter with a spermatozoon, the pronuclei fuse to restore a single diploid nucleus containing a full set of chromosomes. This is the start to embryo formation. Subsequently, the embryo goes through a series of mitotic cell divisions called cleavage that increases the number of cells without significantly increasing their size. This leads to the formation of blastomeres that become smaller with each division and undergo compaction [1; 2; 3].

Following this, the compacted blastomeres continue to divide to form a morula that enters the uterus. A hollow sphere is formed in this cell mass in preparation for implantation into the uterine wall; at this stage the cell mass is known as a blastocyst. The blastocyst develops into two layers: the external cell layer (trophoblast) and the inner cell mass (embryoblast). On the seventh day of post-fertilisation, when the zona pellucida surrounding the morula is disrupted, the blastocyst sinks into the uterine lining allowing implantation to occur and signifying the start of the official embryonic stage. The trophoblastic cells differentiate into two layers, the cytotrophoblast and syncytiotrophoblast, which erodes into maternal tissue to establish the future placenta and is responsible for the uteroplacental circulation. Then, the embryoblast undergoes further differentiation between the 7th and 20th day to produce external and internal germ layers known as ectoderm, mesoderm and endoderm in a process called blastogenesis [1; 2; 3].

The third to eighth weeks of development are known as the embryonic organogenesis period, which involves modification of the ectoderm, mesoderm and endoderm germ layers. This period marks the beginning of foetal development where the major organs of the body are established. The ectodermal germ layer is responsible for formation of organs and structures that maintain contact with the outside world: peripheral nervous system, central nervous system, skin (including hair and nails), sensory epithelium of the eye, nose and ear, pituitary, mammary and sweat glands and enamel of the teeth [3].

It also forms the amniotic sac [1]. The mesoderm forms all the supporting tissues of the body such as muscle tissue, subcutaneous tissue of the skin, cartilage and bone. It also gives rise to the vascular system (heart, arteries, veins, blood, lymph vessels and cells), urogenital system (kidneys and gonads), spleen and cortex of the suprarenal glands. Similarly, the endodermal germ layer generates the epithelial lining of the respiratory tract, gastrointestinal tract, urinary bladder, tympanic cavity and auditory tube. The endodermal layer also produces the parenchyma of the thyroid, parathyroids, pancreas and liver. During organ development, particularly the central nervous system, the initial flat embryonic disc begins to fold cephalocaudally and transversely to establish the head, tail and rounded body form. This embryonic organogenesis period normally ends with the foetus' face appearing as human [3].

The ninth week of gestation until birth involves rapid growth and maturation of organ systems, along with a relative slowdown in foetal head growth. During this period, the foetus grows in length and increases the weight gradually. The third, fourth and fifth months embark in the greatest increase in length (approximately 5 cm per month), whereas the striking increase in weight occurs in the eighth and ninth month (approximately 700 g per month) [1; 3]. Although the foetus is continuously developing throughout the gestation period, it is not capable of physically living outside the uterus before the 22nd gestation week. However, if a foetus was delivered at 25 weeks, with an average body weight of 500 g, it may survive with intensive care [4]. Although survival rate increases with increasing total body weight and gestational age at delivery, some foetuses are left with disability and some die [5]. A study conducted in the UK and Ireland in 2006 documented a survival rate of 7% for 22 weeks, 42% for 24 weeks and 78% for babies born at 28 weeks [6]. Normally, a foetus is delivered at the 40th gestational week when its average body weight is roughly around 3400 g, with boys usually heavier than girls [1; 3].

The process of giving birth is divided into three stages that starts with effacement and dilatation of the cervix, continues with active labour until delivery of the foetus and ends with delivery of the placenta and foetal membranes. Once the foetus is delivered, it is known as a neonate for the first 28 days of its life after delivery. During this period, it will need to adapt to the extrauterine environment. As a foetus, the oxygen is received via the placenta. Conversely, in the neonatal period, the newborns will have to breathe oxygen from the

atmosphere through their lungs; a mechanism to which the respiratory system has to acclimatise [1; 3].

4.2.1 Placenta

The placenta was named after a Latin word, “circular cake” by an Italian professor and surgeon, Realdus Columbus in 1559 [7]. Its name justifies the appearance of a full term placenta: a blue-red coloured discoid shaped organ weighing on average between 500 g to 600 g, with a diameter of 15 cm to 25 cm and approximately 3 cm thick at delivery [8; 9]. Similar thickness is observed using MRI at late gestation. Throughout the pregnancy, the placenta gradually enlarges by increasing its thickness and surface area approximately proportional to the expanding uterus; a growth that adapts to the increasing metabolic requirements of the growing foetus. Hence, the placenta often covers 15% to 30% of the internal surface of the uterus during the whole gestation [2; 3]. The placenta’s role ends at birth, when the placenta becomes separated and is delivered safe from the uterine environment minutes after the baby.

The placenta is the only organ biologically developed by the mother and child, consisting of foetal and maternal parts that establish symbiotic dependence in the intrauterine environment. It plays a vital role in nurturing the growing foetus, provides immunological defence and acts as a partial barrier against cell transfer from the foetus to mother and vice versa, during gestational period. Its main functions include acting as the foetal lung to exchange gaseous products between the maternal and foetal bloodstreams, assisting in metabolic exchange by providing substrates for foetal metabolism and disposing waste products and being responsible for hormone production [2; 3].

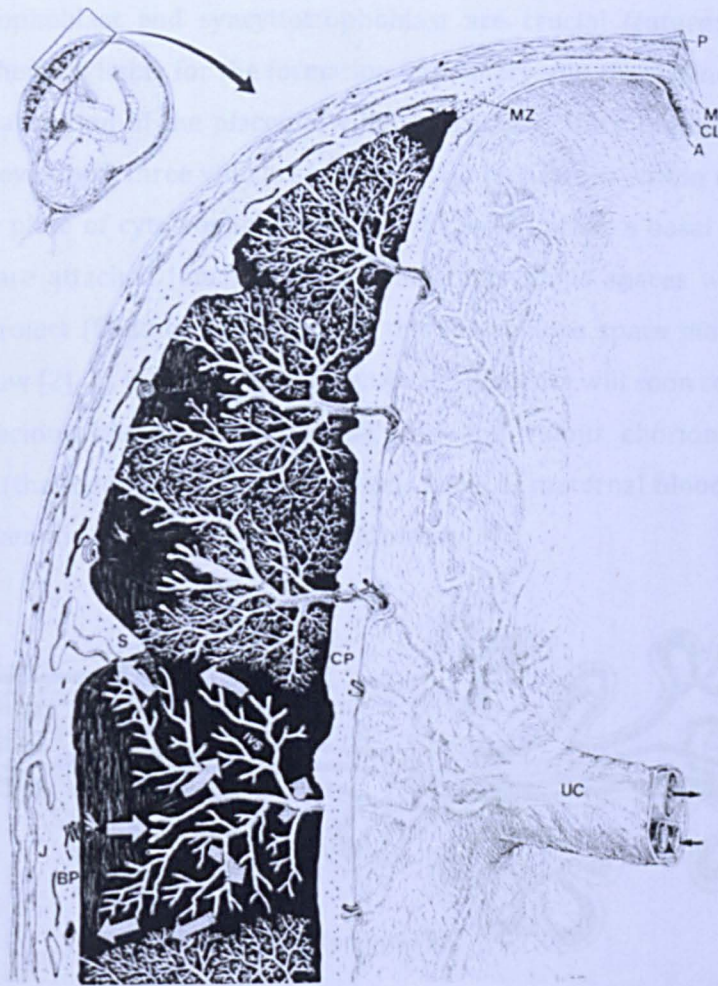


Figure 4.1: A schematic representation of matured human placenta. BP: basal plate, CP: chorionic plate, IVS: intervillous space, S: placental septum, J: junction zone, UC: umbilical cord, P: perimetrium, M: myometrium, CL: chorion laeve, A: amnion and MZ: marginal zone between the placenta and foetal membrane [10].

Placental development begins with the implantation of the blastocyst into the maternal endometrium on the sixth to seventh day following conception. The outer layer of the blastocyst, the trophoblast, is the coating responsible for the formation of the placenta. Initially, trophoblast is composed of mono-nucleated cells (cytotrophoblast) that undergo differentiation into oligo-nucleated syncytiotrophoblast. The inner layer of mononuclear cytotrophoblast cells is known as the base for cell division. These cells begin to migrate into the syncytiotrophoblast layer where they fuse. Subsequently, the cell membranes are lost to form the multinucleated outer syncytiotrophoblast layer [11]. This layer will undergo expansion to produce spaces, where the maternal blood supplying the placenta will eventually flow [1; 2].

The cytotrophoblast and syncytiotrophoblast are crucial features within the placenta. They are liable for the formation of primary villi that branch gradually, enabling maturation of the placental villous structure. Once the basic placental system is developed, three villous structures will be present within the placenta: a chorionic plate of cytotrophoblast from which villi arise, a basal plate where some villi are attached (anchoring villi) and intervillous spaces where villous branches project (floating villi); through this intervillous space maternal blood will soon flow [2]. As the pregnancy extends, the placenta will soon consist of two sections, decidua basalis (the maternal site) and villous chorion or chorion frondosum (the foetal site). The intervillous lakes of maternal blood occupy the space between the decidual and chorionic plates [3].

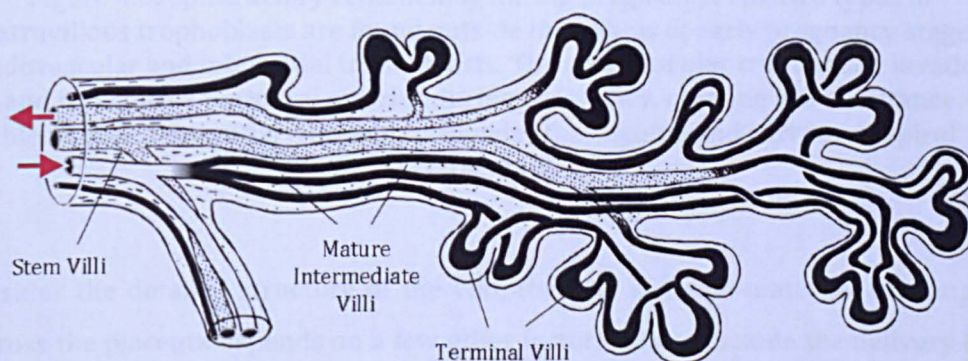


Figure 4.2: Arrangement of foetal capillaries in a group of terminal villi branching from a central mature intermediate villous [12].

While the placenta remains essential in foetal development, the most important element in placental blood flow is the villi in the intervillous space. These villi are indirectly in contact with spiral arteries that change their compliance and undergo remodelling (figure 4.3), so that there is a low resistance maternal blood flow in the uteroplacental unit [13]. This villous area is often in the range of 4 m^2 to 14 m^2 [3]. Furthermore, scientists have identified a few villous parts through histology studies: stem villi, immature and mature intermediate villi and terminal villi. Although all these villi contribute to maternal-foetal exchange (with exception to stem villi), the key villi in intrauterine circulation are the terminal villi that form the final branches of the villous tree since it is in the predominant site for maternal-foetal exchange. It comprises 50% of the villous' surface area [2]. In addition, the intervillous lakes of the fully-grown placenta can hold up to

150 ml of maternal blood. This maternal blood will be renewed every three to four times per minute to facilitate the foetal-maternal exchange [3].

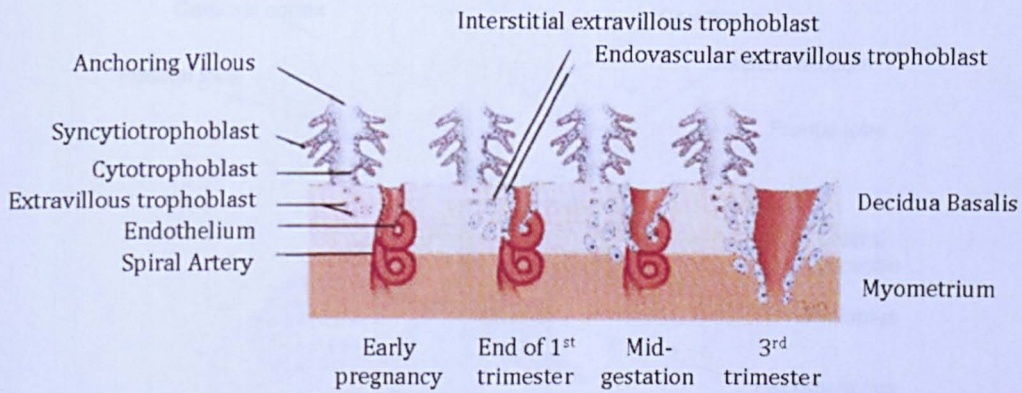


Figure 4.3: Spiral artery remodelling during pregnancy. The two types of extravillous trophoblasts are found outside the villous at early pregnancy stage: endovascular and interstitial trophoblasts. The endovascular trophoblast invades and transforms the spiral arteries during pregnancy, creating low resistance blood flow. Interstitial trophoblast invades the decidua and surrounds spiral arteries [14].

Besides the detailed structure of the villi, the rate of foetal-maternal exchange across the placenta depends on a few other factors. These include the delivery of maternal blood to the placenta, foetal blood flow and foetal blood volume. These factors are in turn dependent on the pattern of maternal blood movement within the intervillous space, the resistance of spiral arteries, the resistance of venous drainage system and the resistance of the placental vascular bed. A malfunction in the development of the uteroplacental unit can lead to complications in pregnancy. Some of the most common placental disorders include placenta accreta, placenta praevia, placental abruption, pre-eclampsia and intrauterine growth restriction (IUGR) [13; 15; 16].

In conclusion, the placenta is essential in nourishing the growing foetus and maintaining an excellent foetal-maternal communication throughout pregnancy.

4.2.2 Foetal Brain

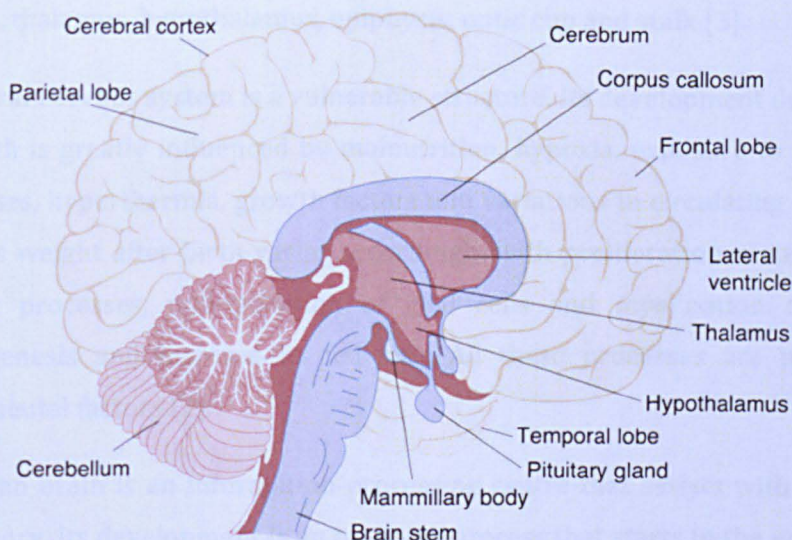


Figure 4.4: A schematic representation of a human brain [17].

Central to the human nervous system is the brain, which lies within the skull. It is a very complex organ that weighs roughly 3 lb or 1.5 kg in an adult, while it is only 25% off its adult weight at birth [2]. The average adult brain volume of a male and female (excluding meninges, cerebral spinal fluid (CSF), and other non-brain tissue) is approximately 1260 cm^3 and 1130 cm^3 , respectively [18]. The brain is attached to the spinal cord that makes up the central nervous system (CNS). The CNS starts developing in the middle of the third week of pregnancy with the appearance of neural plate, originating from ectoderm. Then, edges of the neural plate fold, leading to appearance of neural folds, one on each side of the midline. These fuse into the neural tube that spreads both cranially and caudally [3; 19].

When the cranial and caudal ends close, the caudal portion forms the spinal cord and the cephalic portion forms the brain. The brain consists of three vesicles: the rhombencephalon (hindbrain), mesencephalon (midbrain) and prosencephalon (forebrain). The rhombencephalon is responsible for the formation of medulla oblongata, involved in autonomic functions (respiration rate, cardiac rate, perspiration, digestion); cerebellum, that acts as a coordination centre for posture and movement; and pons, that provides a pathway for nerve fibres between the spinal cord and cerebellar cortices and the cerebrum. The

mesencephalon acts as a communication centre for visual and auditory reflex actions. As for prosencephalon, it is liable for formation of cerebral hemispheres, pituitary, thalamus, hypothalamus, epiphysis, optic cup and stalk [3].

The central nervous system is a vulnerable structure. Its development during and after birth is greatly influenced by malnutrition, hypoxia, exposure to radiation and viruses, hyperthermia, growth factors and variations in circulating hormone levels. Its weight after birth varies accordingly with proliferation of axonal and dendritic processes, multiplication of glial cells and myelination of axons, synaptogenesis and increase in cell size. All these processes are pliable to environmental factors [2].

The human brain is an information-processing centre that assists with learning and memory. Its development is an on-going process that starts in the womb and progresses throughout one's life. It is important in exerting control of all other organs in the body, such as breathing, sleeping, circulation, cardiac cycle, swallowing and sucking. It also plays an important role in sustaining vital bodily functions. These processes begin during foetal development and will continue to take place when the baby emerges from the protective intrauterine environment. It is also responsible as an information processing centre that assists with learning and memory.

4.2.3 Foetal Respiratory System

The survival of the foetus at birth is dependent on the sufficient development of the respiratory system in utero [20]. The human respiratory system consisting of two lungs of a light, porous and spongy texture, located near the backbone on either side of the heart is developed in the late embryo stage; fourth week of pregnancy. The weight of adult lungs differs between genders with the right lung slightly larger than the left lung. The lungs are usually heavier in male compared to female, with a weight proportion of 1 to 37 and 1 to 43 respectively to the size of the body [21]. Adult lungs weigh a total of 2.3 kg and have a total surface area of 70 m². It contains approximately 2400 km of airways, comprising 300 to 500 million alveoli [22]. At birth, the lungs appear pinkish white. However, this colour gradually becomes dark slate gray, mottled in patches and this mottling becomes black with advancement in age and carbon deposition [21].

This respiratory system begins at the nasal cavity and branches out into two parts: conducting portion (nasal cavity, pharynx, larynx, trachea, bronchi and bronchioles) and respiratory portion (respiratory bronchioles, alveolar ducts, alveolar sacs and alveoli). Although the respiratory system is reasonably developed by the second trimester [19], it lies dormant throughout foetal life. However, once the umbilical cord is cut at birth, the respiratory system should be prepared to acclimatise and become fully functional to accommodate the infant's gas exchange needs.

The lung development occurs in five stages: embryonic stage (4th – 7th weeks), pseudoglandular stage (8th – 16th weeks), canalicular stage (17th – 26th weeks), terminal sac stage (26th week – 36th week) and alveolar stage (late foetal to childhood). Its development results from the outgrowth of the ventral wall of the foregut: endoderm and mesoderm [3]. The embryonic stage marks the initial formation of the respiratory diverticulum and the major bronchopulmonary segments within the bilateral pleural cavities. By the end of fourth week, the end of the laryngotracheal tube bifurcates into two bronchial buds. These bronchial buds develop into primordial right and left primary bronchi that then undergo branching morphogenesis to form three secondary bronchi and lobes in the right side and two secondary bronchi and two lobes in the left side. This branching process progresses throughout the seventh week into the pseudoglandular stage to form a bronchopulmonary segments [19; 23].

By the end of pseudoglandular stage, the major structures of the lungs are formed and lined with the columnar epithelial cells. At this stage, the pulmonary arterial system will also be present but not ready for gas exchanges. Hence, a foetus delivered at this stage will not be able to live. During the canalicular stage, the mesoderm undergoes transformation to develop the pulmonary capillaries and connective tissue components of the respiratory system. In addition to this, the respiratory bronchioles will be developed through progressive differentiation and subdividing of bronchi, while the epithelial cells undergo thinning. These respiratory bronchioles gradually divide to form alveolar ducts. By this point, the blood vessels grow intensively into the developing lungs and are in contact with the walls of the respiratory bronchioles. Although the lungs are almost functional by the end of canalicular stage, the immaturity of the foetal respiratory system may risk the survival of the foetus delivered at 24 weeks [19; 23].

The terminal sac stage is associated with differentiation of the epithelium lining of the alveoli into two types of cells: type I alveolar pneumocytes (squamous epithelium) cells that are responsible for gas exchange after birth and type II alveolar (secretory epithelial) cells that produce pulmonary surfactant, the material spread over the surface of alveoli. The pulmonary surfactant reduces the surface tension of the alveoli and assists with breathing; preventing the collapse of alveoli during expiration by reducing the inspiratory force required to inflate the alveoli. The greatest production of pulmonary surfactant in one's life takes place in the last few weeks before birth. At this stage of pregnancy, the foetus' respiratory passageways are usually filled with 90% to 95% amniotic fluid [19]. In addition, the formation of alveoli increases greatly in the last four weeks of pregnancy, resulting in an exponential increase in the respiratory surface area of the lung. All these developments are important in the preparation and adaptation of the newborn's first breath [19; 23].

Lung development is an ongoing process that progresses after birth. This period is called alveolar stage. It is dominated by an increase in the number of respiratory bronchioles and alveoli, rather than expansion in the size of each alveolus. The main mechanism for increasing alveolar numbers during this period is the formation of secondary connective tissue septae that are responsible for the division of the existing alveolar sacs. Initially, the secondary septa are quite thick but they then transform into thin mature septa that are able to participate in full respiratory exchange. They are also responsible for the development of approximately 90% or 300 million alveoli found in matured human lung. It is estimated that only one-sixth of alveoli present in adults are developed before birth, the remaining alveoli are formed during the first 10 years of postnatal life [3; 19].

4.2.4 Foetal Liver

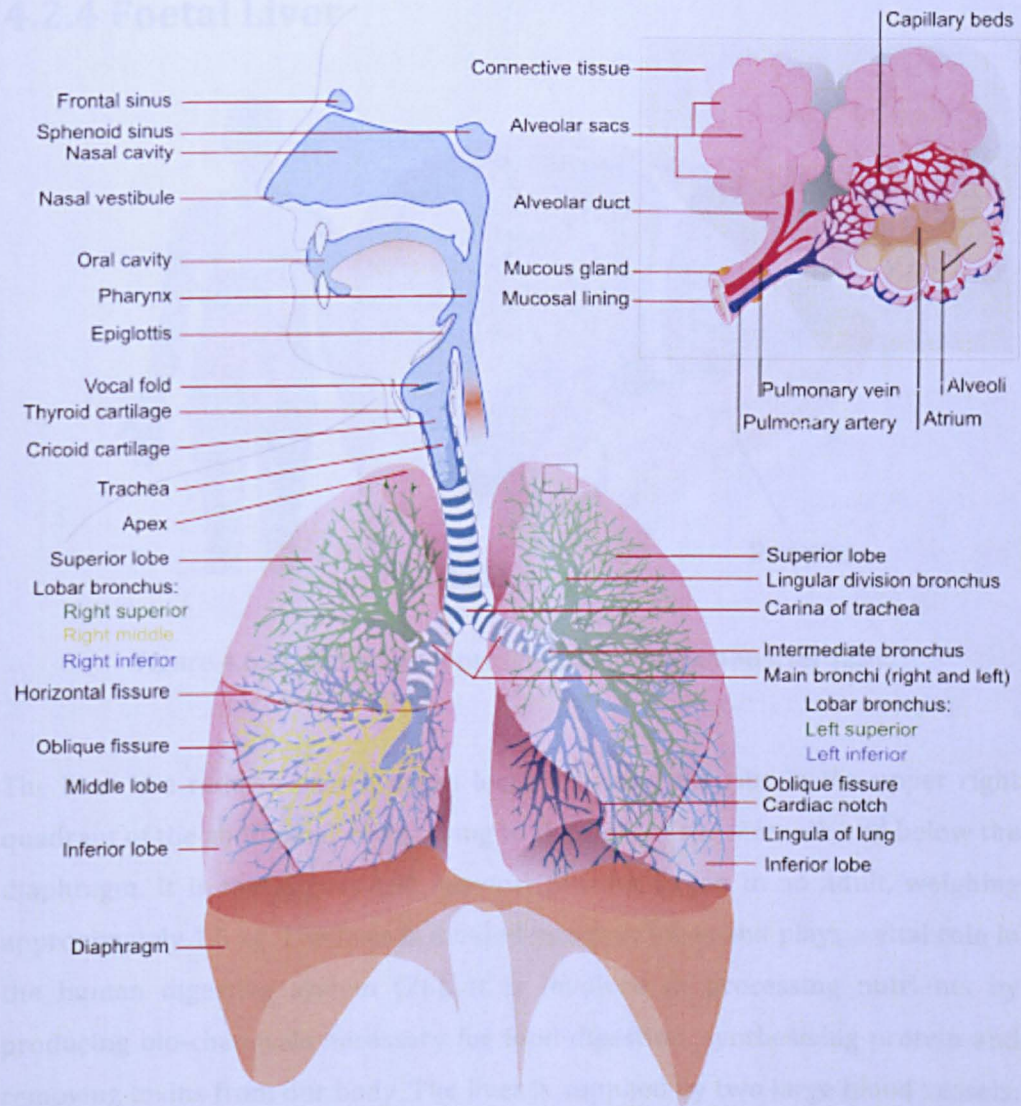


Figure 4.5: A schematic representation of a human respiratory system [24].

4.2.4 Foetal Liver

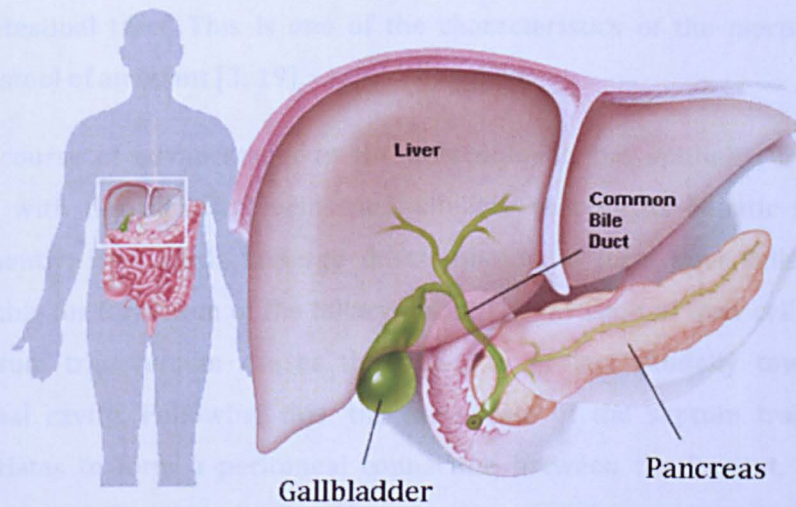


Figure 4.6: A schematic representation of a human liver [25].

The liver is a reddish brown organ located behind the ribs in the upper right quadrant of the abdominal cavity, lying to the right of the stomach and below the diaphragm. It is the largest and heaviest internal organ in an adult, weighing approximately 1.5 kg. The liver is divided into four lobes and plays a vital role in the human digestive system [26]. It is involved in processing nutrients by producing bio-chemicals necessary for food digestion, synthesising protein and removing toxins from our body. The liver is supplied by two large blood vessels: the hepatic artery that carries blood from aorta to the liver and the portal vein that transports blood containing digested nutrients from the gastrointestinal tract, spleen and pancreas to the liver.

Liver development starts early in the third week of pregnancy. It results from the sudden outgrowth of the endodermal epithelium, also known as hepatic diverticulum or liver bud that originates at the distal end of the foregut. This hepatic diverticulum consists of rapidly proliferating cells that pierce through the mesodermal plate connecting the pericardial cavity and the stalk of the yolk sac called the septum transverse. While this process continues, the connection between the foregut and hepatic diverticulum is constricted, resulting in the formation of the bile duct that is responsible for development of a small ventral outgrowth. This outgrowth gives rise to the development of cystic duct and gallbladder. At approximately the 12th week of gestation, the hepatic cells starts

producing bile largely through the breakdown of haemoglobin. The dark green bile stored within the gallbladder is now ready to be released to the gastrointestinal tract. This is one of the characteristics of the meconium, the earliest stool of an infant [3; 19].

In this course of advancement in the development, the epithelial liver cords interact with the umbilical veins and vitelline that forms hepatic sinusoids. Subsequently, liver cords undergo differentiation to form liver cells that are responsible for formation of the biliary ducts. The invasion of liver cells through the septum transversum causes the organ to project caudally towards the abdominal cavity. Following this, the mesoderm of the septum transversum differentiates to form a peritoneal connection between the foregut, liver and abdominal wall. Together they are known as the ventral mesentery. At the end of this differentiation, the liver will still be in contact with the septum transversum. The area of septum with densely packed mesoderm will form the central tendon of the diaphragm. The liver's surface area in contact with the future diaphragm is known as the bare area of the liver. Unlike the majority of liver's surface area, the bare area is never covered by peritoneum [3].

During the tenth week of development, the foetal liver weighs approximately 10% of the total foetal body weight. Although this may be due to the presence of large number of sinusoids, there is also a large composition of proliferating cells that lie between the hepatic cells and walls of the vessels within the liver. They play an important role in hematopoietic function, which involves production of red and white blood cells, but this activity gradually subsides while approaching the last two-months of pregnancy [3; 19].

The liver plays an important role in the human digestive system. Although it is only 5% of the total body weight at birth, it is an essential organ for survival, supporting every other organ in the body.

4.2.5 Foetal Urinary System

Homeostasis is an equilibrium property that needs to be achieved to ensure that the internal organs in living organisms function properly. Like other creatures, humans are required to take in nutrients and water for survival. However, this

intake should be regulated through homeostatic functions that include regulating temperature, blood acidity and other variables. This homeostatic function is assisted by the urinary system that plays an important role in excreting fluids and chemicals, maintaining the acid-base homeostasis and regulating the electrolytes in the body. The human's urinary system consists of two kidneys, two ureters, bladder and urethra. The kidneys lie below the ribcage and close to the lumbar spine. They are reddish brown bean shaped organs that are about the size of a human fist [27]. They are surrounded by the peri-nephric fat and receive blood from the renal arteries that are supplied by the abdominal aorta. The weight of an adult kidney differs between genders with the left kidney being slightly larger than the right kidney [28]. The weight of a female kidney is between 115 g and 155 g, while the male kidney weighs between 125 g and 170 g [29]. The weight of the two adult kidneys in proportion to the body is approximately 1 to 240 [21].

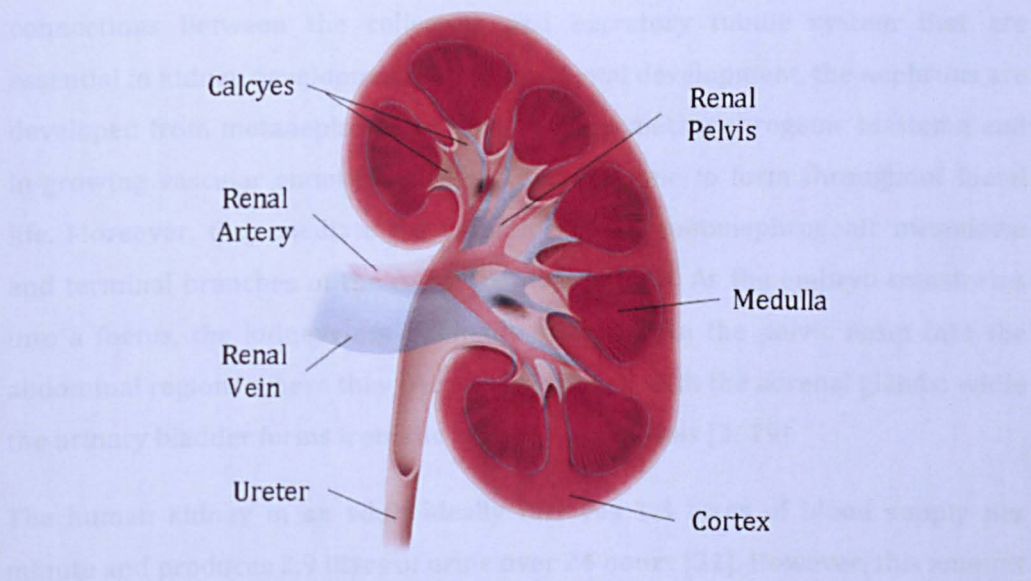


Figure 4.7: A schematic representation of a human kidney [30].

The urinary system is developed from mesodermal tissue of the early embryo in the pelvic basin. During foetal life, its development takes place in three overlapping stages from the cranial to caudal segments: pronephros, mesonephros and metanephros (the definite kidney). The development of pronephros begins on the 23rd to 24th day of gestation. At this stage, seven to ten solid cell groups are present in the cervical region. They form vestigial excretory units, nephrotomes that are non-functional. In the fourth week of gestation, when

the pronephric system gradually disappears, the first excretory tubules of the mesonephros and mesonephric ducts are derived from the intermediate mesoderm in the thoracic and lumbar regions. The tubules lengthen rapidly and attain a cluster of capillaries that will form a glomerulus that will later be placed in Bowman capsule. This structure establishes the renal corpuscle with a large excretory unit (nephron) with its own collecting duct, mesonephric duct. These tubules and ducts function briefly in the human urinary system. However, they transform to operate as tubes for sperm transportation from the testes to the urethra in a male. Conversely, these ducts regress and gradually disappear in the female body [2; 3; 19].

The metanephros begins developing in the fifth week of gestation. It starts when the ureteric bud (metanephric diverticulum) grows as a result of metanephric outgrowth. This bud is responsible for the formation of the entire collecting system (ureter, renal pelvis, calyces and collecting tubules). It establishes good connections between the collecting and excretory tubule system that are essential in kidney development. In normal foetal development, the nephrons are developed from metanephrogenic diverticulum, metanephrogenic blastema and in-growing vascular endothelial cells. They continue to form throughout foetal life. Moreover, they mediate the induction of the metanephrogenic mesoderm and terminal branches of the collecting duct system. As the embryo transforms into a foetus, the kidneys are gradually shifted from the pelvic basin into the abdominal regions where they become associated with the adrenal glands; while the urinary bladder forms from the base of the allantois [3; 19].

The human kidney in an adult ideally receives 1.3 litres of blood supply per minute and produces 2.9 litres of urine over 24 hours [31]. However, this amount can vary accordingly under different circumstances that disrupt the water loss mechanism, such as sweating or kidney abnormalities. This includes congenital anomalies of the urinary system that occurs in 3% to 4% of all human birth. One of the most severe renal abnormalities is renal agenesis where the kidneys are not present in the body due to faulty production in the embryo. Other kidney malformations include multicystic dysplastic kidney and hypoplastic kidney. In cases where the kidneys have migrated abnormally, patients can have pelvic kidneys, horseshoe kidney and other ectopic kidneys. It is important to note that renal tract malformation can occur in all stages of life (foetal, neonatal, childhood and adulthood) [19; 32].

The kidneys play a dominant role in maintaining body's fluid balance by regulating the composition and volume of the extracellular fluid by separating mineral, toxins, urea, salt and waste products from the blood system. It is undoubtedly one of the most important organs in human body.

4.3 Conclusion

With numerous studies suggesting foetal development in the intrauterine environment plays an important role in determining one's health later in life, embryology studies are becoming more important. Here, the effect of maternal smoking and maternal diabetes will be discussed by studying the foetal growth and development of placenta, foetal brain, liver, lungs, and kidneys.

4.4 References

- [1] J.E. Jirásek, and G. Clerici. (2001), *An Atlas of the Human Embryo and Fetus*, Parthenon Publishing Group Limited, New York, USA.
- [2] R. Harding, and A.D. Bocking. (2001), *Fetal growth and development*, Cambridge University Press, Cambridge, United Kingdom.
- [3] T.W. Sadler. (2006), *Langman's Medical Embryology*, Lippincott Williams & Wilkins, Pennsylvania, USA.
- [4] M.C. Allen, P.K. Donohue, and A.E. Dusman. (1993), The Limit of Viability -- Neonatal Outcome of Infants Born at 22 to 25 Weeks' Gestation. *New England Journal of Medicine* **329** 1597-1601.
- [5] D. El-Metwally, B. Vohr, and R. Tucker. (2000), Survival and neonatal morbidity at the limits of viability in the mid 1990s: 22 to 25 weeks. *The Journal of Pediatrics* **137** 616-622.
- [6] EPICure. (2008), Survival after birth before 27 weeks of gestation.
- [7] A.D. Garnica, and W.Y. Chan. (1996), The role of the placenta in fetal nutrition and growth. *Journal of the American College of Nutrition* **15** 206-22.
- [8] T. Burkhardt, L. Schaffer, C. Schneider, R. Zimmermann, and J. Kurmanavicius. (2006), Reference values for the weight of freshly delivered term placentas and for placental weight-birth weight ratios. *European Journal of Obstetrics & Gynecology and Reproductive Biology* **128** 248-252.
- [9] C.G. Kaplan. (2008), Gross pathology of the placenta: weight, shape, size, colour. *Journal of Clinical Pathology* **61** 1285-1295.
- [10] K. Benirschke, and P. Kaufmann. (2000), *Pathology of the Human Placenta*, Springer, New York.
- [11] A.J.G. Potgens, U. Schmitz, P. Bose, A. Versmold, P. Kaufmann, and H.G. Frank. (2002), Mechanisms of Syncytial Fusion: A Review. *Placenta* **23** S107-S113.
- [12] P. Kaufmann, T.M. Mayhew, and D.S. Charnock-Jones. (2004), Aspects of Human Fetoplacental Vasculogenesis and Angiogenesis. II. Changes During Normal Pregnancy. *Placenta* **25** 114-126.
- [13] P. Gowland. (2005), Placental MRI. *Seminars in Fetal and Neonatal Medicine* **10** 485-490.
- [14] Y. Wang, and S. Zhao. (2010), *Placental Blood Circulation*, San Rafael (CA): Morgan & Claypool Life Sciences.

- [15] R.J. Moore, B.K. Strachan, D.J. Tyler, K.R. Duncan, P.N. Baker, B.S. Worthington, I.R. Johnson, and P.A. Gowland. (2000), In utero Perfusing Fraction Maps in Normal and Growth Restricted Pregnancy Measured Using IVIM Echo-Planar MRI. *Placenta* **21** 726-732.
- [16] G. Keith M. (2002), The Role of the Placenta in Fetal Programming - A Review. *Placenta* **23** S20-S27.
- [17] M. Oscar-Berman, B. Shagrin, D.L. Evert, and C. Epstein. (1997), Impairments of brain and behavior: the neurological effects of alcohol. *Alcohol health and research world* **21** 65-75.
- [18] K.P. Cosgrove, C.M. Mazure, and J.K. Staley. (2007), Evolving Knowledge of Sex Differences in Brain Structure, Function, and Chemistry. *Biological Psychiatry* **62** 847-855.
- [19] B.M. Carlson. (1999), *Human embryology & developmental biology*, Mosby, St. Louis.
- [20] M. Post, and I. Copland. (2002), Overview of lung development. *Acta Pharmacologica Sinica* **23**.
- [21] H. Gray. (1918), *Anatomy of the Human Body* (W.H. Lewis, Ed., Bartleby.com, New York.
- [22] R.H. Notter. (2000), *Lung surfactants: basic science and clinical applications*, N.Y: Marcel Dekker, New York.
- [23] J.P.T. Ward, J. Ward, and R.M. Leach. (2010), *The Respiratory System at a Glance*, Wiley-Blackwell.
- [24] M.R. Villarreal. (2008), Respiratory System Complete. in "http://en.wikipedia.org/wiki/File:Respiratory_system_complete_en.svg" , Hamburg, Germany.
- [25] L. WebMD. (2009), Picture of the Gallbladder. in "<http://www.webmd.com/digestive-disorders/picture-of-the-gallbladder>".
- [26] S. Sherlock, and J. Dooley. (2007), Frontmatter. in "Diseases of the Liver and Biliary System", Blackwell Science Ltd.
- [27] G.A. Tanner. (1975), Kidney Function. in "Basic Physiology for the health sciences (E. E. Selkurt)" (B.a.C. Little, Ed., Boston.
- [28] B. Glodny, V. Unterholzner, B. Taferner, K. Hofmann, P. Rehder, A. Strasak, and J. Petersen. (2009), Normal kidney size and its influencing factors - a 64-slice MDCT study of 1.040 asymptomatic patients. *BMC Urology* **9** 19.

-
- [29] W.F. Boron, and E.L. Boulpaep. (2009), Medical physiology : a cellular and molecular approach.
- [30] Anatomy of the Kidney. in ["http://childrenshospital.org/az/Site1207/mainpageS1207P0.html"](http://childrenshospital.org/az/Site1207/mainpageS1207P0.html).
- [31] H.W. Smith, W. Goldring, and H. Chasis. (1938), The Measurement of the Tubular Excretory Mass, Effective Blood Flow and Filtration Rate in the Normal Human Kidney. The Journal of clinical investigation **17** 263-78.
- [32] L. Kerecuk, M.F. Schreuder, and A.S. Woolf. (2008), Renal tract malformations: perspectives for nephrologists. Nature Clinical Practice Nephrology **4** 312-325.

Chapter 5

The Effect of Maternal Diabetes on Placental Blood Flow

5.1 Overview

This chapter will discuss the methods used to explore placental blood flow by measuring blood perfusion in the entire placenta, basal plate and chorionic plate. The chapter starts with a short literature review of placental MRI and its application to study uteroplacental disturbances in compromised pregnancies. Previous methods used for quantifying blood flow will also be covered: Doppler Ultrasound and Spin Labelling. Following these discussions, this chapter will progress to the introduction of Intra Voxel Incoherent Motion (IVIM), the placental assessment technique that was applied in this study.

This chapter is divided into two sections. The first part aims to investigate the reliability and reproducibility of the measurements of placental perfusion acquired using the IVIM program. The motivation to perform the reliability tests originated from a lack of published studies investigating such reliability. The author, with the help of two other observers, Dr Nia Wyn Jones and Dr Ruta Deshpande, conducted the data analysis for the reliability tests. The second part demonstrates the application of the IVIM technique to study the effect of maternal diabetes on placental blood flow. The author will address the methods used to acquire, process and statistically analyse placental perfusion. In addition, the author also measured the placental volume to demonstrate the effect of maternal diabetes on placental growth. Finally, the chapter is concluded by

demonstration and discussion of the results obtained from analysing the data of both the non-diabetic controls and diabetic patients involved in this study.

The MATLAB code for the IVIM program was originally written by Professor Penny Gowland but has since undergone various modifications. The author has modified the program to increase the accuracy of data analysis by automatically removing data points corrupted due to noise or movement, as well as to optimise the processing time for data collection and data storage. These modifications will be discussed in detail in section 5.3.3.

5.2 Introduction

Uteroplacental and fetoplacental blood flows are essential requisites for successful foetal growth and development. This complex system has been extensively studied using invasive methods such as the distribution of radioactive microspheres, angiography [1], monitoring disappearance of diffusible indicators such as Xenon-133 injected locally into intervillous space [2; 3; 4], measurement of variations in heat conductance with electromagnetic transducers [5] or thermistors [6; 7] and time activity analysis of short-lived radiotracers such as indium-133m injected intravenously [7; 8]. However, with development in technology, non-invasive ultrasound and MRI have been employed as diagnostic tools to understand the pathophysiological mechanisms that affect foetal growth. Recent advances in research have focussed on identifying the symptoms and aetiologies of pre-eclampsia along with abnormal placental perfusion in intrauterine growth restriction (IUGR) [9; 10; 11; 12; 13; 14; 15] and maternal diabetes [16; 17]. These studies are conducted throughout gestation [12; 15; 18; 19] and after delivery [15; 20] to monitor the effect of transformations of the placental system during gestation on health and disease.

In diabetic pregnancy, foetal growth throughout gestation seems to be abnormal due to hyperglycemia and hyperinsulinemia effects [21]. Hence, placental structure and function undergo various transformations depending on a number of factors in the intrauterine environment: the quality of glycemic control achieved across the critical periods of placental development, the method of treatment for diabetes and the degree of diabetic management [16]. Normally,

the placenta is embedded into the uterine wall and placental development starts with the formation of villous and extravillous structures that originate from proliferation and differentiation of trophoblast. Following this, the spiral arteries in the uterus are remodelled to be low resistance vessels [22]. Then, in the second half of the gestation, the villi undergo various steps of maturation and result in placental mass expansion [23; 24]. These steps of maturation are described in detail in section 4.2.1.

The placenta is the only organ that can store excess foetal glucose in the fetoplacental system. It converts the glucose to glycogen and stores it around the villous vessels and capillaries. However, excessive foetal growth may occur if hyperglycemia, hyperinsulinemia or dyslipidaemia exceeds the capacity of placenta to protect the foetus [16]. Understanding the importance of the placenta in foetal development, many obstetricians and clinicians have devoted their time to examine the placental system in various pregnancy conditions, in order to identify foetuses at risk of complicated pregnancy.

In recent years, three-dimensional (3D) Power Doppler sonography has been used as a research tool to investigate in vivo placental perfusion. It is also known as amplitude based colour Doppler, angio-mode, colour Doppler energy and colour power imaging [25]. The received signal in Power Doppler depends on the amplitude component that represents the number of moving scatterers in the blood volume [26]. The theory behind the computation of the number of moving blood cells representation is based on power integration that originates from intensity, strength, energy and amplitude of Doppler shifted ultrasound signals [27]. These signals correspond to the zero lag of autocorrelation instead of the mean Doppler frequency shift, and eliminates the information regarding velocity and flow direction [27; 28].

Power Doppler sonography is very sensitive to blood flow. Its ability to detect small blood movements with low blood flow is one of the many reasons for its success as a non-invasive placental imaging technique [15; 29]. Power Doppler is also angle independent [30; 31], enabling better detection and visualisation of indirect branching of the vessels in placenta. This is because Power Doppler is based on amplitude of the scatterers, which is velocity independent. Hence, the number of scatterers in the volume remains the same when the Power Doppler angle is changed, causing the power to be consistent. [32]. Power Doppler is very

dependent on the pulse repetition frequency setting. It is not affected by aliasing because it has no information on velocity [25; 30; 31; 32].

Nonetheless, motion artefacts are a major limitation in the Power Doppler imaging technique. This may result from unavoidable foetal movement, maternal breathing movements, bowel peristalsis or transducer motion [29; 33]. Furthermore, obstetric scans can become increasingly challenging to perform across gestation since there is a demand for a bigger field of view for the growing foetus or placenta [12]. Moreover, issues relating to increased foetal depth and variation in tissues intervening between the transducer and region of interest are often common in late gestation. This is because ultrasound relies on absorption and scattering characteristics of specific tissues to determine the penetration depth of the ultrasound beam [34]. Nevertheless, all these concerns with ultrasound can be overcome using MRI.

While ultrasound remains the primary diagnostic tool for placental development and function, MRI has been suggested as an alternative to ultrasound [35]. Being an imaging procedure using non-ionising radiation, it is apparently safe for pregnancy studies [7]. Postnatal follow up studies after MRI scans have established that there is no evidence of increased occurrence of disease or disability (including hearing deficiency) to the children [36; 37; 38; 39; 40; 41]. Moreover, as a fast imaging modality, unavoidable foetal motion and maternal movements do not significantly degrade the image quality [42; 43; 44; 45; 46]. MRI is also capable of acquiring images with greater tissue contrast in larger field of view than ultrasound [44; 47]. This is advantageous in measurements of placental perfusion.

Initially, MRI was employed in assessment in placenta praevia. This work was published in 1986 [48]. Following this, in 1995, Baker et al. [49] reported the use of MRI in quantifying in-utero foetal liver, brain and placental volumes. Since then, its role in clinical research into placental function has expanded to placental spectroscopy and perfusion in an effort to understand placental function and pathophysiological mechanisms that cause delay in foetal development. Until 1998, the only possible way to monitor placental blood flow was by using a radioisotope technique [48; 50; 51]. This was potentially dangerous for the foetus. However, later that year, the foetal MRI research group at the University of Nottingham applied a high speed imaging technique, Echo Planar Imaging

(EPI) to image fetuses using short imaging times. This technique was advantageous in many ways. The foetal scans were achievable in a reasonable imaging time, less than 15 minutes. It was also capable of freezing physiological motion and producing images with limited movement artefacts since the susceptibility of the uterine environment is almost similar to that of the foetus [51]. A detailed theory and application of EPI is described in section 2.3.3.4.

Besides EPI, placental perfusion has also been measured using an arterial spin labelling technique. This technique is based on application of flow sensitive alternating inversion recovery (FAIR), which compares the rate of magnetisation recovery following selective and non-selective inversion pulses. It is particularly useful in measuring perfusion in one directional blood flow. However, in the placenta, perfusion can be overestimated since blood flows in a variety of directions. Nevertheless, this technique can be advantageous in measuring blood movement within the placenta, since it is this movement that ensures the maternal blood circulates effectively around the foetal villi [35].

In this study, we applied EPI to investigate the effect of maternal diabetes on placental blood flow. The acquired EPI images were analysed using Intra Voxel Incoherent Motion (IVIM), a method developed by learning spin echo signals are sensitive to motion [52]. The reliability and reproducibility of this method was tested with the aim of establishing if the measurement errors from the test were small enough for the protocol to be used in a clinical environment. Section 5.2.2 of Chapter 5 details the concept of reliability testing. Following the reliability tests, the IVIM method was applied to study the effect of maternal diabetes on placental blood flow.

5.2.1 Intra Voxel Incoherent Motion (IVIM)

The IVIM method was adapted from the sequence developed by Stejskal and Tanner; a spin echo pulse sequence in which pulsed magnetic gradients are employed to make the spin echo amplitude dependent on the spins' random Brownian motion [53]. Spin echo amplitude depends on gradient pulse strength and duration. It can be used to measure molecular diffusion coefficient, with unit $\text{mm}^2 \text{s}^{-1}$. The IVIM method applies a principle that monitors the movement (diffusion) of blood within tissues and models them as random motion. In

practice, IVIM will be sensitive to any motion leading to net dephasing of spins (non zero curl of the velocity field) [54].

The quasi-random movement of blood detected using the IVIM method should result in a bi-exponential spin echo signal attenuation curve [37; 55; 56; 57], which arises from the two (water) compartments within the region of interest: fast and slow decaying components. The fast decaying component arises from the effect of spins from blood, which is characterised as pseudo-diffusion coefficient or decay rate constant (D^*), while the slow decaying component arises from non-blood spins moving between and within cells, which is characterised as the apparent diffusion coefficient or self-diffusion characteristic (D). The signal attenuation due to the pulse gradient is also linked to the perfusion factor (f). It represents the fraction of voxels associated to fast decaying components, given in terms of fraction of spins within the volume of interest, which are in the blood compartment [54]. In other words, it is the percentage volume of flowing blood in each voxel compared to the total voxel volume of water.

The perfusion factor (f) is dependent on the range of displacements of the molecules in the vascular geometry, direction to which the sequence is sensitised, time intervals between the diffusion gradient application and the velocity of the blood water molecules [54]. The pseudo-diffusion coefficient (D^*) related to the signal attenuation at the lower pulse gradient amplitude is associated with the macroscopic circulation of blood in capillaries. This is a measurement of the blood flowing inside a single voxel linked with randomly oriented vessels with a variety of velocities and diffusion mimicked on a relatively large scale. In cases where the voxels are associated with vessels with higher velocity blood and wide distribution of velocities, the pulse gradient amplitude will quickly dephase, resulting in zero affect to the IVIM analysis. On the other hand, the apparent diffusion coefficient (D) relates to the signal attenuation at higher values of pulse gradient [37; 58]. Mathematically, the signal attenuation resulting from circulating blood and water diffusion in a particular sample can be expressed as below:

$$S(b) = S(0) \left[(1-f)e^{-bD} + f e^{-bD^*} \right] \quad (\text{Eq 5.1})$$

where $S(b)$ represents the signal intensity for different diffusion weighting factor, b and $S(0)$ is the signal intensity when $b = 0$. For a more detailed description and application of IVIM, readers are advised to refer to section 2.3.3.5 of Chapter 2.

The focus of this study was to measure the perfusion, f and self-diffusion, D factors for each pixel within the placenta, basal plate and chorionic plate since the blood movement through the placenta is incoherent resulting in similar signal attenuation to diffusion [37]. The self-diffusion characteristic was investigated having seen data from Dr Caroline Wright of University of Manchester (personal communication), highlighting an interesting pattern of the D parameter in pregnant patients suffering from pre-eclampsia. Although measurement of D^* is saved from the computational analysis, it was not used in this study since previous work has demonstrated an unacceptably high, error in fitting for D^* due to noise in the fit, reducing the significance of D^* measurements [37; 59]. For this reason, only results from f and D are presented here.

All these measurements were conducted on different pulse gradient amplitudes, with the objective of producing and studying placental blood flow maps in normal and diabetic pregnancy. Our hypothesis was that the placental blood flow would be greater in diabetic pregnancy.

5.2.2 Reliability and Reproducibility

The term reliability refers to the study of the consistency of repeated measures with respect to the mean value of all the measurements [60]. A reliable measuring method would signify that measurements are reproducible at different time intervals (test-retest reliability) and the observers conducting the measurements produce repeated results: reliability of the measurements for the same observer over a period of time (intra-observer reliability) and reliability of measurement between different observers on the same subject (inter-observer reliability) were assessed [61].

Reproducibility is a type of reliability that describes the repeatability of the measurements made on a subject under different conditions: measurement made by different observers, measurement conducted using different measuring methods or measurement made over a period of time that can be indirectly

influenced [60]. Reliability and reproducibility can be studied using several indicators. This includes intra-class correlation coefficient (ICC), limit of agreement (LOA) and the Bland Altman plot [60; 62; 63].

Intra-class correlation is a correlation statistic that gives the ratio of between-group variance to the total variance (eg: intra or inter-observer variance of the total variance in mean f measurement). The ICC results can vary in the range of 0 (no agreement) to +1 (perfect agreement). The measurement of these variables are interchangeable [61; 64]. ICC can be classified as follows; values less than 0.20 represent poor correlation, 0.21-0.40 fair, 0.41-0.60 moderate, 0.61-0.80 good and 0.81-1.00 very good correlation [64]. The ICC assessment is conducted to test the agreement between more than one variable or target with no intrinsic connection (the measurements are interchangeable such that the test-retest reliability can be conducted) [61; 65]. The ICC measurements can be expressed as below:

$$ICC = \frac{BMS - EMS}{BMS + [1 - k]EMS} \quad (\text{Eq 5.2})$$

or

$$ICC = \frac{\text{subject variability}}{\text{subject variability} + \text{random error}}$$

where BMS represents between target mean square, EMS is the error mean square that gives the error between targets and k is the number of observers [63]. Although the ICC is a clear method of assessing agreement between measurements of two or more observers or methods, it suffers from a high dependence on the inconsistency between targets of the results. Hence, the ICC value will be greater if the variability between the targets (BMS) is greater whilst the error variance (EMS) remains unchanged. Moreover, it does not provide an indication of the magnitude of agreement between observers or measurements [61; 63].

Limits of agreement (LOA) and Bland Altman plots are techniques employed to study the randomness of the measurement obtained. The LOA gives the range in which 95% of values lie, computed from differences between measurements obtained from two different methods [60]. In order to calculate LOA, one needs to calculate the mean and standard deviation of the differences between the

measurements (paired differences). If these paired differences are normally distributed, LOA can be calculated using the equation below:

$$LOA = d \pm \left(1.96 \times SD_{diff} \right)$$

(Eq 5.3)

where d represents mean difference and SD_{diff} is the standard deviation of the differences [66].

The Bland Altman plots allow observers to graphically observe extreme outliers affecting the sampled data, although ICC is better at computing the heterogeneity of the measurements [61]. Once the LOA is calculated, the Bland Altman graph is plotted by drawing the mean of two measurements on x-axis and the differences between the two measurements on the y-axis. Then, solid horizontal lines are drawn to indicate the mean difference and dashed horizontal lines are drawn to represent the upper and lower LOA. This graph will assist as an illustration of bias between the measurements by providing a graphical representation of values for the reliability tests and statistical results generated through LOA test. The plot will also provide information relating the size of the differences between two variables, distribution around the absolute zero and distribution with increasing mean values. If the mean difference is smaller and the range between the upper and lower LOA is narrower, the measurements are of better agreement. However, the decision on whether it is a good agreement is often a matter of clinical judgement [61].

5.3 Method

This section is divided into three parts. The first part details the patient recruitment criteria, scanning protocol and the technique used in image analysis (computational program). The second part details the approach undertaken to test the reliability and reproducibility of the techniques used to study placental blood flow. The final part details the approach taken to measure placental perfusion and diffusion, along with placental volume, in non-diabetic and diabetic pregnancies.

5.3.1 Recruitment Criteria

Following Nottingham Research Ethics Committee approval, Dr Ruta Deshpande conducted the search for participants with pre-gestational diabetes and non-diabetic controls. Diabetic participants were first approached by their usual clinician and requested to participate in the study, while non-diabetic controls were recruited by using posters and leaflets in the Ultrasound Department, Queen's Medical Centre (QMC), Nottingham. Only participants aged 18 years or over, with a viable singleton pregnancy and registered to deliver at QMC were eligible to participate in this study. All the participants were matched for age, parity and maternal Body Mass Index (BMI); these details along with ethnicity were noted at the initial recruitment stage. All participants gave informed written consent to participate in the study. Participant's height, weight and glycated haemoglobin A1c (HbA1c) levels were noted at each scan session. In addition, birth weights and gender of the participants' babies, gestation at delivery and mode of delivery were collected following their delivery. In line with the hospital policy at the time of recruitment, gestational age was calculated from the crown rump length measurement in the first trimester of pregnancy.

5.3.2 Scanning Protocol

All women underwent two scans, at 22 – 26 weeks and 33 – 37 weeks. For simplicity, these gestational time points will henceforth be referred to as 24 weeks and 35 weeks gestational age (GA), respectively. Scans were performed on a 1.5 Tesla Philips Achieva MRI system equipped with a body transmit coil and either a 5-element SENSE cardiac or 4-element SENSE torso receive coil, depending on the woman's size. These coils were usually placed between the mother's umbilicus and pubic symphysis. Women were placed in the scanner feet first and lay on their right side in the decubitus position to avoid vena caval compression. All these scans were conducted with a specific absorption rate of $< 2.0 \text{ W kg}^{-1}$.

Non-breath hold Half Fourier Single Shot Turbo Spin-Echo (HASTE) and Balanced Fast Field Echo (bFFE) were applied to acquire images encompassing the whole foetus in three orthogonal planes. These images were used to assist in

identifying the location of umbilical cord insertion in the placenta. It was also used in measurement of the placental volume.

- The HASTE sequence acquired 123 slices over all three orthogonal directions in 147 seconds (TE = 120 ms, flip angle = 90° , $0.78 \times 0.78 \times 6.00 \text{ mm}^3$ and FOV = $400 \times 300 \times 400 \text{ mm}^3$)
- The bFFE sequence acquired 130 slices in 167 seconds (TR = 5.8 ms, TE = 2.3 ms, flip angle = 70° , $0.78 \times 0.78 \times 6.00 \text{ mm}^3$ and FOV = $400 \times 300 \times 400 \text{ mm}^3$)

The placental perfusion studies were conducted using the EPI technique. Respiratory-gated standard pulsed gradient spin echo sequence (PGSE) was applied.

- The PGSE sequence acquired 5 transverse slices encompassing the placenta in 108 seconds (TR = 3000 ms, TE = 95 ms, slice gap = 18 mm, $1.46 \times 1.46 \times 7 \text{ mm}^3$, FOV = $350 \times 350 \times 107 \text{ mm}^3$ and 12 b values = 0, 1, 3, 15, 47, 80, 115, 206, 246, 346, 468 and 800 s mm^{-2})

This acquisition was repeated five times for each patient to average out the motion artefacts. All patients were requested to remain as still as possible during these acquisitions to avoid motion artefacts.

5.3.3 Data Analysis

The MR images acquired using HASTE and bFFE sequences were used in measuring placental volume. This measurement was conducted by drawing an approximate freehand mask around the placenta using Analyze 9.0 (Mayo Clinic, Rochester, MN, USA). Figure 5.1 shows a HASTE image in the sagittal plane.

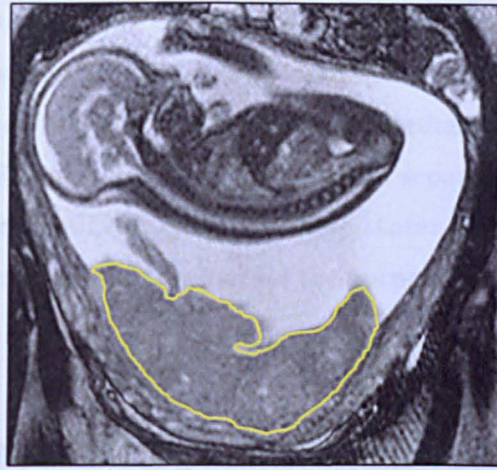


Figure 5.1: The ROI of placenta drawn (yellow line) on the HASTE image.

All the PGSE data acquired for this study were analysed using a computational program developed on MATLAB (R2010a; MathWorks Inc, Natick, MA, USA). This program was developed based on the IVIM principle discussed in the introduction, section 5.2.1 and theory, section 2.3.3.5. Initially, this program was developed with the aim of measuring perfusion in the whole placenta. However, the program has since been modified to restrict the perfusion measurement to either the basal plate or chorionic plate only. Moreover, the program was also modified to simultaneously measure the perfusion in the same slice of all the five acquisitions acquired from a single patient.

Although the PGSE data acquired for this study was respiratory-gated, gross movement occasionally occurred. Since image registration was not possible, other pragmatic solutions were used. This will be discussed in detail in the section 5.5, discussion and conclusion.

5.3.3.1 Motion Correction

Prior to data analysis, each observer inspected all the placental images (all the b -value images) of the selected slice acquired using different diffusion weighting. In most cases, the central slice with the largest placental area was selected for data analysis. This is demonstrated in figure 5.2 and 5.3. The inspection was conducted on all five acquisitions to identify gross movement in the placenta. If there was no obvious movement in the placenta between acquisitions, the

volumes of all the acquisitions of one slice were concatenated together for the data analysis. However, if there was noticeable movement between the acquisitions, the observers selected and grouped together slices corresponding to different positions. Regions of interest were drawn separately in each group and separate maps were produced for each group. Later, the histograms of each individual maps were averaged together for the purpose of data analysis.

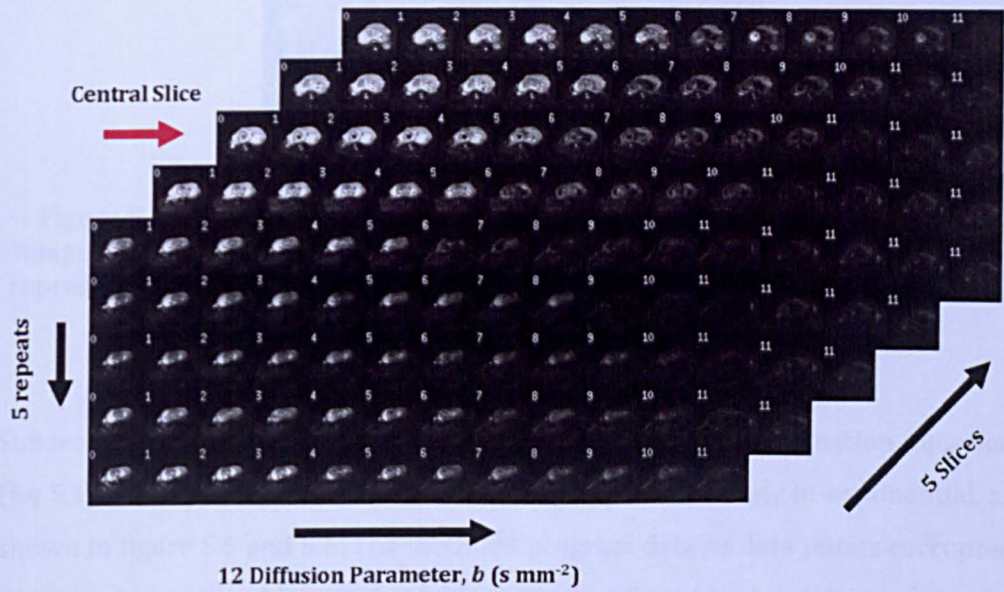


Figure 5.2: Placenta images of all 5 slices acquired with increasing diffusion weighting parameter (b). The diffusion weighting parameter increases gradually from image labelled as 0 to 11.

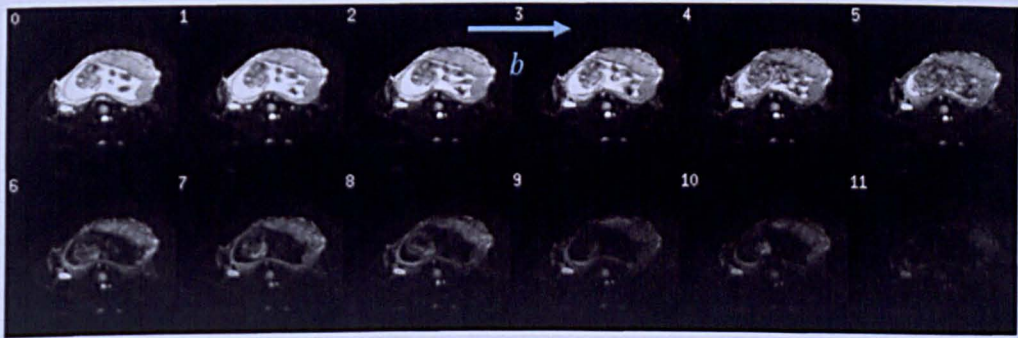


Figure 5.3: The central slice of the placenta images of a single PGSE acquisition with increasing diffusion weighting parameter (b). The diffusion weighting parameter increases gradually from image labelled as 0 to 11.

Following this, the acquisitions consisting of the selected slice were loaded into the IVIM program. In the IVIM program, the observers were expected to draw the

region of interest (ROI) for the basal plate and chorionic plate in a single intermediate b volume (figure 5.4). The region sandwiched between these two plates was automatically computed as the ROI of the entire placenta.

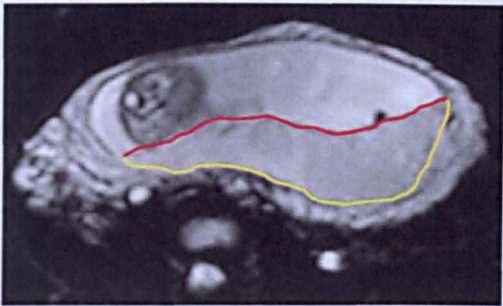


Figure 5.4: The representation of ROIs drawn on the intermediate b volume image of the placenta. The yellow line represents the ROI of basal plate, red line represents the ROI of chorionic plate and the region between the yellow and red line represents the ROI of the entire placenta.

Subsequently, these three ROIs were fitted into the signal attenuation equation (Eq 5.1) on a voxel by voxel basis. This fitting appears strongly bi-exponential, as shown in figure 5.5 and 5.6. The modified program detects data points corrupted by excessive motion, identified as lying more than 2 standard deviations from the fitted line of the ROI's averaged signal. These data sets were excluded from the data analysis and the data was refitted accordingly (figure 5.5).

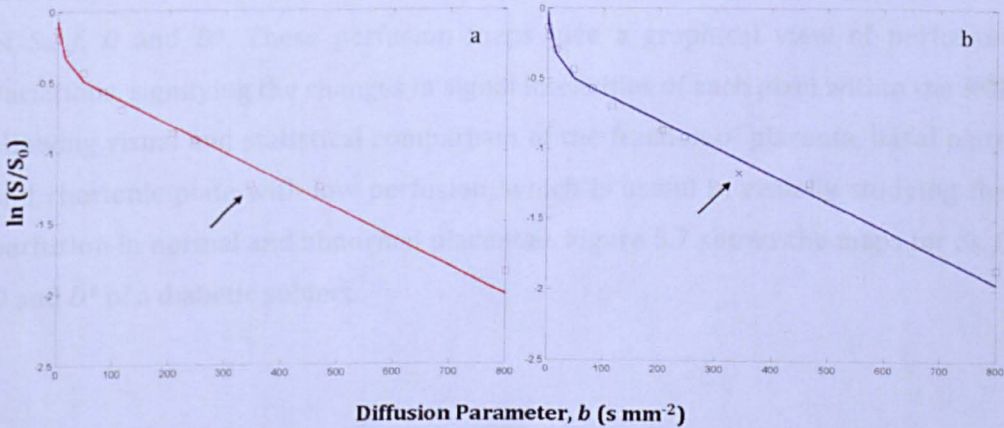


Figure 5.5: The bi-exponential signal decay curve of the ROI obtained through application of different diffusion weighting, b (red line). Images corrupted by excessive movement and artefact, identified as lying more than 2 standard deviation of the fitted line would be excluded from data analysis (representation shown by the arrow). This data would be refitted accordingly to produce a new bi-exponential signal attenuation curve (blue line).

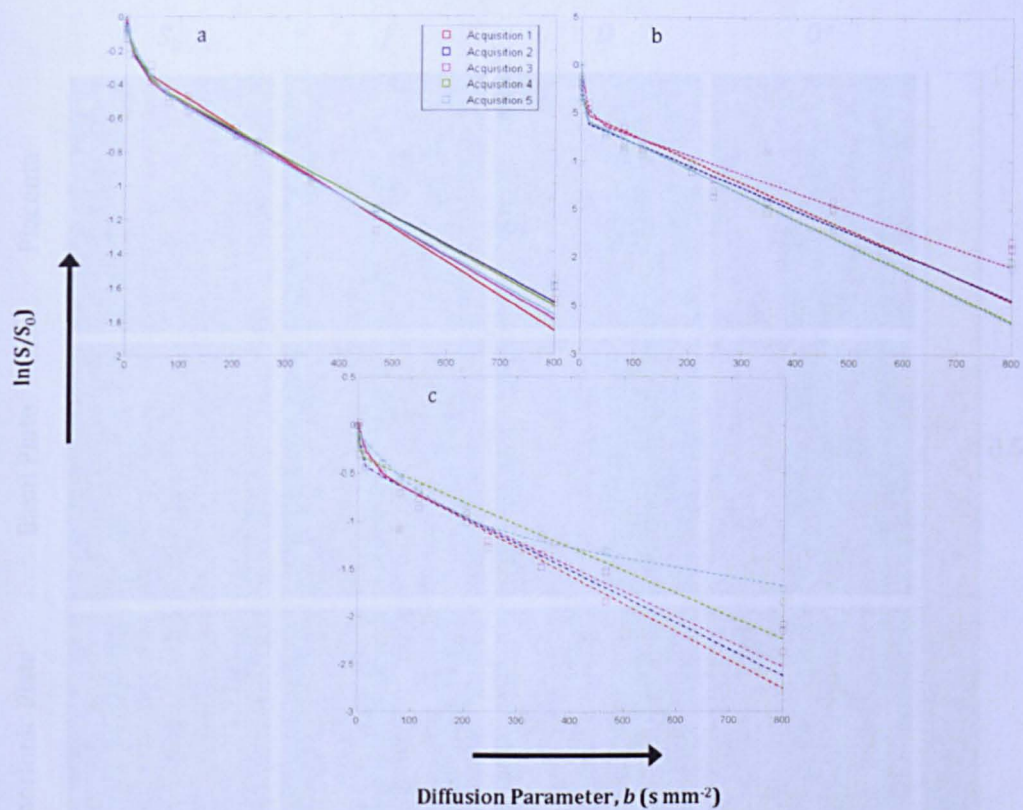


Figure 5.6: Bi-exponential signal decay plot of the (a) placenta, (b) basal plate and (c) chorionic plate of 5 different acquisition of a single slice.

Once the signal decay curves have been fitted, the program proceeds to produce four maps of colour coded ROIs with respect to the amplitude, fitting parameters of S_0 , f , D and D^* . These perfusion maps give a graphical view of perfusion variations, signifying the changes in signal intensities of each pixel within the ROI allowing visual and statistical comparison of the fraction of placenta, basal plate and chorionic plate with low perfusion, which is useful in visually studying the perfusion in normal and abnormal placentae. Figure 5.7 shows the maps for S_0 , f , D and D^* of a diabetic subject.

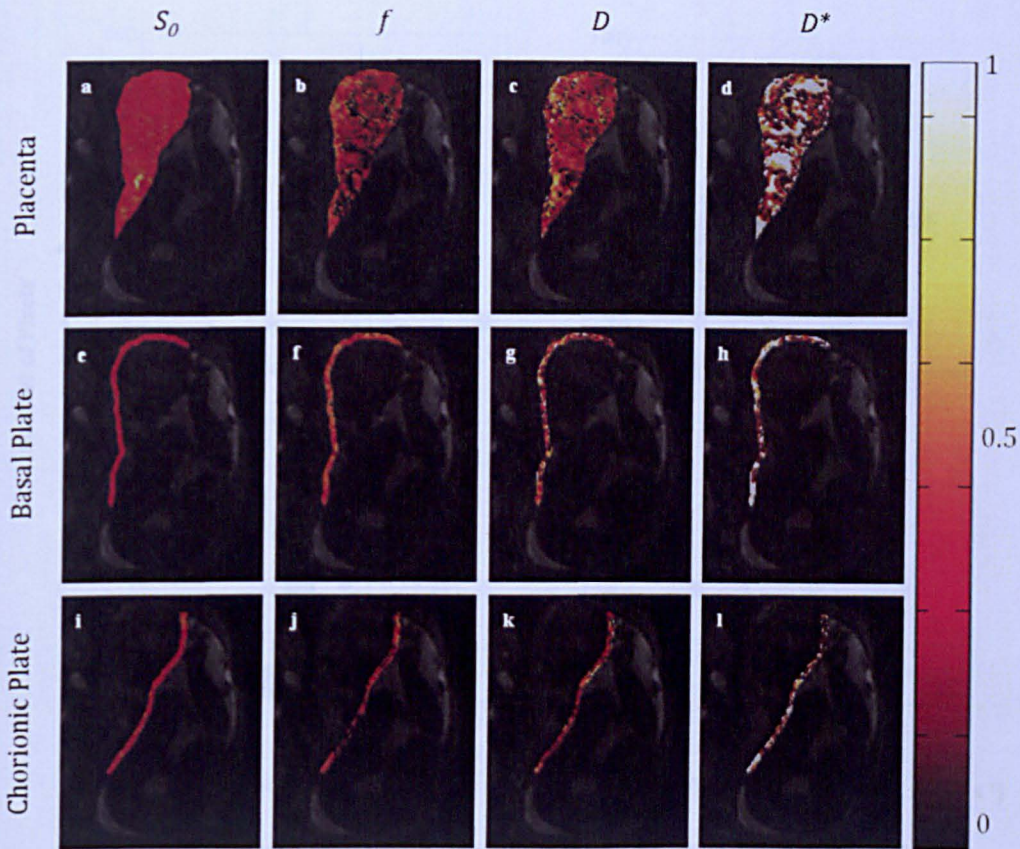


Figure 5.7: Colour map of placenta (a – d), basal plate (e – h) and chorionic plate (i – l) of S_0 (a, e and i), f (b, f and j), D (c, g and k) and D^* (d, h and l) for a diabetic subject at 35 weeks. S_0 , f , D and D^* were scaled between 0 and 1.

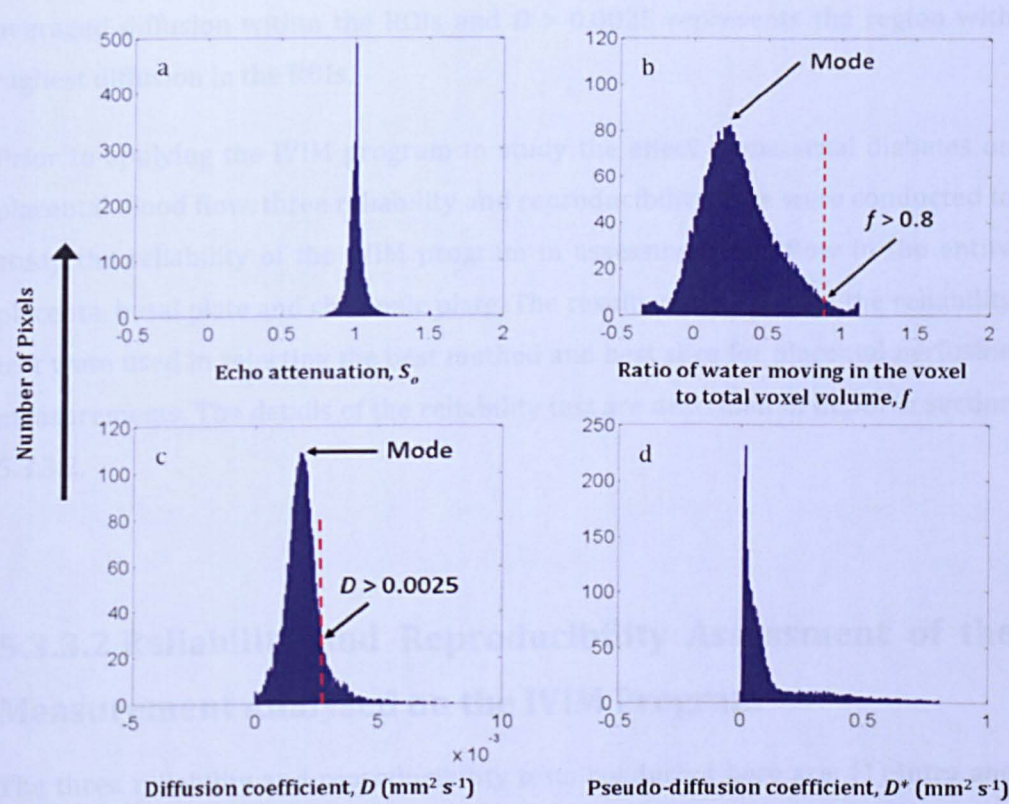


Figure 5.8: Averaged histograms of (a) S_0 , (b) f , (c) D and (d) D^* of the placenta from a healthy pregnant patient at 24 weeks.

The averaged histograms of the five acquisitions for S_0 , f , D and D^* were then displayed as shown in figure 5.8. The histogram of f , interpreted as the fraction of moving blood volume, is used to evaluate the mode f , mean f and fraction of pixels with $f > 0.8$ in the histogram. The fractional ratio with value more than 0.8 represents the placental region with highest blood flow. This value was chosen following on from earlier work on the differences in the blood flow of placentae of normal pregnancy and pregnancies affected by pre-eclampsia and growth restriction, where there were more areas with reduced perfusion in the latter pregnancies ($f < 0.2$) [13]. Our hypothesis was that diabetic placenta would have increased perfusion, and hence the decision to measure the fraction of pixels with $f > 0.8$.

Similarly, the histogram of D , interpreted as apparent diffusion coefficient rising from non-blood spins moving between and within the cells, was used to evaluate the mode D , mean D and fraction of pixels with $D > 0.0025$ in the histogram. The mode D represents the peak diffusion within the ROIs, mean D representing the

averaged diffusion within the ROIs and $D > 0.0025$ represents the region with highest diffusion in the ROIs.

Prior to applying the IVIM program to study the effect of maternal diabetes on placental blood flow, three reliability and reproducibility tests were conducted to study the reliability of the IVIM program in assessing blood flow in the entire placenta, basal plate and chorionic plate. The results obtained from the reliability test were used in selecting the best method and best slice for placental perfusion measurements. The details of the reliability test are described in depth in section 5.3.3.2.

5.3.3.2 Reliability and Reproducibility Assessment of the Measurement Analysed on the IVIM Program

The three reliability and reproducibility tests conducted here are: (1) intra and inter-observer reliability test of the method used in placental perfusion analysis (as described in section 5.3.3.1), (2) comparison between two techniques employed in placental perfusion analysis (single versus multiple masks) and (3) inter-slice comparison of placental perfusion measurement between two slices adjacent to each other.

Three observers performed the reliability and reproducibility study of placental perfusion analyses: the author (observer 1), Dr Nia Wyn Jones (observer 2) and Dr Ruta Deshpande (observer 3). Due to time constraint, the reliability and reproducibility test were only conducted based on values for mode f , mean f and fraction of pixels with $f > 0.8$. For the purpose of consistency throughout the reliability study, the PGSE data of five pregnant subjects were randomly selected: two controls and three diabetic women. Moreover, the reliability tests were conducted using the PGSE data obtained from both 24 weeks and 35 weeks, resulting in 10 sets of data. This was to avoid potential bias resulting from the pregnancy conditions and gestational age at the time of the scan. All the analyses were performed blind to gestational age, maternal BMI, diabetic status, complications of pregnancy, the other observers' results and the observer's own previous measurement results.

The results from all the reliability tests were statically computed using the Statistical Package for the Social Sciences (SPSS: Version 17.0; Chicago, IL, USA). The distribution of the data obtained from all the individual reliability tests were assessed using the Kolmogorov-Smirnov test. Following this, the reliability of the measurements and methods used in the study were assessed using two-way mixed ICCs with absolute agreement and 95% confidence intervals. Then, the LOA were computed and the Bland Altman graphs were plotted to express the differences as percentage of the mean measurements based on measurements done by the three observers.

The intra-observer reliability was assessed by comparing the differences in the two measurements made by the same observer for each data set. Inter-observer reliability test was assessed by comparing the first measurement of each observer against the first measurement of the other observers' measurements.

5.3.3.2.1 Intra-observer and Inter-observer Reliability Test

Three observers conducted the intra and inter-observer reliability test using the analysis method demonstrated in section 5.3.3.1. Each observer repeated the placental perfusion measurement twice for data sets at each gestation for all five subjects. As a result, each observer conducted the analysis twice for all the 10 data sets. The reliability test was conducted on the measurement of mode, mean and fraction of pixels with $f > 0.8$, which were obtained from the averaged histogram. The measurement of mean f and fraction of pixels with $f > 0.8$ were compared and the measurement with best reliability was used in single versus multiple masking comparison and slice-by-slice comparison reliability study, along with mode f .

5.3.3.2.2 Comparison between Single and Multiple Masking

Motion will cause exact ROI delineation to vary between repeats, but human error in drawing ROIs will increase if more ROIs need to be drawn. Therefore, two methods of drawing ROIs (for the placenta, basal plate and chorionic plate) were investigated. In the first method, the same set of ROIs was used for all repeats (subject to correction for gross motion as explained in section 5.3.3.1). In

the second method, a different ROI was drawn for each repeat. In both cases, the maps were created for each set separately and the histograms were averaged. The measurement was conducted by a single observer who repeated the measurement twice for both masking methods, for each gestation for all five subjects. The intra-observer reliability was found for each masking method by comparing the two repeated masking measurements. Then, the ICC and LOA results were compared to identify the most reliable masking method.

5.3.3.2.3 Slice-by-Slice Comparison

Two slices of placenta adjacent to each other (the slice with the largest placental area and the slice next to it) were selected by an observer to study the differences in the placental perfusion. For each slice of a particular subject, all the volumes of the five acquisitions were combined. Then, the data analysis was conducted as described in section 5.3.3.1. For both the slices, the mode, mean and fraction of pixels with $f > 0.8$ were computed from the averaged histogram. These values were used in the slice-by-slice comparison test.

5.3.3.3 The Application of the IVIM Program to Study the Effect of Maternal Diabetes on Placental Blood Flow

The best method and best slice for reproducible placental perfusion analysis were identified from the results of the reliability tests. These approaches were applied in conjunction with the method described in section 5.3.3.1 to study the effect of maternal diabetes on placental blood flow. For the purpose of this study, perfusion analysis was only done on a single slice for each subject at each gestational time point. The data analysis was conducted on all the data collected from both diabetic and non-diabetic control pregnant women at 24 weeks and 35 weeks gestational age. The averaged histograms of fraction of moving blood volume (f) and apparent diffusion coefficient rising from non-blood spins moving between and within the cells (D) were used in evaluation of mode f , mean f , fraction of pixels with $f > 0.08$, mode D , mean D and fraction of pixels with $D > 0.0025$.

The distributions of mode f , mean f , fraction of pixels with $f > 0.08$, mode D , mean D and fraction of pixels with $D > 0.0025$ along with clinical data were tested for normality using the Kolmogorov-Smirnov test on SPSS software. The normally distributed results were expressed by their mean and standard deviation. Then, the statistical comparisons of clinical data between two groups at each gestation were performed using an independent samples t-test for normally distributed data and a Mann Whitney test for non-parametric data. Subsequently, statistical comparison for placental perfusion measurements was performed using the repeated measures analysis of variance (ANOVA) to access the changes in the placental perfusion and diffusion with time. The results were presented as a ratio of variation explained by the model to unexplained factors. Statistically significant results were determined by using p-values. For the purpose of this study, p-values less than 0.05 were considered significant. These values were used in studying the placental perfusion difference in diabetic and non-diabetic control pregnant mothers.

In addition, the placental volume was measured by drawing approximate freehand mask around the placenta using Analyze 9.0. This measurement was conducted on either HASTE or bFFE images acquired from all the diabetic and non-diabetic control pregnant women at 24 weeks and 35 weeks.

5.4 Results

5.4.1 Reliability and Reproducibility Assessment of the Measurement Analysed on the IVIM Program

5.4.1.1 Intra-observer and Inter-observer Reliability Test

Mean f measurements generally demonstrated the best intra and inter-observer reliability followed by mode f and fraction of pixels with $f > 0.8$, with most mean f ICCs demonstrating very good correlation (> 0.81). In general, observer 1 scored the best intra-observer results for mean f , fraction of pixels with $f > 0.8$ and mode f measurements for placenta, basal plate and chorionic plate across all gestations. This is evident from the narrower LOA for observer 1 compared to other

observers in the Bland Altman plots for all these measurements (figure 5.9, 5.10 and 5.11). Observer 1's LOA for mean f measurements: $\pm 5\%$ for the whole placenta, $\pm 9\%$ for the basal plate and $\pm 11\%$ for the chorionic plate, fraction of pixels with $f > 0.8$ measurements: $\pm 15\%$ for the whole placenta, $\pm 38\%$ for the basal plate and $\pm 23\%$ for the chorionic plate and mode f measurements: $\pm 0.01\%$ for the whole placenta and $\pm 18\%$ for the basal plate (observer 3 had narrower LOA at $\pm 39\%$ for chorionic plate).

The intra and inter-observer results were generally best for placenta and less consistent for basal plate and chorionic plate, with chorionic plate usually demonstrating the weakest ICC results and wider LOA. In addition, the LOA were generally wider at 35 weeks compared to 24 weeks. Table 5.1, 5.2 and 5.3 lists the ICC results for intra and inter-observer reliability for mean f , fraction of pixels with $f > 0.8$ and mode f measurements for placenta, basal plate and chorionic plate across all gestation, 24 weeks and 35 weeks.

With the reliability test demonstrating weakest ICCs and LOA for fraction of pixels with $f > 0.8$, the subsequent reliability tests were only based on mean f and mode f measurements.

Region of Interest	Intra-observer ICCs for Mean <i>f</i> of Three Observers (95% CI)			Inter-observer ICCs for Mean <i>f</i> of Three Observers (95% CI)
	Observer 1	Observer 2	Observer 3	
	All gestation			
Placenta	0.961 (0.857 – 0.990)	0.918 (0.706 – 0.979)	0.874 (0.542 – 0.968)	0.911 (0.745 – 0.975)
Basal Plate	0.953 (0.824 – 0.988)	0.928 (0.739 – 0.982)	0.851 (0.535 – 0.960)	0.878 (0.546 – 0.969)
Chorionic Plate	0.871 (0.588 – 0.966)	0.741 (0.287 – 0.927)	0.868 (0.551 – 0.966)	0.655 (0.311 – 0.887)
	24 weeks			
Placenta	0.956 (0.642 – 0.995)	0.879 (0.273 – 0.987)	0.715 (-0.173 – 0.966)	0.784 (0.344 – 0.972)
Basal Plate	0.962 (0.715 – 0.996)	0.839 (0.001 – 0.982)	0.904 (0.447 – 0.989)	0.811 (0.380 – 0.976)
Chorionic Plate	0.952 (0.599 – 0.995)	0.627 (-0.576 – 0.955)	0.969 (0.779 – 0.997)	0.624 (0.112 – 0.945)
	35 weeks			
Placenta	0.959 (0.719 – 0.996)	0.936 (0.607 – 0.993)	0.892 (0.185 – 0.988)	0.947 (0.789 – 0.994)
Basal Plate	0.956 (0.687 – 0.995)	0.977 (0.801 – 0.998)	0.827 (0.056 – 0.980)	0.936 (0.542 – 0.993)
Chorionic Plate	0.745 (0.006 – 0.969)	0.823 (0.012 – 0.980)	0.708 (-0.214 – 0.965)	0.329 (-0.033 – 0.848)

Table 5.1: Intra-observer and inter-observer reliability results (ICC) for mean f of placenta, basal plate and chorionic plate computed from two measurements made by each observer at different gestational stage.

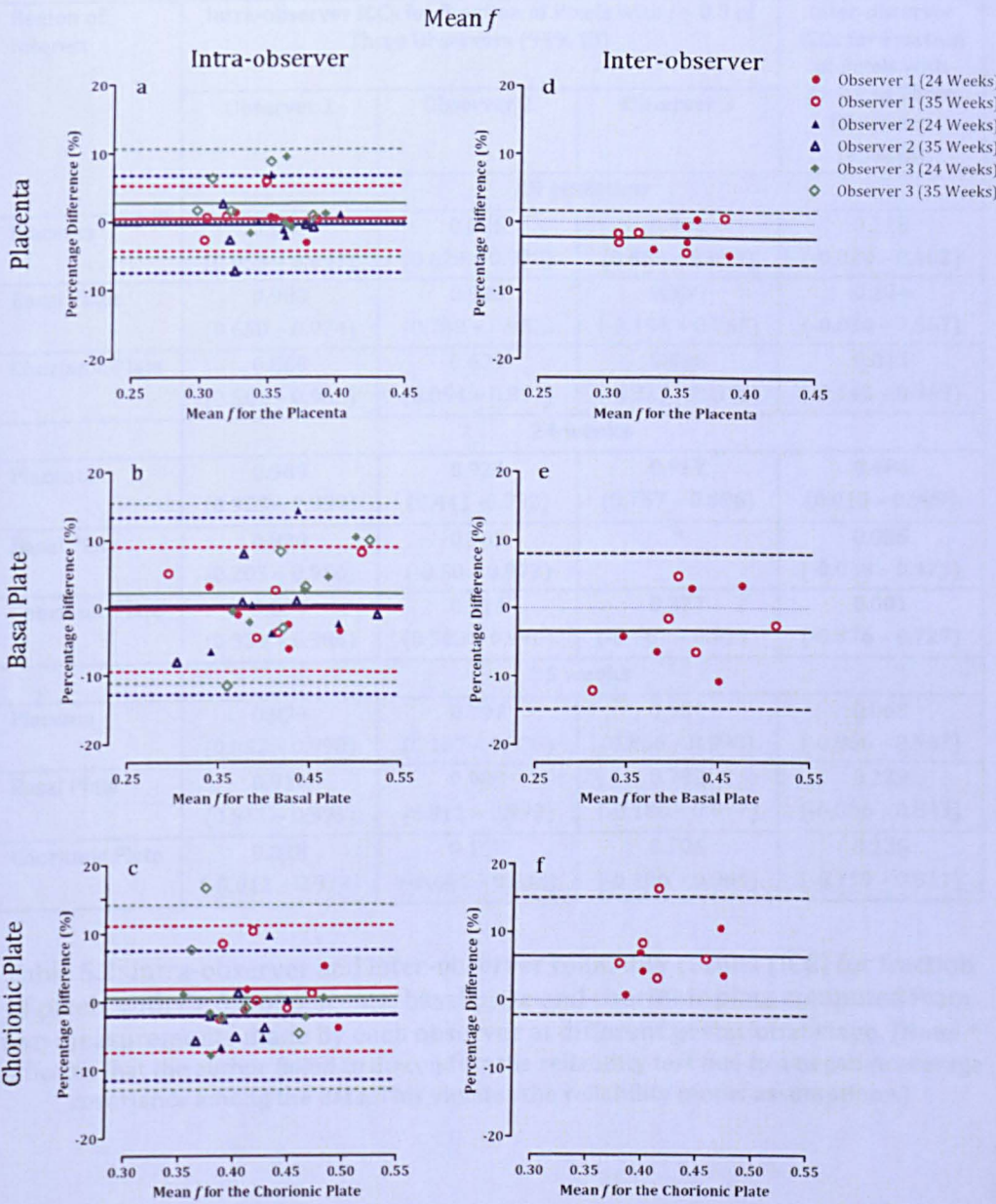


Figure 5.9: Bland Altman plots of mean f of the whole placenta (a and d), basal plate (b and e) and chorionic plate (c and f). These Bland Altman plots express the intra-observer (a – c) or inter-observer (d – f) mean percentage differences based on measurements made by three observers. The solid lines refer to mean percentage differences (1st measurement – 2nd measurement), whereas dotted lines refer to LOA between measurements.

Region of Interest	Intra-observer ICCs for Fraction of Pixels with $f > 0.8$ of Three Observers (95% CI)			Inter-observer ICCs for Fraction of Pixels with $f > 0.8$ of Three Observers (95% CI)
	Observer 1	Observer 2	Observer 3	
	All gestation			
Placenta	0.988 (0.953 – 0.997)	0.886 (0.629 – 0.970)	0.971 (0.869 – 0.993)	0.218 (-0.029 – 0.602)
Basal Plate	0.900 (0.650 – 0.974)	0.928 (0.739 – 0.982)	0.339 (-0.198 – 0.765)	0.204 (-0.034 – 0.587)
Chorionic Plate	0.868 (0.564 – 0.965)	0.639 (0.054 – 0.897)	0.486 (-0.223 – 0.846)	0.014 (-0.143 – 0.369)
	24 weeks			
Placenta	0.989 (0.923 – 0.999)	0.924 (0.441 -0.992)	0.967 (0.757 – 0.996)	0.486 (0.010 – 0.909)
Basal Plate	0.830 (0.203 – 0.980)	0.763 (-0.50 – 0.972)	*	0.055 (-0.028 – 0.473)
Chorionic Plate	0.874 (0.339 – 0.986)	0.914 (0.503 – 0.990)	0.377 (-0.767 – 0.914)	0.001 (-0.376 – 0.727)
	35 weeks			
Placenta	0.979 (0.852 – 0.998)	0.797 (0.107 – 0.976)	0.981 (0.866 – 0.998)	0.068 (-0.066 – 0.587)
Basal Plate	0.917 (0.511 – 0.991)	0.989 (0.911 – 0.999)	0.792 (-0.186 – 0.977)	0.239 (-0.086 – 0.843)
Chorionic Plate	0.818 (-0.012 – 0.979)	0.107 (-0.641 – 0.834)	0.706 (-0.166 – 0.964)	0.226 (-0.119 – 0.811)

Table 5.2: Intra-observer and inter-observer reliability results (ICC) for fraction of pixels with $f > 0.8$ of placenta, basal plate and chorionic plate computed from two measurements made by each observer at different gestational stage. (Note: * indicates that the author failed to do conduct the reliability test due to a negative average covariance among the data. This violates the reliability model assumptions.)

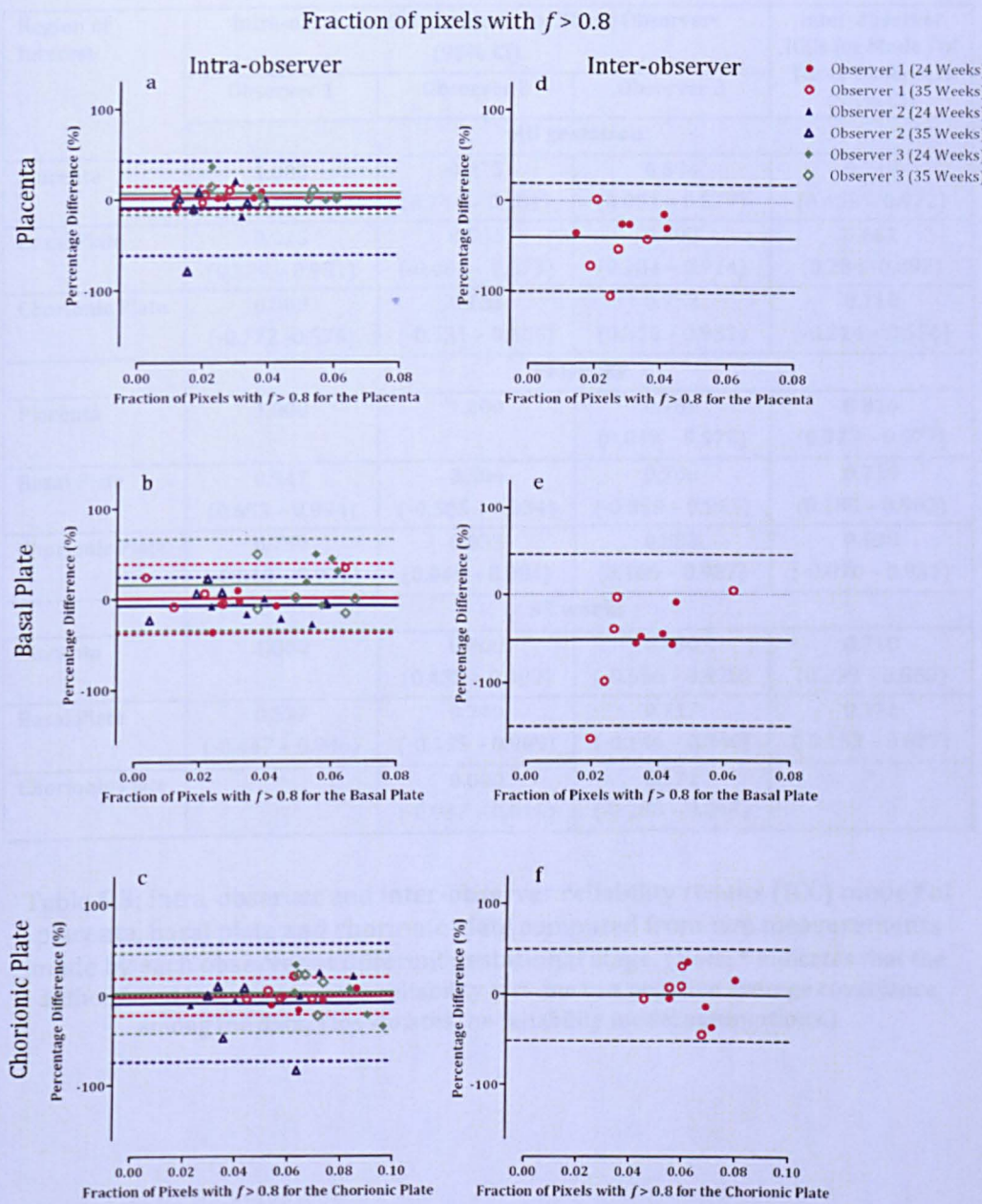


Figure 5.10: Bland Altman plots of fraction of pixels with $f > 0.8$ of the whole placenta (a and d), basal plate (b and e) and chorionic plate (c and f). These Bland Altman plots express the intra-observer (a – c) or inter-observer (d – f) mean percentage differences based on measurements made by three observers. The solid lines refer to mean percentage differences (1st measurement – 2nd measurement), whereas dotted lines refer to LOA between measurements.

Region of Interest	Intra-observer ICCs for Mode <i>f</i> of Three Observers (95% CI)			Inter-observer ICCs for Mode <i>f</i> of Three Observers (95% CI)
	Observer 1	Observer 2	Observer 3	
	All gestation			
Placenta	1.000	0.925 (0.744 – 0.981)	0.594 (0.051 – 0.877)	0.748 (0.455 – 0.922)
Basal Plate	0.925 (0.728 – 0.981)	0.566 (-0.081 – 0.873)	0.698 (0.204 – 0.914)	0.661 (0.284 -0.892)
Chorionic Plate	0.000 (-0.772 -0.575)	0.135 (-0.531 – 0.686)	0.752 (0.310 – 0.931)	0.110 (-0.214 – 0.576)
	24 weeks			
Placenta	1.000	1.000	0.789 (0.049 – 0.975)	0.816 (0.373 – 0.977)
Basal Plate	0.947 (0.653 – 0.994)	0.504 (-0.505 – 0.934)	0.708 (-0.053 – 0.963)	0.719 (0.185 – 0.962)
Chorionic Plate	0.759 (-0.010 – 0.971)	0.853 (0.048 – 0.984)	0.883 (0.186 – 0.987)	0.538 (-0.070 – 0.931)
	35 weeks			
Placenta	1.000	0.900 (0.438 – 0.989)	0.430 (-0.556 – 0.920)	0.710 (0.239 – 0.960)
Basal Plate	0.577 (-0.447 – 0.946)	0.740 (-0.155 – 0.969)	0.717 (-0.144 – 0.966)	0.371 (-0.153 – 0.887)
Chorionic Plate	*	0.000 (-0.947 – 0.818)	0.372 (-0.288 – 0.894)	*

Table 5.3: Intra-observer and inter-observer reliability results (ICC) mode *f* of placenta, basal plate and chorionic plate computed from two measurements made by each observer at different gestational stage. (Note: * indicates that the author failed to do conduct the reliability test due to a negative average covariance among the data. This violates the reliability model assumptions.)

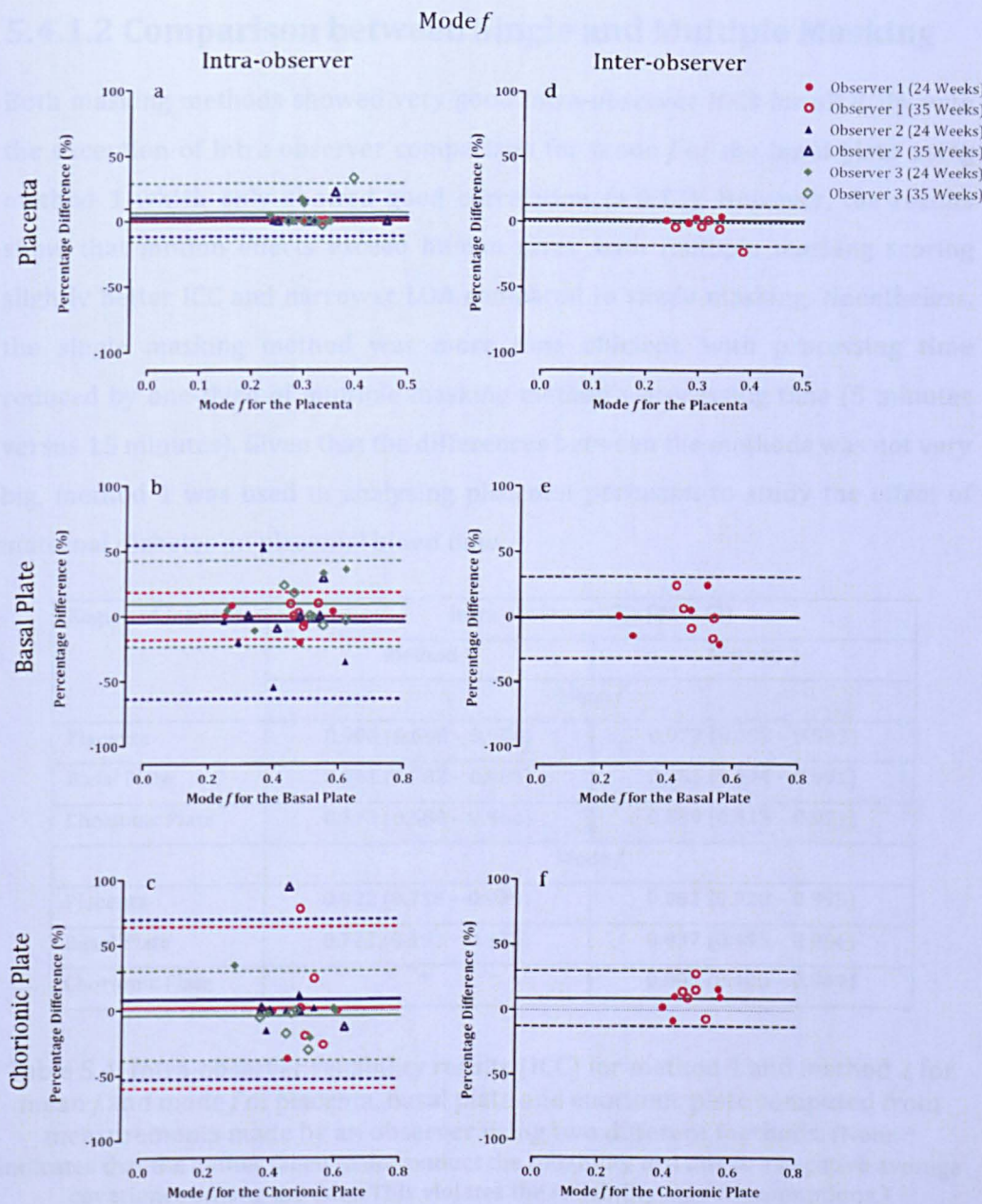


Figure 5.11: Bland Altman plots of mode f of the whole placenta (a and d), basal plate (b and e) and chorionic plate (c and f). These Bland Altman plots express the intra-observer (a – c) or inter-observer (d – f) mean percentage differences based on measurements made by three observers. The solid lines refer to mean percentage differences (1st measurement – 2nd measurement), whereas dotted lines refer to LOA between measurements.

5.4.1.2 Comparison between Single and Multiple Masking

Both masking methods showed very good intra-observer ICCs for all ROIs, with the exception of intra-observer comparison for mode *f* of the basal plate using method 1 which only showed good correlation (> 0.72). However, the results show that motion effects exceed human error with multiple masking scoring slightly better ICC and narrower LOA compared to single masking. Nonetheless, the single masking method was more time efficient, with processing time reduced by one-third of multiple masking method's processing time (5 minutes versus 15 minutes). Given that the differences between the methods was not very big, method 1 was used in analysing placental perfusion to study the effect of maternal diabetes on placental blood flow.

Region of Interest	Intra-observer ICCs (95% CI)	
	Method 1	Method 2
	Mean <i>f</i>	
Placenta	0.908 (0.680 – 0.976)	0.972 (0.898 – 0.993)
Basal Plate	0.941 (0.782 – 0.985)	0.965 (0.874 – 0.991)
Chorionic Plate	0.873 (0.588 – 0.966)	0.889 (0.615 – 0.971)
	Mode <i>f</i>	
Placenta	0.922 (0.735 – 0.980)	0.981 (0.928 – 0.995)
Basal Plate	0.721 (0.192 – 0.923)	0.837 (0.495 – 0.956)
Chorionic Plate	*	0.808 (0.400 – 0.949)

Table 5.4: Intra-observer reliability results (ICC) for method 1 and method 2 for mean *f* and mode *f* of placenta, basal plate and chorionic plate computed from measurements made by an observer using two different methods. (Note: * indicates that the author failed to do conduct the reliability test due to a negative average covariance among the data. This violates the reliability model assumptions.)

5.4.1.3 Statistical Analysis Comparison between Single and Multiple Masking

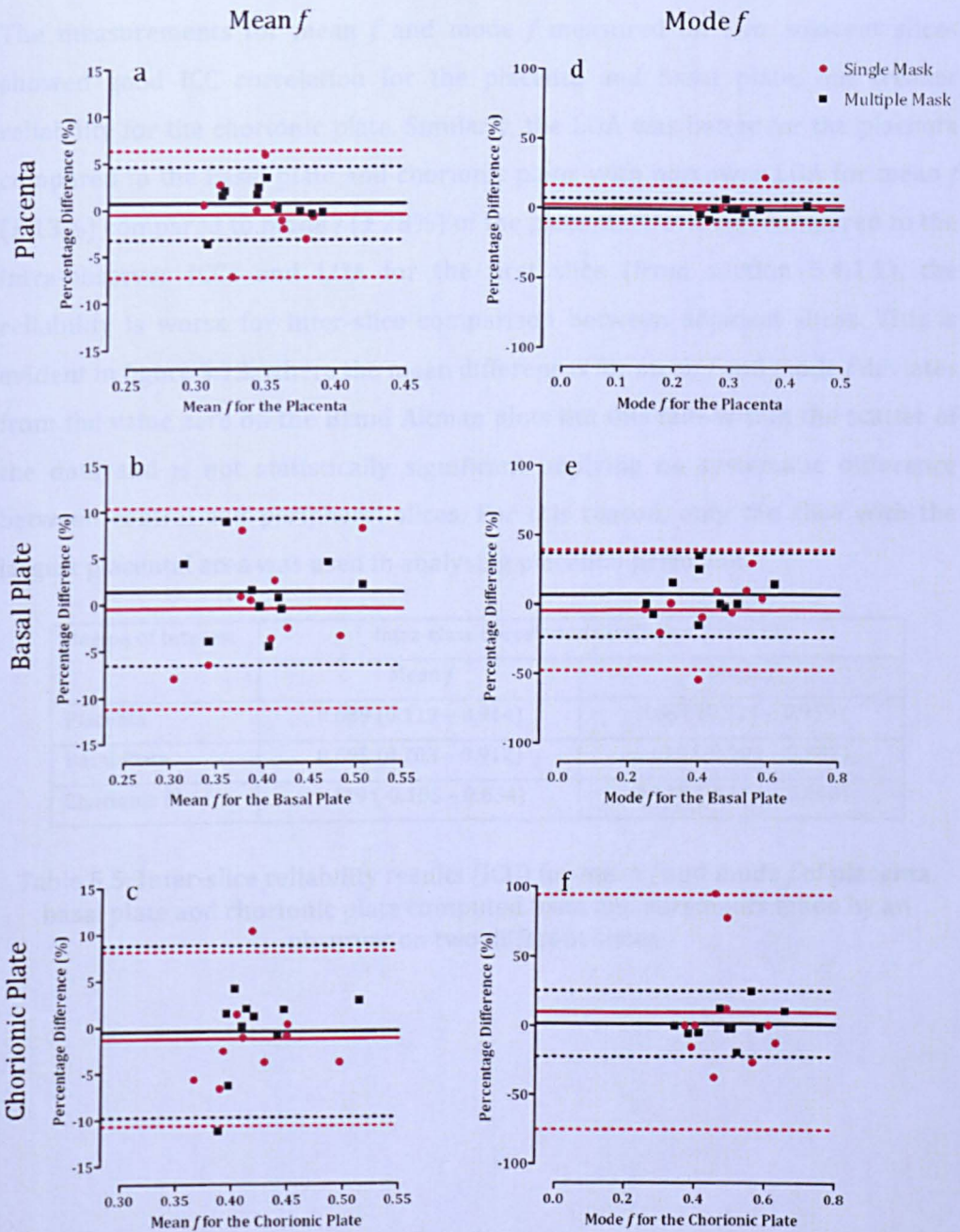


Figure 5.12: Bland Altman plots of mean f (a – c) and mode f (d – f) of the whole placenta (a and d), basal plate (b and e) and chorionic plate (c and f). These Bland Altman plots express the differences in percentage of their means and done based on measurements made by a single observer, the author. The solid lines refer to mean percentage differences (1st measurement – 2nd measurement), whereas dotted lines refer to LOA between measurements.

5.4.1.3 Slice-by-Slice Comparison

The measurements for mean f and mode f measured on two adjacent slices showed good ICC correlation for the placenta and basal plate, but weaker reliability for the chorionic plate. Similarly, the LOA was better for the placenta compared to the basal plate and chorionic plate, with narrower LOA for mean f ($\pm 13\%$) compared to mode f ($\pm 28\%$) of the placenta. However, compared to the intra-observer ICCs and LOA for the first slice (from section 5.4.1.1), the reliability is worse for inter-slice comparison between adjacent slices. This is evident in figure 5.13, where the mean differences for mean f and mode f deviates from the value zero on the Bland Altman plots but this falls within the scatter of the data and is not statistically significant implying no systematic difference between central and peripheral slices. For this reason, only the slice with the largest placental area was used in analysing placental perfusion.

Region of Interest	Intra-class Correlation Coefficient (95% CI)	
	Mean f	Mode f
Placenta	0.689 (0.119 – 0.914)	0.847 (0.521 – 0.959)
Basal Plate	0.695 (0.203 – 0.912)	0.610 (-0.001 – 0.887)
Chorionic Plate	0.479 (-0.105 – 0.834)	0.110 (-0.424 – 0.646)

Table 5.5: Inter-slice reliability results (ICC) for mean f and mode f of placenta, basal plate and chorionic plate computed from measurements made by an observer on two different slices.

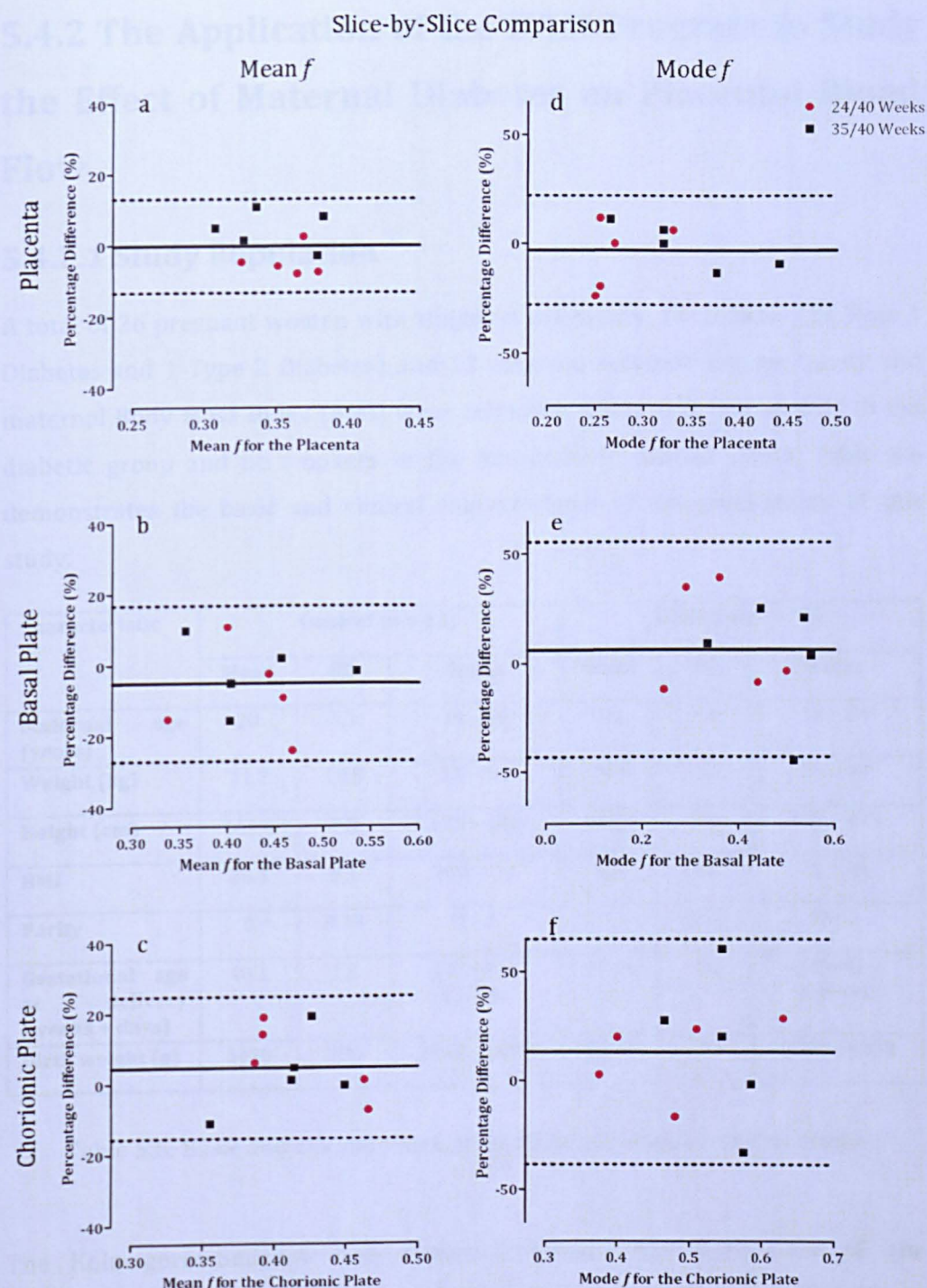


Figure 5.13: Bland Altman plots of mean f (a – c) and mode f (d – f) of the whole placenta (a and d), basal plate (b and e) and chorionic plate (c and f). These Bland Altman plots express the differences in percentage of their means and done based on measurements made by a single observer, the author. The solid lines refer to intra-slice mean percentage differences (measurement of 1st slice – measurement of 2nd slice), whereas dotted lines refer to LOA between measurements.

5.4.2 The Application of the IVIM Program to Study the Effect of Maternal Diabetes on Placental Blood Flow

5.4.2.1 Study Population

A total of 26 pregnant women with singleton pregnancy, 14 diabetic (13 Type 1 Diabetes and 1 Type 2 Diabetes) and 12 controls, matched for age, parity and maternal Body Mass Index (BMI) were recruited. There was one smoker in the diabetic group and no smokers in the non-diabetic control group. Table 5.6 demonstrates the basic and clinical characteristics of the participants of this study.

Characteristic	Control (n = 12)			Diabetes (n = 14)		
	Mean	SD	Range	Mean	SD	Range
Maternal age (years)	29	4.3	19 – 35	30	4.4	19 – 34
Weight (kg)	71.7	10.8	55 – 94	70.9	10.2	56 – 90
Height (cm)	164.6	7.0	155 – 180	163.9	5.2	153 – 173
BMI	26.3	3.1	20.5 – 31	26.2	3.5	22 – 34
Parity	0	0.39	0 – 1	1	0.65	0 – 2
Gestational age at delivery (weeks + days)	40.1	1.5	(37+0) – (41+4)	37.48	1.33	(35+4) – (39+4)
Birth weight (g)	3418	496	2350 – 4070	3419	641	1800 – 4280

Table 5.6: Basic and clinical characteristics of participants of this study.

The Kolmogorov-Smirnov test confirmed normal distribution for all the demographic data, with exception to parity, birth weight centiles and HbA1c in first trimester. There was no significant difference in any of the demographic characteristics (age, BMI, parity and ethnicity) between groups. The range of the gestational ages at the time of scans was 22 – 26 weeks and 33 – 37 weeks. The average gestational ages for the scans was 24 weeks + 1 day (SD = 5 days) and 34 weeks + 4 days (SD = 4 days) in the non-diabetic control group and 24 weeks + 2 days (SD = 5 days) and 34 weeks + 3 days (SD = 7 days) in the diabetic group. Seven pregnant subjects withdrew from the study after their first scan: one

control pregnant woman (did not attend second scan) and six pregnant women with diabetes. The pregnant women with diabetes who withdrew from the study were either too big for the magnet bore (one pregnant women), were experiencing morning sickness during the second scan (one pregnant women), delivered before scan (one pregnant women) or failed to attend second scanning session (three pregnant women). However, there were no differences in the demographics or delivery outcomes between women who completed the study and those who withdrew.

5.4.2.2 Clinical Outcomes

For birth weight, there was no significant difference ($p = 0.395$) between the two groups. The average birth weight of babies born to pregnant mothers in the control group was 3418 g (SD = 496 g) and diabetic group was 3419 g (SD = 641 g). Nonetheless, the mothers with diabetes delivered their babies at a significantly earlier gestation ($p < 0.001$), 37 weeks + 4 days (SD = 9 days), whereas control mothers delivered their babies at 40 weeks + 0 days (SD = 10 days). Moreover, after correcting for gestational age, babies born to mothers with diabetes were significantly larger than controls (median birth weight centile 88 for diabetes group and 33 for control group; $p = 0.009$). Data also shows that there was a higher number of deliveries by caesarean section (CS) in the diabetes group (five emergency and two elective CS in diabetic versus one elective CS in the controls, Fisher's exact test $p = 0.036$).

5.4.2.3 The Application of the IVIM

For the purpose of this study, only one of the five placental slices was assessed to investigate placental perfusion and diffusion. The most commonly used slice for this study was the central slice with the largest placental area compared to all the five slices.

Figure 5.14, 5.15 and 5.16 demonstrates the difference in mean f , mode f , mean D , fraction of pixels with $D > 0.0025$ and mode D of placenta, basal plate and chorionic plate for the control and diabetic group across gestation, while figure 5.17 demonstrates the comparison between average measurements for mean f ,

mode f , mean D , fraction of pixels with $D > 0.0025$ and mode D of placenta, basal plate and chorionic plate for the control and diabetic group at 24 weeks and 35 weeks.

The statistical test conducted on mode f , mean f , mode D , mean D and fraction of pixels with $D > 0.0025$ confirmed that the data were normally distributed for both diabetic and control groups at 24 weeks and 35 weeks. Although the statistical test conducted on fraction of pixels with $f > 0.08$ showed that the data were normally distributed, these data were not used in investigating the effect of maternal diabetes on placental perfusion, since this element failed to demonstrate reliability and reproducibility in the placenta, basal plate and chorionic plate. The average value for all the measurements made for diabetic and control groups across the two gestations is demonstrated in tables 5.7 and 5.8. These tables also contain p-values obtained from statistical comparison performed using repeated measures analysis of variance (ANOVA). These values provide information on the effect of gestation and group on placental perfusion and diffusion.

There was no significant difference in the mean f measurements of the diabetic and control group across gestation. Conversely, for mode f , there was a significant increase in the mode f of both basal plate and chorionic plate across gestation, suggesting increase in the peak blood flow within these regions across gestation. Moreover, the mode f measurements were generally higher in the control group at 24 weeks but at 35 weeks, the mode f measurements were usually higher in the diabetic group. This was not significant but similar trends were seen for all regions.

Region of Interest	Group	24 weeks Mean (SD)	35 weeks Mean (SD)	p-value		
				Across Gestation	Gestation and Group	Group
	Mean <i>f</i>					
Placenta	Diabetic	0.3546 (0.0379)	0.3577 (0.0332)	0.445	0.632	0.490
	Control	0.3781 (0.0502)	0.3637 (0.0393)			
Basal Plate	Diabetic	0.3932 (0.0422)	0.4124 (0.0826)	0.441	0.270	0.270
	Control	0.4369 (0.0581)	0.4264 (0.0714)			
Chorionic Plate	Diabetic	0.4386 (0.0664)	0.4644 (0.0621)	0.166	0.390	0.591
	Control	0.4276 (0.0662)	0.4404 (0.0421)			
	Mode <i>f</i>					
Placenta	Diabetic	0.2714 (0.0533)	0.3300 (0.0393)	0.586	0.065	0.850
	Control	0.3267 (0.0672)	0.3000 (0.0632)			
Basal Plate	Diabetic	0.3657 (0.1201)	0.4738 (0.1103)	0.003*	0.113	0.375
	Control	0.4200 (0.1100)	0.4618 (0.1141)			
Chorionic Plate	Diabetic	0.4596 (0.1103)	0.5988 (0.1351)	0.012*	0.339	0.952
	Control	0.4817 (0.1573)	0.5609 (0.1583)			

Table 5.7: The average measurement and standard deviation for the mean *f* and mode *f* of placenta, basal plate and chorionic plate for the control and diabetic group computed from measurements made by one observer using method described in section 5.3.3.1. (Note: * indicates statistically significant p-values.)

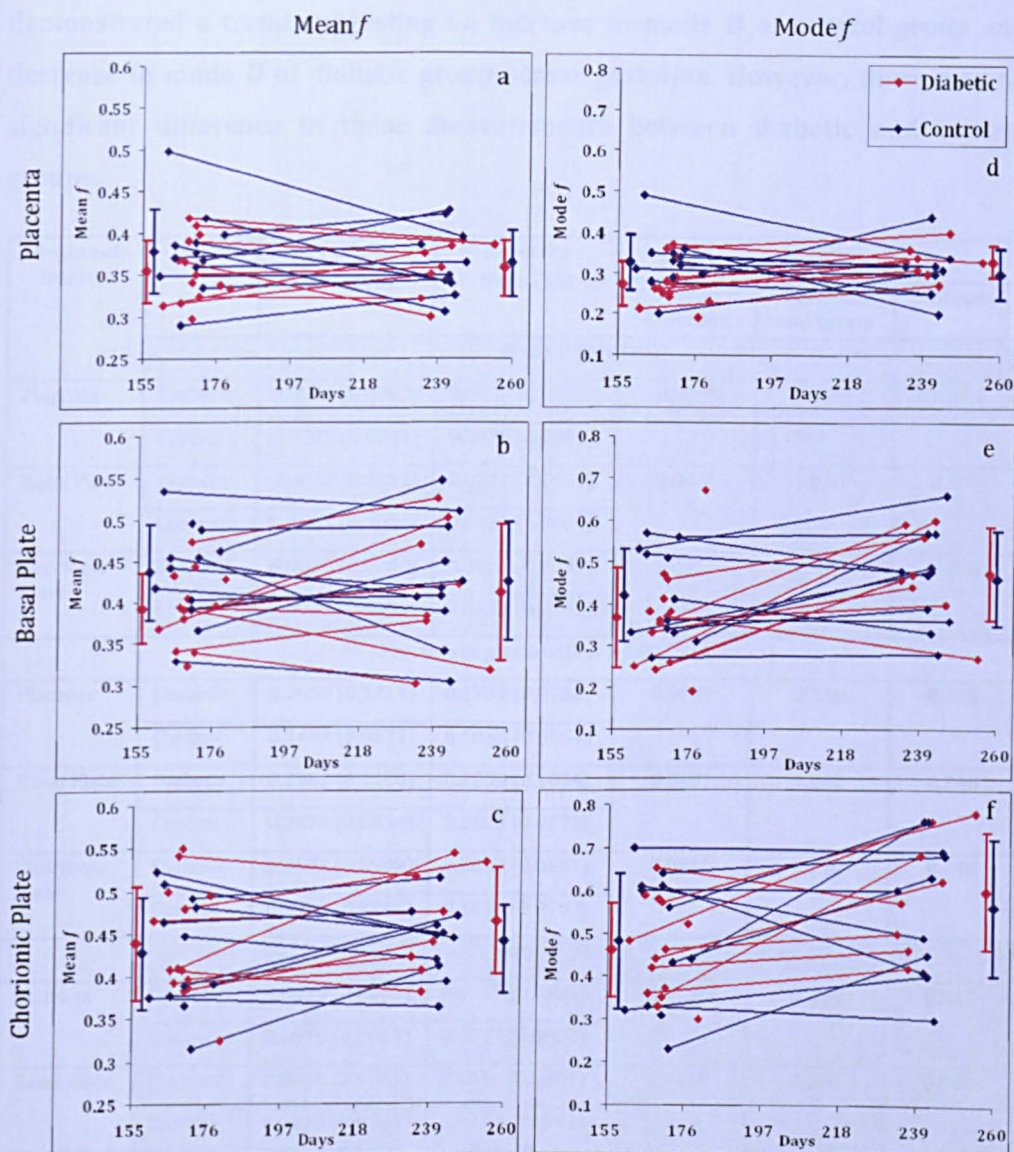


Figure 5.14: Scatter plot of the difference in mean f (a – c) and mode f (d – f) of the whole placenta (a and d), basal plate (b and e) and chorionic plate (c and f) across two gestations for diabetic and control mothers. Marker lines are added allowing comparison of the two measurements for each individual subject. The mean value and the standard deviation are also displayed for the two groups on the left and right of the image [red – diabetic; blue – control].

The repeated measures of ANOVA confirmed that there were significant changes in D across gestation in both diabetic and control groups. There were significant decreases in mean D , fraction of pixels with $D > 0.0025$ and mode D in the placenta and chorionic plate across gestation, with a slight trend for mean D and mode D to be greater in the control subjects. In addition, ANOVA test confirmed there was a significant change in the mean D measurement of the placenta and basal plate across gestation and group. Moreover, mode D of basal plate

demonstrated a trend suggesting an increase in mode D of control group and decrease in mode D of diabetic group across gestation. However, there was no significant difference in these measurements between diabetic and control groups.

Region of Interest	Group	24 weeks Mean (SD)	35 weeks Mean (SD)	p-value		
				Across Gestation	Gestation and Group	Group
	Mean D (mm ² s ⁻¹)					
Placenta	Diabetic	0.0021 (0.0003)	0.0017 (0.0003)	0.009*	0.015*	0.344
	Control	0.0021 (0.0002)	0.0018 (0.0002)			
Basal Plate	Diabetic	0.0022 (0.0003)	0.0017 (0.0004)	0.001*	0.020*	0.299
	Control	0.0023 (0.0004)	0.0021 (0.0004)			
Chorionic Plate	Diabetic	0.0028 (0.0004)	0.0021 (0.0003)	0.001*	0.440	0.845
	Control	0.0029 (0.0006)	0.0022 (0.0005)			
	Fraction of pixels with $D > 0.0025$ (mm ² s ⁻¹)					
Placenta	Diabetic	0.2660 (0.1214)	0.1732 (0.0782)	0.002*	0.110	0.325
	Control	0.2403 (0.0877)	0.1868 (0.0564)			
Basal Plate	Diabetic	0.2952 (0.1120)	0.2030 (0.1054)	0.013*	0.062	0.748
	Control	0.2873 (0.0854)	0.2625 (0.0722)			
Chorionic Plate	Diabetic	0.4681 (0.0999)	0.2822 (0.0651)	0.001*	0.718	0.748
	Control	0.4970 (0.1245)	0.2817 (0.0907)			
	Mode D (mm ² s ⁻¹)					
Placenta	Diabetic	0.0019 (0.0003)	0.0017 (0.0002)	0.015*	0.346	0.617
	Control	0.0019 (0.0003)	0.0017 (0.0002)			
Basal Plate	Diabetic	0.0018 (0.0003)	0.0016 (0.0004)	0.044*	0.056	0.440
	Control	0.0018 (0.0003)	0.0018 (0.0002)			
Chorionic Plate	Diabetic	0.0019 (0.0005)	0.0014 (0.0003)	0.001*	0.983	0.578
	Control	0.0021 (0.0007)	0.0015 (0.0003)			

Table 5.8: The average measurement and standard deviation for mean D , fraction of pixels with $D > 0.0025$ and mode D of placenta, basal plate and chorionic plate for the control and diabetic group computed from measurements made by one observer using method described in section 5.3.3.1. (Note: * indicates statistically significant p-values.)

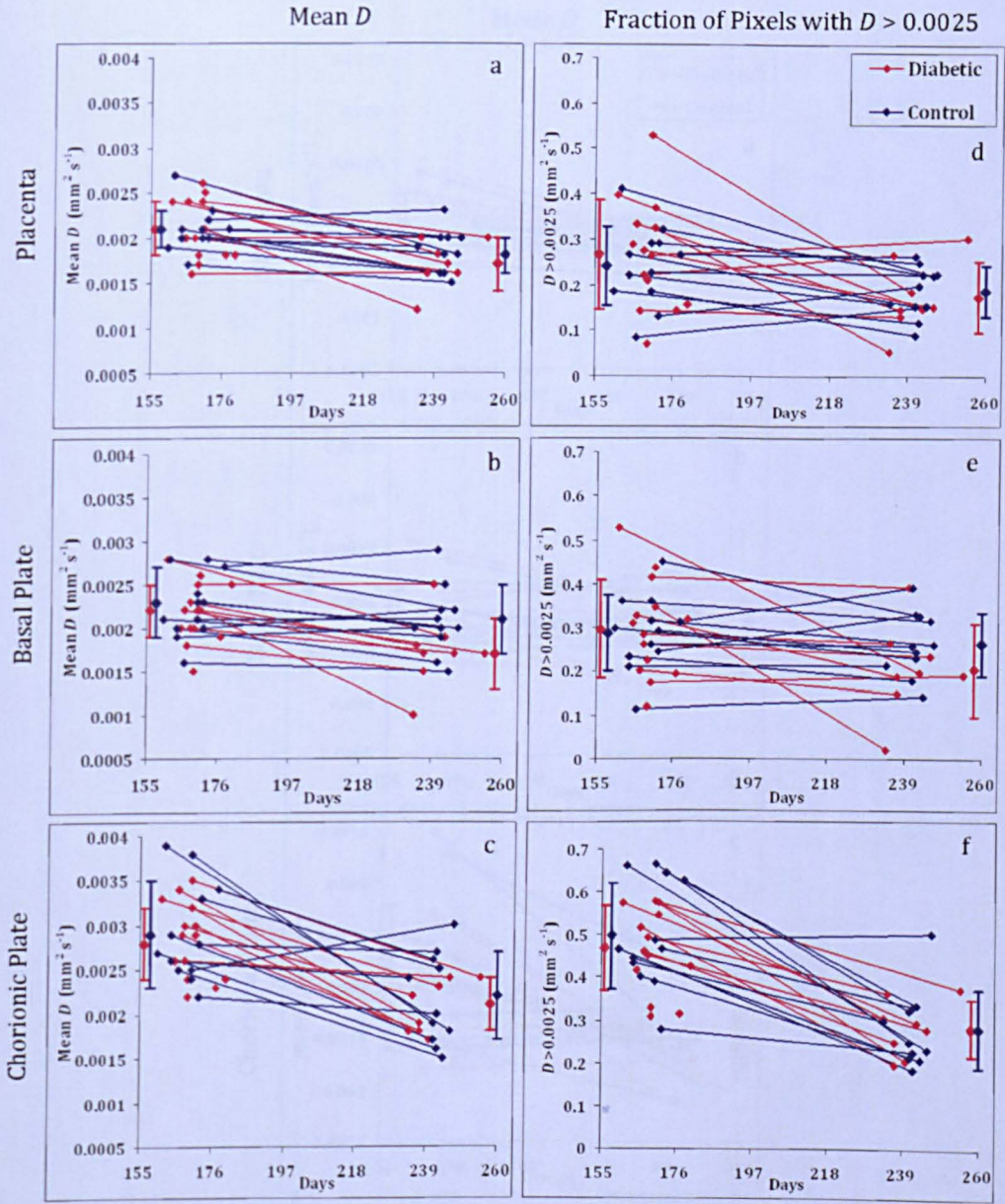


Figure 5.15: Scatter plot of the difference in mean D (a – c) and fraction of pixels with $D > 0.0025$ (d – f) of the whole placenta (a and d), basal plate (b and e) and chorionic plate (c and f) across two gestations for diabetic and control mothers. Marker lines are added allowing comparison of the two measurements for each individual subject. The mean value and the standard deviation are also displayed for the two groups on the left and right of the image [red – diabetic; blue – control].

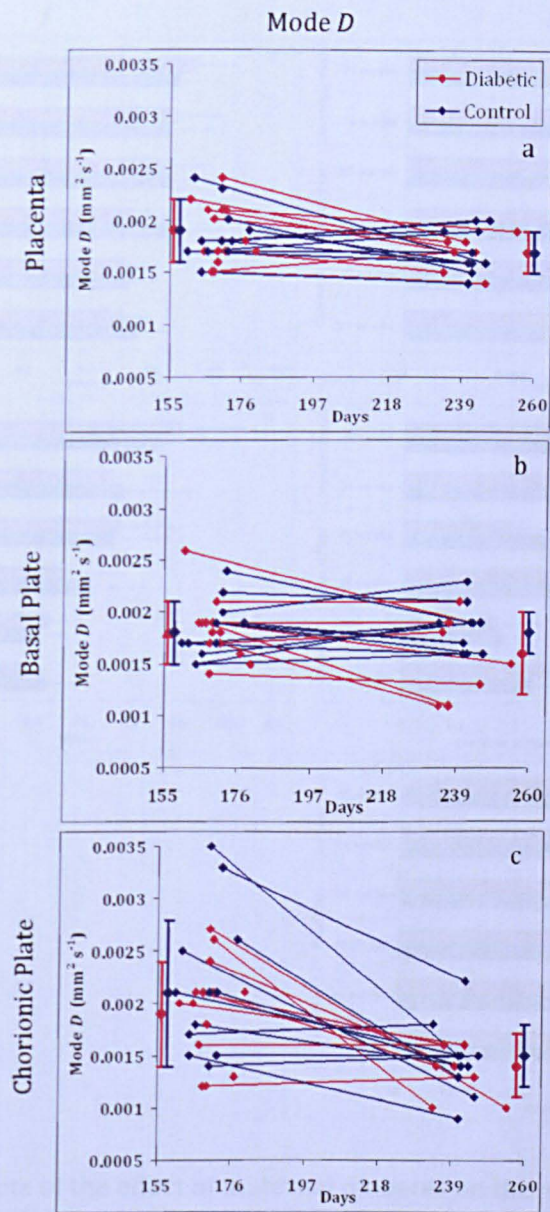


Figure 5.16: Scatter plot of the difference in mode D of the whole placenta (a), basal plate (b) and chorionic plate (c) across two gestations for diabetic and control mothers. Marker lines are added allowing comparison of the two measurements for each individual subject. The mean value and the standard deviation are also displayed for the two groups on the left and right of the image [red – diabetic; blue – control].



Figure 5.17: Boxplots of the effect of maternal diabetes on the mean and standard deviation of mean f (a), mode f (b), mean D (c), fraction of pixels with $D > 0.0025$ (d) and mode D (e) value of the whole placenta, basal plate and chorionic plate across two gestations for diabetic and control mothers [red – diabetic; blue – control].

As expected, the placental volume measurements demonstrated an increase from 411 cm^3 ($\text{SD} = 93 \text{ cm}^3$) to 805 cm^3 ($\text{SD} = 198 \text{ cm}^3$) in the controls and 459 cm^3 ($\text{SD} = 141 \text{ cm}^3$) to 800 cm^3 ($\text{SD} = 143 \text{ cm}^3$) in the diabetic group at 24 weeks and 35 weeks, respectively. However, there was no significant difference in the placenta volume between the groups at 24 weeks ($p = 0.374$) or 35 weeks ($p = 0.960$). Figure 5.18 demonstrates the placental volume across the two gestations in diabetic and non-diabetic pregnancies.

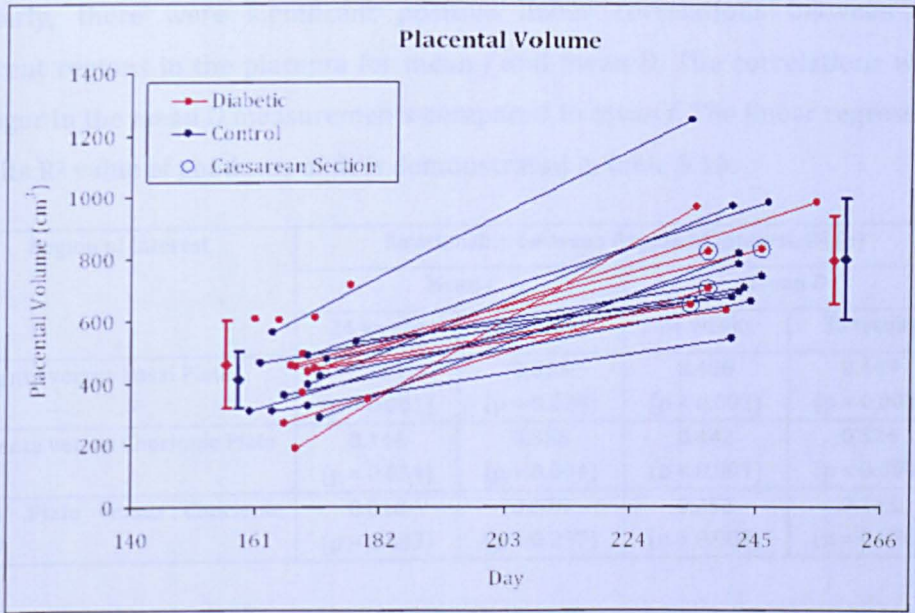


Figure 5.18: Scatter plot of the placental volume at two gestations for foetuses of diabetic and control mothers. Marker lines are added allowing comparison of the two measurements for each individual subject. The mean value and the standard deviation are also displayed for the two groups on the left and right of the image [red – diabetic; blue – control; open circles at 2nd time point: caesarean delivery].

5.4.2.4 Comparison of Mean *f* and Mean *D* Measurements

Direct comparison of the results obtained from mean *f* and mean *D* measurements in the placenta showed that mean *D* increases with increasing mean *f*. There were significant positive linear correlations between mean *f* and mean *D* for the placenta, basal plate and chorionic plate at both time points, with exception of the chorionic plate measurement at 35 weeks. The strongest correlation was between mean *f* and mean *D* measurement in the basal plate, followed by placenta at 35 weeks. These correlations are shown in table 5.9.

Region of Interest	Relationship between Mean <i>f</i> and Mean <i>D</i> , R ² (p)	
	24 weeks	35 weeks
Placenta	0.244 (p = 0.010)	0.463 (p = 0.001)
Basal Plate	0.359 (p = 0.001)	0.620 (p < 0.001)
Chorionic Plate	0.465 (p = 0.001)	0.088 (p = 0.141)

Table 5.9: Relationship between mean *f* and mean *D* for placenta, basal plate and chorionic plate: linear correlation statistics (R² value of the goodness of fit) together with the p values.

Similarly, there were significant positive linear correlations between the different regions in the placenta for mean f and mean D . The correlations were stronger in the mean D measurements compared to mean f . The linear regression with its R^2 value of goodness of fit is demonstrated in table 5.10.

Region of Interest	Relationship between Region of Interest, R^2 (p)			
	Mean f		Mean D	
	24 weeks	35 weeks	24 weeks	35 weeks
Placenta versus Basal Plate	0.381 (p = 0.001)	0.265 (p = 0.024)	0.488 (p < 0.001)	0.449 (p = 0.002)
Placenta versus Chorionic Plate	0.146 (p = 0.054)	0.388 (p = 0.004)	0.442 (p < 0.001)	0.524 (p < 0.001)
Basal Plate versus Chorionic Plate	0.010 (p = 0.633)	0.075 (p = 0.257)	0.252 (p = 0.009)	0.163 (p = 0.086)

Table 5.10: Relationship between region of interest for mean f and mean D : linear correlation statistics (R^2 value of the goodness of fit) together with the p values.

5.5 Discussion and Conclusion

The placenta is a unique foetal organ separating the foetal and maternal circulation. It plays a vital role in foetal development by conducting functional activities for most foetal organs (except central nervous system and locomotor apparatus) from its early development until birth [67]. The placental structure is large with a fetal vascular bed that comprises a tree-like network. A mature placenta is composed of a basal plate and chorionic plate that border the intervillous space. The basal plate is the region embedded into the maternal uterine wall, where the spiral arteries and veins are located, establishing the intimate relationship between blood flow in the fetal and maternal circulation in the intervillous space. Initially, the maternal spiral arteries are transformed into inelastic tubes, where the maternal blood spurts in a jet like manner through these vessels to produce the low pressure in the intervillous space. The jets of blood flow are dependent on placental structure [37]. The maternal and foetal blood is in close proximity, with the vascular villous tree projecting from the chorionic plate into the intervillous space [67].

The placentae of patients suffering from intrauterine growth restriction and maternal diabetes are often associated with abnormal placental perfusion. In

maternal diabetes, the placenta is often linked to increased villous volume histologically. However, studies have shown that there is no difference in fetoplacental angiogenesis in diabetic pregnancies with or without complications [68]. Hence, antenatal assessment of placental vascular function will be valuable in assessment of foetal well-being.

In recent years, non-invasive MRI has been acknowledged as a diagnostic tool in the study of the fetoplacental environment to improve the understanding of pathophysiological mechanisms [35; 69]. MRI employs ultrafast imaging sequences that can effectively suppress foetal motion artefacts without sedation. Moreover, it is capable of producing images with high tissue contrast that enables simultaneous visualisation of fetomaternal structure in larger field of view using the multiplanar reconstruction capabilities [69; 70; 71; 72; 73]. This is advantageous in imaging the placenta, uterine wall, amniotic fluid and foetus [35; 74; 75].

Placental MRI is normally conducted using T_1 and T_2 weighted sequences, with placental images appearing more informative in T_2 -weighted images with relatively higher signal intensity compared to T_1 -weighted images [35]. It is useful in the assessment and documentation of placental location, structure, perfusion and its alterations in compromised pregnancy [76]. In this study, we applied EPI to study placental perfusion in non-diabetic and diabetic pregnancy. EPI can be conducted in a short imaging time, allowing the whole scanning procedure to be quick and comfortable for the patient.

All the data acquired using EPI were analysed based on the IVIM technique. Standard image registration could not be applied to the acquired data due to several factors: (1) dramatic change in image contrast with increasing diffusion parameter (b), (2) non-rigid body distortion of the abdomen in general and the placenta which is relatively amorphous in shape and very distortable, unlike other organs (eg: brain, kidney and liver) where image registration has been possible and (3) separate movement of the mother and foetus. So, a pragmatic approach was taken (as discussed in section 5.3.3.1). Ideally, the placental image could be manually segmented for each acquisition and each outlined ROI could be co-registered together. Unfortunately, this would be very time consuming and additional work is required to understand how manual outline of the high b -value ROIs relate to the outline of low b -value ROIs.

5.5.1 Reliability and Reproducibility of the IVIM Program

Prior to applying the IVIM program to study the effect of maternal diabetes on placental blood flow, the program was tested for reliability and reproducibility of the perfusion measurements based on the fraction of moving blood (f) within the placenta. This study was conducted due to lack of published literature exploring the reliability of MRI perfusion measurements. The average blood flow distribution (mean f), high blood flow region associated with upper end of the flow distribution (fraction of pixels with $f > 0.8$) and peak blood flow (mode f) were investigated, since preliminary work suggested that there were difference in these elements between the non-diabetic and diabetic placentae [77]. Moreover, it has been published [51] that perfusion factor (f) and apparent diffusion coefficient (D) results are more reproducible compared to pseudo-diffusion coefficient (D^*). It has previously been reported that five acquisitions of placental data are required to achieve results with 15% confidence for the SNR achievable at 0.5 T [51]. However, this should be explored again at 1.5 T in future studies.

The data showed that mean and mode f were more reliable parameters for placental perfusion assessment compared to fraction of pixels with $f > 0.8$. The LOA for fraction of pixels with $f > 0.8$ were also wider and the ICCs demonstrated poor reliability. This is possibly because regions with high blood flow may include data points affected by noise and physiological variation (maternal and foetal heart rate along with maternal breathing). For this reason, the subsequent reliability studies were conducted based on mean and mode f measurements. Overall, observer 1 showed the best intra-observer reliability with narrowest LOA. This is reasonable since observer 1 had significantly more experience in examining the placental images acquired using PGSE sequence and conducting placental perfusion analysis on the IVIM program. However, the LOA of the measurements made by other observers were not too discrepant, suggesting that the reliability could be improved with possible further training. It is also important to note that the LOA were wider for all observers for basal plate and chorionic plate. The ROI of basal plate and chorionic plate were small, mostly five to six voxels in depth in the MRI images. Hence, movements along these plates

could cause errors in the perfusion measurement in these regions and is a possible explanation for the lower degrees of reliability seen.

The inter-observer reliability test showed narrower range of LOA for mode and mean f compared to the fraction of pixels with $f > 0.8$ of the placenta at both 24 weeks and 35 weeks. The LOA were generally wider at 35 weeks, suggesting less reliability at this gestation. This may be because the placental images appear much darker and more distorted at 35 weeks compared to 24 weeks, making ROI masking more difficult at 35 weeks. In comparison to a reliability test conducted on renal perfusion measurement that demonstrated a coefficient of variance of 42% for mean f [78], the inter-observer reliability of mean and mode f showed a better reliability at $\pm 5\%$ and $\pm 9\%$ for the placenta, $\pm 15\%$ and $\pm 23\%$ for the basal plate and $\pm 15\%$ and $\pm 30\%$ for the chorionic plate, respectively. As for measurements of fraction of pixels with $f > 0.8$, the inter-observer reliability was reduced with LOA closer to $\pm 100\%$.

Both single and multiple masking methods showed good intra-observer reliability. While the single masking method demonstrated better ICCs and narrower LOA compared to multiple masking method, the inter-method comparison demonstrated reasonably narrow LOA, with narrowest LOA for the placenta. As expected, the LOA were wider in the basal plate and chorionic plate since the slightest movement in the abdomen can compromise the placental perfusion measurements in these regions. While multiple masking method is more reliable in measuring placental perfusion in the basal plate and chorionic plate since it involves drawing the ROIs on each repeat separately, overcoming motion issues within this region, multiple masking method is time inefficient and prone to human error. Therefore, single masking method was employed in this study.

A similar trend was seen for slice-by-slice comparison, with mean and mode f measurement demonstrating the best LOA for the placenta, followed by the basal plate and then chorionic plate. In this study, 5 slices of 7 mm thickness with an 18 mm slice gap were acquired. As observed, poorer reliability is expected in the chorionic plate since the vessels spread out from the cord and their distribution may vary greatly across the surface of the placenta, resulting in different perfusion measurements. These results give an indication as to how sensitive the results are to the positioning of slice by the radiographer. One major limitation in

the reliability and reproducibility study is the small number of data included in this test (data of 5 subjects scanned at 24 weeks and 35 weeks) and further subjects would strengthen the findings.

To conclude, IVIM provides a robust method for studying the unique physiology of the placenta. Its intervillous space filled with voluminous maternal blood increases the sensitivity of the PGSE sequence to f and D . These parameters provide reliable information to study the in-vivo hemodynamic environment of the placenta. Strategically, since the reliability of f has been investigated, reliability of D should also be investigated in future.

5.5.2 The Application of the IVIM Program to Study the Effect of Maternal Diabetes on Placental Blood Flow

There were no significant differences in the mean f measurements of the placenta, basal plate and chorionic plate across gestation or between the two groups, whereas, the mode f demonstrated significant increase in the peak blood flow in the chorionic plate and basal plate across gestation. This may be because pixels with very large values of f create noise in the mean f , which does not propagate into the mode f . The blood flow is expected to increase in the chorionic plate as the foetus grows. This is an adaptation to sustain foetal growth. Our finding agrees with this expectation and it is the first study attempting to measure chorionic plate flow, which has a potential to provide valuable information to study pregnancy complicated by placental vascular dysfunction, such as is the case in foetal growth restriction. Similarly, the blood flow in the basal plate (representing spiral artery blood flow) is also expected to increase to sustain growing foetus and maintain blood flow in the growing placentae. Conversely, the lack of change in placental blood flow is anticipated since the placenta grows with gestation, increasing the area for feto-maternal exchange but the perfusion per unit volume is likely to be optimised for exchange throughout pregnancy.

Blood flow is generally expected to be greater in larger blood vessels; for instance, flow in the spiral arteries in the basal plate is likely to physiologically

vary across gestation, as indicated by mean f and fraction of pixels with $f > 0.8$, compared to mode f . The high variability in f may be a useful biomarker in future data analysis. The mode f was generally higher in the control group at 24 weeks, but at 35 weeks, mode f was usually higher in diabetic subjects. This result may be a statistical fluke but could also indicate adaptation to large foetal demands (macrosomic foetuses).

The IVIM measurements of D showed striking and significant decrease across gestation for the placenta, basal plate and chorionic plate with a trend for D to be higher in the control group for the basal plate and chorionic plate. However, there was no significant difference in these measurements between diabetic and control groups. The value D is related to molecular mobility of water. This depends on physical characteristics of the tissue such as cell size and membrane permeability that affects the random Brownian motion of water within the placenta [37].

Studies have suggested a significant increase in the villous tissue in the placenta across gestation [79; 80; 81]. Therefore, increased villous branching could increase tissue density and hence, decrease effective mean free path of blood movement within the intervillous space. This would result in dephasing of the IVIM signal and hence, reduced D . In comparison to normal placentae, there is evidence of more voluminous foetal capillary beds with greater diameter, length and surface area in the diabetic placentae [19]. Moreover, studies have reported evidence of fibrinoid necrosis and atherosclerosis in the decidual bed of diabetic placentae [82], that could possibly be the cause of even shorter diffusion distance within the diabetic placentae. This could explain our findings that show a more pronounced decrease in the D of the diabetic placentae. Histological examination of the placentae of these subjects after birth and correlation to the MRI findings would strengthen the findings of this study and is a limitation of this work.

In the chorionic plate, the blood vessels are expected to expand with increasing placental size to sustain the needs of the growing foetus. So, the blood vessels per unit volume are expected to decrease, which might result in decreased D since blood has greater diffusion coefficient from the tissue. In the basal plate region, the spiral arteries are expected to open wider with increasing gestation allowing blood flow to increase across gestation, possibly causing diffusion to increase across gestation. However, the data here indicates that diffusion in this region

decreases with gestation. It is important to note that the D measurement can be contaminated by flow due to data points used for the IVIM fitting, and additional methods of acquiring and fitting the data should be used to investigate this.

Direct comparison of the mean f and mean D measurements showed that there was significant positive correlation between these two measurements, suggesting mean D increases with mean f in the placenta, basal plate and chorionic plate regardless of the gestational stage; the strongest correlation was in basal plate at 35 weeks. There was also a significant positive correlation between the mean f and mean D measurements between the different regions of the placenta. However, these correlations were not strong and the statistical analysis may be misleading since it looks for an association between measurements rather than agreement. It does not take into account any systematic bias between two elements. Moreover all these measurement points were not evenly scattered. Future work using simulations could investigate whether such correlations will arise due to biases in the fitting process.

Foetal growth depends on two factors: the foetal nutrient demand and maternal-placental supply. These factors are related to placental size, utero-placental blood flow and placenta's transfer capabilities. If the maternal-placental supply is less than the demand, the foetus adapts by increasing the placental size in order to achieve sufficient nutrient supply [83] and hence, the increase in placental weight. The MR measurements of placental volume in this study indicated that there was no significant difference between the diabetic and control groups. Nonetheless, several studies have documented an increase in the placental size, placental weights [84; 85] and placental ratios [86] (placental weight to birth weight) in pregnancies complicated by gestational diabetes to sustain the large demands of macrosomic fetuses [21; 83]. With this understanding, it would be tempting to speculate that increased placental weight, with a lack of change in placental volume in diabetic pregnancies explains the mechanism of decreased D and increased f (due to increased resistance following villous branching) in diabetic placentae, since tissue will be denser and blood must flow faster to percolate through the diabetic placentae. However, this speculation may be fictitious since Clarson et al. [87] reported that there was no difference in the placental weight of diabetic and normal pregnancies.

Whilst this work presents a novel technique for placental perfusion and diffusion measurements, there are three major problems. Firstly, from the reliability assessment, differences between intra and inter-observer variability (where latter was calculated based on first set of intra-observer variability results) indicates an effect of fatigue in the intra-observer results even though analysis was conducted in a period of several days and was blinded to gestational age, maternal BMI, diabetic status, complications of pregnancy, other observers' results and observer's own previous measurement results. Moreover, variability between slices (measured by one observer: the author) was more than the intra-observer variability indicating that variability was not due to errors in drawing the ROI. To determine whether this variability is due to biological variability or variation between slices, repeated measurements need to be compared.

Secondly, the f and D measurements for basal plate and chorionic plate regions are made from ROIs of only five to six voxel in depth in the placental images acquired using PGSE sequence. In reality the placenta has no clear-cut margins and we are, in essence, speculating where the basal plate and chorionic plate are located for the purpose of data analysis. Moreover, even though the IVIM program was modified to identify and exclude images corrupted by excessive movement and artefact (data points lying more than 2 standard deviations), these regions are prone to be affected by tissue movement due to breathing and foetal movement.

Thirdly, 2-dimensional images of the placenta were acquired for this study, while the placenta is actually a 3-dimensional organ. Although the sampling of the placenta was predetermined before the study, with the radiographer required to image the central slice closest to the cord insertion transversely, it raises the question as to how representative the imaged placental region is to the entire placental volume. Five slices of 7 mm thickness with 18 mm slice gap were acquired in this study. A comparison of the measurements between the central slice and a peripheral slice demonstrated a decrease in the f measurement in the peripheral slices. Whilst this was not statistically significant in the small data set (5 subjects scanned at 24 weeks and 35 weeks), one should consider performing a 3D acquisition and analysis of the placenta in order to overcome concerns about the representativeness of the analysed area.

At present, the ROI of each acquisition is fitted individually before averaging the histogram of the five acquisitions to measure f and D . Whilst this method is more time efficient than the multiple masking method, ideally the data analysis could be improved by fitting a different ROI for all the five acquisition. Alternatively, signals could be averaged over the ROI's pixel in five acquisitions together before fitting the ROI into the signal attenuation equation (Eq 5.1). This would reduce the processing time and average out the movement or noise in the ROI for all the acquisitions.

Future work will correlate MR measures with maternal levels of hyperglycemia and will further investigate the use of the IVIM model in the placenta, basal plate and chorionic plate to understand how changes in flow and diffusion may affect the modelled parameters: f , D and D^* . This work provides a novel technique that has a potential to be employed as a clinical and research tool to study the development of placental perfusion and diffusion in pregnancies complicated by maternal diabetes, IUGR and pre-eclampsia. It will also be useful in assisting obstetricians to understand the functionality of placenta in normal pregnancy.

5.6 References

- [1] M. Panigel, A.E. James Jr, M. Siegel, and M.W. Donner. (1975), Radionuclide and angiographic studies of placental circulation in man and rhesus monkey. *European Journal of Obstetrics & Gynecology and Reproductive Biology* **5** 251-262.
- [2] K. Kaauaaaur, P. Jouppila, J. Kuikka, H. Luotola, J. Toivanen, and A. Rekonen. (1980), Intervillous Blood Flow in Normal and Complicated Late Pregnancy Measured by Means of an Intravenous ¹³³Xe Method. *Acta Obstetricia et Gynecologica Scandinavica* **59** 7-10.
- [3] A. Rekonen, H. Luotola, M. Pitkanen, J. Kuikka, and T. Pyorala. (1976), Measurement of Intervillous and Myometrial Blood Flow by an Intravenous ¹³³Xe Method *BJOG: An International Journal of Obstetrics & Gynaecology* **83** 723-728.
- [4] J.A. Clavero, J. Negueruela, L. Ortiz, J.A. De los Heros, and S.P. Modrego. (1973), Blood flow in the intervillous space and fetal blood flow. *American Journal of Obstetrics and Gynecology* **116** 340-346.
- [5] N.S. Assali, L. Rauramo, and T. Peltonen. (1960), Measurement of uterine blood flow and uterine metabolism. *American Journal of Obstetrics and Gynecology* **79** 86-98.
- [6] M. Åkerlund, L.P. Bengtsson, and A.M. Carter. (1975), A Technique for Monitoring Endometrial or Decidual Blood flow with an Intra-Uterine Thermistor Probe. *Acta Obstetricia et Gynecologica Scandinavica* **54** 469-477.
- [7] K.R. Duncan, P. Gowland, S. Francis, R. Moore, P.N. Baker, and I.R. Johnson. (1998), The investigation of placental relaxation and estimation of placental perfusion using echo-planar magnetic resonance imaging. *Placenta* **19** 539-543.
- [8] N.O. Lunell, B. Sarby, R. Lewander, and L. Nylund. (1979), Comparison of uteroplacental blood flow in normal and in intrauterine growth-retarded pregnancy. Measurements with Indium-113m and a computer-linked gammacamera. *Gynecologic and obstetric investigation* **10** 106-18.
- [9] S.S. Ong, D.J. Tyler, R.J. Moore, P.A. Gowland, P.N. Baker, I.R. Johnson, and T.M. Mayhew. (2004), Functional Magnetic Resonance Imaging (Magnetization Transfer) and Stereological Analysis of Human Placentae in Normal

- Pregnancy and in Pre-eclampsia and Intrauterine Growth Restriction. *Placenta* **25** 408-412.
- [10] D.J. Roberts, and M.D. Post. (2008), The placenta in pre-eclampsia and intrauterine growth restriction. *Journal of Clinical Pathology* **61** 1254-1260.
- [11] V.A. Rodie. (2006), Pre-eclampsia and eclampsia: pathophysiology and treatment options. *Revista Brasileira De Hipertensao* **13** 88 - 95.
- [12] M. Damodaram, L. Story, E. Eixarch, A. Patel, A. McGuinness, J. Allsop, J. Wyatt-Ashmead, S. Kumar, and M. Rutherford. Placental MRI in Intrauterine Fetal Growth Restriction. *Placenta* **31** 491-498.
- [13] S.T. Francis, K.R. Duncan, R.J. Moore, P.N. Baker, I.R. Johnson, and P.A. Gowland. (1998), Non-invasive mapping of placental perfusion. *The Lancet* **351** 1397-1399.
- [14] S. Sankaran, and P.M. Kyle. (2009), Aetiology and Pathogenesis of IUGR. *Best Practice & Research Clinical Obstetrics & Gynaecology* **23** 765-777.
- [15] C. Guiot, P. Gaglioti, M. Oberto, E. Piccoli, R. Rosato, and T. Todros. (2008), Is three-dimensional power Doppler ultrasound useful in the assessment of placental perfusion in normal and growth-restricted pregnancies? *Ultrasound in Obstetrics & Gynecology* **31** 171-176.
- [16] G. Desoye, and S. Hauguel-de Mouzon. (2007), The Human Placenta in Gestational Diabetes Mellitus. *Diabetes Care* **30** S120-S126.
- [17] O. Björk, and B. Persson. (1984), Villous structure in different parts of the cotyledon in placentas of insulin-dependent diabetic women. *Acta Obstetricia et Gynecologica Scandinavica* **63** 37-43.
- [18] M.R. Jackson, T.M. Mayhew, and P.A. Boyd. (1992), Quantitative description of the elaboration and maturation of villi from 10 weeks of gestation to term. *Placenta* **13** 357-370.
- [19] T.M. Mayhew, F.B. Sorensen, J.G. Klebe, and M.R. Jackson. (1994), Growth and maturation of villi in placentae from well-controlled diabetic women. *Placenta* **15** 57-65.
- [20] T.M. Mayhew, and I. Sisley. (1998), Quantitative studies on the villi, trophoblast and intervillous pores of placentae from women with well-controlled diabetes mellitus. *Placenta* **19** 371-377.
- [21] G. Desoye, and L. Myatt. (2004), *The placenta*, Lippincott Williams & Wilkins, Philadelphia.

- [22] T.W. Sadler. (2006), *Langman's Medical Embryology*, Lippincott Williams & Wilkins, Pennsylvania, USA.
- [23] T.M. Mayhew. (2002), Fetoplacental Angiogenesis During Gestation is Biphasic, Longitudinal and Occurs by Proliferation and Remodelling of Vascular Endothelial Cells. *Placenta* **23** 742-750.
- [24] P. Kaufmann, T.M. Mayhew, and D.S. Charnock-Jones. (2004), Aspects of human fetoplacental vasculogenesis and angiogenesis. II. Changes during normal pregnancy, Elsevier, Kidlington, ROYAUME-UNI.
- [25] H. Pairleitner, H. Steiner, G. Hasenoehrl, and A. Staudach. (1999), Three-dimensional power Doppler sonography: imaging and quantifying blood flow and vascularization. *Ultrasound in Obstetrics and Gynecology* **14** 139-143.
- [26] J. Noguchi, K. Hata, H. Tanaka, and T. Hata. (2009), Placental Vascular Sonobiopsy Using Three-dimensional Power Doppler Ultrasound in Normal and Growth Restricted Fetuses. *Placenta* **30** 391-397.
- [27] J. Rubin, R. Adler, J. Fowlkes, S. Spratt, J. Pallister, J. Chen, and P. Carson. (1995), Fractional moving blood volume: estimation with power Doppler US. *Radiology* **197** 183-190.
- [28] H. Weskott. (1997), Amplitude Doppler US: slow blood flow detection tested with a flow phantom. . *Radiology* **202** 125-130.
- [29] R.O. Bude, and J.M. Rubin. (1996), Power Doppler sonography. *Radiology* **200** 21-3.
- [30] C.B. Meyerowitz, A.C. Fleischer, D.R. Pickens, G.B. Thurman, A.D. Borowsky, G. Thirsk, and C.G. Hellerqvist. (1996), Quantification of tumor vascularity and flow with amplitude color Doppler sonography in an experimental model: preliminary results. *Journal of Ultrasound in Medicine* **15** 827-33.
- [31] J.M. Rubin, R.O. Bude, P.L. Carson, R.L. Bree, and R.S. Adler. (1994), Power Doppler US: a potentially useful alternative to mean frequency-based color Doppler US. *Radiology* **190** 853-856.
- [32] Z. Guo, and A. Fenster. (1996), Three-dimensional power Doppler imaging: A phantom study to quantify vessel stenosis. *Ultrasound in Medicine & Biology* **22** 1059-1069.
- [33] D. Levine, and R.R. Edelman. (1997), Fast MRI and its application in obstetrics. *Abdominal Imaging* **22** 589-596.
- [34] C. Garel, H. Brisse, G. Sebag, M. Elmaleh, J.-F. Oury, and M. Hassan. (1998), Magnetic resonance imaging of the fetus. *Pediatric Radiology* **28** 201-211.

- [35] P. Gowland. (2005), Placental MRI. *Seminars in Fetal and Neonatal Medicine* **10** 485-490.
- [36] S. Wolff, L.E. Crooks, P. Brown, R. Howard, and R.B. Painter. (1980), Tests for DNA and chromosomal damage induced by nuclear magnetic resonance imaging. *Radiology* **136** 707-710.
- [37] R.J. Moore, B.K. Strachan, D.J. Tyler, K.R. Duncan, P.N. Baker, B.S. Worthington, I.R. Johnson, and P.A. Gowland. (2000), In utero Perfusing Fraction Maps in Normal and Growth Restricted Pregnancy Measured Using IVIM Echo-Planar MRI. *Placenta* **21** 726-732.
- [38] P.N. Baker, I.R. Johnson, P.R. Harvey, P.A. Gowland, and P. Mansfield. (1994), A three-year follow-up of children imaged in utero with echo-planar magnetic resonance. *American Journal of Obstetrics and Gynecology* **170** 32-3.
- [39] P. Mansfield, M.K. Stehling, R.J. Ordidge, R. Coxon, B. Chapman, A. Blamire, P. Gibbs, I.R. Johnson, E.M. Symonds, B.S. Worthington, and R.E. Coupland. (1990), Echo planar imaging of the human fetus in utero at 0.5 T. *British Journal of Radiology* **63** 833-841.
- [40] A. Reid, F.W. Smith, and J.M. Hutchison. (1982), Nuclear magnetic resonance imaging and its safety implications: follow-up of 181 patients. *The British journal of radiology* **55** 784-6.
- [41] F.W. Smith, A.H. Adam, and W.D. Phillips. (1983), NMR imaging in pregnancy. *Lancet* **1** 61-2.
- [42] D. Levine, H. Hatabu, J. Gaa, M.W. Atkinson, and R.R. Edelman. (1996), Fetal anatomy revealed with fast MR sequences. *Am. J. Roentgenol.* **167** 905-908.
- [43] D. Prayer, P.C. Brugger, and L. Prayer. (2004), Fetal MRI: techniques and protocols. *Pediatric Radiology* **34** 685-693.
- [44] D. Pugash, P.C. Brugger, D. Bettelheim, and D. Prayer. (2008), Prenatal ultrasound and fetal MRI: The comparative value of each modality in prenatal diagnosis. *European Journal of Radiology* **68** 214-226.
- [45] Y. Yamashita, T. Namimoto, Y. Abe, M. Takahashi, J. Iwamasa, K. Miyazaki, and H. Okamura. (1997), MR imaging of the fetus by a HASTE sequence. *American Journal of Roentgenology* **168** 513-9.
- [46] L.M. Lan, Y. Yamashita, Y. Tang, T. Sugahara, M. Takahashi, T. Ohba, and H. Okamura. (2000), Normal Fetal Brain Development: MR Imaging with a

- Half-Fourier Rapid Acquisition with Relaxation Enhancement Sequence1. Radiology **215** 205-210.
- [47] Cornelia F Hagmann, Nicola J. Robertson, Wee C. Leung, Kling W. Chong, and L.S. Chitty. (2008), Foetal brain imaging: ultrasound or MRI. A comparison between magnetic resonance imaging and a dedicated multidisciplinary neurosonographic opinion. *Acta Pædiatrica* **97** 414-419.
- [48] Powell, C. M, Buckley, J, Price, H, Worthington, S. B, Symonds, and M. E. (1986), Magnetic resonance imaging and placenta previa, Elsevier, New York, NY, ETATS-UNIS.
- [49] P.N. Baker, I.R. Johnson, P.A. Gowland, J. Hykin, V. Adams, P. Mansfield, and B.S. Worthington. (1995), Measurement of fetal liver, brain and placental volumes with echo-planar magnetic resonance imaging. *BJOG: An International Journal of Obstetrics & Gynaecology* **102** 35-39.
- [50] J. Bodis, K. Zambo, Z. Nemessanyi, E. Mate, and I.F. Csaba. (1985), Application of the parametric scan in the investigation of uteroplacental blood flow. *European Journal of Nuclear Medicine and Molecular Imaging* **10** 286-287.
- [51] P.A. Gowland, S.T. Francis, K.R. Duncan, A.J. Freeman, B. Issa, R.J. Moore, R.W. Bowtell, P.N. Baker, I.R. Johnson, and B.S. Worthington. (1998), In vivo perfusion measurements in the human placenta using echo planar imaging at 0.5 T. *Magnetic Resonance in Medicine* **40** 467-473.
- [52] E.L. Hahn. (1950), Spin Echoes. *Physical Review* **80** 580-594.
- [53] E.O. Stejskal, and J.E. Tanner. (1965), Spin Diffusion Measurements: Spin Echoes in the Presence of a Time-Dependent Field Gradient. *Journal of Chemical Physics* **42** 288-292.
- [54] J.J. Neil, C.S. Bosch, and J.J.H. Ackerman. (1994), An evaluation of the sensitivity of the intravoxel incoherent motion (IVIM) method of blood flow measurement to changes in cerebral blood flow. *Magnetic Resonance in Medicine* **32** 60-65.
- [55] R. Turner, D. Le Bihan, and A. Scott Chesnicks. (1991), Echo-planar imaging of diffusion and perfusion. *Magnetic Resonance in Medicine* **19** 247-253.
- [56] D. Le Bihan, E. Breton, D. Lallemand, P. Crenier, M.E. Cabanis, and Laval-Jedntet. (1986), MR imaging of intravoxel incoherent motions: application to diffusion and perfusion in neurological disorders. *Radiology* **161** 401-407.

- [57] D. Le Bihan. (1991), Molecular diffusion nuclear magnetic resonance imaging. *Magnetic resonance quarterly* **7** 1-30.
- [58] J.M. Rachel. (May 2001), The Application of Magnetic Resonance Imaging to Obstetrics. in "Physics and Astronomy", University of Nottingham, Nottingham.
- [59] R.J. Moore, B. Issa, P. Tokarczuk, K.R. Duncan, P. Boulby, P.N. Baker, R.W. Bowtell, B.S. Worthington, I.R. Johnson, and P.A. Gowland. (2000), In vivo intravoxel incoherent motion measurements in the human placenta using echo-planar imaging at 0.5 T. *Magnetic Resonance in Medicine* **43** 295-302.
- [60] J.W. Bartlett, and C. Frost. (2008), Reliability, repeatability and reproducibility: analysis of measurement errors in continuous variables. *Ultrasound in Obstetrics and Gynecology* **31** 466-475.
- [61] N. Patton, T. Aslam, and G. Murray. (2005), Statistical strategies to assess reliability in ophthalmology. *Eye* **20** 749-754.
- [62] A.M. Euser, F.W. Dekker, and S. le Cessie. (2008), A practical approach to Bland-Altman plots and variation coefficients for log transformed variables. *Journal of Clinical Epidemiology* **61** 978-982.
- [63] G. Rankin, and M. Stokes. (1998), Reliability of assessment tools in rehabilitation: an illustration of appropriate statistical analyses. *Clinical Rehabilitation* **12** 187-199.
- [64] K.O. McGraw, and S.P. Wong. (1996), Forming inferences about some intraclass correlation coefficients. *Psychological Methods; Psychological Methods* **1** 30-46.
- [65] J.M. Bland, and D.G. Altman. (1990), A note on the use of the intraclass correlation coefficient in the evaluation of agreement between two methods of measurement. *Computers in Biology and Medicine* **20** 337-340.
- [66] J.M. Bland, and D.G. Altman. (2010), Statistical methods for assessing agreement between two methods of clinical measurement. *International Journal of Nursing Studies* **47** 931-936.
- [67] K. Benirschke, and P. Kaufmann. (2000), *Pathology of the Human Placenta*, Springer, New York.
- [68] T.M. Mayhew. (2002), Enhanced fetoplacental angiogenesis in pre-gestational diabetes mellitus: the extra growth is exclusively longitudinal

- and not accompanied by microvascular remodelling. *Diabetologia* **45** 1434-1439.
- [69] W. Blaicher, P.C. Brugger, C. Mittermayer, J. Schwindt, J. Deutinger, G. Bernaschek, and D. Prayer. (2006), Magnetic resonance imaging of the normal placenta. *European Journal of Radiology* **57** 256-260.
- [70] N. Girard, C. Gire, S. Sigaudy, G. Porcu, C. d'Ercole, D. Figarella-Branger, C. Raybaud, and S. Confort-Gouny. (2003), MR imaging of acquired fetal brain disorders. *Child's Nervous System* **19** 490-500.
- [71] C. Raybaud, O. Levrier, H. Brunel, N. Girard, and P. Farnarier. (2003), MR imaging of fetal brain malformations. *Child's Nervous System* **19** 455-470.
- [72] T. Huisman, E. Martin, R. Kubik-Huch, and B. Marincek. (2002), Fetal magnetic resonance imaging of the brain: technical considerations and normal brain development. *European Radiology* **12** 1941-1951.
- [73] R.A. Kubik-Huch, T.A. Huisman, J. Wisser, N. Gottstein-Aalame, J.F. Debatin, B. Seifert, M.E. Ladd, T. Stallmach, and B. Marincek. (2000), Ultrafast MR imaging of the fetus. *AJR. American journal of roentgenology* **174** 1599-606.
- [74] B. Ertl-Wagner, A. Lienemann, A. Strauss, and M. Reiser. (2002), Fetal magnetic imaging: indications, technique, anatomical considerations and a review of fetal abnormalities. *European Radiology* **12** 1931-1940.
- [75] W.D. Murphy, D.H. Feiglin, C.C. Cisar, A.M. Al-Malt, and E.M. Bellon. (1990), Magnetic resonance imaging of a third trimester abdominal pregnancy. *Magnetic Resonance Imaging* **8** 657-659.
- [76] D. Prayer. (2011), *Fetal MRI*, Springer.
- [77] D. Anblagan, R. Deshpande, N.W. Jones, C. Costigan, N.R. Fenning, P. Mansell, G. Bugg, L. Leach, and P.A. Gowland. (2010), The Effect of Maternal Diabetes on Placental Blood Flow Assessed Using IVIM. in "International Society for Magnetic Resonance in Medicine 19th Annual Meeting & Exhibition", Montreal, Canada.
- [78] M.F. Muller, P.V. Prasad, and R.R. Edelman. (1998), Can the IVIM model be used for renal perfusion imaging? *European Journal of Radiology* **26** 297-303.
- [79] T. Francois. (1983), Histomorphometry of the human placenta in class B diabetes mellitus. *Placenta* **4** 1-12.

- [80] T. Francois. (1981), Histomorphometry of the placenta of the diabetic woman: Class A diabetes mellitus. *Placenta* **2** 241-251.
- [81] T. Francois. (1985), Histomorphometry of the human placenta in class C diabetes mellitus. *Placenta* **6** 69-81.
- [82] E.A. Reece, D.R. Coustan, and S.G. Gabbe. (2004), *Diabetes in Women*, Lippincott Williams and Wilkins, Philadelphia.
- [83] E. Taricco, T. Radaelli, M.S. Nobile de Santis, and I. Cetin. (2003), Foetal and Placental Weights in Relation to Maternal Characteristics in Gestational Diabetes. *Placenta* **24** 343-347.
- [84] M. Winick, and A. Noble. (1967), Cellular growth in human placenta: II. Diabetes mellitus. *The Journal of Pediatrics* **71** 216-219.
- [85] N. Richard L. (1987), Do placental weights have clinical significance? *Human Pathology* **18** 387-391.
- [86] T.T. Lao, C.P. Lee, and W.M. Wong. (1997), Placental weight to birthweight ratio is increased in mild gestational glucose intolerance. *Placenta* **18** 227-230.
- [87] C. Clarson, G.J.M. Tevaarwerk, P.G.R. Harding, G.W. Chance, and M. Daria Haust. (1989), Placental weight in diabetic pregnancies. *Placenta* **10** 275-281.

Chapter 6

The Effect of Maternal Diabetes on Foetal Adiposity

6.1 Overview

The chapter starts with a short literature review detailing the effect of maternal diabetes on foetal growth and the adverse outcome in these pregnancies, namely macrosomia (foetuses considered large for their gestational age). For this reason, the ability to detect foetal adiposity is highly desirable to make prenatal diagnosis and expedite delivery or pre-arrange caesarean section for foetuses in compromised pregnancies. Here, the author describes the present ultrasound techniques available to identify foetuses exposed to the risk of macrosomia before birth. Following these discussions, the chapter will progress to detail the techniques applied by the author to acquire, process and estimate foetal adiposity using MRI sequence and MATLAB codes developed by the author with the guidance of Professor Penny Gowland.

This chapter is divided into two sections. The first part aims to investigate the reliability and reproducibility of the measurements of foetal adiposity using the MATLAB program. The author, with the help of three other observers, Professor Penny Gowland, Dr Nia Wyn Jones and Dr Ruta Deshpande, conducted the data analysis for the reliability tests. The second part demonstrates the application of the foetal adiposity measuring technique to study the effect of maternal diabetes on foetal adiposity. The author will address the methods used to acquire, process and statistically analyse foetal adiposity. In addition, the author with the help of Kirsty Allcock, a medical student at the University of Nottingham, conducted other data analyses such as measurement of shoulder width, foetal length, placental (reported in Chapter 5) and foetal volume to demonstrate the effect of

maternal diabetes on foetal growth. Finally, the chapter is concluded by demonstration and discussion of the results obtained from analysing the data of both the non-diabetic control and diabetic patients involved in this study (the same group of patients as in chapter 5).

6.2 Introduction

Pregnancy complicated by diabetes, either pre-existing or diagnosed during gestation, often results in macrosomic infants with increased body fat [1; 2; 3]. These infants usually have abnormally broader shoulders that expose them to an increased risk of shoulder dystocia [4; 5] and brachial plexus injury, which may be permanent. They are also exposed to the risk of clavicular and humeral fracture, hypoxic brain damage, birth asphyxia, hypoglycemia and foetal death. These infants often suffer prolonged labour that may require caesarean section delivery [6; 7; 8; 9; 10; 11; 12; 13].

The term macrosomia refers to foetuses that are large for their gestational age or infants with birth weight more than 4000 g (above the 90th percentile for birth weight) at delivery, irrespective of their gestational age, gender or birth order [10; 14; 15]. For all the reasons discussed above, obstetricians pay great importance to the accurate estimation of foetal weight to predict and prepare for the birth of macrosomic infants. Unfortunately, macrosomia can only be determined with certainty after delivery. Hence, it would be highly desirable to make a prenatal diagnosis to expedite the delivery or pre-arrange for caesarean section to reduce the risk of birth trauma.

In current clinical practice, ultrasonography is the most commonly employed tool to estimate foetal weight. This estimation is done based on measurement of segments of the body such as biparietal diameter, head circumference, abdominal circumference and femur length. Unfortunately, even with the most ideal ultrasound conditions, these measurements are subject to inevitable inaccuracies, with a mean percentage error of 7% – 10%. Low birth weights tend to be overestimated and high birth weights underestimated [16; 17].

Ultrasound as described in section 3.1 uses a high frequency sound pulse transmitted into the body and detects sound waves that are partially reflected from layers between different tissues. The estimation of foetal adiposity becomes very challenging with penetration of ultrasound beams constrained by fatty maternal structures, especially when the foetal head is buried deep inside the maternal pelvis [18]. Furthermore, obtaining clear ultrasound images becomes significantly more difficult in patients suffering from oligohydramnios or maternal obesity. With all these limitations, ultrasound, of course, does not permit direct determination of foetal fat content or body composition.

Whilst ultrasound remains the predominant modality for foetal assessment in pregnancy due to its availability and low cost, Magnetic Resonance Imaging (MRI) has been emerging as a complementary non-invasive choice of investigation. To date, MRI has been operated clinically in compromised pregnancies to image abnormal structures that could not be adequately visualised using ultrasound or are better visualised by MRI, for example abnormalities related to the central nervous system (particularly ventriculomegaly), thoracic anomalies, pulmonary malformations, gastrointestinal tract and genitourinary system [19; 20; 21]. Furthermore, MRI has been employed as a research tool to measure placental blood flow in pregnancy complicated by pre-eclampsia and foetal growth restriction [22].

MRI is a promising tool in measuring foetal anthropometry, and could potentially be used to detect macrosomia. It is a fast imaging modality with an ability to obtain images in any orientation with excellent tissue contrast; enabling us to differentiate fat from lean body mass accurately [23; 24]. The water and fat composition in the body can be differentiated by using water suppression or by T_1 weighting (as fat has a short T_1). Here, both these techniques were combined to obtain a fat-only image. While these techniques were used in this study, there are other alternative methods to measure fat in MRI, in particular Dixon's method.

Dixon's method relies on acquiring images at carefully chosen echo times by using pixel-by-pixel image algebra to calculate the fat or water only image. The basic idea of Dixon is two images are acquired: one at a TE when fat and water are in phase and the other when fat and water are out of phase. These two images can either be added or subtracted to calculate the water or fat only image,

respectively. While this technique seems straightforward, in practice variation in static field (B_0), presence of eddy current and susceptibility effects will need to be considered along with variation in echo amplitudes. These will possibly give rise to shimming problems.

Studies have previously observed a marked increase in the prevalence of macrosomia in diabetic pregnancies [14]. Therefore, in this study, a scanning and analysis protocol was developed to estimate foetal fat composition, which would potentially allow clinicians to identify foetuses at risk of complicated delivery due to the fat distribution. Two approaches were considered: measuring foetal fat across the abdomen or across the whole body, with the objective to produce, quantify and study foetal adiposity distribution in non-diabetic control and diabetic pregnancies. While the protocol and the reliability of the foetal adiposity quantification program will be discussed in detail in the next section, readers are directed to section 5.2.2 of Chapter 5 for more information about reliability and reproducibility tests.

In addition, data from other secondary in-utero anthropometric measurements such as foetal volume, foetal length and shoulder width will also be presented to study the effect of maternal diabetes on foetal growth. The hypothesis for this study was that the foetal adiposity, foetal volume, foetal length and shoulder width would be greater in foetuses of diabetic mothers.

6.3 Method

This section is divided into three parts. The first part details the patient recruitment criteria, scanning protocol and the technique used to analyse foetal adiposity (computational program). The second part details the approach undertaken to test the reliability and reproducibility of the techniques used to measure foetal adiposity. The final part details the approach taken to measure foetal fat volume, foetal volume, foetal length and shoulder width in normal and diabetic pregnancies.

6.3.1 Recruitment Criteria

Following Nottingham Research Ethics Committee approval, Dr Ruta Deshpande conducted the search for participants with pre-gestational diabetes and non-diabetic controls. Diabetic participants were first approached by their usual clinician who proposed participation in the study, while non-diabetic controls were recruited by using posters and leaflets at the Ultrasound Department, Queen's Medical Centre (QMC), Nottingham. Only participants aged 18 years or over, with a viable singleton pregnancy and registered to deliver at QMC were eligible to participate in this study. All the participants were matched for age, parity and maternal Body Mass Index (BMI); these details along with ethnicity were recorded at the initial recruitment stage. All participants gave informed written consent to participate in the study. Participant's height, weight and glycated haemoglobin A1c (HbA1c) levels were recorded at each scan session. In addition, birth weights and gender of the participants' babies and the gestation and mode of delivery were collected following their delivery. In line with the hospital policy at the time of recruitment, gestational age was calculated from the crown rump length measurement in the first trimester of pregnancy.

6.3.2 Scanning Protocol

Prior to MR scans at each visit, ultrasound scans were conducted to measure foetal head circumference, abdominal circumference and femur length. Following this, the MR scans were performed on a 1.5 Tesla Philips Achieva MRI system based on the initial scanning procedure mentioned in section 5.3.2: the patient was positioned in the scanner with receiver coil placed between the mother's umbilicus and pubic symphysis.

All women underwent two scans, at 22 – 26 weeks and 33 – 37 weeks. For simplicity, these gestational time points will henceforth be referred to as 24 weeks and 35 weeks gestational age (GA), respectively. All the MR scans conducted in this study are with a specific absorption rate of $< 2.0 \text{ W kg}^{-1}$. Non-breath hold Half Fourier Single Shot Turbo Spin-Echo (HASTE) and balanced Fast Field Echo (bFFE) were applied to acquire images encompassing the whole foetus in three orthogonal planes. These images were used to assist in identifying

the location and orientation of the foetus. They were also used in measurement of the foetal volume, placental volume (which was reported in Chapter 5), foetal length and shoulder width.

- The HASTE sequence acquired 123 slices over all three orthogonal directions in 147 seconds (TE = 120 ms, flip angle = 90° , $0.78 \times 0.78 \times 6.00 \text{ mm}^3$ and FOV = $400 \times 300 \times 400 \text{ mm}^3$)
- The bFFE sequence acquired 130 slices in 167 seconds (TR = 5.8 ms, TE = 2.3 ms, flip angle = 70° , $0.78 \times 0.78 \times 6.00 \text{ mm}^3$ and FOV = $400 \times 300 \times 400 \text{ mm}^3$)

The T_1 -weighted water suppressed images of fat (*FAT* images) based on chemical shifts method were acquired in a breath hold to reduce the effect of foetal motion (Figure 6.1). Two sequences were applied.

- Twelve slices were acquired at regular intervals encompassing the whole foetus (head to rump) in 13.5 seconds, (TR = 147 ms, TE = 4.6 ms, $1.875 \times 1.875 \times 6.00 \text{ mm}^3$, slice gap = 20 mm and FOV = $402 \times 292 \times 450 \text{ mm}^3$). This sequence will henceforth be referred to as *TOTAL* sequence.
- Twelve contiguous slices were acquired over the foetal abdomen (shoulders to rump) in 13.5 seconds (TR = 147 ms, TE = 4.6 ms, $1.875 \times 1.875 \times 6.00 \text{ mm}^3$, slice gap = 0 mm and FOV = $402 \times 72 \times 450 \text{ mm}^3$) to allow the subjective assessment of intra-abdominal fat. This sequence will henceforth be referred to as *ABDO* sequence.

In both cases, the regularly spaced slices were positioned randomly with respect to the foetus to allow an unbiased estimate of the fat in the volume of interest. All patients were requested to remain as still as possible during these acquisitions to avoid motion artefacts.

6.3.3 Data Analysis

6.3.3.1 Foetal Adiposity Quantification Program

Image Analysis

The *FAT* images, acquired using the *TOTAL* and *ABDO* sequences, showed foetal and maternal fat and little else (Figure 6.1) but the foetal fat distribution was too complex to allow manual segmentation. Hence, the fat volume was quantified using a semi-automated approach based upon pixel intensity, taking account of partial volume effects.

The *FAT* images were loaded into GIMP 2.2.13 (GNU Image Manipulation Program, www.gimp.org) allowing the observer to draw an approximate freehand mask around the foetus to segment the region of interest from the maternal fat, as shown in Figure 6.2b. This avoided the results being dominated by the maternal fat and reduced the effect of image inhomogeneity (as seen in Figure 6.1), which occurred at late gestation when the mother's subcutaneous fat was located close to the edge of the transmit coil, or during foetal motion, as seen in Figure 6.2a. The mask and images were then loaded into a MATLAB (R2009b, The MathWorks Inc, Natick, MA, USA) program written in-house to compute the intensity histogram in N_{bins} ($N_{bins} = 200$) within the masked region, which was then smoothed (rectangular window of width 5 points).

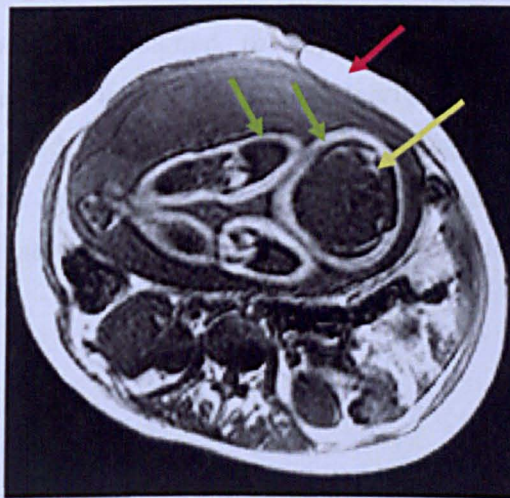


Figure 6.1: Image of an MRI acquisition using the *FAT* protocol of a transverse plane through the foetal thorax. Maternal subcutaneous (red arrow) and intra-abdominal fat can be seen surrounding the pregnancy sac. Foetal fat surrounding the foetal abdomen and legs (green arrow) and foetal intra-abdominal fat (yellow arrow) can be seen.

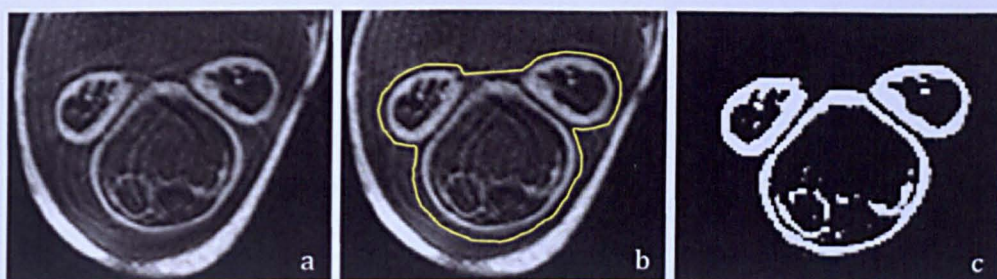


Figure 6.2: (a) *FAT* image of a transverse plane through the foetal thorax showing intra-abdominal fat around kidney (b) Fat roughly masked around the foetus. (c) Fat image after scaling of intensity histogram.

The resulting histogram (h_j) was bimodal with a large peak corresponding to background noise and a smaller second peak for fat voxels. Initially, the large background noise peak was removed from the histogram (red line on Figure 6.3) and the position of the second peak was established (i_{peak} , Figure 6.3). Following this, a scaling function (blue dashed line on Figure 6.3) was then designed using the equation below:

$$S_j = \begin{cases} 1 - e^{-\left(\frac{j - 2i_{peak}}{i_{peak}}\right)^2} & \text{for } 2i_{peak} < j < N_{bins} \\ S_j = 0 & \text{for } 0 < j < 2i_{peak} \end{cases} \quad (\text{Eq 6.1})$$

This scaling factor was designed to suppress noise signal enabling the measurement of zero fat in images, which clearly contained no fat. A scaled histogram was obtained from the product of the histogram and scaling function (black dotted line on Figure 6.3). The masked image was remapped with pixel values given by the value in the scaled histogram to give a foetal fat image (Figure 6.2c).

Validity of the Foetal Adiposity Quantification Process

Prior to the data analysis, the procedure defined in the image analysis section was validated using a phantom. The phantom was made up of 250 mg adipose and 1250 mg pure fat placed in 1 glass bottle and 100 mg pure fat in another 100 mg bottle. It was placed into a plastic box containing 1000 ml of water and scanned using the

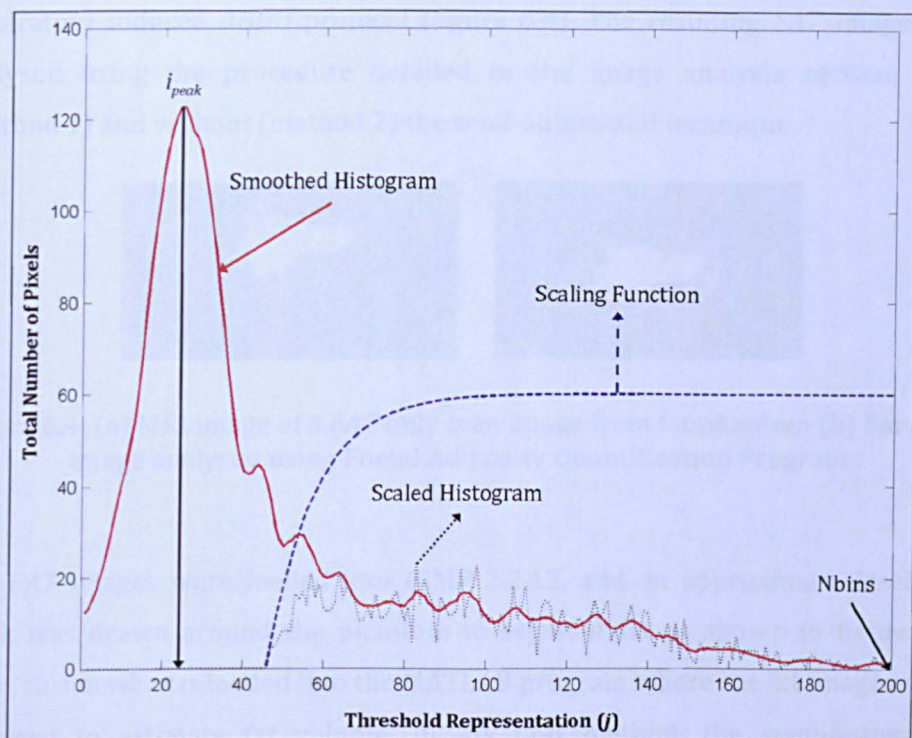


Figure 6.3: Raw histogram of the pixel intensity showing peak due to noise and high intensity tail due to foetal fat signal (red solid line); scaling function to determine the threshold separating fat and background noise signals (blue dashed line – increased scaling by 60) and scaled histogram (black dotted line).

The Estimated Fat Volume (EFV) was then calculated from the following equation:

$$EFV = X \times Y \times (Z + G) \times \sum_j^{Nbins} h_j \times S_j \quad (\text{Eq 6.2})$$

where X, Y and Z are voxel dimensions in mm, and G = slice gap. Subsequently, the estimated fat volume was divided by the foetal volume and converted into a percentage to compensate for variation in fat volume secondary to foetal size.

Validity of the Foetal Adiposity Quantification Program

Prior to the data analysis, the procedure detailed in the image analysis section was validated using a phantom. This phantom was made up of 250 ml saline and 150 ml goose fat placed in a glove that was tied tightly to exclude air bubbles. It was placed into a plastic box containing 1600 ml of saline and scanned using the

respiratory induced *ABDO* protocol (figure 6.4). The resulting *FAT* image was analysed using the procedure detailed in the image analysis section, with (method 1) and without (method 2) the semi-automated technique.

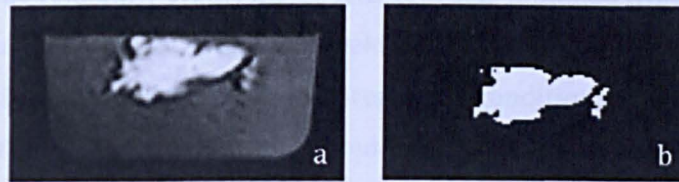


Figure 6.4: (a) MRI image of a *FAT* only scan image from fat phantom (b) Fat only image analysed using Foetal Adiposity Quantification Program

The *FAT* images were loaded into GIMP 2.2.13, and an approximate freehand mask was drawn around the phantom to segment fat as shown in figure 6.4. Then, this mask was loaded into the MATLAB program where the fat images were analysed to estimate fat volume. In the first method, the semi-automated technique described in the image analysis section was employed to segment the phantom's fat. The second method required the observer to manually select the minimum fat threshold associated with the fat images. Since the resulting histogram (h_j) was usually bimodal with one large peak corresponding the background noise and a second smaller peak for the fat voxels (figure 6.3), the observer was requested to manually select the second peak or subsequent peaks possibly relating to the fat pixels. This was done to segment the fat images from the selected minimum threshold onwards. Then, the estimated fat of the phantom from method 1 and method 2 were compared to the actual fat volume of the phantom.

Reliability and Reproducibility of the Foetal Fat Measurement Analysed Using the Foetal Adiposity Quantification Program

A reliability and reproducibility test was conducted on the estimated foetal fat measurement computed from the Foetal Adiposity Quantification Program. This assessment was conducted with the aim to establish if the measurement errors from the test were small enough for the program to be used in a clinical environment. It is also an assessment undertaken to check on the validity of the Foetal Adiposity Quantification Program.

Four observers, who have experience in looking at foetal MRI scans, conducted foetal fat measurements: the author (DA), Professor Penny Gowland (PG), Dr Nia Wyn Jones (NJ) and Dr Ruta Deshpande (RD). For the purpose of consistency throughout the reliability study, the *TOTAL* data sets obtained from five pregnant subjects scanned at 24 weeks and 35 weeks were randomly selected. This was to avoid potential bias resulting from the pregnancy conditions and gestational age at the date of scan. Each observer repeated the foetal fat measurements twice for each data set of all the ten *TOTAL* data sets. All the analyses were performed blind to gestational age, maternal BMI, diabetic status, complications of pregnancy, the other observer results and their own previous measurement results. The measurements obtained from the Foetal Adiposity Quantification Program were tested for intra and inter-observer reliability using the Statistical Package for the Social Sciences (SPSS: Version 17.0; Chicago, IL, USA).

The distribution of the data obtained from all the individual reliability tests were assessed using the Kolmogorov-Smirnov test. The normally distributed results were expressed by their mean and standard deviation. Then, the intra-observer reliability was assessed by comparing the differences in the two measurements made by the same observer for each data set. Inter-observer reliability test was assessed by comparing the first measurement of each observer against the first measurement of other observers' measurements. The results were studied using several indicators: intra-class correlation coefficient (ICC), limit of agreement (LOA) and Bland Altman plot. The ICC evaluates the proportion of variance between observations attributed to the measurement technique and also reflects the variability between subjects. They can be grouped with values less than 0.20 representing poor correlation, 0.21 – 0.40 fair, 0.41 – 0.60 moderate, 0.61 – 0.80 good and 0.81 – 1.00 very good correlation [25].

The intra-observer limits of agreement were calculated by estimating the mean and standard deviation of the difference between two measurements made by each observer. It gives a range where 95% of these differences lie within 1.96 standard deviations of the mean. Once the LOA is calculated, the results are graphically illustrated using the Bland Altman plots. The Bland Altman graph plots the mean of two measurements on the x-axis and the differences between the two measurements on the y-axis (expressed as a percentage of their means in this thesis).

6.3.3.2 The Application of Foetal Adiposity Quantification Program to Study the Effect of Maternal Diabetes on Foetal Adiposity

Following the reliability test, the method described in section 6.3.1.1 was applied in conjunction with the Foetal Adiposity Quantification Program to study the effect of maternal diabetes on foetal adiposity. The data analysis was conducted on all the *TOTAL* data collected from both diabetic and non-diabetic control pregnant women at 24 weeks and 35 weeks gestational age (GA). Again all analyses were performed blind to gestational age, maternal BMI, diabetic status and complications of pregnancy.

6.3.3.3 Intra-abdominal Fat

In addition to the foetal fat measurement, three observers conducted an intra-abdominal fat analysis independently: the author, Professor Penny Gowland and Dr Ruta Deshpande. This subjective assessment was conducted on the 12 contiguous slices acquired over the foetal abdomen using the *ABDO* protocol (figure 6.5). Each observer examined whether the images showed evidence of intra-abdominal (visceral) fat in the foetus. A score of 2 was given for *FAT* images with definite intra-abdominal fat, a score of 1 for possible and 0 for no intra-abdominal fat. The predominant score (2 or 3 out of 3 independent observers) was taken to represent the existence of intra-abdominal fat in the foetus.

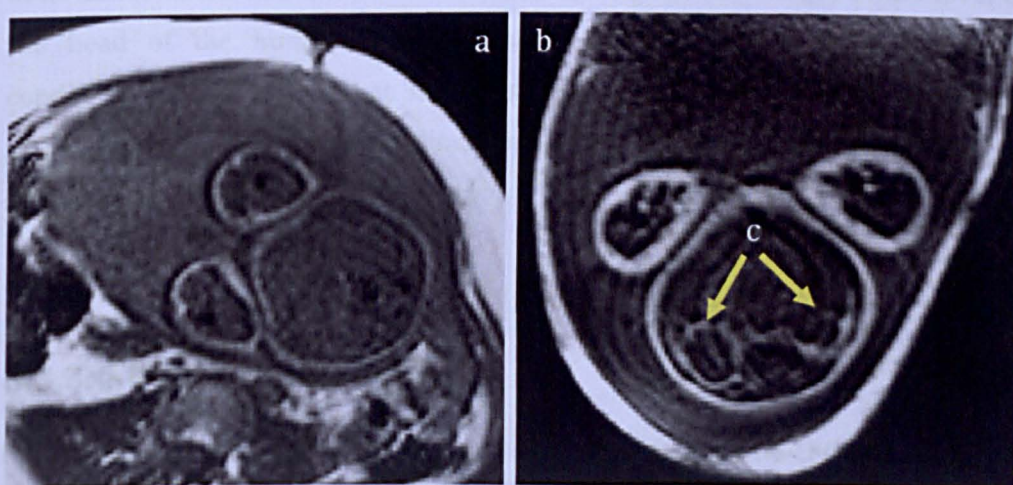


Figure 6.5: Fat only image of a transverse plane through the foetal thorax: (a) Control, (b) Diabetic and (c) Intra-abdominal fat visible around the foetal kidney.

6.3.3.4 Foetal Volume

The MR images acquired using bFFE sequence was used in measuring foetal volume. This measurement was conducted by drawing an approximate freehand mask around the foetus using Analyze 9.0 (Mayo Clinic, Rochester, MN, USA). From the foetal volume measurement, the fat free volume of the foetus is computed: foetal volume – foetal fat volume. All the analyses were performed blind to gestational age, maternal BMI, diabetic status and complications of pregnancy.

6.3.3.5 Foetal Length and Shoulder Width

The MRI images acquired using HASTE and bFFE were also used in the measurement of foetal length and shoulder width. The foetal length was measured as crown to heel distance: the length of the skull (crown to base of the brain stem), foetal spine, thigh and lower leg to the heel. Initially, the scans were rotated to obtain the best possible coronal view of the head and spinal column. Then, the distance from the crown to the coccyx was measured by following the curvature of the spine. Occasionally, observer had to make partial measurement on separate images from the crown to the base of the lungs and then to the coccyx (6 cases at 24 weeks and all cases at 35 weeks). The femur length was measured from the hip to the centre of the knee, while the lower leg length was measured from the centre of the knee to the heel. The shoulder width was determined as the maximum transverse width on the MR images at the level of the head of the humerus. The shoulder width measurements were only conducted on data collected at 35 weeks. All the measurements were conducted using Analyze 9.0; the observer blinded to gestational age, maternal BMI, diabetic status and complications of pregnancy.

6.3.3.6 Foetal Volume Index

Foetal volume and length information were used to compute the foetal volume index, FVI (l m^{-3}) akin to the ponderal index, PI (kg m^{-3}) used in neonatal practice to standardise the foetal size according to length.

$FVI = \text{Volume} \times \text{Length}^{-3}$	(Eq 6.3)
$PI = \text{Weight} \times \text{Length}^{-3}$	(Eq 6.4)

The FVI will differ numerically to the PI, since the density of the foetal fat is estimated as 0.9 kg l⁻¹ and the fat free tissue at birth is 1.064 kg l⁻¹ (lower than in adults due to the differences in hydration) [26].

6.3.3.7 Statistical Analysis to Study the Effect of Maternal Diabetes on Foetal Growth

The distributions of the measurements obtained from all the individual analyses and clinical outcomes were tested for normality using the Kolmogorov-Smirnov test in the SPSS software. The normally distributed results were expressed using the mean and standard deviation. Then, statistical comparisons between two groups at each gestation were performed using an independent samples t-test for normally distributed data and a Mann Whitney test for non-parametric data. Fisher’s exact test was used for comparison of two dichotomous variables with small numbers. The statistically significant results were determined by using the p-values. For the purpose of this study, the p-values less than 0.05 were considered significant. These values were used in studying the effect of maternal diabetes on foetal growth by reviewing the results obtained from diabetes and control pregnant mothers.

In addition, correlation statistics were performed to study the relationship between MR and clinical measurements.

6.4 Results

6.4.1 Foetal Adiposity Quantification Program

6.4.1.1 Validity of the Foetal Adiposity Quantification Program

Using the semi-automated method described in the image analysis of section 6.3.3.1, the Foetal Adiposity Quantification Program measured a fat volume of 133.01 ml for the fat only phantom. However, without the semi-automated approach, where the observer chooses the minimum threshold to estimate fat, the Foetal Adiposity Quantification Program measured a fat volume of 144.06 ml for the fat only phantom. This calculated volume equates to 88.7% and 96.0% of the true fat volume, respectively.

6.4.1.2 Reliability and Reproducibility of the Foetal Fat Measurement Analysed Using the Foetal Adiposity Quantification Program

Four observers analysed ten datasets: five datasets acquired at 24 weeks and five datasets acquired at 35 weeks gestation. All the measurements were normally distributed. The intra-observer and inter-observer reliability test for estimated foetal fat volume produced by the Foetal Adiposity Quantification Program demonstrated very good reliability for all four observers at all gestations and at 35 weeks, with ICC results > 0.99 . However, measurement of the estimated foetal fat volume at 24 weeks demonstrated a slightly poorer reliability. The ICC results of intra and inter-observer reliability tests for estimated foetal fat volume are given in table 6.1.

Gestational Age	Intra-observer ICCs for Estimated Foetal Fat Volume for Four Observers (95% CI)				Inter-observer ICCs for Estimated Foetal Fat Volume
	Observer 1 (DA)	Observer 2 (PG)	Observer 3 (NJ)	Observer 4 (RD)	
All Gestations	1.000 (0.999 - 1.000)	0.997 (0.988 - 0.999)	0.998 (0.991 - 0.999)	0.998 (0.991 - 0.999)	0.998 (0.996 - 1.000)
24 weeks	0.985 (0.885 - 0.998)	0.730 (-0.102 - 0.968)	0.830 (0.169 - 0.980)	0.681 (-0.117 - 0.960)	0.513 (0.087 - 0.917)
35 weeks	1.000 (0.897 - 1.000)	0.992 (0.939 - 0.999)	0.993 (0.952 - 0.999)	0.994 (0.953 - 0.999)	0.996 (0.985 - 1.000)

Table 6.1: Intra-observer and inter-observer reliability results (ICC) for estimated foetal fat volume computed from two measurements made by each observer at the two different gestational ages.

Overall, observer 1 had the best ICCs for the intra and inter-observer reliability test compared to the other observers across all gestations. This is also evident from observing the narrower LOA for observer 1 compared to other observers in the Bland Altman plots for estimated foetal fat volume measurements (figure 6.6c). While the intra-observer LOA for observer 1 was $\pm 5\%$ for 35 weeks, this reliability was reduced at 24 weeks with LOA closer to $\pm 300\%$. Similarly, the inter-observer LOA for estimated foetal fat volume were narrower at 35 weeks compared to 24 weeks. These LOA results are demonstrated using Bland Altman plots in figure 6.6.

Based on ICC and LOA results, it can be summarised that the reliability of the program is better at 35 weeks, when foetal fat is more distinctive. Moreover, at 35 weeks, there were no bias between observers and clinically acceptable limits of agreement were seen.

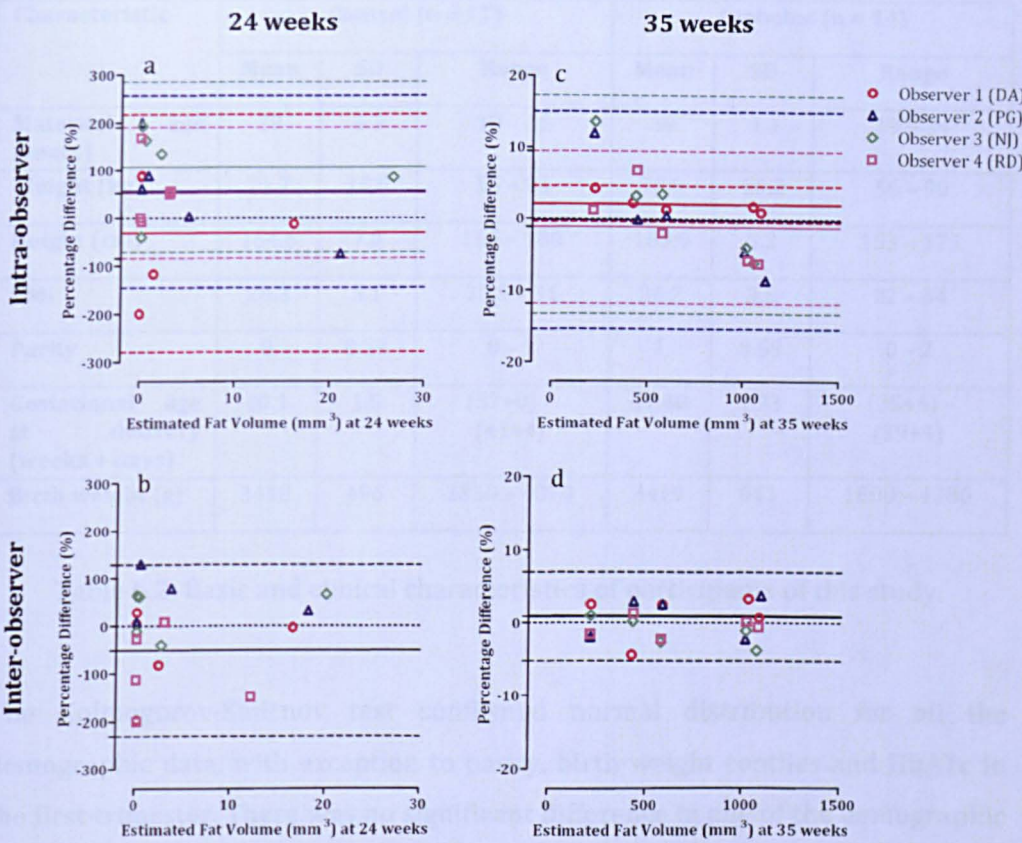


Figure 6.6: Bland Altman plots of estimated foetal fat volume at 24 weeks (a and b) and 35 weeks (c and d). These Bland Altman plots express the intra-observer (a and c) or inter-observer (b and d) mean percentage differences based on measurements made by three observers. The solid lines refer to mean percentage differences (1st measurement – 2nd measurement), whereas dashed lines refer to LOA between measurements.

6.4.2 The Effect of Maternal Diabetes on Foetal Growth

6.4.2.1 Study Population

A total of 26 pregnant women with singleton pregnancies: 14 pre-gestational diabetics (13 Type 1 Diabetes and 1 Type 2 Diabetes) and 12 non-diabetic controls, matched for age, parity and maternal Body Mass Index (BMI) were recruited. There was one smoker in the diabetic group and no smokers in the non-diabetic control group. Table 6.2 demonstrates the basic and clinical characteristics of the participants of this study.

Characteristic	Control (n = 12)			Diabetes (n = 14)		
	Mean	SD	Range	Mean	SD	Range
Maternal age (years)	29	4.3	19 – 35	30	4.4	19 – 34
Weight (kg)	71.7	10.8	55 – 94	70.9	10.2	56 – 90
Height (cm)	164.6	7.0	155 – 180	163.9	5.2	153 – 173
BMI	26.3	3.1	20.5 – 31	26.2	3.5	22 – 34
Parity	0	0.39	0 – 1	1	0.65	0 – 2
Gestational age at delivery (weeks + days)	40.1	1.5	(37+0) – (41+4)	37.48	1.33	(35+4) – (39+4)
Birth weight (g)	3418	496	2350 – 4070	3419	641	1800 – 4280

Table 6.2: Basic and clinical characteristics of participants of this study.

The Kolmogorov-Smirnov test confirmed normal distribution for all the demographic data, with exception to parity, birth weight centiles and HbA1c in the first trimester. There was no significant difference in any of the demographic characteristics (age, BMI, parity and ethnicity) between groups. The range of the gestational ages at the time of scans was 22 – 26 weeks and 33 – 37 weeks. The average gestational ages for the scans was 24 weeks + 1 day (SD = 5 days) and 34 weeks + 4 days (SD = 4 days) in the non-diabetic control group and 24 weeks + 2 days (SD = 5 days) and 34 weeks + 3 days (SD = 7 days) in the diabetic group. Seven pregnant subjects withdrew from the study after their first scan: one control pregnant woman (did not attend second scan) and six pregnant women with diabetes. The pregnant women with diabetes who withdrew from the study were either too big for the magnet bore (one pregnant women), experiencing morning sickness when the second scan was due (one pregnant women), delivered before the scan (one pregnant women) or failed to attend the second scanning session (three pregnant women). However, there were no differences in the demographics or delivery outcomes between women who completed the study and those who withdrew.

6.4.2.2 Ultrasound Measurements and Clinical Outcomes

The foetal abdominal circumference was measured using ultrasound prior to the MR scans at 24 weeks and 35 weeks. The mean foetal abdominal circumference

at 24 weeks was not significantly different ($p = 0.72$) for pregnancies complicated by diabetes at 19.6 cm (SD = 1.1 cm) compared to controls at 19.4 cm (SD = 1.1 cm). However, at 35 weeks, the foetal abdominal circumference was significantly larger ($p = 0.021$) in the diabetes group at 32.6 cm (SD = 2.5 cm) compared to controls at 30.7 cm (SD = 0.8 cm), with significantly more babies with foetal abdominal circumference above the 95th centile for gestational age (9 fetuses of diabetic mothers versus 0 fetuses of control mothers; $p = 0.001$, Fisher's exact test).

The mothers with diabetes delivered their babies at a significantly earlier gestation ($p < 0.001$), 37 weeks + 3 days (SD = 9 days), whereas control mothers delivered their babies at 40 weeks + 0 days (SD = 10 days). As for the birth weight, there was no significant difference between the two groups with $p = 0.994$. The average birth weight of babies born to pregnant mothers of the control group was 3418 g (SD = 496 g) and diabetic group was 3419 g (SD = 641 g). However, after correcting for gestational age, babies born to mothers with diabetes were significantly larger than controls (median birth weight centile 88 for the diabetes group and 33 for the control group; $p = 0.009$).

Data also shows that there was a higher number of deliveries by caesarean section (CS) in the diabetes group (five emergency and two elective CS in diabetic versus one elective CS in control, Fisher's exact test $p = 0.036$). The caesarean sections are indicated in figure 6.7. However, only four CS are labelled in these figures since three diabetic (two emergency and one elective CS) and one control pregnant (elective CS) woman who underwent CS did not attend a second scan session. There was one case of shoulder dystocia in the diabetes group where the baby weighed 4200 g at 37 weeks + 1 day. This baby also suffered a fractured humerus. Conversely, there was no cases of shoulder dystocia in the control group, although one woman sustained a third degree tear while delivering a baby weighing 3400 g at 41 weeks + 1 day.

6.4.2.3 Foetal MR Measurements

Very little foetal fat (generally less than 2% volume) was observed at 22 – 26 weeks of gestation. In addition, the measurement of estimated foetal fat volume and percentage foetal fat volume is not normally distributed at 24 weeks. For this

reason, the statistical analysis of these two measurements across gestation was not performed. At 35 weeks, mean foetal fat measurements were significantly greater ($p = 0.009$) in foetuses of diabetic mothers at 1090 cm^3 ($SD = 420\text{ cm}^3$) compared to foetuses of controls 540 cm^3 ($SD = 350\text{ cm}^3$). The corresponding mean foetal fat percentages at 35 weeks were significantly higher ($p = 0.012$) in foetuses of diabetic mothers at 40.4% ($SD = 11.9\%$) compared to foetuses of controls 22.5% ($SD = 13.8\%$).

The data showed increased foetal fat volume and percentage foetal fat across gestation and to a greater extent in foetuses of diabetic mothers compared to controls. Figure 6.7 and 6.8 demonstrates the total foetal fat volume and percentage foetal fat volume across two gestations for foetuses of diabetic and control mothers.

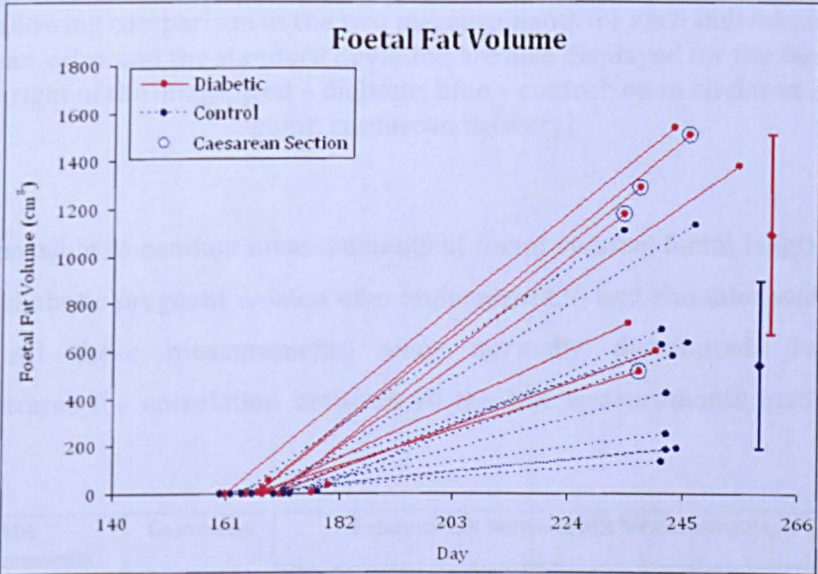


Figure 6.7: Scatter plot of the difference in foetal fat volume across two gestations for foetuses of diabetic and control mothers. Marker lines are added allowing comparison of the two measurements for each individual subject. The mean value and the standard deviation are also displayed for the two groups on the right of the image, [red – diabetic; blue – control; open circles at 2nd time point: caesarean delivery]

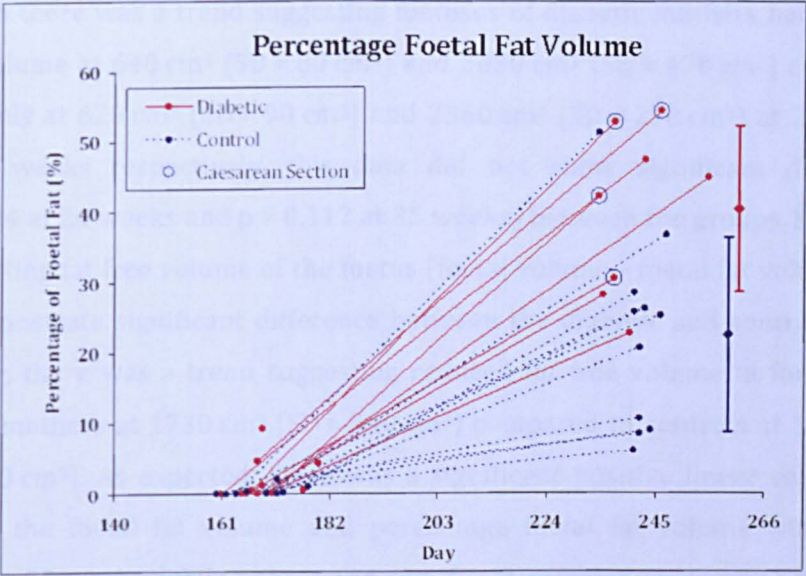


Figure 6.8: Scatter plot of the difference in percentage foetal fat volume across two gestations for foetuses of diabetic and control mothers. Marker lines are added allowing comparison of the two measurements for each individual subject. The mean value and the standard deviation are also displayed for the two groups on the right of the image, [red – diabetic; blue – control; open circles at 2nd time point: caesarean delivery].

It was possible to conduct measurements of foetal volume, foetal length (except for one diabetic pregnant women who underwent CS) and shoulder width on all scans. All these measurements were normally distributed. Table 6.3 demonstrates the correlation between all the MR measurements made in this study.

MR Measurements	Gestations	Relationship between MR Measurements, R ² (p)		
		Foetal Volume	Foetal Length	Shoulder Width
Foetal Fat	24 weeks	0.060 (p = 0.229)	0.173 (p = 0.035)	–
	35 weeks	0.474 (p = 0.001)	0.303 (p = 0.022)	0.365 (p = 0.006)
Percentage Foetal Fat	24 weeks	0.024 (p = 0.449)	0.126 (p = 0.075)	–
	35 weeks	0.208 (p = 0.049)	0.130 (p = 0.155)	0.208 (p = 0.050)
Foetal Volume	24 weeks	N/A	0.400 (p = 0.001)	–
	35 weeks		0.590 (p < 0.001)	0.493 (p = 0.001)
Foetal Length	24 weeks	0.400 (p = 0.001)	N/A	–
	35 weeks	0.590 (p < 0.001)		0.101 (p = 0.215)

Table 6.3: Correlation statistics between MR measurements collected for this study.

Although there was a trend suggesting fetuses of diabetic mothers had greater foetal volume at 640 cm³ (SD = 80 cm³) and 2650 cm³ (SD = 470 cm³) compared to controls at 620 cm³ (SD = 90 cm³) and 2360 cm³ (SD = 270 cm³) at 24 weeks and 35 weeks respectively, this data did not show significant difference (p = 0.494 at 24 weeks and p = 0.112 at 35 weeks) between the groups. Similarly, the resulting fat free volume of the foetus (foetal volume – foetal fat volume) did not demonstrate significant difference between the diabetic and control group. However, there was a trend suggesting reduced fat free volume in fetuses of diabetic mothers at 1730 cm³ (SD = 340 cm³) compared to controls at 1760 cm³ (SD = 320 cm³). As expected, there was a significant positive linear correlation between the foetal fat volume and percentage foetal fat volume with foetal volume at 35 weeks, while poorer non-significant correlations were observed at 24 weeks. Figure 6.9 demonstrates the foetal volume of fetuses of diabetic and control mothers.

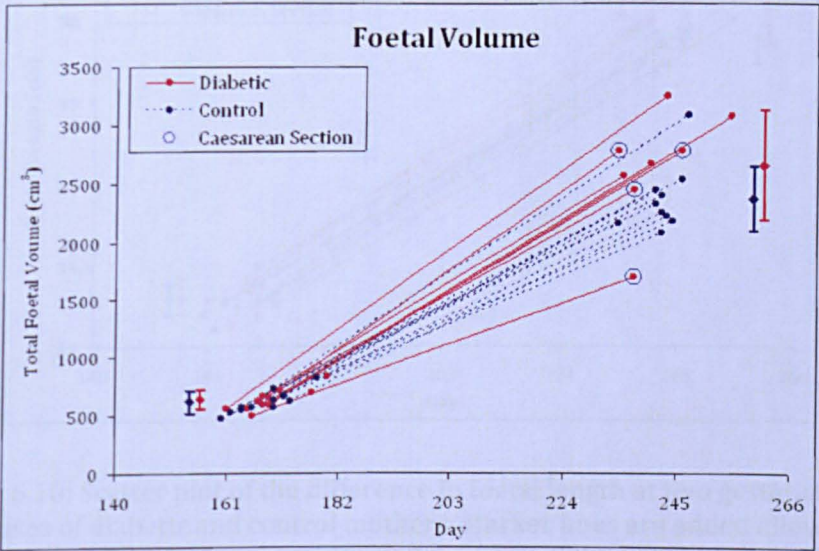


Figure 6.9: Scatter plot of the difference in foetal volume at two gestations for fetuses of diabetic and control mothers. Marker lines are added allowing comparison of the two measurements for each individual subject. The mean value and the standard deviation are also displayed for the two groups on the right of the image, [red – diabetic; blue – control; open circles at 2nd time point: caesarean delivery].

Similarly, the length of fetuses of diabetic mothers was greater at both time points but the data only confirmed this to be significant at 35 weeks (p = 0.625 at 24 weeks and p = 0.029 at 35 weeks): mean foetal length was 32.9 cm (SD = 1.0 cm) and 48.2 cm (SD = 0.9 cm) in the control group and 33.1 cm

(SD = 1.1 cm) and 49.6 cm (SD = 1.1 cm) in the diabetic group at 24 weeks and 35 weeks, respectively. The foetal length measurements demonstrated significant positive correlation to the foetal fat volume and foetal volume at 24 weeks and 35 weeks. Figure 6.10 demonstrates the foetal length of fetuses of diabetic and control mothers.

In addition, the fetuses' shoulder width at 35 weeks demonstrated a trend to be greater in the fetuses of diabetic mothers at 12.8 cm (SD = 1.8 cm) compared to fetuses from control pregnancies at 11.9 cm (SD = 1.3 cm), but this difference was not statistically significant ($p = 0.248$). However, significant positive correlation was seen between shoulder width and foetal fat volume, percentage fat volume and foetal volume.

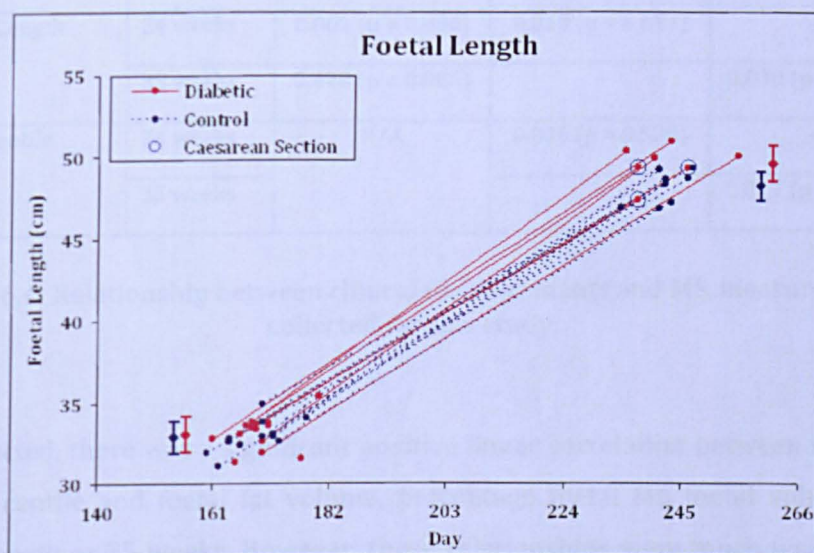


Figure 6.10: Scatter plot of the difference in foetal length at two gestations for fetuses of diabetic and control mothers. Marker lines are added allowing comparison of the two measurements for each individual subject. The mean value and the standard deviation are also displayed for the two groups on the right of the image, [red – diabetic; blue – control; open circles at 2nd time point: caesarean delivery].

From the foetal volume and foetal length measurements, the foetal volume index (FVI) was computed. The results demonstrated no significant differences ($p = 0.624$ at 24 weeks and $p = 0.866$ at 35 weeks) between the two groups with values of 17.3 L m^{-3} (SD = 1.7 L m^{-3}) and 21.2 L m^{-3} (SD = 2.0 L m^{-3}) in the control and 17.7 L m^{-3} (SD = 2.1 L m^{-3}) and 21.4 L m^{-3} (SD = 3.1 L m^{-3}) in the diabetic group at 24 weeks and 35 weeks, respectively.

6.4.2.4 Correlation between Clinical Measurements and Foetal MR Measurements

MR Measurements	Gestations	Relationship of Clinical Measure to MR Measurement, R ² (p)		
		Birth Weight Centile	HbA1c First trimester	HbA1c Third trimester
Foetal Fat	24 weeks	0.012 (p = 0.606)	0.021 (p = 0.620)	-
	35 weeks	0.496 (p = 0.001)	-	0.056 (p = 0.609)
Percentage Foetal Fat	24 weeks	0.015 (p = 0.555)	0.024 (p = 0.600)	-
	35 weeks	0.362 (p = 0.008)	-	0.092 (p = 0.508)
Foetal Volume	24 weeks	0.010 (p = 0.634)	0.001 (p = 0.954)	-
	35 weeks	0.559 (p < 0.001)	-	0.001 (p = 0.987)
Foetal Length	24 weeks	0.001 (p = 0.896)	0.018 (p = 0.651)	-
	35 weeks	0.428 (p = 0.006)	-	0.030 (p = 0.742)
Birth Centile	24 weeks	N/A	0.035 (p = 0.520)	-
	35 weeks		-	0.017 (p = 0.671)

Table 6.4: Relationship between clinical measurements and MR measurements collected for this study.

As expected, there was a significant positive linear correlation between the birth weight centile and foetal fat volume, percentage foetal fat, foetal volume and foetal length at 35 weeks. However, these relationships were much weaker and non-significant at 24 weeks. Indeed there was no significant correlation between HbA1c at either time point to any parameter studied.

At 35 weeks, the single case of shoulder dystocia had one of the highest measured foetal fat volumes of all the subjects included in this study and the percentage foetal fat was higher than any other subject who delivered vaginally. However, the MR measures for this subject at 24 weeks did not appear greater than other subjects. In addition, there was one subject in the control group who had foetal fat volumes and percentage foetal fat similar to the diabetic macrosomic infants. This subject had a normal delivery of a 3520 g female foetus at 39 weeks. This baby had not been anticipated to be macrosomic and birth weight was on the 70th centile.

6.4.2.5 Intra-abdominal fat

The foetal fat images at 24 weeks did not show convincing intra-abdominal fat. However, at 35 weeks, the intra-abdominal scores were more defined and significantly greater ($p = 0.047$) in foetuses of diabetic mothers: 6 scored definite, 1 scored possible and 1 scored zero intra-abdominal fat. In controls, 2 scored definite, 6 scored possible and 3 scored zero abdominal fat. At 35 weeks, the fat scores showed a significant but weak positive linear correlation with foetal fat volume ($R^2 = 0.349$, $p = 0.008$), percentage fat volume ($R^2 = 0.317$, $p = 0.012$), foetal volume ($R^2 = 0.244$, $p = 0.032$) and birth centile ($R^2 = 0.493$, $p = 0.001$).

6.5 Discussion and Conclusion

Macrosomia remains a significant obstetric problem that occurs in 6% – 10% of all pregnancies [12; 27; 28]. The risk of macrosomia is particularly high in pregnancies associated with maternal diabetes, with 50% of babies born to mothers with maternal diabetes being above the 90th centile for birth weight [29; 30]. With increasing birth weight, there is an increasing risk of birth trauma to both mother and baby, in particular shoulder dystocia leading to foetal clavicular and humeral fractures, brachial nerve palsies and occasionally cerebral hypoxic damage [4]. Consequently, the risk of shoulder dystocia is much higher in women with diabetes, despite the increased rate of caesarean sections [31]. For this reason, it would be ideal to determine and prepare for the delivery of macrosomic infants before birth.

At present, foetal growth during pregnancy is assessed by ultrasound scanning, with the risk of macrosomia being related to the foetal abdominal circumference. However, although ultrasound is useful in monitoring intra-uterine growth retardation, foetal size is often underestimated particularly when the foetus is large and the technique is therefore not sensitive in the detection of the macrosomic foetus. In contrast to ultrasound, it has been reported that birth weight estimation is more accurate using MRI compared to ultrasound for infants at term, although no attempt was made to overview foetal fat [32]. Since there currently is no validated or accepted method of accurately diagnosing

macrosomia antepartum, MR techniques potentially provide an attractive development to study foetal anthropometry.

Foetal MRI represents a non-invasive imaging technique that allows a detailed visualisation of the foetus in the utero-maternal environment. It is credited for its ability to produce images of foetus in any orientation with excellent soft tissue contrast, enabling us to differentiate fat from lean body mass accurately. Learning this, Peterson et al. [24] and Deans et al. [23] designed methods to measure subcutaneous foetal fat at term to either predict an infant's birth weight or assess percentage foetal fat with respect to other foetal tissue. While their work was novel, these studies were not quantitative and lacked sensitivity in measuring foetal fat. In addition, these studies were only conducted on pregnant patients at late gestations (36 weeks – 41 weeks) and thus, failed to observe foetal fat at all gestations to compile growth curves. Therefore, T_1 weighted water suppression scans were designed to measure foetal adiposity in utero at 24 weeks and 35 weeks. The resulting images clearly showed foetal and maternal fat and little else.

Although there are other alternative methods to measure fat with MRI, in particular Dixon's method, T_1 weighted water suppression is more advantageous in overcoming shimming errors. While shimming is not really a problem in the foetus since amniotic fluid ensures that the foetus is well matched to its surroundings and the near spherical shape of the uterus ensures a relatively homogeneous field within, maternal bowel gas can perturb the local magnetic field. In addition, although T_1 weighting is not sensitive to shimming effects, it can be perturbed by radio frequency pulse errors, especially when the foetus is lying away from the isocentre near term. Therefore, the water suppressed T_1 weighted imaging along with histogram based image analysis (Foetal Adiposity Quantification Program) is ideal to minimise this effect.

The foetal fat volume measured using the Foetal Adiposity Quantification Program demonstrated very good intra-observer and inter-observer reliability at third trimester and poorer reliability at second trimester, with observer 1 demonstrating the best ICCs and LOA. This is expected since observer 1 had most experience looking at foetal fat images and developed the Foetal Adiposity Quantification Program. Nonetheless, the foetal fat measurements made by other observers were not too discrepant, suggesting that the reliability could be

improved with possible further training. The reliability was poorer at 24 weeks because the amount of foetal fat present at this stage was very small.

In addition, the techniques employed here clearly identify the expected excess body fat in the foetuses of mothers with diabetes, which adds to the validity and potential clinical utility of this technique. However, the absolute accuracy of the fat volumes measured with this method remains unproven since the validity of the program was conducted based on a fat only phantom containing a fairly irregular block of fat and water. Ideally, the phantom should have included distributed fat, bone and other tissue along with saline to possibly create a better model of the intra-uterine environment to validate the program. Nevertheless, the semi-automated method used here provided a reasonable measure of the phantom fat volume, in comparison to the actual phantom fat volume. In addition, the measurement from semi-automated method was reasonably good with respect to the program requiring user inputs to measure foetal fat volume.

Besides foetal fat volume measurements, it was also possible to measure foetal volume, foetal length and shoulder width from the HASTE and bFFE images acquired for this study. These are promising foetal anthropometry measures that can potentially be used by a clinician to identify macrosomic foetuses with excess fat accumulation. The data shows that there was very little fat present at 24 weeks, but a considerable quantity was present at 35 weeks (sometimes a litre or more). It was also possible to identify intra-abdominal fat in some *FAT* images at 35 weeks.

At 35 weeks, the data demonstrates a significant increase in the foetal fat volume, percentage foetal fat, foetal length, abdominal circumference and birth weight centiles in the foetuses of diabetic mothers compared to controls. Similar trends were noticed in measurements of foetal volume, shoulder width and FVI. The MR scans obtained for the current study shows that the foetuses of diabetic mothers were of increased size (volume), predominantly due to accelerated fat accumulation in the third trimester of pregnancy and not due to increased fat-free tissue. This was confirmed by a significant positive linear correlation between foetal fat volume and percentage foetal fat with foetal volume at 35 weeks. It is also important to note that there were positive linear correlation between foetal fat volume and percentage foetal fat with birth centile and intra-abdominal fat. However, all these correlations were not strong and even much

weaker at 24 weeks, possibly because very little foetal fat is present at 24 weeks and the fetuses are much smaller at this stage.

While the data clearly shows significant increase in the foetal length of fetuses of diabetic mothers compared to controls at 35 weeks, this data contradicts the large published study by Persson et al. [29] that suggested that maternal diabetes does not have an effect on actual foetal length at birth. However, the difference in this study was clinically small at, on average, 1.4 cm. In addition, the measurement of fetuses shoulder width was higher in the diabetic group compared to controls, although the differences were not significant. However, the limitation of this study is that it deals with a small number of subjects in assessing any possible differences in the foetal length and shoulder width. Nonetheless, it is of interest that the fetus with the greatest shoulder width in this study is from a pregnancy complicated by diabetes and suffered the consequence of shoulder dystocia.

Foetal length varies considerably and has a modulatory influence on the interpretation of foetal volume and foetal weight. In this study, the foetal length showed a weak positive correlation with foetal volume ($R^2 = 0.590$, $p < 0.001$) and birth centile ($R^2 = 0.428$, $p = 0.006$). In neonatal practice, ponderal index ($\text{weight} \div \text{height}^3$) is used as an index of foetal adiposity, instead of body mass index ($\text{weight} \div \text{height}^2$). However, de Bruin et al. [33] commented on the moderate association between ponderal index and fat content in infants, with a closer association with $\text{weight} \div \text{height}$.

While it is reasonable to assume pregnancies complicated by diabetes might provide an initial group to trial the efficacy and accuracy of MR scanning in the detection of the macrosomic fetus, it is of interest to correlate the foetal fat volume at 35 week to maternal glycaemic control in the third trimester, albeit a non-significant very weak correlation ($R^2 = 0.056$, $p = 0.609$). This contradicts a published work that reported a strong positive correlation between foetal adiposity and insulin resistance, even with adjustment of potential confounders [34]. The results here may be related to the small number included in this study.

Moreover, it is also clear that the intra-abdominal fat is associated with insulin resistance and type II diabetes in adults [35], and at a greater extent in offspring of mothers with type II maternal diabetes, a mechanism that cannot be explained by a genetic basis alone [36]. In this study, there was a significant detection of

foetal intra-abdominal fat in foetuses of diabetic mothers. This observation of foetal intra-abdominal fat being more prevalent in foetuses of diabetic mothers is in accordance with the concept of the in-utero foetal metabolic programming of adults [36]. So, it would be of interest to prove the value of researching the pathogenesis of the 'metabolic syndrome' and type II diabetes in infants of the diabetic group. While this observation clearly needs confirmation, it suggests that the mechanism of foetal programming may be amenable to investigation using foetal MRI.

Some studies have reported that the overall fat distribution in different region of body is an important predisposition to aberrancies in lipid and glucose metabolism [37]. In addition, central adiposity has been associated with high triglyceride levels, low high density lipoprotein levels [38] along with non insulin dependent diabetes and glucose intolerance [39]. Therefore, it would be interesting to use the *ABDO* protocol instead of the *TOTAL* protocol to determine the foetal fat volume around the foetal abdominal region. This will potentially provide an insight into the future metabolic programming of the infant. However, a possible limitation for this imaging technique would be the inconsistency in positioning the slab of interest around the foetal abdominal region in foetuses that are often lying in any random orientation.

One limitation of the current study is that foetal length at birth was not measured, as this is not current practice in the investigating obstetric unit. Therefore, no attempt was made to correlate the MR measures to the gold standard foetal length. Moreover, due to this limitation, ponderal index at birth could not be computed as an independent index of foetal adiposity. A second issue is that the study is conducted with a relatively small number of volunteers. However, this study was simply designed as a feasibility study to validate and assess the reliability and potential of the technique, and even with these small numbers, some indicative findings have emerged. Foetal size is of course only one part of the equation in determining possible difficulties at delivery and the risk of shoulder dystocia, but MR scans could also be used to determine the anatomy of the maternal birth canal.

This preliminary study has demonstrated that T_1 weighted water suppressed MRI scans provide a convenient and reliable method for measuring foetal fat volume in-utero. The combination of foetal fat volume with foetal volume measurements

strengthens the reliability of the present study to allow detection of a macrosomic foetus with excess foetal growth due to adipose tissue and may assist in the identification of foetuses at risk of birth trauma. This technique clearly illustrates the differences in body composition between foetuses of mothers with and without diabetes. A larger study is now required to determine whether this MR technique can be prospectively used to screen women at increased risk of delivering macrosomic infants, in particular pregnant women with gestational diabetes. Another promising area for this application is the ability to distinguish small foetuses suffering from IUGR from normal foetuses considered small for their gestation.

6.6 References

- [1] P. Dandona, H.S. Besterman, D.B. Freedman, F. Boag, A.M. Taylor, and A.G. Beckett. (1984), Macrosomia despite well-controlled diabetic pregnancy. *Lancet* **1** 737.
- [2] B. Persson, and U. Hanson. (1998), Neonatal morbidities in gestational diabetes mellitus. *Diabetes Care* **21 Suppl 2** B79-84.
- [3] J.L. Kitzmiller. (1986), Macrosomia in infants of diabetic mothers: characteristics, causes, prevention. *in* "Diabetes and Pregnancy, Teratology, Toxicology and Treatment" (L. Jovanovic, C.M. Peterson, and K. Fuhrmann, Eds.), Praeger, New York.
- [4] D.S. Acker, B.P. Sachs, and E.A. Friedman. (1985), Risk Factors for Shoulder Dystocia. *Obstetrics & Gynecology* **66** 762-768.
- [5] H.D. Modanlou, W.L. Dorchester, A. Thorosian, and R.K. Freeman. (1980), Macrosomia--maternal, fetal, and neonatal implications. *Obstetrics and gynecology* **55** 420-4.
- [6] W.N. Spellacy, S. Miller, A. Winegar, and P.Q. Peterson. (1985), Macrosomia--maternal characteristics and infant complications. *Obstetrics and gynecology* **66** 158-61.
- [7] T.S. Nesbitt, W.M. Gilbert, and B. Herrchen. (1998), Shoulder dystocia and associated risk factors with macrosomic infants born in California. *American Journal of Obstetrics and Gynecology* **179** 476-480.
- [8] K.R. Lipscomb, K. Gregory, and K. Shaw. (1995), The outcome of macrosomic infants weighing at least 4500 grams: Los Angeles County + University of Southern California experience. *Obstetrics & Gynecology* **85** 558-564.
- [9] A. Ferber. (2000), Maternal Complications of Fetal Macrosomia. *Clinical Obstetrics and Gynecology* **43** 335-339.
- [10] M.E. Boyd, R.H. Usher, and F.H. McLean. (1983), Fetal macrosomia: prediction, risks, proposed management. *Obstetrics and gynecology* **61** 715-22.
- [11] A.A. Meshari, S. De Silva, and I. Rahman. (1990), Fetal macrosomia--maternal risks and fetal outcome. *International Journal of Gynecology & Obstetrics* **32** 215-222.
- [12] K. Wollschlaeger, J. Nieder, I. Köppe, and K. Härtlein. (1999), A study of fetal macrosomia. *Archives of Gynecology and Obstetrics* **263** 51-55.

- [13] J. Berard, P. Dufour, D. Vinatier, D. Subtil, S. Vanderstichele, J.C. Monnier, and F. Puech. (1998), Fetal macrosomia: risk factors and outcome: A study of the outcome concerning 100 cases > 4500 g. *European Journal of Obstetrics & Gynecology and Reproductive Biology* **77** 51-59.
- [14] R. Schwartz, and K.A. Teramo. (1999), What is the significance of macrosomia? *Diabetes Care* **22** 1201-1205.
- [15] E. Oral, A. Cagdas, A. Gezer, S. Kaleli, K. Aydinli, and F. Ocer. (2001), Perinatal and maternal outcomes of fetal macrosomia. *European Journal of Obstetrics & Gynecology and Reproductive Biology* **99** 167-171.
- [16] R.L. Schild. (2007), Three-dimensional volumetry and fetal weight measurement. *Ultrasound in Obstetrics and Gynecology* **30** 799-803.
- [17] P.N. Baker, I.R. Johnson, P.A. Gowland, J. Hykin, P.R. Harvey, A. Freeman, V. Adams, P. Mansfield, and B.S. Worthington. (1994), Fetal weight estimation by echo-planar magnetic resonance imaging. *The Lancet* **343** 644-645.
- [18] C. Garel, H. Brisse, G. Sebag, M. Elmaleh, J.-F. Oury, and M. Hassan. (1998), Magnetic resonance imaging of the fetus. *Pediatric Radiology* **28** 201-211.
- [19] C. Garel. (2008), Fetal MRI: what is the future? *Ultrasound in Obstetrics and Gynecology* **31** 123-128.
- [20] E.H. Whitby, M.N.J. Paley, A. Sprigg, S. Rutter, N.P. Davies, I.D. Wilkinson, and P.D. Griffiths. (2004), Comparison of ultrasound and magnetic resonance imaging in 100 singleton pregnancies with suspected brain abnormalities. *BJOG: An International Journal of Obstetrics & Gynaecology* **111** 784-792.
- [21] M. Cannie, J. Jani, S. Dymarkowski, and J. Deprest. (2006), Fetal magnetic resonance imaging: luxury or necessity? *Ultrasound in Obstetrics and Gynecology* **27** 471-476.
- [22] P. Gowland. (2005), Placental MRI. *Seminars in Fetal and Neonatal Medicine* **10** 485-490.
- [23] H.E. Deans, F.W. Smith, D.J. Lloyd, A.N. Law, and H.W. Sutherland. (1989), Fetal fat measurement by magnetic resonance imaging. *British Journal of Radiology* **62** 603-607.
- [24] L.J. Peterson, J. Crues, E. Durak, and C.M. Peterson. (1993), Magnetic Resonance Imaging in Pregnancies Complicated by Gestational Diabetes Predicts Infant Birthweight Ratio and Neonatal Morbidity. *American Journal of Perinatology* **10** 432-437.

- [25] K.O. McGraw, and S.P. Wong. (1996), Forming inferences about some intraclass correlation coefficients. *Psychological Methods;Psychological Methods* **1** 30-46.
- [26] Z. Wang, S. Heshka, J. Wang, L. Wielopolski, and S.B. Heymsfield. (2003), Magnitude and variation of fat-free mass density: a cellular-level body composition modeling study. *American Journal of Physiology - Endocrinology And Metabolism* **284** E267-E273.
- [27] H.M. Schrader, L. Jovanovic-Peterson, W.C. Bevier, and C.M. Peterson. (1995), Fasting plasma glucose and glycosylated plasma protein at 24 to 28 weeks of gestation predict macrosomia in the general obstetric population. *American Journal of Perinatology* **12** 247-251.
- [28] J.W. Weeks, T. Pitman, and J.A. Spinnato li. (1995), Fetal macrosomia: Does antenatal prediction affect delivery route and birth outcome? *American Journal of Obstetrics and Gynecology* **173** 1215-1219.
- [29] M. Persson, D. Pasupathy, U. Hanson, and M. Norman. (2011), Birth Size Distribution in 3,705 Infants Born to Mothers With Type 1 Diabetes. *Diabetes Care* **34** 1145-1149.
- [30] M.E. Inge, W.d.V. Harold, and H.A.V. Gerard. (2004), Risk of complications of pregnancy in women with type 1 diabetes: nationwide prospective study in the Netherlands. *BMJ* **328** 915.
- [31] G. Hawthorne, S. Robson, E.A. Ryall, D. Sen, S.H. Roberts, and M.P. Ward Platt. (1997), Prospective population based survey of outcome of pregnancy in diabetic women: results of the Northern Diabetic Pregnancy Audit, 1994. *BMJ* **315**.
- [32] M.V. Zaretsky, T.F. Reichel, D.D. McIntire, and D.M. Twickler. (2003), Comparison of magnetic resonance imaging to ultrasound in the estimation of birth weight at term. *American Journal of Obstetrics and Gynecology* **189** 1017-1020.
- [33] N.C. de Bruin, K.A. van Velthoven, T. Stijnen, R.E. Juttman, H.J. Degenhart, and H.K. Visser. (1995), Body fat and fat-free mass in infants: new and classic anthropometric indexes and prediction equations compared with total-body electrical conductivity. *The American Journal of Clinical Nutrition* **61** 1195-1205.
- [34] P.M. Catalano, L. Presley, J. Minium, and S. Hauguel-de Mouzon. (2009), Fetuses of obese mothers develop insulin resistance in utero. *Diabetes Care* **32** 1076-80.

- [35] D.B. Carr, K.M. Utzschneider, R.L. Hull, K. Kodama, B.M. Retzlaff, J.D. Brunzell, J.B. Shofer, B.E. Fish, R.H. Knopp, and S.E. Kahn. (2004), Intra-Abdominal Fat Is a Major Determinant of the National Cholesterol Education Program Adult Treatment Panel III Criteria for the Metabolic Syndrome. *Diabetes* **53** 2087-2094.
- [36] U. Simeoni, and D.J. Barker. (2009), Offspring of diabetic pregnancy: Long-term outcomes. *Seminars in Fetal and Neonatal Medicine* **14** 119-124.
- [37] P. Bjorntorp. (1991), Metabolic implications of body fat distribution. *Diabetes Care* **14** 1132-43.
- [38] S.M. Haffner, M.P. Stern, H.P. Hazuda, J. Pugh, and J.K. Patterson. (1987), Do upper-body and centralized adiposity measure different aspects of regional body-fat distribution? Relationship to non-insulin-dependent diabetes mellitus, lipids, and lipoproteins. *Diabetes* **36** 43-51.
- [39] G.K. Dowse, P.Z. Zimmet, H. Gareeboo, K.G.M.M. Alberti, J. Tuomilehto, C.F. Finch, P. Chitson, and H. Tulsidas. (1991), Abdominal Obesity and Physical Inactivity as Risk Factors for NIDDM and Impaired Glucose Tolerance in Indian, Creole, and Chinese Mauritians. *Diabetes Care* **14** 271-282.

Chapter 7

The Effect of Maternal Smoking on Foetal Organ Growth

7.1 Overview

This chapter starts with a short literature review detailing the effect of maternal smoking on foetal growth and the adverse outcome in these pregnancies, highlighting the long-term health risks to foetuses exposed to maternal smoking. Following these discussions, this chapter will progress to describe the techniques applied to acquire, process and estimate foetal organ volumes using MRI sequences and two segmentation methods: a semi automatic approach based on the concept of edge detection and a stereological method, the Cavalieri technique. The author will address the individual method used to measure and statistically analyse the effect of maternal smoking on foetal brain, lungs, liver and kidneys volumes. In addition, the foetal volume, placental volume, foetal length and shoulder width will also be reviewed. The author conducted these measurements with the assistance of Alexander Joseph Parker, a medical student at University of Aberdeen and Kirsty Allcock, a medical student at the University of Nottingham. Finally, the chapter is concluded by a demonstration and discussion of the results obtained from analysing the data of both the smoker and control mothers involved in this study.

7.2 Introduction

In recent years, data collected through clinical and experimental studies, including epidemiologic data, indicates foetal development and the intrauterine environment plays an important role in determining one's health later in life [1]. Although the foetal development stage is known to be fairly adaptive to exposure to adverse environmental conditions, such as maternal smoking, it may affect the structure, physiology and function of various organ systems, since human growth and development rates are highest during foetal life, when essential foetal organs are being developed [2]. This may lead to foetal growth restriction and increased the risk of metabolic and cardiovascular diseases during childhood and adulthood [3; 4].

For decades, both the United States of America and Great Britain have been continuously admonishing the adverse effects of maternal cigarette smoking during pregnancy through the media and counter-advertising. Although these public health campaigns have successfully persuaded 20% of pregnant women to quit smoking before the initial prenatal visit, approximately 15% - 20% of pregnant women still continue to smoke [5; 6; 7]. Moreover, smoking habits are growing among women who are of childbearing age, pregnant and breastfeeding [6; 8; 9].

Prenatal exposure to maternal cigarette smoking (PEMCS) is associated with miscarriage, gestational bleeding, placental abruption, placenta praevia, sudden infant death syndrome (SIDS) and respiratory disorders [10; 11; 12; 13]. In addition, follow up studies of children exposed to maternal smoking in utero show evidence suggesting an increased incidence of psychiatric disorders, behavioural problems and neonatal altered auditory responsiveness [14; 15; 16]. Recent studies conducted on children born to smoking and non-smoking mothers, demonstrated poorer performance on cognitive tasks and language development among children of smoking mothers [17; 18; 19]. There was also evidence of attention deficit hyperactivity [20].

Furthermore, PEMCS is also known to be a major risk factor for intrauterine growth restriction (IUGR) and small for gestational age (SGA) [12; 21; 22; 23]. The exposed infants are often at risk of perinatal mortality and reduced birth weight [23; 24; 25; 26]. These individuals born smaller at birth are usually of

decreased fat free mass [27]. However, they are categorised as a high-risk group for obesity and obesity-associated disorders such as cardiovascular problems and diabetes, during childhood and adolescence [28; 29; 30].

Cigarette smoke contains thousands of different compounds that may be harmful to the human body. Nicotine and carbon monoxide have been identified as two major compounds that may have harmful effects on the developing foetus during pregnancy. They cross the placenta and can be detected in the foetal circulation, amniotic fluid and breast milk of smoking mothers. There is evidence of an increased concentration of nicotine and carbon monoxide in the foetal circulation; which exceed the maternal concentration by 15% [31; 32]. In addition, studies have shown an increased concentration of nicotine within the amniotic fluid, which is 88% higher than maternal plasma [5; 32].

Nicotine is an active element that has a half-life of 1 to 2 hours. It can be metabolised into many different compounds by the liver and is eliminated by the kidney. One of the major metabolites is cotinine, which is excreted with a half-life of 15 to 20 hours [33]. Nicotine can affect the foetus in many ways: (a) maternally inhaled nicotine induces vasoconstriction of the uteroplacental vasculature, subsequently leading to uteroplacental under-perfusion which can result in a reduction in nutrient and oxygen flow to the foetus causing a decrease in foetal heart rate and an increase in mean arterial pressure; [34] (b) nicotine suppresses the mother's appetite, leading to poor nutrition and energy intake and results in reducing the energy supply to the foetus; and (c) nicotine causes alterations in the cellular growth and activity of the central and peripheral nervous system [14; 35].

Conversely, carbon monoxide binds with haemoglobin to form carboxyhaemoglobin that leads to depletion in the level of oxygen supplied for foetal tissue oxygenation, causing hypoxia-ischemia. Recent studies in animal models demonstrate evidence of ischaemic injury in the foetal lungs, liver, kidneys and placenta. It is suggested that the intracellular damage is secondary to an increase in the production of oxygen-derived free radicals in the reperfused hypoxic tissues [36; 37]. Moreover, there is published work suggesting maternal smoking decreases foetal lung and liver volume [38], as well as kidney weight (rat studies) [39]. It also causes foetal resorption and brain cell damage in offspring exposed to nicotine [35; 40; 41; 42]. There is also evidence of reduced

perfusion in the placenta of women who smoke [43; 44; 45], possibly because of reduced capillary volume fraction and increased thickness of villous membranes in the placental tissues of smokers, increasing the resistance within the placenta that decreases uterine blood flow [43; 46]. For all these reasons, clinicians should promote smoking cessation and educate pregnant patients on the adverse effects of smoking to prenatal and perinatal outcomes [5].

In this study, Magnetic Resonance Imaging (MRI) was used to investigate the effect of maternal smoking on foetal growth restriction having previously learnt of its ability to produce detailed visualisation of foetus in utero and maternal structures, including the birth cavity. Moreover, echo planar imaging has been used to estimate foetal volume and foetal organ volume [47; 48]. It has also been possible to use MRI to study growth patterns of the foetal brain, lungs and liver [49]. The motivation for this study originated from a lack of published studies investigating the effect of maternal smoking on foetal organ growth in human subjects. Here, a description of methods used to acquire, process and statistically analyse the data of foetal brain, lungs, liver and kidneys is presented. In addition, the measurements of foetal volume, placental volume, foetal length and shoulder width in both exposed and non-exposed infants is presented. These data are used in evaluating foetal growth from the second to the third trimester. The hypothesis for this study was that the foetal organ volume, foetal and placental volume, foetal length and shoulder width would be reduced in fetuses exposed to maternal smoking. In addition, a further hypothesis was made that the major effect would be on the brain and kidney volume.

7.3 Method

7.3.1 Recruitment Criteria

Following Nottingham Research Ethics Committee approval, Dr Nia Wyn Jones conducted the search for smoking and non-smoking pregnant participants by using posters and leaflets at the Ultrasound Department, Queen's Medical Centre (QMC), Nottingham. Only participants aged 18 years or over, with a viable singleton pregnancy with maternal Body Mass Index (BMI) less than 35 and

registered to deliver at QMC were eligible to participate in this study. All the participants were matched for age, parity, maternal BMI and education level (not reported here); these details along with ethnicity were recorded at the initial recruitment stage. All participants gave informed written consent to participate in the study. Participant's height and weight were recorded at each scan session. In addition, birth weights and sex of the participants' babies and the gestation and mode of delivery were collected following their delivery. For simplicity, foetuses exposed to maternal smoking will be referred to as the exposed group and foetuses of control mothers will be referred to as the non-exposed group.

7.3.2 Scanning Protocol

Prior to MR scans at each visit, ultrasound scans were conducted to measure foetal head circumference, abdominal circumference and femur length. Following this, the MR scans were performed on a 1.5 Tesla Philips Achieva MRI system based on the initial scanning procedure mentioned in section 5.3.2: the patient was positioned in the scanner with receiver coil placed between the mother's umbilicus and pubic symphysis.

In line with the hospital policy at the time of recruitment (which was earlier than the diabetic study), the gestational age was calculated from the last menstrual period and confirmed at 13 weeks of gestation by using Crown Rump Length (CRL) measurements. All women underwent two scans, at two time points of 22 – 27 weeks and 33 – 38 weeks. For simplicity, these gestational time points will henceforth be referred to as 25 weeks and 36 weeks gestational age (GA), respectively.

Non-breath hold HALf Fourier Single Shot Turbo Spin-Echo (HASTE) and Balanced Fast Field Echo (bFFE) were applied to acquire images encompassing the whole foetus in three orthogonal blocks (figure 7.1) without a breath hold to allow for motion effects to be averaged out. All these scans were conducted with a specific absorption rate of $< 2.0 \text{ W kg}^{-1}$.

- The HASTE sequence acquired 123 slices over all three orthogonal directions in 147 seconds ($TE = 120 \text{ ms}$, flip angle = 90° , $0.78 \times 0.78 \times 6.00 \text{ mm}^3$ and $FOV = 400 \times 300 \times 400 \text{ mm}^3$)

- The bFFE sequence acquired 130 slices in 167 seconds ($TR = 5.8$ ms, $TE = 2.3$ ms, flip angle = 70° , $0.78 \times 0.78 \times 6.00$ mm³ and $FOV = 400 \times 300 \times 400$ mm³)
- To study the brain, three high resolution HASTE were applied in transverse, sagittal and coronal planes (HASTEbrain, 34 slices in 35.8 seconds, $TE = 120$ ms and $0.59 \times 0.59 \times 4.50$ mm³ voxels)

Figure 7.2 shows the MR images of a foetus acquired using HASTE, bFFE and HASTEbrain sequence in a sagittal plane. Patients were also requested to remain as still as possible during these acquisitions to avoid motion artefacts.

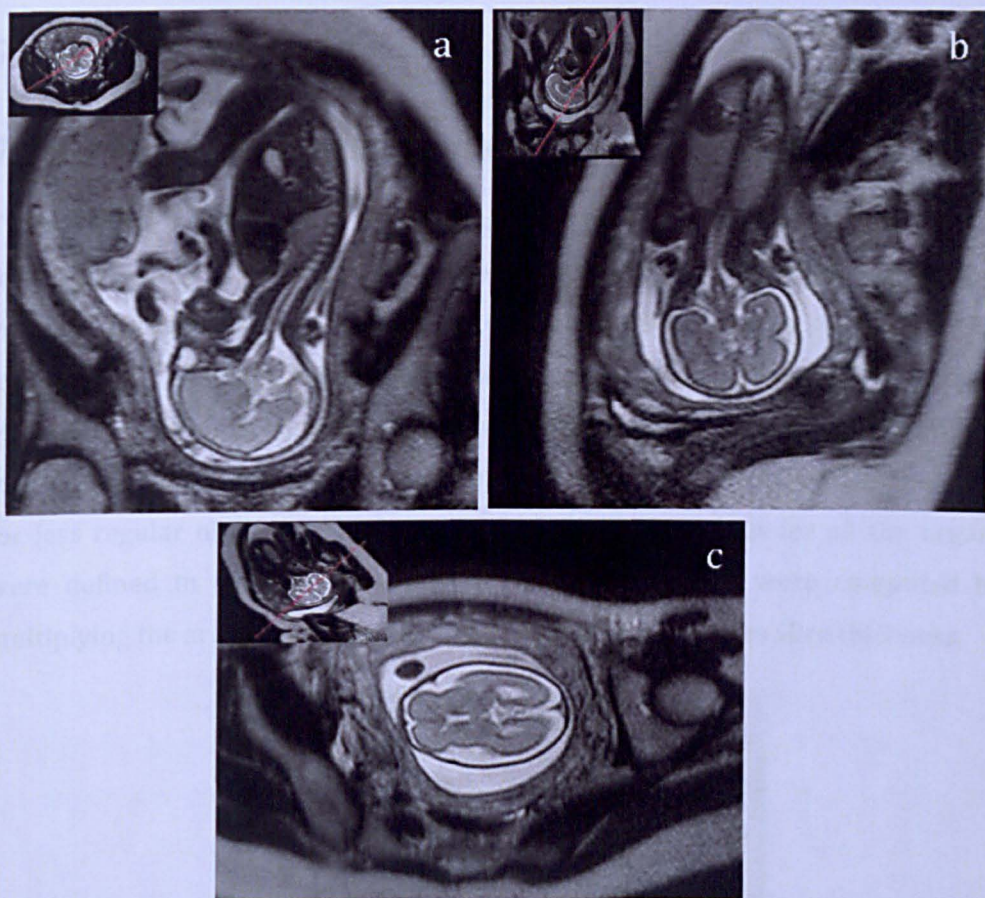


Figure 7.1: Magnetic Resonance Images through foetus (HASTEbrain sequences): (a) Sagittal plane; (b) Coronal plane and (c) Transverse plane

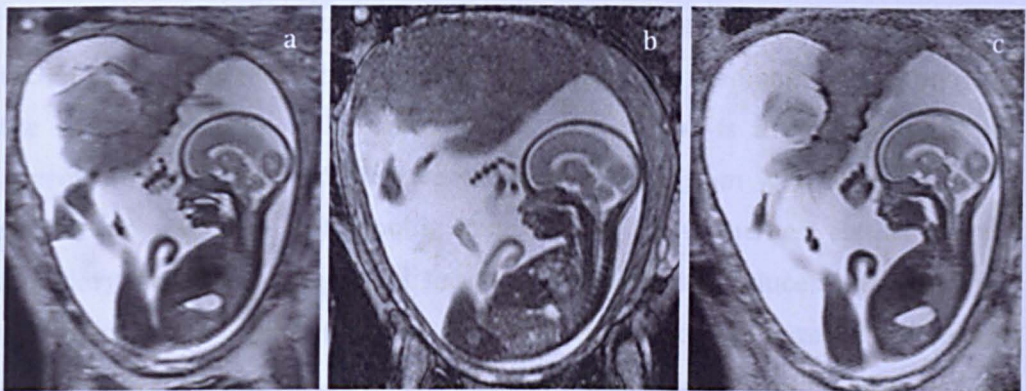


Figure 7.2: MR images acquired in sagittal plane using (a) HASTE, (b) bFFE and (c) HASTEbrain sequences.

7.3.3 Data Analysis

7.3.3.1 Foetal Organ, Placenta and Foetal Volume

The resulting images (Figure 7.3) showed clear delineation of foetal organs in the maternal womb. Two approaches were employed to measure foetal organ volumes, placental volume and foetal volume: a semi automatic segmentation method using an image processing software, Analyze 9.0 (Mayo Clinic, Rochester, MN, USA) for regular shaped objects and a stereological method, the Cavalieri technique using EasyMeasure software (University of Liverpool, Liverpool, UK) for less regular objects. In both cases, the region of interest for all the organs were defined in each slice and the total organ volumes were computed by multiplying the area of the organ summed over all slices by the slice thickness.

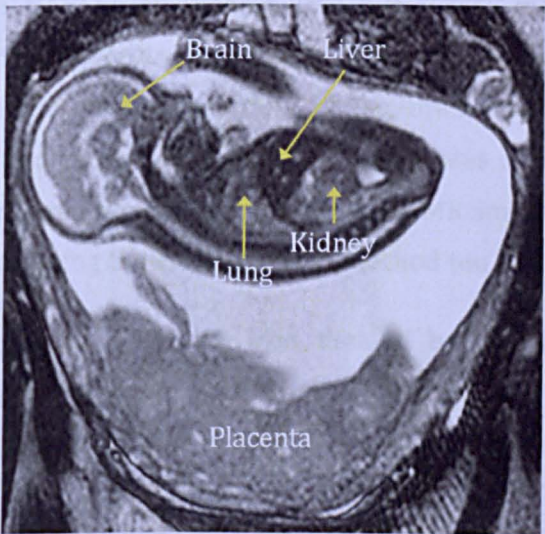


Figure 7.3: MR Image through foetus (HASTEbrain sequences) in sagittal plane. The image clearly shows foetal brain, lung, liver, kidney and placenta.

The semi automatic approach is based on the concept of edge detection. In this technique, the observer initially places the cursor on the image at any point on the edge that needs to be traced. Then, the cursor is dragged around the approximate boundary of the target organ; the program will detect edges of similar contrast to the initial point, snapping the line to the best estimate of the boundary to define a region of interest. This method reduces inter-observer variability due to inconsistent human interference. The semi automatic approach was employed in measuring the volumes of foetal kidneys and lungs on at least two sets of images. Measurements were generally conducted in the coronal and sagittal planes of HASTEbrain for foetal lungs and bFFE for foetal kidneys. In addition, the semi automatic approach was also employed in measuring foetal volume and placental volume by drawing mask around the foetus and placenta on bFFE images. In all these measurements, HASTEbody was used if HASTEbrain and bFFE data sets were affected by significant artefact (generally motion or image non-uniformity artefacts).

The Cavalieri technique is a stereological method based on a set of parallel, systematic plane sections that are separated at a known distance apart. A grid is superimposed on the image and the volume can be estimated by selecting points lying on the region of interest in the image. Then, the volume of the region of interest in that slice is estimated by multiplying the fraction of points within the area of interest by the total area of the whole image [50]. Here, the Cavalieri technique with a 20×20 pixels grid along with point counting techniques was employed to measure the volumes of the foetal liver and brain in three orientations of the HASTEbrain images [51; 52]. These measurements were conducted using the EasyMeasure software [53]. The Cavalieri technique was chosen as the method of segmentation of the brain and liver due to the inconsistent shape and pattern of folding in various areas of the brain, while the contrast of the liver was generally quite poor on MR images (darker organ), making segmentation using the edge detection method too difficult.

The estimated organ volumes were also divided by the foetal volume and converted into a percentage to compensate for variation in organ volume secondary to foetal size, irrespective of gestational age, sex and maternal complication.

7.3.3.2 Foetal Length and Shoulder Width

The foetal length and shoulder width were measured at 25 weeks and 36 weeks using the method described in section 6.3.3.5. All the measurements were conducted using Analyze 9.0; the observer blinded to gestational age, maternal BMI, smoking status and complications of pregnancy.

7.3.3.3 Statistical Analysis to Study the Effect of Maternal Smoking on Foetal Growth

The distributions of the measurements obtained from all the individual analyses were tested for normality using the Kolmogorov-Smirnov test in the SPSS software. The normally distributed results were expressed by their mean and standard deviation. Then, the clinical outcomes and ultrasound measurements were compared between groups at each gestational age using an independent t-test for normally distributed data and a Mann Whitney test for non-parametric data. Subsequently, statistical comparison was performed using the repeated measures analysis of variance (ANOVA) to assess the changes in the foetal organ volumes, foetal and placental volume, foetal length and shoulder width between the two groups (smokers and controls) across two separate time points. The results were presented as a ratio of variation explained by the model to unexplained factors. The statistically significant results were determined by using the p-values. To counteract the potential problem of multiple comparisons, a post hoc Bonferroni correction was applied. The correction was made based on n dependent or independent hypotheses on the data of foetal organ volumes, foetal and placental volume, foetal length and shoulder width. The Bonferroni correction is one way of checking for probability of making one or more false discoveries (familywise error rate). Each individual statistical significance was corrected $\frac{1}{n}$ times and checked if the statistical hypotheses for maternal smoking effects persisted for individual measurements. For the purpose of this study, p-values less than 0.05 after application of the Bonferroni correction were considered significant.

7.4 Results

7.4.1 The Effect of Maternal Smoking on Foetal Growth

7.4.1.1 Study Population

A total of 18 healthy pregnant women with a singleton pregnancy, 10 smokers and 8 controls, matched for age, parity and maternal Body Mass Index (BMI) were recruited. Table 7.1 demonstrates the basic and clinical characteristics of the participants of this study.

Characteristic	Normal (n = 8)			Smoker (n = 10)		
	Mean	SD	Range	Mean	SD	Range
Maternal age (years)	29.5	4.9	20 – 36	24.7	4.2	18 – 29
Weight (kg)	71.1	11.2	59 – 92	65.9	13.8	48 – 88
Height (cm)	167.5	6.5	157 – 176	166.4	4.1	160 – 175
BMI	24.5	3.7	23 – 30	23.4	5.5	17 – 33
Parity	0.5	0.8	0 – 2	1.2	1.2	0 – 3
Gestational age at delivery (weeks + days)	39.9	1.4	(37+2) – (41+6)	39.6	1.0	(37+5) – (41+4)
Birth weight (g)	3586	485	2880 – 4220	3005	542	2500 – 4140

Table 7.1: Basic and clinical characteristics of participants of this study.

The Kolmogorov-Smirnov test confirmed a normal distribution for all the demographic data, with the exception of height, parity and gestational age at delivery. There was no significant difference in any of the demographic characteristics (BMI, parity and ethnicity) between groups. The range of the gestational ages at the time of scans was 22 – 27 weeks and 33 – 38 weeks. The average gestational ages for the scans were 24 weeks + 5 day (SD = 6 days) and 36 weeks + 0 days (SD = 8 days) in the control group and 24 weeks + 0 days (SD = 5 days) and 35 weeks + 2 days (SD = 6 days) in the smoker group. These differences in gestational ages between groups were not statistically significant at 25 (p = 0.075) or 36 weeks (p = 0.122).

7.4.1.2 Ultrasound Measurements and Clinical Outcomes

The foetal head and abdominal circumference along with femur length were measured using ultrasound prior to the MR scans at 25 weeks and 36 weeks. The mean foetal head circumference (FHC) at 25 weeks was significantly smaller ($p = 0.05$) in exposed fetuses at 21.9 cm (SD = 0.9 cm) compared to the non-exposed at 22.7 cm (SD = 0.6 cm). Similarly, at 36 weeks, the mean FHC was significantly smaller ($p = 0.031$) in the exposed group at 31.2 cm (SD = 0.9 cm) compared to the non-exposed group at 32.8 cm (SD = 1.8 cm). Figure 7.4 (a) demonstrates the foetal head circumference of exposed and non-exposed fetuses at two gestations.

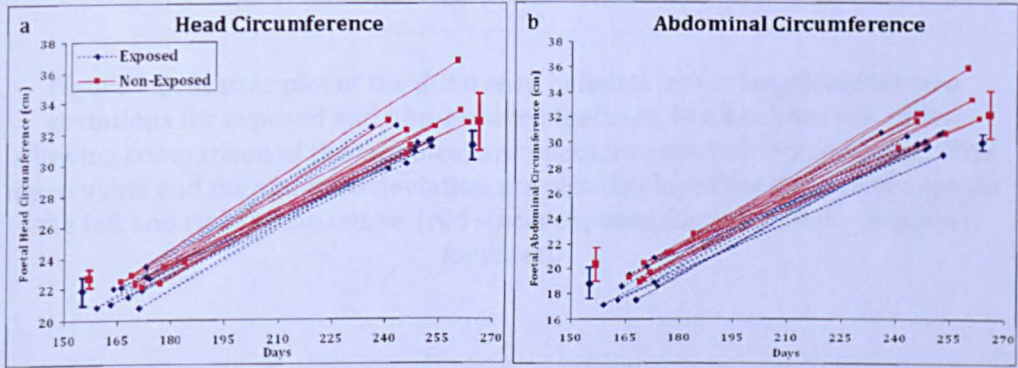


Figure 7.4: Scatter plot of the difference in foetal (a) head circumference and (b) abdominal circumference across two gestations for exposed and non-exposed fetuses. Marker lines are added allowing comparison of the two measurements for each individual subject. The mean value and the standard deviation are also displayed for the two groups on the left and right of the image, [red – non-exposed fetuses; blue – exposed fetuses].

The mean foetal abdominal circumference (FAC) at 25 weeks was significantly smaller ($p = 0.025$) in exposed fetuses at 18.8 cm (SD = 1.2 cm), compared to the non-exposed fetuses at 20.3 cm (SD = 1.3 cm). A similar significant trend was observed at 36 weeks ($p = 0.006$): mean FAC of exposed fetuses was 30.1 cm (SD = 0.6 cm) and non-exposed was 32.2 cm (SD = 1.9 cm). Figure 7.4 (b) demonstrates the foetal abdominal circumference of exposed and non-exposed fetuses at two gestations.

At 25 weeks, the femur lengths were significantly smaller ($p = 0.006$) in exposed fetuses at 4.2 cm (SD = 0.2 cm) compared to the non-exposed at 4.6 cm (SD = 0.2 cm). However, at 36 weeks, there were no significant differences ($p = 0.112$) in femur length of exposed and non-exposed at 6.7 cm (SD = 0.2 cm)

and 7.0 cm (SD = 0.5 cm), respectively. Figure 7.5 demonstrates the femur length of exposed and non-exposed fetuses at two gestations.

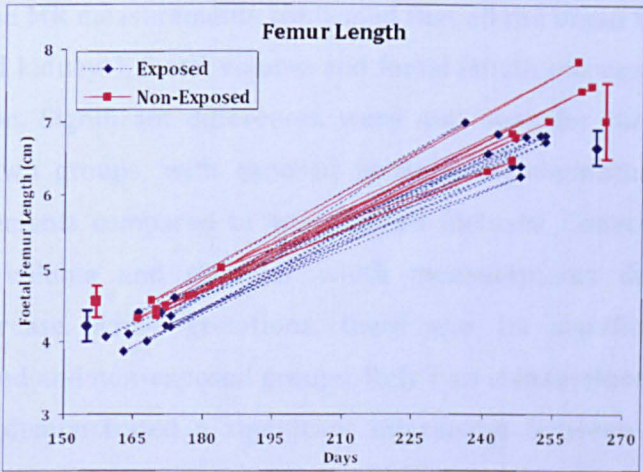


Figure 7.5: Scatter plot of the difference in foetal femur length across two gestations for exposed and non-exposed fetuses. Marker lines are added allowing comparison of the two measurements for each individual subject. The mean value and the standard deviation are also displayed for the two groups on the left and right of the image, [red – non-exposed fetuses; blue – exposed fetuses].

As for birth weight, exposed infants were significantly smaller ($p = 0.031$) at 3000 g (SD = 540 g) compared to the non-exposed infants at 3590 g (SD = 490 g). However, there was no significant difference ($p = 0.651$) in the average gestational age at delivery, with exposed fetuses delivered at 39 weeks + 4 days (SD = 7 days), while non-exposed fetuses were delivered at 39 weeks + 6 days (SD = 10 days).

7.4.1.3 Foetal MR Measurements

It was possible to conduct measurements of organ volumes (brain, lungs and kidneys), placental volume, shoulder width, foetal volume and length using the data acquired from all the participants of this study. However, it was not possible to measure liver volume using the data acquired from all the participants of this study. Since foetal organ measurements (brain, lungs, liver and kidneys) were conducted on at least two sets of images, these measurements for each organ were averaged; the individual measurements varied by approximately 0% – 11%

of the mean across all fetuses. All these measurements were normally distributed.

As expected, the MR measurements confirmed that all the organ volumes (brain, lungs, liver and kidneys), foetal volume and foetal length increased significantly across gestation. Significant differences were also seen for these parameters between the two groups, with exposed fetuses demonstrating significantly lower measurements compared to non-exposed fetuses. Conversely, although the placental volume and shoulder width measurements demonstrated a significant increase across gestations, there was no significant difference between exposed and non-exposed groups. Only two measurements, kidney and foetal volume demonstrated a significant interaction between gestation and group, with the measurements significantly lower in the exposed group compared to non-exposed group.

The average value for all the measurements made on exposed and non-exposed fetuses across the two gestations is demonstrated in table 7.2. This table also contains the p-values obtained from statistical comparison performed using repeated measures analysis of variance (ANOVA). These values provide information on the effect of maternal smoking at each gestation and group for foetal organ growth, foetal growth and placental growth.

Measurements	Group	25 weeks	36 weeks	p-value		
		Mean ± SD	Mean ± SD	Gestation	Gestation and Group	Group
Brain Volume (cm ³)	Smoker	65.4 ± 7.9	242.2 ± 18.8	< 0.001*	0.134	0.001*
	Control	81.2 ± 14.0	282.8 ± 39.5			
Lung Volume (cm ³)	Smoker	33.8 ± 4.7	95.4 ± 19.3	< 0.001*	0.159	0.002*
	Control	46.8 ± 7.8	124.4 ± 25.6			
Liver Volume (cm ³)	Smoker	52.0 ± 8.7	189.7 ± 34.1	< 0.001*	0.076	0.035*
	Control	60.7 ± 9.4	212.6 ± 60.4			
Kidney Volume (cm ³)	Smoker	12.9 ± 4.5	32.4 ± 9.1	< 0.001*	0.004*	0.001*
	Control	19.4 ± 3.8	51.0 ± 10.2			
Foetal Volume (cm ³)	Smoker	569.9 ± 88.6	2186.5 ± 156.3	< 0.001*	0.004*	0.001*
	Control	749.3 ± 105.5	2890.7 ± 440.7			
Placenta Volume (cm ³)	Smoker	317.9 ± 127.0	759.0 ± 177.8	< 0.001*	0.690	0.118
	Control	422.6 ± 111.6	823.7 ± 169.6			
Shoulder Width (cm)	Smoker	7.1 ± 0.8	11.0 ± 1.0	< 0.001*	0.431	0.290
	Control	7.3 ± 0.5	11.8 ± 1.2			
Foetal Length (cm)	Smoker	32.1 ± 1.6	47.4 ± 1.9	< 0.001*	0.646	0.002*
	Control	35.2 ± 2.0	49.7 ± 1.9			

Table 7.2: The mean measurement and standard deviation for absolute organ volumes (brain, lungs, liver and kidneys), placental volume, shoulder width, foetal volume and length at 25 weeks and 36 weeks. Comparisons are made using repeated measures ANOVA with the Bonferroni correction applied across ROIs. (Note: * indicates statistically significant p-values.)

Figure 7.6 and 7.7 demonstrates the effect of maternal smoking on foetal organ volumes (brain, lungs, liver and kidneys), while figure 7.8 and 7.9 demonstrates the effect of maternal smoking on foetal volume, placental volume, foetal length and shoulder width at two gestations.

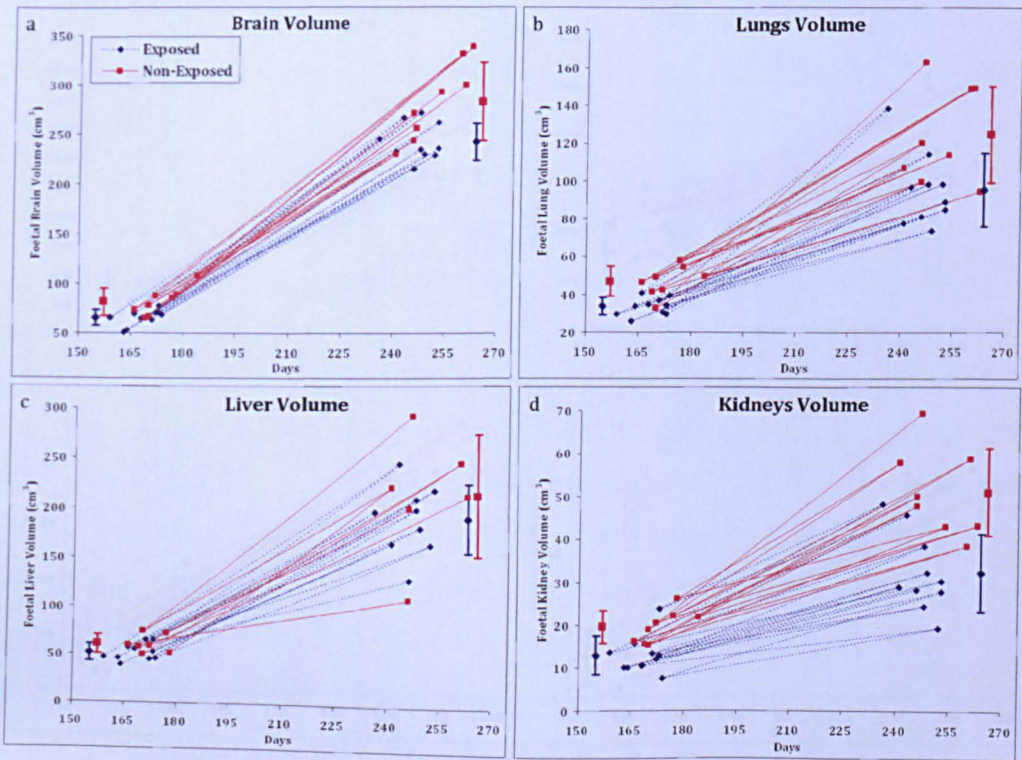


Figure 7.6: Scatter plot of the difference in foetal organ volumes: (a) brain, (b) lungs, (c) liver and (d) kidneys for exposed and non-exposed fetuses across two gestations. Marker lines are added allowing comparison of the two measurements for each individual subject. The mean value and the standard deviation are also displayed for the two groups on the left and right of the image, [red – non-exposed fetuses; blue – exposed fetuses].

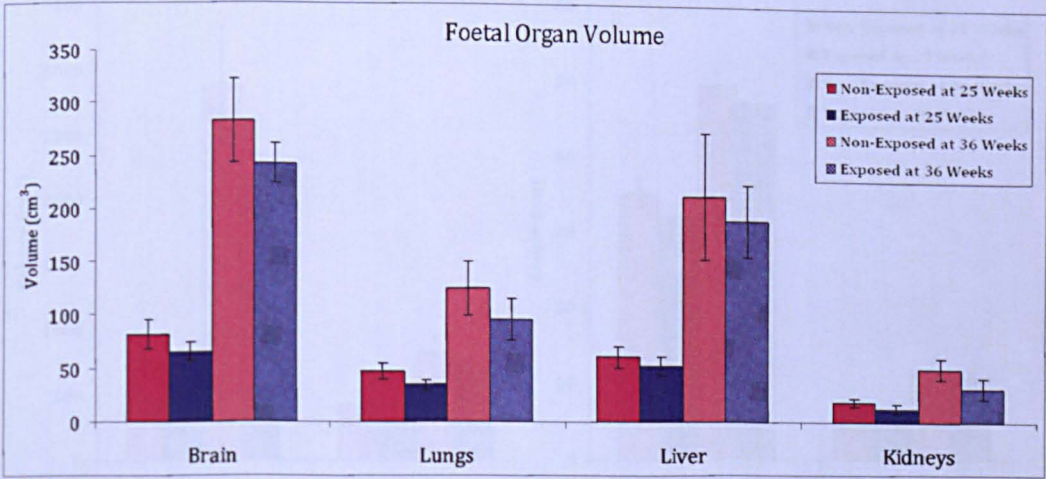


Figure 7.7: Boxplots of the effect of maternal smoking on foetal organ volumes: the mean and standard deviation of the brain, lungs, liver, and kidneys volume for exposed and non-exposed fetuses at 25 weeks and 36 weeks are plotted separately.

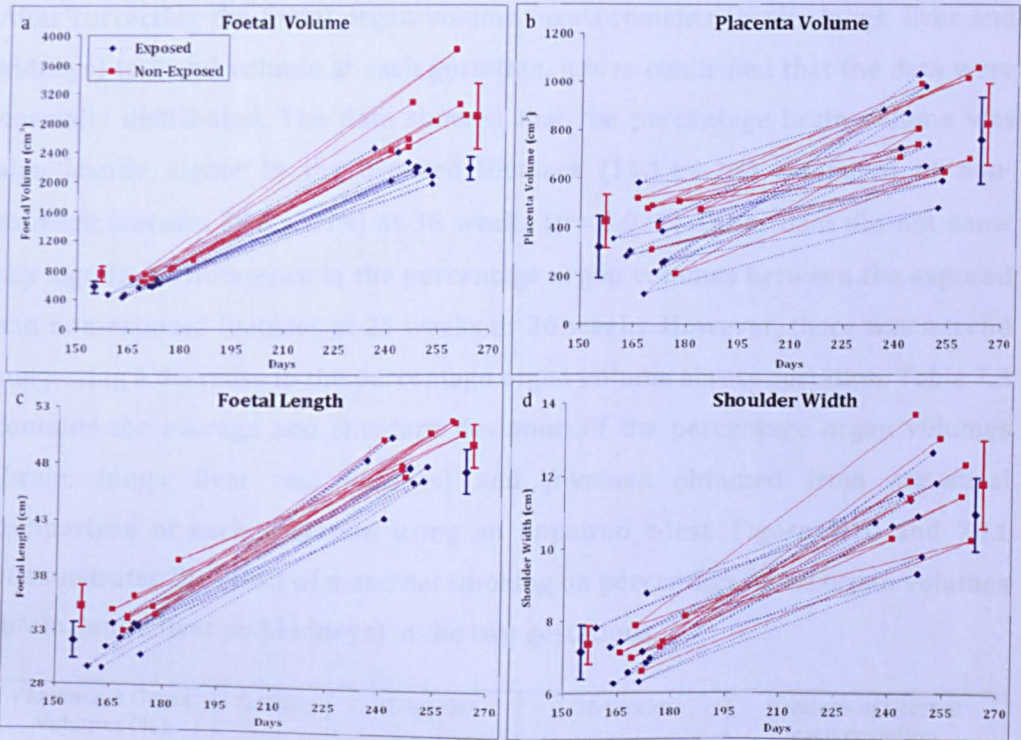


Figure 7.8: Scatter plot of the difference in (a) foetal volume, (b) placental volume, (c) foetal length and (d) shoulder width for exposed and non-exposed fetuses across two gestations. Marker lines are added allowing comparison of the two measurements for each individual subject. The mean value and the standard deviation are also displayed for the two groups on the left and right of the image, [red - non-exposed fetuses; blue - exposed fetuses].

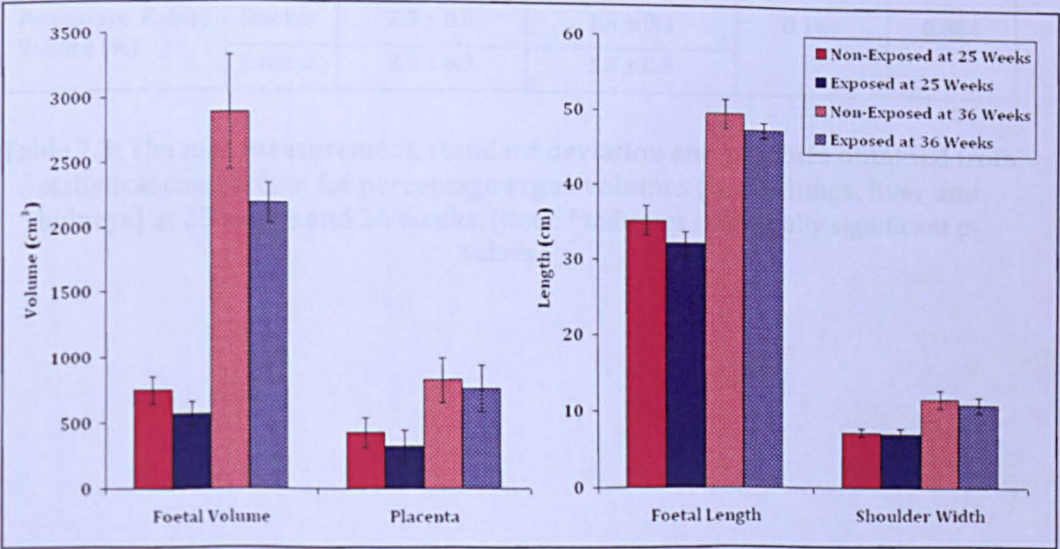


Figure 7.9: Boxplots of the effect of maternal smoking on foetal volume, placental volume, foetal length and shoulder width. The mean and standard deviation of each individual measurement for exposed and non-exposed fetuses at 25 weeks and 36 weeks are plotted separately.

After correcting the foetal organ volume measurements (brain, lungs, liver and kidneys) to foetal volume at each gestation, it was confirmed that the data were normally distributed. The data showed that the percentage brain volume was significantly higher in the exposed fetuses ($11.1 \pm 1.1\%$) compared to non-exposed fetuses ($9.8 \pm 1.1\%$) at 36 weeks ($p = 0.027$). Other data did not show any significant difference in the percentage organ volumes between the exposed and non-exposed fetuses at 25 weeks or 36 weeks. However, there was a trend suggesting a decrease in the percentage organ volume across gestation. Table 7.3 contains the average and standard deviation of the percentage organ volumes (brain, lungs, liver and kidneys) and p-values obtained from statistical comparison at each gestation using an unpaired t-test. Figure 7.10 and 7.11 demonstrates the effect of maternal smoking on percentage foetal organ volumes (brain, lungs, liver and kidneys) at the two gestations.

Percentage Organ Volumes (%)	Group	25 weeks	36 weeks	p-values of t-test at each gestation	
		Mean \pm SD	Mean \pm SD	25 weeks	36 weeks
Percentage Brain Volume (%)	Smoker	11.8 \pm 1.1	11.1 \pm 1.1	0.113	0.027*
	Control	10.8 \pm 0.8	9.8 \pm 1.1		
Percentage Lung Volume (%)	Smoker	6.0 \pm 0.8	4.4 \pm 0.7	0.468	0.900
	Control	6.3 \pm 1.0	4.3 \pm 0.6		
Percentage Liver Volume (%)	Smoker	9.2 \pm 1.2	8.6 \pm 1.5	0.229	0.315
	Control	8.4 \pm 1.2	7.7 \pm 1.9		
Percentage Kidney Volume (%)	Smoker	2.3 \pm 0.6	1.5 \pm 0.3	0.184	0.084
	Control	2.9 \pm 0.3	1.8 \pm 0.5		

Table 7.3: The mean measurement, standard deviation and p-values obtained from statistical comparison for percentage organ volumes (brain, lungs, liver and kidneys) at 25 weeks and 36 weeks. (Note: * indicates statistically significant p-values.)

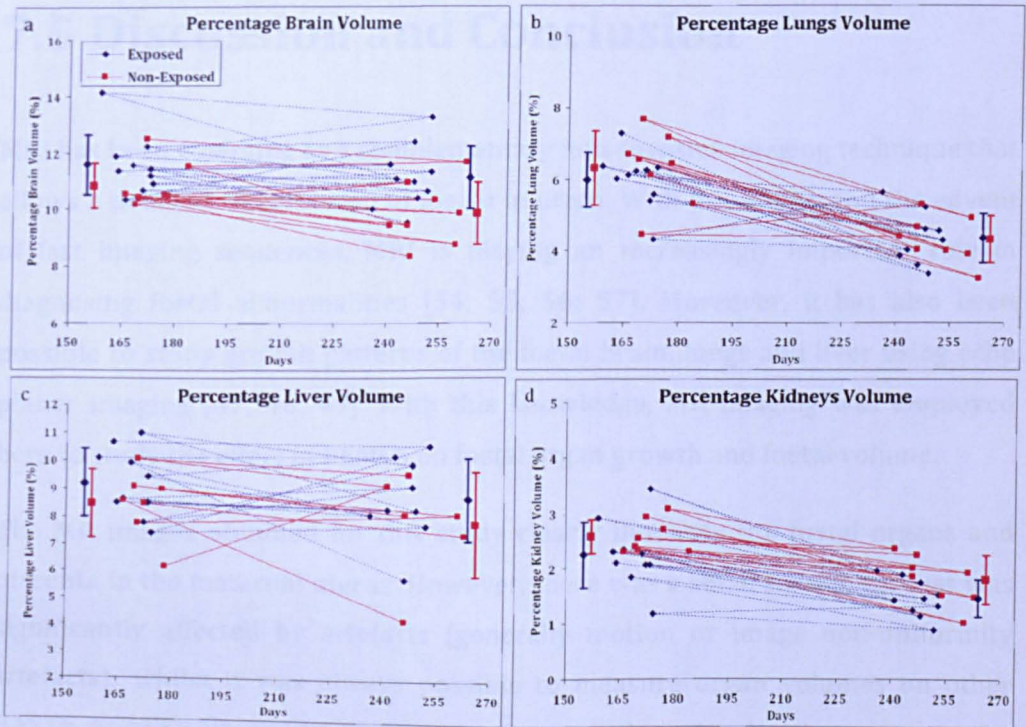


Figure 7.10: Scatter plot of the difference in foetal organ volumes: (a) brain, (b) lungs, (c) liver and (d) kidneys for exposed and non-exposed fetuses across two gestations. Marker lines are added allowing comparison of the two measurements for each individual subject. The mean value and the standard deviation are also displayed for the two groups on the left and right of the image, [red – non-exposed fetuses; blue – exposed fetuses].

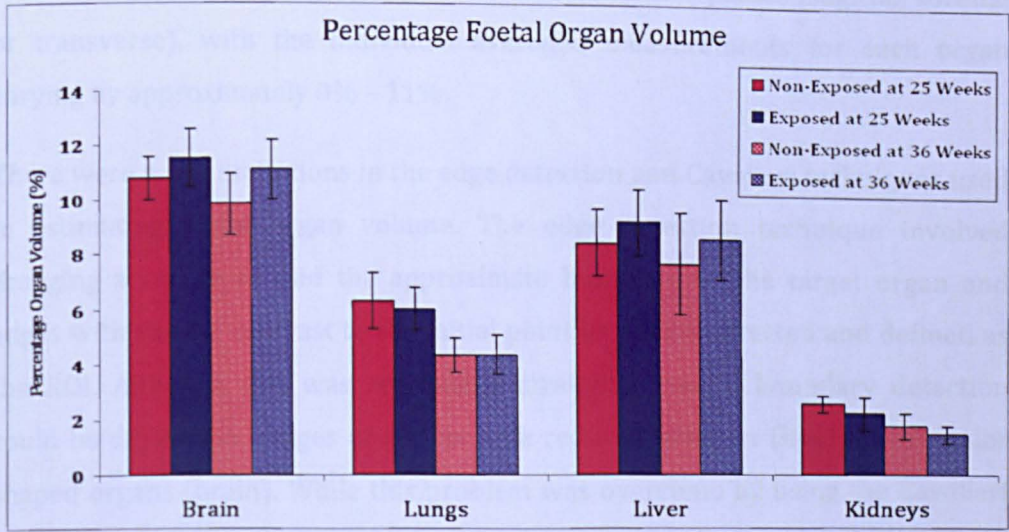


Figure 7.11: Boxplots of the effect of maternal smoking on percentage foetal organ volumes: the mean and standard deviation of the brain, lungs, liver, and kidneys volume for exposed and non-exposed fetuses at 25 weeks and 36 weeks are plotted separately.

7.5 Discussion and Conclusion

MRI has been emerging as a complementary non-invasive imaging technique that allows a detailed visualisation of foetus in utero. With this ability and the advent of fast imaging sequences, MRI is playing an increasingly important role in diagnosing foetal abnormalities [54; 55; 56; 57]. Moreover, it has also been possible to study growth patterns of the foetal brain, lungs and liver using echo planar imaging [47; 48; 49]. With this knowledge, MR imaging was employed here to study the effect of PEMCS on foetal organ growth and foetal volume.

The MR images obtained for this study clearly illustrate the foetal organs and placenta in the maternal uterus. However, there was a small sample set that was significantly affected by artefacts (generally motion or image non-uniformity artefacts); whilst it was always possible to measure organ volumes on other HASTE or bFFE images in such cases, there will have been some errors in the final results. In addition, even though MRI techniques are robust in acquiring anatomical images, foetal imaging is more challenging with unpredictable foetal positions and some foetal parts can lie outside the selected field of view of the MR image (especially at third trimester). However, this was overcome by effectively oversampling and routinely acquiring repeated data in different orientations. Measurements of each organ were made on at least two planes (sagittal, coronal or transverse), with the individual averaged measurements for each organ varying by approximately 0% – 11%.

There were a few limitations in the edge detection and Cavalieri techniques used in estimating foetal organ volume. The edge detection technique involved dragging a cursor around the approximate boundary of the target organ and edges with similar contrast to the initial point would be detected and defined as the ROI. Although this was reasonably straight forward, boundary detection could be difficult in images of organs with reduced contrast (liver) or irregular shaped organs (brain). While this problem was overcome by using the Cavalieri technique, the stereology method can be tricky since observers need to decide how to assign points at the organ boundaries.

The results from the present study demonstrate that PEMCS affects the growth of the foetus. In general, the ultrasound data demonstrated that the head circumference and abdominal circumference of exposed fetuses were

significantly lower compared to non-exposed fetuses at 25 weeks and 36 weeks. A similar trend was observed for femur length, where exposed fetuses had shorter femur lengths compared to non-exposed fetuses. However, the data only showed a significant difference between the groups at 25 weeks. These data contradict previous published work, which suggests PEMCS has a greater effect on peripheral tissues; where the significant decrease seen in the femur length of exposed fetuses at mid-pregnancy persisted across gestation [58]. Our data may be affected by the trend for the exposed group to have been scanned earlier than the non-exposed group, although statistical analysis failed to demonstrate a significant difference in the timing of the MR scans.

In addition, the birth weights of exposed fetuses were significantly lower compared to non-exposed fetuses. This study confirms that smoking during pregnancy increases the risk of low birth weight. Other studies investigating the effect of passive and active smoking during pregnancy have proposed foetal weight reduction is secondary to a decrease in fat free mass [27; 59; 60; 61; 62]. Ideally, this can be investigated in future using the techniques described in Chapter 6. In addition, it has been reported that PEMCS enhances the risk of low birth weight in infants of twin pregnancies [63]. However, as expected studies have proposed that infant's birth weight can be improved by reducing the level of exposure (less than 8 cigarettes per day) [64].

Correspondingly, although the MR measurements suggest that the foetal volume and length increases significantly across gestation in both groups, the exposed fetuses demonstrated a significantly reduced foetal volume and length compared to non-exposed fetuses at both gestations. These data suggest that fetuses exposed to maternal smoking are at risk of being small for gestational age. This agrees with the work of Mitchell et al. [22] and Fortier et al. [65], which independently proposed that PEMCS increases the risk of delivering babies who are small for gestational age. In addition, despite a trend suggesting that foetal shoulder widths were reduced in fetuses of the exposed group, this data did not demonstrate significant difference between the exposed and non-exposed groups.

While foetal organ volumes increase across gestation, the data show that PEMCS has a negative effect on foetal organ volumes. Here, the exposed fetuses had significantly lower absolute brain, lungs, liver and kidneys volumes compared to

non-exposed fetuses. When the organ volumes were corrected to foetal volume, the percentage volume of brain, lungs, liver and kidneys demonstrated a decrease across gestation. This is understandable since foetal organs are expected to grow with the foetal size at each gestation. In addition, at 36 weeks, the data showed a significantly lower percentage of brain volume in fetuses not exposed to maternal smoking. This may indicate that although absolute brain volume measurements are reduced, brain size and growth is relatively preserved compared to other organ volumes in the exposed group and reflected by the higher percentage brain volume.

The data suggest that PEMCS predominantly affects the growth of the foetal kidney; with absolute kidney volume significantly reduced in fetuses exposed to maternal smoking. This result is supported by findings presented by Pausova et al. [39] that documented a decrease in the kidney weight in pups of pregnant rats exposed to nicotine. Similarly, it is reported that there is a positive association between kidney malformation and maternal smoking [66]. Whilst the interaction of carbon dioxide and nicotine in kidney organogenesis is not clear, maternal smoking can cause disturbances in the interaction between the ureteric bud and the metanephric mesenchyme. Moreover, numerous immature renal corpuscles have been observed in fetuses exposed to maternal smoking, suggesting a disturbed kidney development [67].

The absolute foetal brain volume results agree with the clinical results of decreased head circumference. This is possibly due to interference of nicotine with foetal brain development that results in synaptic dysfunction and increased cell damage, loss and death in cortex and cerebellum [35; 68; 69]. In addition, PEMCS is also reported to cause reduction in corpus callosum of female fetuses [14]. With this set of data, it is tempting to speculate that reduced growth of the foetal brain and head circumference is one of the mediators in the relationship between PEMCS and behaviour in offspring, as several studies have demonstrated poorer cognitive function and neuropsychological abilities at early stages of school in infants exposed to PEMCS [70; 71].

PEMCS also affects the growth of foetal lungs, where exposed fetuses have reduced absolute lung volume compared to the non-exposed fetuses. This agrees with animal studies demonstrating reduced lung weight in rat pups, possibly due to reduction in the airway size [72]. While it is not clear how carbon

dioxide interferes with foetal lung growth, recent studies have suggested nicotine interferes with the integrity of the alveoli [33]: increasing the number of foetal alveolar type II pneumocytes and decreasing the alveolar type I pneumocytes in the foetal lung. Moreover, studies have reported the absence of microvilli in the exposed alveolar surface where gas exchange occurs and increased numbers of lamellar bodies in type II cells. These lamellar bodies serve to package the surfactant that plays a role in decreasing surface tension in the alveolar membrane that is required to assist neonatal respiration [73]. In addition, nicotine is also reported to interfere with the elastic tissue formation in the rat neonatal lung, with subsequent development of emphysema like damage in the neonatal lungs [74].

While there are very few studies on the effect of PEMCS on human foetuses, a study on exposed human foetal lung showed changes in the connective tissue, evidence of hyperplasia of the bronchi muscular membrane and intensified apoptosis of lung parenchyma cells [67]. Cellular differentiation in these tissues usually occurs during the canalicular stage that takes place around 17th – 26th weeks of gestation, which would possibly cause a prolonged slow down in foetal lung growth across gestation. There is also evidence suggesting increased risk of reduced respiratory function in infants exposed to maternal smoking during pregnancy [75]. With all these findings, it would be interesting to study the dynamics of foetal lung fluid production and its retention within the future airway in foetuses exposed to maternal smoking. This will assist in characterising foetal breathing movement in association with PEMCS since these functions are considered to be major determinants of foetal lung growth [76].

In studying the effect of PEMCS on the foetal liver, the MR measurements of foetal liver showed significant decrease in the absolute liver volume of exposed foetuses compared to non-exposed foetuses. This is possibly due to pronounced abnormal changes in the haematopoiesis (blood formation) and cell proliferation around the liver tissues, as seen in liver tissues of exposed rat pups [67]. In addition, PEMCS has also been associated with significantly altered transcript expression (mRNA) in the liver, with increased response in the male foetuses [77]. Moreover, it has been suggested that intracellular damage can occur in the liver due to increased production of oxygen-derived free radicals in the reperfused hypoxic tissues, which can possibly take place due to maternal

smoking [37]. All these effects might be contributing factors to reduced liver volume in foetuses exposed to maternal smoking.

The placental volume data demonstrated a trend of reduced placental volume in PEMCS. However, this result did not show significant difference between the smoking and non-smoking mothers and agrees with the findings of Ellard et al. [62] that reported placental weights were unaffected by maternal smoking. However, several studies have documented a negative effect of PEMCS on placental structure (more obvious in placentae of heavy smokers): evidence of increased apoptotic and damaged cells and reduced invasion of cytotrophoblasts (CTB), which performs critical functions including the generation of a syncytiotrophoblastic layer of transport epithelium and the generation of specialised CTB population that anchors the placenta to uterine wall and remodels the uterine vasculature [36; 78; 79]. Further studies are in progress and will involve relating placental diffusion in PEMCS to placental weight and morphology.

In conclusion, the results of the present study demonstrate that intrauterine exposure to cigarette smoking significantly affects foetal organ growth, predominantly the foetal kidneys. Cigarette compounds possibly influence excessive cell death and inhibit general growth of foetal tissue within specific organs. Hence, the reduced organ volume and foetal size (volume and birth weight). Moreover, PEMCS could perhaps be the plausible mechanism behind the potential overall increased risk of miscarriage, sudden infant death syndrome and multiple malformations in infants of smoking mothers.

7.6 References

- [1] P.D. Gluckman, M.A. Hanson, C. Cooper, and K.L. Thornburg. (2008), Effect of In Utero and Early-Life Conditions on Adult Health and Disease. *New England Journal of Medicine* **359** 61-73.
- [2] W.J. Larsen, L.S. Sherman, S.S. Potter, and W.J. Scott. (2001), *Human Embryology*, Livingstone, New York.
- [3] C.W. Kuzawa. (2005), Fetal origins of developmental plasticity: Are fetal cues reliable predictors of future nutritional environments? *American Journal of Human Biology* **17** 5-21.
- [4] D.O. Mook-Kanamori, E.A.P. Steegers, P.H. Eilers, H. Raat, A. Hofman, and V.W.V. Jaddoe. (2010), Risk Factors and Outcomes Associated With First-Trimester Fetal Growth Restriction. *JAMA: The Journal of the American Medical Association* **303** 527-534.
- [5] R.L. Andres, and M.-C. Day. (2000), Perinatal complications associated with maternal tobacco use. *Seminars in Neonatology* **5** 231-241.
- [6] E. Oken, E.B. Levitan, and M.W. Gillman. (2007), Maternal smoking during pregnancy and child overweight: systematic review and meta-analysis. *International Journal Obesity* **32** 201-210.
- [7] C. Syme, M. Abrahamowicz, A. Mahboubi, G.T. Leonard, M. Perron, L. Richer, S. Veillette, D. Gaudet, T. Paus, and Z. Pausova. (2009), Prenatal Exposure to Maternal Cigarette Smoking and Accumulation of Intra-abdominal Fat During Adolescence. *Obesity* **18** 1021-1025.
- [8] C.T. Orleans, D.C. Barker, N.J. Kaufman, and J.F. Marx. (2000), Helping pregnant smokers quit: meeting the challenge in the next decade. *Tobacco Control* **9** iii6-iii11.
- [9] T. Taylor, D. Lader, A. Bryant, L. Keyse, and M.T. Joloza. (2006), *Smoking-related behaviour and attitudes, 2005*, Office for National Statistics, London.
- [10] B. Haglund, and S. Cnattingius. (1990), Cigarette smoking as a risk factor for sudden infant death syndrome: a population-based study. *American Journal Public Health* **80** 29-32.
- [11] H.V. Meredith. (1975), Relation between tobacco smoking of pregnant women and body size of their progeny: a compilation and synthesis of published studies. *Human Biology* **47** 451-72.

- [12] P.-H. Persson, L. Grennert, G. Gennser, and S. Kullander. (1978), A Study of Smoking and Pregnancy with Special Reference to Fetal Growth. *Acta Obstetricia et Gynecologica Scandinavica* **57** 33-39.
- [13] G.S. Berkowitz, and E. Papiernik. (1993), Epidemiology of preterm birth. *Epidemiologic Reviews* **15** 414-43.
- [14] T. Paus, I. Nawazkhan, G. Leonard, M. Perron, G.B. Pike, A. Pitiot, L. Richer, S. Veillette, and Z. Pausova. (2008), Corpus callosum in adolescent offspring exposed prenatally to maternal cigarette smoking. *NeuroImage* **40** 435-441.
- [15] L.S. Wakschlag, B.B. Lahey, R. Loeber, S.M. Green, R.A. Gordon, and B.L. Leventhal. (1997), Maternal Smoking During Pregnancy and the Risk of Conduct Disorder in Boys. *Arch Gen Psychiatry* **54** 670-676.
- [16] P.A. Fried, B. Watkinson, and R. Gray. (1992), A follow-up study of attentional behavior in 6-year-old children exposed prenatally to marihuana, cigarettes, and alcohol. *Neurotoxicology and Teratology* **14** 299-311.
- [17] P.A. Fried, and B. Watkinson. (1988), 12- and 24-month neurobehavioural follow-up of children prenatally exposed to marihuana, cigarettes and alcohol. *Neurotoxicology and Teratology* **10** 305-313.
- [18] P.A. Fried, and B. Watkinson. (1990), 36- and 48-Month Neurobehavioral Follow-up of Children Prenatally Exposed to Marijuana, Cigarettes, and Alcohol. *Journal of Developmental & Behavioral Pediatrics* **11** 49-58.
- [19] J.L. Gusella, and P.A. Fried. (1984), Effects of maternal social drinking and smoking on offspring at 13 months. *Neurobehavioral Toxicology & Teratology*. **6** 13-17.
- [20] S. Milberger, J. Biederman, S.V. Faraone, and J. Jones. (1998), Further evidence of an association between maternal smoking during pregnancy and attention deficit hyperactivity disorder: findings from a high-risk sample of siblings. *Journal of Clinical Child Psychology* **27** 352-8.
- [21] B.L. Horta, C.G. Victora, A.M. Menezes, R. Halpern, and F.C. Barros. (1997), Low birthweight, preterm births and intrauterine growth retardation in relation to maternal smoking. *Paediatric and Perinatal Epidemiology* **11** 140-151.
- [22] E.A. Mitchell, J.M.D. Thompson, E. Robinson, C.J. Wild, D.M.O. Becroft, P.M. Clark, N. Glavish, N.S. Pattison, and J.E. Pryor. (2002), Smoking, nicotine

- and tar and risk of small for gestational age babies. *Acta Pædiatrica* **91** 323-328.
- [23] M.S. Kramer. (1987), Determinants of low birth weight: methodological assessment and meta-analysis. *Bulletin of the World Health Organization* **65** 663-737.
- [24] E.L. Abel. (1980), Smoking during pregnancy: a review of effects on growth and development of offspring. *Human Biology* **52** 593-625.
- [25] R.D. Walsh. (1994), Effects of maternal smoking on adverse pregnancy outcomes: Examination of the criteria of causation. *Human Biology* **66** 1059-1092.
- [26] M.B. Meyer, B.S. Jonas, and J.A. Tonascia. (1976), Perinatal events associated with maternal smoking during pregnancy. *American Journal of Epidemiology* **103** 464-476.
- [27] C.A. Lindsay, A.J. Thomas, and P.M. Catalano. (1997), The effect of smoking tobacco on neonatal body composition. *American Journal of Obstetrics and Gynecology* **177** 1124-1128.
- [28] R. von Kries, A.M. Toschke, B. Koletzko, and W. Slikker. (2002), Maternal Smoking during Pregnancy and Childhood Obesity. *American Journal of Epidemiology* **156** 954-961.
- [29] A. Toschke, B. Koletzko, W. Slikker, M. Hermann, and R. von Kries. (2002), Childhood obesity is associated with maternal smoking in pregnancy. *European Journal of Pediatrics* **161** 445-448.
- [30] C. Power, and B.J.M.H. Jefferis. (2002), Fetal environment and subsequent obesity: a study of maternal smoking. *International Journal of Epidemiology* **31** 413-419.
- [31] E.P. Hill, J.R. Hill, G.G. Power, and L.D. Longo. (1977), Carbon monoxide exchanges between the human fetus and mother: a mathematical model. *American Journal of Physiology - Heart and Circulatory Physiology* **232** H311-H323.
- [32] W. Luck, H. Nau, R. Hansen, and R. Steldinger. (1985), Extent of nicotine and cotinine transfer to the human fetus, placenta and amniotic fluid of smoking mothers. *Developmental Pharmacology and Therapeutics* **8** 384-95.
- [33] D.S. Lambers, and K.E. Clark. (1996), The maternal and fetal physiologic effects of nicotine. *Seminars in Perinatology* **20** 115-126.

- [34] M.E. Quigley, K.L. Sheehan, M.M. Wilkes, and S.S. Yen. (1979), Effects of maternal smoking on circulating catecholamine levels and fetal heart rates. *American Journal of Obstetrics and Gynecology* **133** 685-90.
- [35] T.A. Slotkin. (1998), Fetal Nicotine or Cocaine Exposure: Which One is Worse? *Journal of Pharmacology and Experimental Therapeutics* **285** 931-945.
- [36] P.C. Czekaj, A.P. Pałasz, T.L.-W. Lebda-Wyborny, G.N.-D. Nowaczyk-Dura, W.K. Karczewska, E.F. Florek, and M.K. Kamiński. (2002), Morphological changes in lungs, placenta, liver and kidneys of pregnant rats exposed to cigarette smoke. *International Archives of Occupational and Environmental Health* **75** 27-35.
- [37] K. Kusterer, C. Blochle, T. Konrad, K.D. Palitzsch, and K.H. Usadel. (1993), Rat liver injury induced by hypoxic ischemia and reperfusion: protective action by somatostatin and two derivatives. *Regulatory Peptides* **44** 251-256.
- [38] D.J. Garvey, and L.D. Longo. (1978), Chronic Low Level Maternal Carbon Monoxide Exposure and Fetal Growth and Development. *Biology of Reproduction* **19** 8-14.
- [39] Z. Pausova, T. Paus, L. Sedova, and J. Berube. (2003), Prenatal exposure to nicotine modifies kidney weight and blood pressure in genetically susceptible rats: A case of gene-environment interaction. *Kidney International* **64** 829-835.
- [40] T.A. Slotkin, L. Orband-Miller, and K.L. Queen. (1987), Development of [3H]nicotine binding sites in brain regions of rats exposed to nicotine prenatally via maternal injections or infusions. *Journal of Pharmacology and Experimental Therapeutics* **242** 232-237.
- [41] H.A. Navarro, F.J. Seidler, J.P. Eylers, F.E. Baker, S.S. Dobbins, S.E. Lappi, and T.A. Slotkin. (1989), Effects of prenatal nicotine exposure on development of central and peripheral cholinergic neurotransmitter systems. Evidence for cholinergic trophic influences in developing brain. *Journal of Pharmacology and Experimental Therapeutics* **251** 894-900.
- [42] H.A. Navarro, F.J. Seidler, W.L. Whitmore, and T.A. Slotkin. (1988), Prenatal exposure to nicotine via maternal infusions: effects on development of catecholamine systems. *Journal of Pharmacology and Experimental Therapeutics* **244** 940-944.

- [43] G.J. Burton, M.E. Palmer, and K.J. Dalton. (1989), Morphometric differences between the placental vasculature of non-smokers, smokers and ex-smokers. *BJOG: An International Journal of Obstetrics and Gynaecology* **96** 907-915.
- [44] W.J. Van der Velde, J.H.J. Copius Peereboom-Stegeman, P.E. Treffers, and J. James. (1983), Structural changes in the placenta of smoking mothers: A quantitative study. *Placenta* **4** 231-240.
- [45] E. Jauniaux, and G.J. Burton. (1992), The effect of smoking in pregnancy on early placental morphology. *Obstetrics and Gynecology* **79** 645-8.
- [46] L.C. Castro, R. Allen, D. Ogunyemi, K.A.Y. Roll, and L.D. Platt. (1993), Cigarette Smoking During Pregnancy: Acute Effects on Uterine Flow Velocity Waveforms. *Obstetrics and Gynecology* **81** 551-555.
- [47] A.S. Garden, and N. Roberts. (1996), Fetal and fetal organ volume estimations with magnetic resonance imaging. *American Journal of Obstetrics and Gynecology* **175** 442-448.
- [48] P.N. Baker, I.R. Johnson, P.A. Gowland, A. Freeman, V. Adams, and P. Mansfield. (1994), Estimation of fetal lung volume using echo-planar magnetic resonance imaging. *Obstetrics and Gynecology* **83** 951-4.
- [49] P.N. Baker, I.R. Johnson, P.A. Gowland, J. Hykin, P.R. Harvey, A. Freeman, V. Adams, P. Mansfield, and B.S. Worthington. (1994), Fetal weight estimation by echo-planar magnetic resonance imaging. *The Lancet* **343** 644-645.
- [50] C.-O. LM, and N. Roberts. (1993), Unbiased volume estimation with coaxial sections: an application to the human bladder. *Journal of Microscopy* **170** 25-33.
- [51] N. Roberts, A.S. Garden, L.M. Cruz-Orive, G.H. Whitehouse, and R.H.T. Edwards. (1994), Estimation of fetal volume by magnetic resonance imaging and stereology. *British Journal of Radiology* **67** 1067-1077.
- [52] Q.Y. Gong, N. Roberts, A.S. Garden, and G.H. Whitehouse. (1998), Fetal and Fetal Brain Volume Estimation in the Third Trimester of Human Pregnancy Using Gradient Echo MR Imaging. *Magnetic Resonance Imaging* **16** 235-240.
- [53] N. Roberts, M.J. Puddephat, and V. McNulty. (2000), The benefit of stereology for quantitative radiology. *British Journal of Radiology* **73** 679-697.

- [54] M. Cannie, J. Jani, S. Dymarkowski, and J. Deprest. (2006), Fetal magnetic resonance imaging: luxury or necessity? *Ultrasound in Obstetrics and Gynecology* **27** 471-476.
- [55] C. Raybaud, O. Levrier, H. Brunel, N. Girard, and P. Farnarier. (2003), MR imaging of fetal brain malformations. *Child's Nervous System* **19** 455-470.
- [56] C. Garel. (2008), Fetal MRI: what is the future? *Ultrasound in Obstetrics and Gynecology* **31** 123-128.
- [57] E.H. Whitby, M.N.J. Paley, A. Sprigg, S. Rutter, N.P. Davies, I.D. Wilkinson, and P.D. Griffiths. (2004), Comparison of ultrasound and magnetic resonance imaging in 100 singleton pregnancies with suspected brain abnormalities. *BJOG: An International Journal of Obstetrics and Gynaecology* **111** 784-792.
- [58] V.W.V. Jaddoe, B.O. Verburg, M.A.J. de Ridder, A. Hofman, J.P. Mackenbach, H.t.A. Moll, E.A.P. Steegers, and J.C.M. Witteman. (2007), Maternal Smoking and Fetal Growth Characteristics in Different Periods of Pregnancy. *American Journal of Epidemiology* **165** 1207-1215.
- [59] S.H. Fox, T.D. Koepsell, and J.R. Daling. (1994), Birth Weight and Smoking During Pregnancy-Effect Modification by Maternal Age. *American Journal of Epidemiology* **139** 1008-1015.
- [60] V.W.V. Jaddoe, E.-J.W.M. Troe, A. Hofman, J.P. Mackenbach, H.A. Moll, E.A.P. Steegers, and J.C.M. Witteman. (2008), Active and passive maternal smoking during pregnancy and the risks of low birthweight and preterm birth: the Generation R Study. *Paediatric and Perinatal Epidemiology* **22** 162-171.
- [61] A.J. Wilcox. (1993), Birth Weight and Perinatal Mortality: The Effect of Maternal Smoking. *American Journal of Epidemiology* **137** 1098-1104.
- [62] G.A. Ellard, F.D. Johnstone, R.J. Prescott, W. Ji-Xian, and M. Jian-Hua. (1996), Smoking during pregnancy: the dose dependence of birthweight deficits. *BJOG: An International Journal of Obstetrics & Gynaecology* **103** 806-813.
- [63] H. Pollack, P.M. Lantz, and J.G. Frohna. (2000), Maternal smoking and adverse birth outcomes among singletons and twins. *American Journal of Public Health* **90** 395-400.
- [64] L.J. England, J.S. Kendrick, H.G. Wilson, R.K. Merritt, P.M. Gargiullo, and S.C. Zahniser. (2001), Effects of Smoking Reduction during Pregnancy on the

- Birth Weight of Term Infants. *American Journal of Epidemiology* **154** 694-701.
- [65] I. Fortier, S. Marcoux, and J. Brisson. (1994), Passive Smoking during Pregnancy and the Risk of Delivering a Small-for-Gestational-Age Infant. *American Journal of Epidemiology* **139** 294-301.
- [66] K. Kallen. (1997), Maternal smoking and urinary organ malformations. *International Journal of Epidemiology* **26** 571-574.
- [67] E. Nelson, C. Goubet-Wiemers, Y. Guo, and K. Jodschkeit. (1999), Maternal passive smoking during pregnancy and foetal developmental toxicity. Part 2: histological changes. *Human & Experimental Toxicology* **18** 257-264.
- [68] T.A. Slotkin. (1999), Developmental Cholinotoxicants: Nicotine and Chlorpyrifos. *Environmental Health Perspectives* **107** 71-80.
- [69] S.J. Roza, B.O. Verburg, V.W.V. Jaddoe, A. Hofman, J.P. Mackenbach, E.A.P. Steegers, J.C.M. Witteman, F.C. Verhulst, and H. Tiemeier. (2007), Effects of maternal smoking in pregnancy on prenatal brain development. The Generation R Study. *European Journal of Neuroscience* **25** 611-617.
- [70] J. Peterson, H.G. Taylor, N. Minich, N. Klein, and M. Hack. (2006), Subnormal head circumference in very low birth weight children: Neonatal correlates and school-age consequences. *Early Human Development* **82** 325-334.
- [71] B.S. Peterson, B. Vohr, L.H. Staib, C.J. Cannistraci, A. Dolberg, K.C. Schneider, K.H. Katz, M. Westerveld, S. Sparrow, A.W. Anderson, C.C. Duncan, R.W. Makuch, J.C. Gore, and L.R. Ment. (2000), Regional Brain Volume Abnormalities and Long-term Cognitive Outcome in Preterm Infants. *JAMA: The Journal of the American Medical Association* **284** 1939-1947.
- [72] J.A. Bassi, P. Rosso, A.C. Moessinger, W.A. Blanc, and L. Stanley James. (1984), Fetal Growth Retardation due to Maternal Tobacco Smoke Exposure in the Rat. *Pediatric Research* **18** 127-130.
- [73] G.S. Maritz, and R.A. Thomas. (1995), Maternal nicotine exposure: reponse of type II pneumocytes of neonatal rat pups. *Cell Biology International* **19** 323-332.
- [74] G.S. Maritz, K.M. Woolward, and G. Du Toit. (1993), Maternal nicotine exposure during pregnancy and development of emphysema-like damage in the offspring. *South African Medical Journal* **83** 195-199.

- [75] S.M. Stick, P.R. Burton, L. Gurrin, P.D. Sly, and P.N. LeSouef. (1996), Effects of maternal smoking during pregnancy and a family history of asthma on respiratory function in newborn infants. *The Lancet* **348** 1060-1064.
- [76] J.S. Wigglesworth. (1976), The effects of placental insufficiency on the fetal lung. *Journal of Clinical Pathology. Supplement (Royal College of Pathologists)* **10** 27-30.
- [77] P.J. O'Shaughnessy, A. Monteiro, S. Bhattacharya, and P.A. Fowler. (2011), Maternal Smoking and Fetal Sex Significantly Affect Metabolic Enzyme Expression in the Human Fetal Liver. *Journal of Clinical Endocrinology & Metabolism* **96** 2851-2860.
- [78] T. Zdravkovic, O. Genbacev, M.T. McMaster, and S.J. Fisher. (2005), The adverse effects of maternal smoking on the human placenta: A review. *Placenta* **26, Supplement** S81-S86.
- [79] K.T. Shiverick, and C. Salafia. (1999), Cigarette Smoking and Pregnancy I: Ovarian, Uterine and Placental Effects. *Placenta* **20** 265-272.

Chapter 8

Conclusion

The work described in this thesis was directed at investigating the effect of maternal diabetes and maternal smoking on foetal development using quantitative imaging techniques at 1.5 Tesla using a Philips Achieva MRI system.

Chapter 5 presents a robust method of acquiring placental images using EPI and analysing placental blood flow using the IVIM technique based on perfusion, f and diffusion, D factors. The first part of the chapter investigates the reliability and reproducibility of the IVIM program in measuring placental blood flow in the placenta, basal plate and chorionic plate by reviewing the measurement of average blood flow distribution (mean f), high blood flow region associated with upper end of the flow distribution (fraction of pixels with $f > 0.8$) and peak blood flow (mode f). The data suggest that the IVIM program is a reliable method in measuring placental perfusion; with mean and mode f being more reliable measure for placental perfusion compared to the fraction of pixels with $f > 0.8$. This is possibly because regions with high blood flow may include data points affected by noise and physiological motion (maternal and foetal heart rate along with maternal breathing). For this reason, fraction of pixels with $f > 0.8$ was not used in investigating the effect of maternal diabetes on placental perfusion.

The intra and inter-observer reliability based on intra-class correlation coefficient (ICC) and limit of agreement (LOA) results were comparable for all the observers, with observer 1 demonstrating the best reliability results. This is expected since observer 1 is the author who designed the program and had the most experience dealing with the data analysis of placental perfusion. However, measurements of other observers were not too discrepant, suggesting that the reliability could be improved with possible further training. In general, the reliability results were best in the placental region, followed by basal plate and chorionic plate. This is reasonable since the ROIs of basal plate and chorionic plate were small, mostly five to six voxels in extent in the MR images. Hence,

movements along these plates could cause errors in perfusion measurements in these areas. This is possibly the reason for lower degree of reliability for basal plate and chorionic plate.

In addition, two masking techniques were investigated: the single masking technique that involves drawing a different set of ROI for each repeat and multiple masking technique which uses a same set of ROI for all repeats. Both single and multiple masking techniques demonstrated very good intra-observer reliability. However, the multiple masking technique was employed to investigate the effect of maternal diabetes on placental blood flow since it was more time efficient compared to single masking technique. The placental perfusion comparison made on two adjacent slices demonstrated poor repeatability, but whether this is due to variations in placental structure between slices or whether it is due to the fundamental reproducibility of the data could only be proven by looking at intra-subject reproducibility. Therefore, placental perfusion measurement was only conducted on the MR images with the largest placental volume.

In applying the IVIM program to investigate the effect of maternal diabetes on placental blood flow, the data showed that there were no significant difference in the mean f measurements of placenta, basal plate and chorionic plate across gestation between the diabetic and control groups. However, the peak blood flow (mode f) increased significantly in the chorionic plate and basal plate of both groups across gestation. This is expected in chorionic plate since the growing foetus would require more nutrients and hence, the increased blood flow in this region. Similarly, the blood flow in basal plate (representing spiral artery blood flow) is expected to increase to sustain the growing foetus and maintain blood flow in the growing placentae. Moreover, there was a trend for mode f to be higher in the control group at second trimester, but at third trimester mode f was usually higher in the diabetic subjects. This result may be a statistical fluke but could also indicate adaptation to large foetal demand (macrosomic foetuses).

As for diffusion measurements (D) related to molecular mobility of water, there was a significant decrease in D of placenta, basal plate and chorionic plate across gestation, with a trend for D to be slightly higher in the control group for the basal plate and chorionic plate. This is consistent with increased villous branching across gestation and at a greater extent in diabetic placentae, which

could cause a reduction in the effective mean free path of blood movement within the intervillous space. This is possibly the reason for reduced diffusion across gestation; with an even more pronounced effect in diabetic placentae.

Chapter 6 describes the T_1 weighted water suppressed MRI scans used to acquire foetal fat images in-utero and a MATLAB program developed to estimate foetal fat. The first part of the chapter investigates the reliability of the MATLAB program in measuring foetal fat adiposity. The foetal fat volume measured using the Foetal Adiposity Quantification Program demonstrates very good intra and inter-observer reliability at third trimester but poorer reliability at second trimester; possibly due to very small amount of foetal fat present at second trimester (namely 24 weeks). Although the ICCs and LOA were best for observer 1, the author who designed the MATLAB program, the foetal fat volume measurements made by other observers were comparable, suggesting reliability could be improved with significant additional training.

Following the reliability test, the Foetal Adiposity Quantification Program was used to measure foetal fat volume in fetuses of diabetic and control mothers. The data suggests that foetal fat volume and percentage foetal fat volume were significantly greater in fetuses of diabetic mothers at 35 weeks. Similarly, the measurement of foetal length and abdominal circumference at 35 weeks and birth centile were significantly greater in fetuses of diabetic mothers. Although similar trend was seen for foetal volume, shoulder width and foetal volume index, the difference was not statistically significant between the diabetic and control group. This preliminary study has demonstrated that the technique employed here is a convenient and reliable method for measuring foetal fat volume in-utero. It clearly illustrates the differences in body composition between fetuses of mothers with and without diabetes. The combination of foetal fat volume with foetal volume measurements strengthens the reliability of the present study to allow detection of a macrosomic fetus with excess foetal growth due to adipose tissue and may assist in the identification of fetuses at risk of birth trauma.

Chapter 7 details the HASTE and bFFE scans used to acquire foetal images encompassing the whole fetus in three orthogonal blocks. These images were used to investigate the effect of prenatal exposure to cigarette smoking on foetal and foetal organ growth. The work presented in chapter 7 shows that prenatal exposure to cigarette smoking has significant negative effect on foetal organ

growth and foetal growth, predominantly foetal kidney and foetal volume. The MR measurements conducted using edge detection method and Cavalieri technique demonstrated that foetal organ volume increases significantly across gestation in both exposed and non-exposed group. However, exposed fetuses had significantly lower absolute brain, lungs, liver and kidney volumes compared to non-exposed fetuses. When the organ volumes were corrected to foetal volume, the percentage volume of brain, lungs, liver and kidneys demonstrated a decrease across gestation; possibility because foetal organs are expected to grow accordingly with the foetal size at each gestation. In addition, at 36 weeks, the data showed a significantly lower percentage brain volume in fetuses not exposed to maternal smoking. This may indicate that although absolute brain volume measurements are reduced, brain size and growth is relatively preserved compared to other organ volumes in the exposed group and reflected by the higher percentage brain volume.

Similarly, MR measurements of foetal volume and length demonstrated significant increase across gestation in both exposed and non-exposed group, with these measurements significantly reduced in fetuses exposed to maternal smoking. In addition, the birth weight of exposed fetuses was significantly lower than non-exposed fetuses. This suggests that exposed fetuses are at risk of being small for gestational age. Conversely, despite a trend suggesting that foetal shoulder width were reduced in fetuses of the exposed group, this data did not demonstrate significant difference between the exposed and non-exposed groups.

As for the ultrasound measurements, the data showed that the head and abdominal circumference of exposed fetuses were significantly lower compared to non-exposed fetuses at 25 weeks and 36 weeks. A similar trend was observed for femur length, where exposed fetuses had shorter femur lengths compared to non-exposed fetuses. However, the data only showed a significant difference between the groups at 25 weeks. With all these data, cigarette compounds may possibly contribute to excessive cell death and inhibit general foetal tissue growth within specific organs resulting in reduced organ volume and foetal size (volume and birth weight).

In conclusion, MRI techniques employed in this study have great potential in non-invasive assessment of abnormal placental function and can be used to study

foetal development. This study shows that perturbations in the maternal womb, such as altered nutrition and exposure to harmful cigarette compounds can effect foetal development that may possibly program the foetus to develop disease in adult life. The programming effects on the foetus may be mediated by placental responses to these perturbations, which include abnormal villous branching and capillarisation, altered thickness of the placental barrier and increased toxicity stress in the placenta. Moreover, foetal nutrient consumption and exposure to toxic compound may hinder foetal growth. For these reason, it is important to manage maternal diabetes and cease maternal smoking. This will optimise placental structure and function, as well as foetal growth that are likely to promote lifelong health benefits for the offspring.

8.1 Future Work

At present, the reliability of IVIM program was conducted based on placental perfusion measurement. Ideally, the reliability of placental diffusion, intra-subject reproducibility and the number of acquisition required for reliable placental perfusion measurement should be investigated. Moreover, future work will involve simplifying the IVIM program to reduce processing time and average out movement or noise in the ROI for all the acquisition. Instead of using the current program that fits a ROI to each placenta acquisition, the data analysis can be improved by fitting the ROI once for all five acquisitions. This will involve averaging the ROI's pixel in all five acquisitions together before fitting the ROI to the signal attenuation equation.

To further understand the effect of maternal diabetes in pregnancy, the placental perfusion and diffusion should be correlated with maternal levels of hypoglycemia and foetal growth. This will provide an insight to how placental function varies in diabetes pregnancies and its affects on foetal growth, especially the foetal fat composition. Furthermore, the fast decaying component arising from the effect of spins from blood, which is characterised as pseudo-diffusion coefficient (D^*) should be investigated.

The work presented in Chapter 6 should now be extended to a larger study to determine whether the T_1 weighted water suppressed MRI scans and Foetal

Adiposity Quantification Program can be prospectively used to screen women at increased risk of delivering macrosomic infants, in particular women with gestational diabetes.

Furthermore, while the results reported in Chapter 7 clearly shows that maternal smoking affects foetal growth and foetal organ growth, further studies are now in progress to relate the effect of maternal smoking on placental perfusion and diffusion.

8.2 Final Overview

With advent of fast imaging MR sequences, foetal MRI is playing an increasing important role as complementary diagnosis tool to ultrasound for prenatal management and foetal abnormalities assessment. Although at present, ultrasound still remains as the modality of choice for routine prenatal imaging, the future of foetal MRI may change with advancement in technology, knowledge and management as well as growing medicolegal and socioeconomic pressure.

Appendix

The following publications have arisen from the work described in this thesis:

Journal Papers

1. The Effect of Maternal Diabetes on Fetal Adiposity (under preparation)
D. Anblagan, R. Deshpande, A. Pitiot, N. W. Jones, C. Costigan, G. Bugg, P. Mansell, N. R. Fenning, and P. A. Gowland
2. The Effect of Maternal Smoking on Fetal Organ Growth (under preparation)
D. Anblagan, N. W. Jones, A. J. J. Parker, G. Bugg, C. Costigan, R. Deshpande, L. Coyne, R. Aleong, N. Roberts, Z. Pausova, N. R. Fenning, T. Paus, and P. A. Gowland

Conference Abstracts

Oral Presentations

1. The Effect of Maternal Smoking on Fetal Organ Growth
D. Anblagan, N. W. Jones, A. J. Parker, G. Bugg, C. Costigan, R. Deshpande, L. Coyne, R. Aleong, N. Roberts, Z. Pausova, N. R. Fenning, T. Paus, and P. A. Gowland
International Society for Magnetic Resonance in Medicine (ISMRM) 2012, 20th Annual Meeting, Melbourne, Australia
2. The Effect of Maternal Diabetes on Placental Blood Flow Assessed Using IVIM
D. Anblagan, R. Deshpande, N. W. Jones, C. Costigan, N. R. Fenning, P. Mansell, G. Bugg, L. Leach, and P. A. Gowland
ISMRM 2011, 19th Annual Meeting, Montreal, Canada
3. Assessment of placental blood flow in diabetic pregnancies: Role of Magnetic Resonance Imaging
R. Deshpande, **D. Anblagan**, N. W. Jones, N. R. Fenning, L. Leach, P. Mansell, P. A. Gowland, G. Bugg
Diabetes in Pregnancy 2011, 6th International Symposium, Salzburg, Austria

4. MRI scanning: A novel technique for assessment of foetal adiposity in diabetic pregnancies

R. Deshpande, **D. Anblagan**, N. W. Jones, G. Bugg, L. Leach, P. A. Gowland, N. R. Fenning, P. Mansell

Diabetes in Pregnancy Study Group Meeting 2011, Cambridge, UK

5. MRI assessment of regional fractional moving blood volume within the placenta

R. Deshpande, N. W. Jones, **D. Anblagan**, G. Bugg, N. R. Fenning, L. Leach, P. Mansell, P. A. Gowland

International Society of Ultrasound in Obstetrics and Gynaecology (ISUOG) 2011, Los Angeles, USA

Electronic and Traditional Posters

1. Fetal Growth in Diabetic Pregnancies

D. Anblagan, R. Deshpande, N. W. Jones, A. Pitiot, C. Costigan, K. Allcock, N. R. Fenning, L. Leach, G. Bugg, P. Mansell, and P. A. Gowland

ISMRM 2012, 20th Annual Meeting, Melbourne, Australia

2. IVIM Assessment of the Placenta, Basal Plate and Chorionic Plate in Diabetic Pregnancies

D. Anblagan, R. Deshpande, N. W. Jones, C. Costigan, C. Wright, D. M. Morris, N. R. Fenning, L. Leach, G. Bugg, P. Mansell, and P. A. Gowland

ISMRM 2012, 20th Annual Meeting, Melbourne, Australia

3. The Effect of Maternal Diabetes on Fetal Adiposity

D. Anblagan, R. Deshpande, A. Pitiot, C. Costigan, N. W. Jones, G. Bugg, P. Mansell, N. R. Fenning, L. Leach, and P. A. Gowland

ISMRM 2011, 19th Annual Meeting, Montreal, Canada

4. Measuring Coherent Blood Flow in the Placenta, Basal Plate and Chorionic Plate

D. Anblagan, R. Deshpande, C. Costigan, N. W. Jones, G. Bugg, P. Mansell, N. R. Fenning, L. Leach, and P. A. Gowland

ISMRM 2011, 19th Annual Meeting, Montreal, Canada

5. The Effect of Maternal Smoking on Fetal Lung and Kidney Growth

D. Anblagan, C. Costigan, T. Paus, Z. Pausova, N. W. Jones, G. Bugg,
N. R. Fenning, and P. A. Gowland

ISMRM 2010, 18th Annual Meeting, Stockholm, Sweden

6. Reliability Test for Fetal Fat Programme

D. Anblagan, C. Costigan, A. Pitiot, T. Paus, Z. Pausova, N. W. Jones, G. Bugg,
R. Deshpande, M. Salmam, and P. A. Gowland

ISMRM 2010, 18th Annual Meeting, Stockholm, Sweden

7. Measuring Blood Flow in the Placenta using EPI at 1.5T

D. Anblagan, C. Costigan, R. Deshpande, G. Bugg, P. Mansell and P. A. Gowland

British Chapter ISMRM 2010, 16th Annual Meeting, Nottingham, UK